2005

Early Paleozoic Orogenesis in the Maine-Quebec Appalachians

Christopher Charles Gerbi

EARLY PALEOZOIC OROGENESIS IN THE MAINE-QUEBEC APPALACHIANS

By

Christopher Charles Gerbi

A.B. Amherst College, 1996

M.S. University of California, Davis, 1999

A THESIS

Submitted in Partial Fulfillment of the

Requirements for the Degree of

Doctor of Philosophy

(in Earth Sciences)

The Graduate School

The University of Maine

May, 2005

Advisory Committee:

Scott E. Johnson, Associate Professor of Earth Sciences, Advisor

Charles V. Guidotti, Professor of Earth Sciences

Peter O. Koons, Associate Professor of Earth Sciences

Cees R. van Staal, Research Scientist, Natural Resources Canada

Martin G. Yates, Associate Scientist of Earth Sciences

EARLY PALEOZOIC OROGENESIS IN THE MAINE-QUEBEC APPALACHIANS

By Christopher Charles Gerbi

Thesis Advisor: Dr. Scott E. Johnson

An Abstract of the Thesis Presented
in Partial Fulfillment of the Requirements for the
Degree of Doctor of Philosophy
(in Earth Sciences)
May, 2005

Accretionary orogens, such as the Appalachian orogen, form by episodic docking of oceanic and continental fragments. Two factors that exert significant control on the development of an accretionary orogen are: (1) the nature and source of the accreting fragments, and (2) the thermal and deformational structure of the crust. This study addresses aspects of both of these controls.

In the Northern Appalachians, a long-lived but untested hypothesis suggested that Early Paleozoic accretion in western Maine, which marked the initiation of Appalachian development, involved the docking of an island arc. My goal was to test this hypothesis for the Maine-Québec segment of the orogen, where the Boundary Mountains terrane had been identified as a possible collider. Combining the techniques of mapping, structural analysis, petrography, U-Pb zircon and monazite geochronology, geochemistry, and geochemical modeling, I present the following interpretations related to the geologic history of the region. (1) the Chain Lakes massif, which cores the Boundary Mountains, was an Ordovician arc-marginal basin receiving sediments eroded from a Laurentian

source. (2) Anatexis of the Chain Lakes massif disrupted the original sedimentary-volcanic sequence. (3) The Boil Mountain Complex and Jim Pond Formation, which lie along the southern margin of the Chain Lakes massif, do not represent an ophiolite, as previously thought. (4) The Boundary Mountains represent a Laurentian-derived microcontinent that served as the nucleus for part of a regional arc system that collided with Laurentia in the Ordovician.

The thermal and deformational processes described herein relate, respectively, to anatexis and pluton emplacement. Review and numerical modeling of the causes of low-pressure anatexis, which affected the Chain Lakes massif, indicate that appropriate pressure-temperature conditions are possible in regions of crustal-scale detachment faulting, percolative magma flow, or where thin lithosphere is accompanied by plutonic activity. Analytical kinematic modeling of the consequences of dike-fed pluton emplacement suggests that if published physical properties of granitic magmas are correct, host rocks surrounding an in-situ expanding pluton must deform at rates several orders of magnitude faster than typical tectonic strain rates. Such strain rates almost certainly must be accommodated by processes other than dislocation creep.

ACKNOWLEDGEMENTS

Where to start? It is impossible to spend nearly five years working towards a goal, and achieve that goal, without unrepayable help along the way. Specific acknowledgements related to work associated with each chapter are noted at the end of the chapter. Here I want to acknowledge those that made it all possible.

For getting me off the ground, freely sharing their knowledge of the Boundary Mountains, samples, and maps: Gene Boudette, Gary Boone, and Walt Trzcienski. If all scientists welcomed me to their turf as these three did, we would be well off. Doug Reusch, Spike Berry, and Bob Marvinney of the Maine Geological Survey also shared their time and encouragement as I learned about Appalachian history. I wouldn't have had a rock to look at without the kind permission of the landowners: Penobscot Indian Nation, International Paper, and Plum Creek. With the PIN, I particularly want to thank Sparky Clark and John Banks. Thom Dodd of IP made the permitting run smoothly.

For companionship, assistance, and advice over three seasons in the woods, I thank my field assistants (most of who's job it was to keep me off crutches): Chester, Cosmo, Matthew Dupee, Michelle Fiscus, Greg Gerbi, Pam Gerbi, Ben Hooks, Erwin Melis , Ethan Perry, Doug Reusch, and Jon Riley. In addition to fieldwork, several field trips brought pivotal insights. Among those attending and sharing their experience and ideas: Jean Bédard, Sebastien Castonguay, Jean-Michel Schroetter, Cees van Staal, Johan Lissenberg, Ron Vernon, Tracy Rushmer, Paul Karabinos, Mike Brown, Spike Berry, and Bob Marvinney. It was on one of these trips that I finally grasped the anatectic nature of the Chain lakes massif.

The studies related on the following pages are at heart collaborations. Each of the four main chapters will or do appear as a coauthored journal article. Although the coauthorship does not appear here, I want to acknowledge the advice and assistance of those involved. Besides Scott, the bulk of the debt goes to John Aleinikoff whose interest, thoroughness, patience, and expertise made the SHRIMP parts of this work possible and presentable. Ezra Yacob generously assisted with sample preparation. Joe Wooden, who was in the SHRIMP lab as I worked, kept me from making too many analytical mistakes. Greg Dunning and Jean Bédard helped add pieces of the puzzle as I assembled the whole picture. Reviews of parts of the manuscripts by Walt Trzcienski, Basil Tikoff, Keith Klepeis, Brett Davis, and Doug Reusch improved the writing significantly.

I would not have been able to concentrate on research as I did without the generous stipend support of a National Science Foundation Graduate Research Fellowship, an NSF-supported Research Assistantship, a University Graduate Research Assistantship, and a University of Maine-NSF GK-12 Program Fellowship. Scientific support was from NSF grants EAR-0126004 and EAR-0087661, a U.S.G.S. EDMAP grant, a grant from Sigma Xi, a University of Maine Association of Graduate Students grant, and two grants from the Geological Society of America.

The people make the project, and I hope this work shows the support and involvement of the faculty and graduate students in the Department of Earth Sciences. In particular, I would like to thank Dan Belknap for his leadership, making the Department a wonderful place to be, and Dan Lux for his advice on all things igneous, geochronological, and unrepeatable. And as always, nothing would have gotten done

without Dianne Perro behind the desk. Phaedra Upton, Erwin Melis, Heather Short, Wes Groome, Matt Dupee, Ben Hooks, and Julia Daly kept me thinking and gave me hope.

The members of my advisory committee shaped my scientific experience, and for the progress I like to think I have made, I have them to thank. Help and encouragement ranged from locating a map or a reference, to looking down a microscope together, to collaborating on the electron probe, to alerting me to the history of the Appalachians outside of western Maine, to shaping my understanding of the physical principles of orogenesis, to making sure what I was saying actually made sense let alone was right. Thank you Marty Yates, Charlie Guidotti, Peter Koons, and Cees van Staal.

Of all the people at the University who have mentored me, none has had as profound an effect as Scott Johnson. As is probably too obvious, I have taken to emulating so many of his approaches to science, research, and education. For better or worse, I even use his writing syntax on occasion. Besides the successful and reasoned guidance in all things scientific, Scott has tirelessly championed my interests to the community and in doing so provided me with opportunities I would not otherwise have had. The best thanks I can give him is to make his efforts worthwhile as I begin the next stage of my career. Just in case that doesn't happen, I want to make sure he knows how much I appreciate his guidance.

Even if all the people I have mentioned did what they had done to help me, I wouldn't be where I am today without the giving, support, and encouragement of my wife, Aimée. There aren't enough lobsters and blueberries in Maine to show her how much she means to me. Thank you, Aimée.

TABLE OF CONTENTS

LIST OF TABLES

LIST OF FIGURES

Chapter 1

INTRODUCTION

Understanding the tectonic processes shaping our planet requires multiple approaches. On one hand, direct study of the geologic history of geographic regions provides a catalog of events that have operated in the past – and presumably operate today – that we must explain by physical principles. On the other hand, a clear understanding of the processes acting upon the surface and subsurface also requires studies of the processes themselves. Such a bipartite approach guided the work at hand. This dissertation comprises four separate studies, two of which focus on the geologic history of the Boundary Mountains region of west-central Maine and two of which focus on tectonic processes related to this history.

The Boundary Mountains, located along the southern extent of the border between Quebec and Maine, make up a strong ridge of rock that defines both a political and physiographic boundary. To the north and west of the Boundary Mountains lie rocks of the Laurentian passive margin and successor basins. To the south and east lies the Central Maine Belt, Silurian and Devonian rocks strongly deformed during middle Paleozoic orogenesis. The Boundary Mountains themselves form part of the Iapetan suture zone juxtaposing peri-Laurentian and peri-Gondwanan rocks. As such, understanding the history of the Boundary Mountains provides insight into the manner in which an ocean closed, episodically, in the Paleozoic. In Chapter 2, I discuss the history of the Chain Lakes massif, a particularly enigmatic body of rock that makes up the spine of the Boundary Mountains. In Chapter 3, I broaden the discussion to consider the

assembly of the Boundary Mountains region and its role in the early stages of Appalachian mountain-building.

Chapter 4 contains an evaluation of the tectonic conditions necessary to melt rocks at low pressure. My interpretation of the Chain Lakes massif – that it melted in place after passing through the andalusite field – inspired me to explore this question. Chapter 5 is not directly related to the geologic history of west-central Maine, but instead addresses an age-old problem in geology, namely, how granitic melts propagate from the source region to the level of emplacement. In this chapter, I discuss the consequences of one proposed magma transport mechanism, diking, on the host rocks at the site of pluton emplacement. This chapter (Gerbi et al. 2004) appeared in the Journal of Structural Geology.

In addition to the data included in the chapters, I have compiled the field and analytical data used in these studies that are not otherwise presented. These data comprise a 7.5-minute quadrangle map that I prepared through the U.S.G.S.-sponsored EDMAP program (Appendix A), field data including station locations, lithology, and structural data (Appendix B), complete chemical analyses of muscovite that are included in partial form in Chapter 2 (Appendix C), example distribution coefficients and model melt calculations for the Boil Mountain Complex (Appendix D), and geochemical data gathered for the Skinner pluton but not included in a chapter (Appendix E).

Chapter 2

ORIGIN AND OROGENIC ROLE OF THE CHAIN LAKES MASSIF, MAINE AND QUÉBEC

2.1 Chapter abstract

The Chain Lakes massif has long been an enigmatic component of the Appalachian orogen, but new structural, microstructural, and geochronological information provides the basis for the following new interpretation of the massif and its history. In the Early Paleozoic, sediments and volcanic rocks from Laurentia or a Laurentian-derived microcontinent were deposited in an arc-marginal basin on the western margin of Iapetus. Following intrusion of ultramafic through intermediate arc-related magmas, the sedimentary-volcanic sequence was heated sufficiently to melt in place, resulting in stratigraphic disaggregation and diatexite formation. We dated monazite growth from this metamorphic event at 469 ± 4 Ma. Although some melt may have left the system, much remained, including water dissolved in the melt. Upon crystallization, this water drove thorough retrogression of the massif, causing pervasive pseudomorphism of porphyroblasts. With cooling and crystallization, the Chain Lakes massif became sufficiently rigid that it was not significantly deformed during the Middle Ordovician through Devonian stages of the Appalachian orogeny involving deformation of the Iapetan passive margin of Laurentia and the arrival of several peri-Gondwanan microcontinents.

2.2 Introduction

As the product of numerous superimposed tectonic events, accretionary orogens are difficult to characterize in terms of physical processes, largely because an accurate

description of the geometric, kinematic, and dynamic aspects of an accretionary orogen may be elusive (e.g. Coney 1992; van Staal et al. 1998). A physical characterization of any orogen requires an understanding of both the material structure of the lithosphere prior to collision and how the orogen responded to each collisional event. As previously demonstrated, this notion applies even to the extensive modern Himalayan (Gehrels et al. 2003) and Andean (Ramos 1988) orogens.

The Maine-Québec segment of the northern Appalachian orogen has long been recognized as forming by accretion of island arcs and microcontinental fragments over more than 150 million years of the Paleozoic (e.g. Williams 1978). Nevertheless, researchers are still working to: (1) define the boundaries and histories of the individual blocks that make up the orogen (van Staal et al. 1998; Williams et al. 1999; Tucker et al. 2001; Moench and Aleinikoff 2003), and (2) understand the relationship among accretion, deformation, and magmatism in much of the orogenic belt (West et al. 1995; Brown and Solar 1999; Bradley et al. 2000; Dorais and Paige 2000; Tucker et al. 2001; Guidotti and Johnson 2002; Johnson et al. 2003). The classic story of Ordovician arc collision followed by Devonian and Permian microcontinent collision (e.g. Rast 1989) is complicated by the recognition of numerous chemically, spatially, and chronologically distinct arcs and continental fragments that amalgamated and accreted to Laurentia in the span of Appalachian development. Within the Maine-Québec segment of the northern Appalachians (Fig. 2.1) lies the Chain Lakes massif, a crustal block whose history and role in Appalachian orogenesis have long been poorly understood. In the context of relating the development of the Chain Lakes massif to the early stages of Appalachian growth, we sought to determine the provenance, setting, and history of the massif.

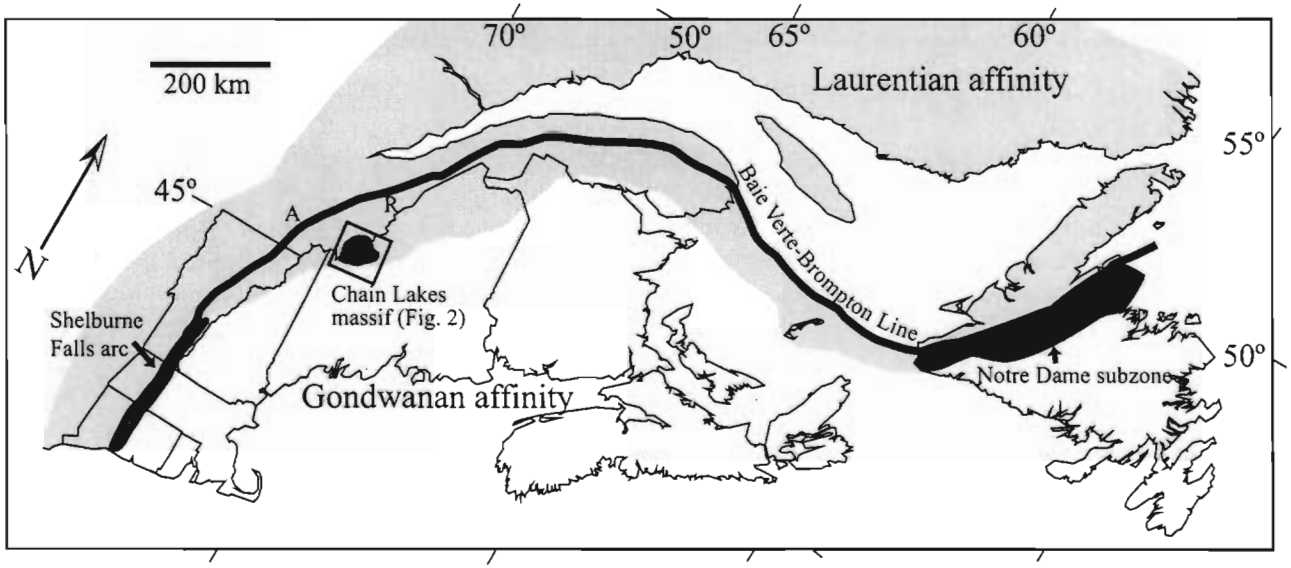

Figure 2.1 Map of the regional tectonic setting. General tectonic association map of New England and Atlantic Canada, showing the locations of the Chain Lakes massif and potentially correlative Shelburne Falls arc and Notre Dame subzone. A = Ascot Complex; R = Rivière des Plante mélange. The Baie Verte- Brompton Line separates allocthonous from autocthonous Appalachian terranes and thrust sheets. Modified from Williams (1978), Karabinos et al., (1998), and van Staal et al. (1998).

As noted by Trzcienski et al. (1992), the Chain Lakes massif, an isolated high-grade quartzofeldspathic terrain, has held an enigmatic position in tectonic reconstructions of northern Appalachian geology. In most models, the massif represents part or all of a microcontinent (Williams and Hatcher 1983; Boone and Boudette 1989) that rifted away from either Laurentia (Waldron and van Staal 2001) or Gondwana (Zen 1983; Kusky et al. 1997) and collided with Laurentia during Taconian (Early Ordovician) orogenic time. In contrast, Trzcienski et al. (1992) suggest that the massif could be essentially autochthonous. Such disparate models yield significantly different interpretations of both microplate formation mechanisms and paleogeography.

Based on field mapping, petrological and structural analysis, and geochronology, we conclude that the Chain Lakes massif represents a metasedimentary sequence that was originally deposited, possibly in the Early Ordovician, adjacent to an arc off the Laurentian margin. After melting in-situ, the massif formed part of the main Notre Dame arc system that collided with Laurentia in the Ordovician to drive the initial stages of Appalachian orogenesis. The results of our work represent a substantial reinterpretation of the Chain Lakes massif and provide important geographical and tectonic constraints on a portion of the early Paleozoic margin of Laurentia. A companion paper (Gerbi et al. in review-c) discusses the regional pre-Silurian tectonic events of the western Maine Appalachians.

2.3 Regional setting and previous work

The Chain Lakes massif is exposed over approximately 900 km^2 along the Maine-Québec border (Fig. 2.2). Weakly metamorphosed Silurian and Devonian strata lie in contact with the massif on the north, west, and southeast. The northern and western

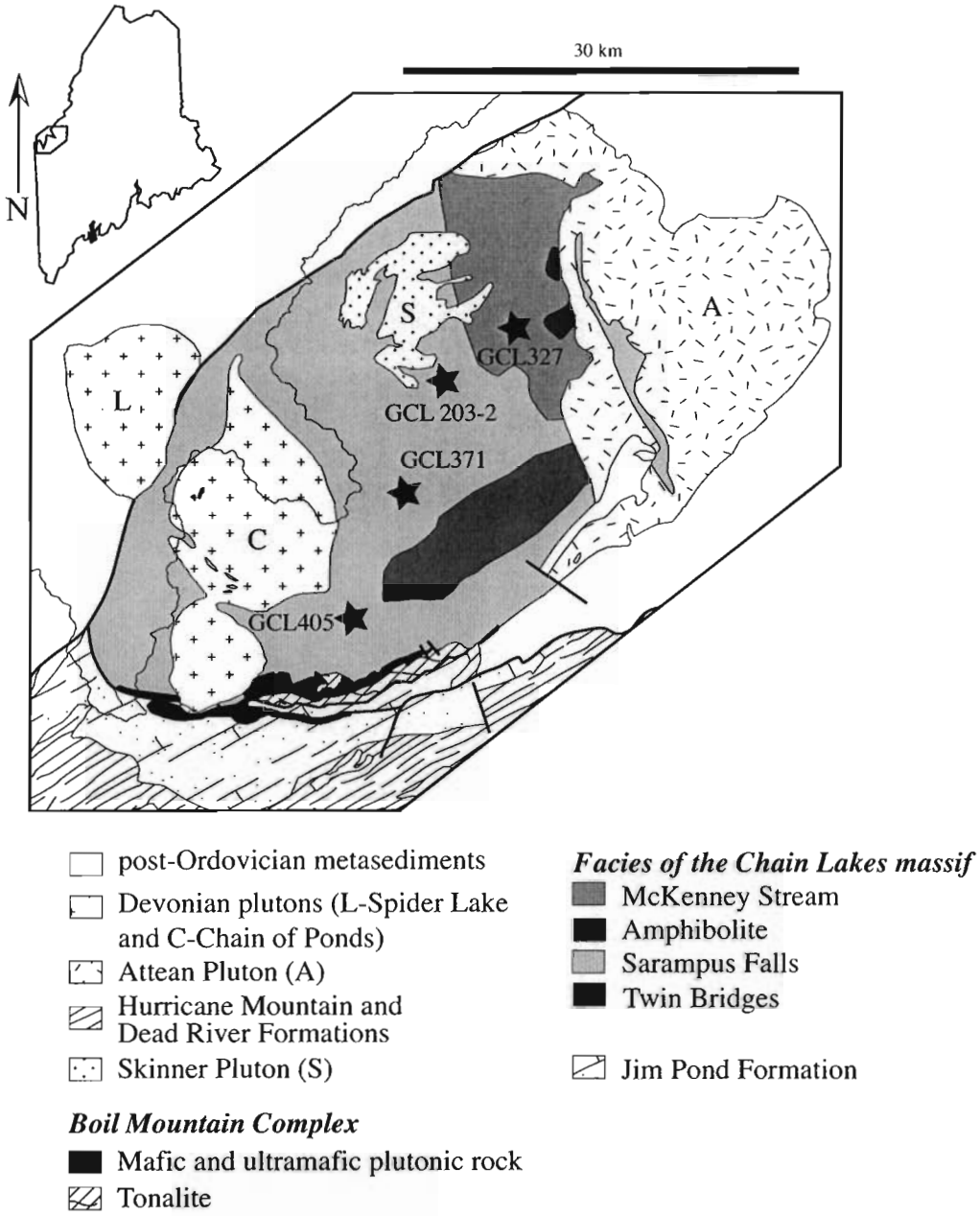

Figure 2.2 Bedrock geologic map of the Chain Lakes massif and surrounding area. Heavy lines mark faults; dotted line represents the international border. Stars and labels refer to geochronologic sample locations. Isolated amphibolite units within Sarampus Falls facies are too small to show at this scale. After Albee and Boudette (1972), Goldsmith (1985), Osberg et al. (1985) Boudette (1991), Moench et al. (1995).

boundaries of the massif are dominantly post-Silurian strike-slip faults (Moench et al. 1995), and the southeastern border is marked by an unconformity, with the Silurian Hardwood Mountain Formation overlying the massif (Moench et al. 1995). The massif was intruded on its eastern margin by the Attean pluton, recently redated at 443 ± 3 Ma (Gerbi et al., in review). To the south of the massif lies the Boil Mountain Complex (Boudette 1982), a unit of mixed ultramafic and mafic plutonic rocks accompanied by extensive tonalite. The Complex, dated at 477 +7/-5 Ma (Gerbi et al. in review-c) and 477 ± 1 Ma (Kusky et al. 1997) likely formed in an supra-subduction zone setting (Coish and Rogers 1987; Gerbi et al. in review-c). Two plutons intruded the interior of the massif: the granodioritic Skinner pluton (Goldsmith 1985), dated at 473 ± 6 Ma (Gerbi et al. in review-c) and the 373 ± 2 Ma Chain of Ponds pluton (Heizler et al. 1988). No contact aureole has been described around the Skinner pluton, but a well-developed aureole is present around the Chain of Ponds pluton (Harwood 1973; Biederman 1984). An increase in seismic velocity suggests that the Chain Lakes massif may be as little as 4 km thick (Stewart et al. 1993), although Spencer et al. (1989) suggest that a reflector at 25 km depth could represent the bottom of the massif. Both studies infer that Grenville basement underlies the massif.

Rocks similar to the Chain Lakes massif crop out in scattered locations to the northeast, along the structural trend of the Appalachians (Fig. 2.1). The most prominent of these are located within the Rivière des Plante ophiolitic mélange in southeastern Québec (Cousineau 1991; Trzcienski et al. 1992). There also, rocks similar to the Chain Lakes massif have been structurally isolated from originally adjacent rocks. Several

additional exposures of similar rocks crop out through the northeast end of the Gaspé Peninsula (Trzcienski et al. 1992).

Although the region around the massif had been previously mapped in a reconnaissance style (Albee 1961), Boudette and colleagues (Boudette 1970; Albee and Boudette 1972; Boudette and Boone 1976; Boudette et al. 1989) in Maine and Marleau (1968) in Québec were the first to recognize and describe the Chain Lakes massif. In aggregate, these studies identified the principal features of the massif, including its overall quartzofeldspathic to semi-pelitic composition, facies distribution, approximate metamorphic grade, gentle domal structure, and the variable presence of lithic fragments and quartz nodules. Most authors inferred that the massif had a sedimentary origin as a diamictite during the Proterozoic (e.g. Boudette et al. 1989). Others suggestions included an impact origin (Boudette and Boone 1982) and that the massif formed as a rift deposit or a boulder pavement in front of a thrust sheet (Trzcienski et al. 1992). In the latter scenario, metamorphism was linked to intrusion of the Attean and Skinner Plutons.

These studies all faced the limitation of poor geochronologic control. The originally widely cited U-Pb age of >1500 Ma (Naylor et al. 1973) for the massif was based on analysis of multi-grain zircon fractions containing numerous age populations derived from Grenville and older basement (Cheatham et al. 1989). Until the present study, the best constraint on the age of the massif was produced by Dunning and Cousineau (1990), who dated single zircons by thermal ionization mass spectroscopy (TIMS) and found a range of ages from Archean to Neoproterozoic. They used these data to constrain the depositional age of the massif as latest Proterozoic or younger. In addition, they interpreted a multigrain monazite date of 468 ± 2 Ma as the time of

metamorphism. Biederman (1984), using Ar-Ar in hornblende from amphibolite, determined a minimum cooling age of 570 Ma, and Cheatham et al. (1989) used whole-rock Rb-Sr analyses to infer an age of 684 ± 76 Ma for the high grade metamorphism. The last two geochronological constraints are potentially suspect: the Ar release spectra of Biederman (1984) have a pronounced saddle shape, and the whole-rock Rb-Sr analyses requires the unrealistic assumption that the Chain Lakes massif had an initially uniform Rb-Sr ratio and that the isotopic system remained closed. Below, we present the results of new U-Pb analyses of zircon and monazite that provide a better indication of the timing of events in the massif.

2.4 Observations

2.4.1 Overview

Because many aspects of the Chain Lakes massif have been described elsewhere (Boudette 1970; Boudette and Boone 1976; Biederman 1984; Boudette et al. 1989; Trzcienski et al. 1992; Moench et al. 1995), here we highlight the salient points from previous work while including new observations derived from mapping and petrography.

The Chain Lakes massif is lithologically distinct from surrounding units and contains substantial internal variability. In contrast to earlier studies, which subdivided the massif into five to seven facies (e.g. Moench et al. 1995), we determined that the massif comprises only four mappable units (the quartzofeldspathic Sarampus Falls, Twin Bridges, and McKenney Stream facies, as well as amphibolite) and that these units have slightly differently distributions than previously portrayed (Fig. 2.2). We combined much of the Bag Pond Mountain and Coburn Gore facies of Moench et al. (1995) with the Sarampus Falls facies, recognized the greater extent of the Twin Bridges facies, and

consolidated the diorite of the eastern side of the massif (Albee and Boudette 1972) with the previously noted amphibolite facies (Goldsmith 1985; Boudette et al. 1989). Although we did not directly observe contacts between adjacent facies, except where noted below, we infer gradational transitions among the quartzofeldspathic facies. Boudette et al. (1989) describe a gross stratigraphy, with the McKenney Stream facies overlain by the other units. In our view, the structure (described below) suggests instead that although a recognizable pseudostratigraphic relationship exists between the Twin Bridges and Sarampus Falls facies, the relationship of these units to the McKenney Stream facies is ambiguous. If the McKenney Stream facies, prior to exhumation, did extend across the entire massif, the moderately dipping fabric in the Sarampus Falls and Twin Bridges facies suggests that the McKenney Stream facies would have overlain both of these units.

The primary distinguishing feature between the three quartzofeldspathic facies is the nature of the compositional banding. Whereas the McKenney Stream facies contains no compositional banding (Fig. 2.3a), schlieric to highly contorted wispy bands are present throughout much of the Sarampus Falls facies (Fig. 2.3b). The Twin Bridges facies contains a strong planar compositional banding (Fig. 2.3c) that is locally crenulated (Fig. 2.3d). In places, the Twin Bridges facies retains lithologic layering on a cm-scale. The orientation of all compositional banding in the massif defines a broad girdle about a northeast-trending, subhorizontal axis (Fig. 2.4a), with banding from the Twin Bridges exhibiting much less variability than that of the Sarampus Falls facies. Our mapping, covered areas not previously mapped at more than a reconnaissance level, revealed relationships consistent with those noted by others (Albee 1961; Boudette 1970; Boudette

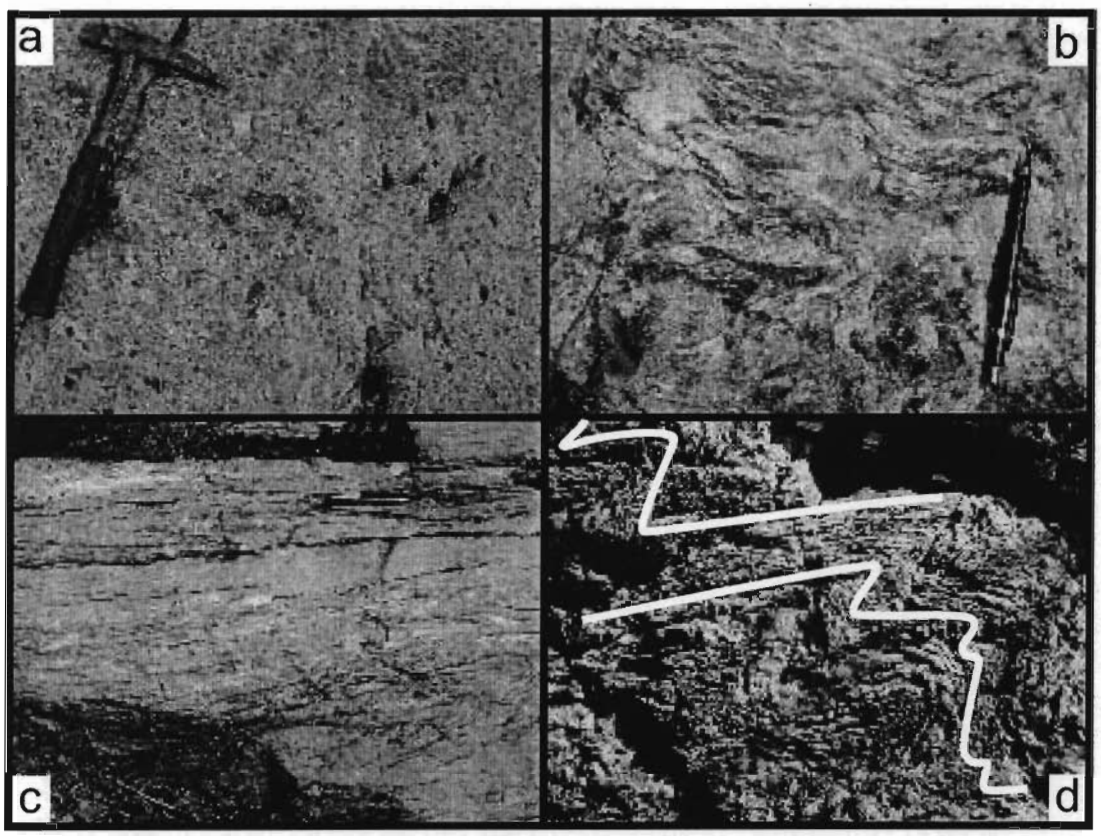

Figure 2.3 Field photographs of units within the Chain Lakes massif. (a) McKenney Stream facies; (b) Sarampus Falls facies; (c) Twin Bridges facies; (d) folded compositional banding (white lines) in the Twin Bridges facies.

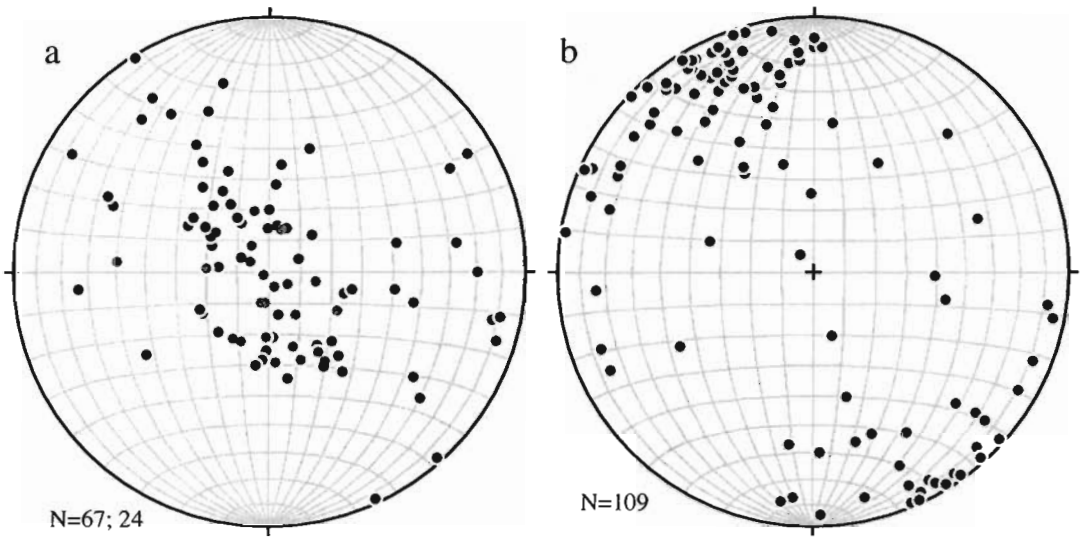

Figure 2.4 Stereograms of structural data. Equal area stereograms illustrating poles to planar features within the Chain Lakes massif. (a) Compositional banding throughout the massif. Banding is defined by aligned biotite-sillimanite schlieren. Gray dots are from the Twin Bridges facies; black dots are from the Sarampus Falls facies. (b) Penetrative foliation, including mylonitic foliation. This fabric is restricted to near the southern margin of the massif.

and Boone 1976; Biederman 1984). The massif is a broad northeast-trending arch with compositional banding dipping shallowly away from the center. A younger, nearly vertical foliation superimposed adjacent to the Boil Mountain Complex (Fig. 2.4b) is defined by the shape-preferred orientation of quartz and clearly overprints compositional banding.

As described below, the Sarampus Falls, Twin Bridges, and McKenney Stream facies are all migmatites, with the following features in common: (1) variable abundance of lithic fragments, (2) nearly ubiquitous 1 to 5 cm, rounded to angular, equant nodules of vein quartz, and (3) a medium-grained equigranular quartz–plagioclase matrix with variably abundant K-feldspar. In several locations throughout the Sarampus Falls and Twin Bridges facies, we observed granofelsic dikes cutting the compositional banding. These dikes are mineralogically and microstructurally similar to the host rock but lack compositional banding and lithic fragments.

Amphibolite crops out in several locations throughout the Chain Lakes massif (Goldsmith 1985; Boudette et al. 1989). These lenses consist of medium-grained, well-foliated hornblende-plagioclase-quartz rocks. Goldsmith (1985) indicated that some of the amphibolite retained pillow structures. The foliation and metamorphic grade in these lenses are consistent with those in the surrounding rocks. As noted above, we include the unit mapped as diorite by Albee and Boudette (1972) in our amphibolite unit

2.4.2 Details of critical features

2.4.2.1 Lithic fragments

Lithic fragments (Fig. 2.5) are relatively evenly distributed in the McKenney Stream facies, irregularly distributed in the Sarampus Falls facies, and variably present in

Figure 2.5 Typical lithic fragments (outlined) within the Sarampus Falls facies.

the Twin Bridges facies. The fragments range in size from less than one centimeter to several meters long with the mode approximately 5-20 cm. In one location, we observed a 10+ m-long block consisting of layered felsic volcanic rocks; Goldsmith (1985), too, noted large felsic volcanic blocks. In general, aspect ratios of the lithic fragments range from 1:1 up to approximately 3:1; nearly all fragments are rounded. The fragments make up no more than 15% of any outcrop and are not in contact, producing a matrix-supported character to the rock. Lithic varieties are all metamorphosed; protoliths were primarily pelite, calcsilicate, amphibolite, and felsic volcanic. Boudette et al. (1989) report, in addition, granitic and gneissic fragments. In most locations, the fragments are not clustered and have no preferred orientation. In some locations, however, elongate fragments of the same lithology are aligned and retain an indication of bedding. This is most common in the Twin Bridges facies.

Foliation within the fragments is generally discordant to the matrix foliation and to internal foliation in other fragments (Boudette et al. 1989). At the grain scale, fragments are fused to the matrix, leaving a somewhat gradational contact (Trzcienski et al. 1992). Despite the metamorphic modifications to the boundaries, most fragments retain a distinct mineralogy and fabric. For example, although relict garnet is absent in the quartzofeldspathic matrix, it is present in some amphibolite and calcsilicate lithologies (Trzcienski et al. 1992). Fragments with a metapelitic appearance are minerallogically similar to the matrix, but with a higher proportion of refractory minerals.

In addition to the lithic fragments, nebulous patches 10-30 cm across are present within the McKenney Stream and Sarampus Falls facies. These patches are rounded, have irregular boundaries, and usually contain quartz-rich segregations defining a fabric

that is commonly continuous with the matrix but highly contorted. Although they bear many similarities to lithic fragments, these patches have much more diffuse boundaries and more irregular internal structure.

2.4.2.2 Compositional segregations

Compositional segregations, present in the Twin Bridges and Sarampus Falls facies, have a range of appearances that lie on a continuum; the overall mineralogy and structure are similar, but the morphology, degree of segregation, and internal deformation vary. Morphologically, the segregations vary from lozenge-shaped clots (Biederman 1984), through wispy schlieren, to distinct planar bands, some of which are crenulated about subhorizontal to shallowly plunging axes. The first two morphologies are present in primarily the Sarampus Falls facies; planar bands characterize the Twin Bridges facies. In addition, lozenges of coarse-grained (4-5 mm) intergrowths of quartz and two feldspars are present in all three facies.

The segregations, ranging from 1 mm to 3 cm in width, are defined by biotite and sillimanite-rich bands alternating with the quartzofeldspathic bands that constitute the majority of the rock. A general correspondence exists between the planarity of the bands and the degree of segregation: more planar segments have sharper, less diffuse boundaries and less modal cross-contamination. In the dark bands, biotite (commonly chloritized) and fibrolitic sillimanite are intergrown. No deformational microstructures are evident in the biotite, but the fibrolite is arrayed in tight to isoclinal folds (Fig. 2.6a). We were unable to determine if individual fibrolite crystals were deformed in the solid state or if the aggregate was folded, leaving the individual fibers strain-free.

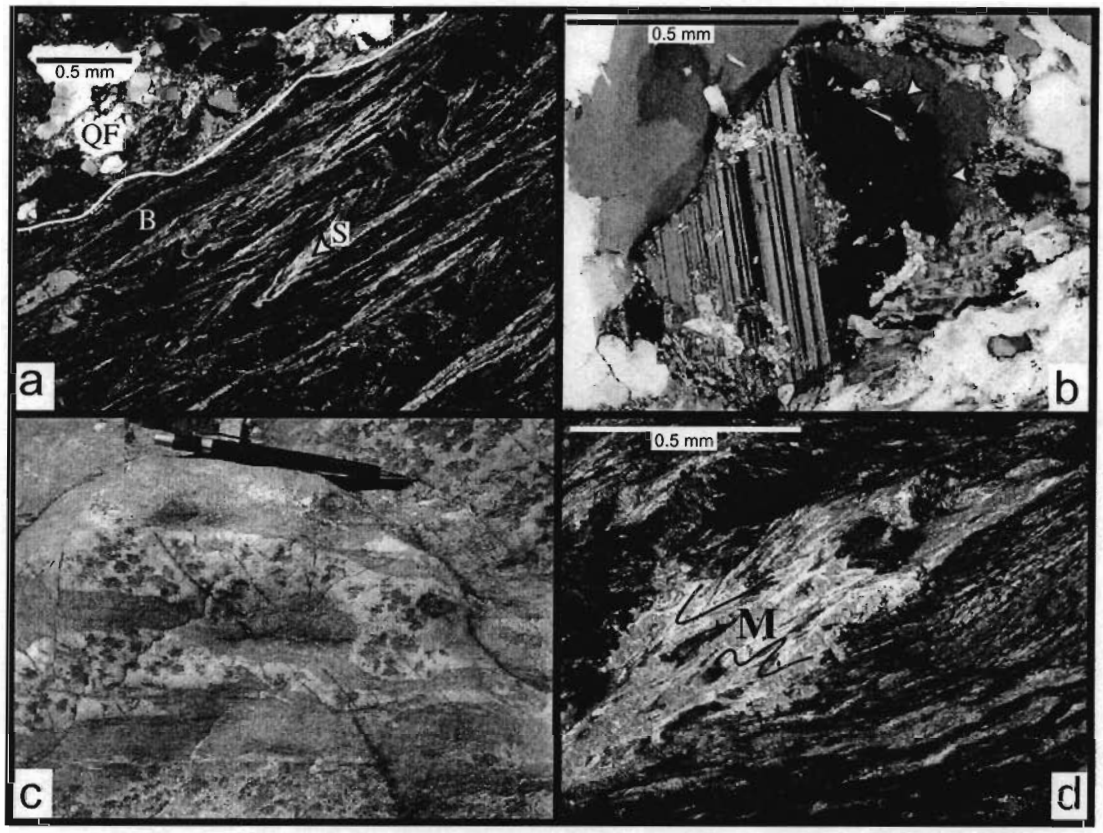

Figure 2.6 Photographs and micrographs of select features within the Chain Lakes massif. (a) Tight to isoclinal folds defined by sillimanite (S; arrow) now partly mimetically replaced by muscovite in schlieren of the Twin Bridges facies. White line separates quartzofeldspathic domain (QF) from biotite (B) and sillimanite domain. Crossed polars. (b) Euhedral plagioclase, partly replaced by white mica, ehibiting oscillatory zoning (arrows). Crossed polars. (c) Patch migmatite or "flecky" gneiss. (d) Single crystal of muscovite (M) replacing sillimanite-rich portion of schliere in the Twin Bridges facies. Lines mark relict folds as seen in (a). Crossed polars.

The quartz and feldspar of the leucocratic zones are medium-grained and equigranular, with interlocking grain boundaries linking quartz and potassium feldspar. Plagioclase grain boundaries vary from interlocking to straight. Muscovite, where present, is generally poikiloblastic. Fibrolite is present in variable abundance throughout the matrix, primarily as relatively isolated aggregates or sprays of needles without any clear preferred orientation. In places, individual fibers cross quartz and muscovite grain boundaries. Mesoscopically, folds are defined by the compositional banding, but at the microscale, only the dark bands exhibit evidence of folding; quartz and feldspar microstructures indicate little solid-state strain in the leucocratic regions. Some of the plagioclase crystals are euhedral and exhibit oscillatory zonation or igneous growth twins (Fig. 2.6b).

2.4.2.3 "Flecky gneiss"

A distinct patchy texture, described in detail by Biederman (1984), consists of nebulous to spidery leucocratic zones containing isolated, equant dark clots within a light gray granofelsic matrix (Fig. 2.6c). This texture is most abundant in the Sarampus Falls facies, but it is also present in the Twin Bridges unit. In the McKenney Stream facies, leucocratic zones are weakly developed or absent (Goldsmith 1985) and only the dark clots are present. Leucocratic zones range in size from 5 cm to greater than a meter long, with shapes from equant to highly oblate, concordant with compositional banding if present. The light matrix consists of quartz + plagioclase ± K-feldspar, with a texture similar to that in the host rock matrix. The primary cause of the color difference between the matrix and the leucocratic zones is a lack of biotite that is present in small amounts in

the host rock matrix. Many of the plagioclase crystals, though altered, retain euhedral outlines.

The flecks themselves presently consist of either coarse grained muscovite or micron to millimeter scale skeletal intergrowths of muscovite and chlorite around primarily quartz inclusions. Accessory amounts of epidote group minerals are present. The flecks are probably pseudomorphs after cordierite (Biederman 1984; Trzcienski et al. 1992), but do not contain any relicts of the original porphyroblasts.

2.4.2.4 Metamorphic assemblages

Aside from scattered amphibolite blocks, the Chain Lakes massif consists of a granofelsic quartz-plagioclase matrix, with variably sized microcline and variably abundant biotite, muscovite, chlorite, and sillimanite. Plagioclase is partially to wholly altered in all samples, but generally retains its euhedral to subhedral form and, in places, concentric zoning typical of crystallization from a melt (Fig. 2.6c). Microcline is generally larger than quartz and plagioclase, and is in most instances unaltered. Sillimanite and biotite, as described above, are most abundant in compositional segregations, but both also occur within the quartzofeldspathic matrix where they exhibit no clear preferred orientation. Muscovite occurs in three settings: (1) as isolated, coarse laths within the matrix, exhibiting no apparent preferred orientation, (2) as mimetic overgrowths within biotite-sillimanite compositional segregations (Fig. 2.6d), and (3) in conjunction with chlorite as fine to coarse-grained pseudomorphs. Fine- and coarse-grained muscovite, arbitrarily divided at ~100 μm size, have similar cation concentrations, with slightly higher silica – 6.2-6.5 versus 6.1-6.2 atoms Si per 22 O – in

the finer-grained fraction (Fig. 2.7; Table 2.1). Chlorite occurs either intergrown with, and presumably as an alteration product of, biotite or as part of pseudomorphs.

In accord with the observations of Trzcienski et al. (1992), we recognize three types of pseudomorphs, in variable concentrations, throughout the McKenney Stream and Sarampus Falls facies. The first is rectangular with fine to coarse muscovite and chlorite as the replacement phases. In one of these pseudomorphs, we identified relict andalusite (Fig. 2.8). The second type of pseudomorph has a roughly hexagonal form with muscovite, chlorite, sillimanite, and biotite as the replacement phases. We interpret this as former garnet. The third type of pseudomorph, comprising fine to coarse muscovite and chlorite, is irregularly shaped and contains numerous inclusions. Faint yellow pinitization in places coupled with the morphology suggests that this pseudomorph was originally cordierite (Trzcienski et al. 1992).

The amphibolite bodies scattered throughout the massif are mineralogically similar equigranular hornblende-plagioclase rocks with up to 10% quartz. In some areas, particularly to the east, the hornblende is poikiloblastic. As noted by Albee and Boudette (Albee and Boudette 1972) for their diorite unit, plagioclase is strongly to totally altered to fine-grained white mica, and in most samples minor to moderate amounts of chlorite and epidote group minerals are present.

With differences in detail, we support the interpretation of Boudette (1970) and Biederman (1984) that the Chain Lakes massif retains evidence of two metamorphic episodes. In the three quartzofeldspathic facies the high grade metamorphic event is represented by quartz + plagioclase + K-feldspar + biotite + sillimanite ± cordierite ± garnet, with andalusite present early in the prograde history. Below we argue that this

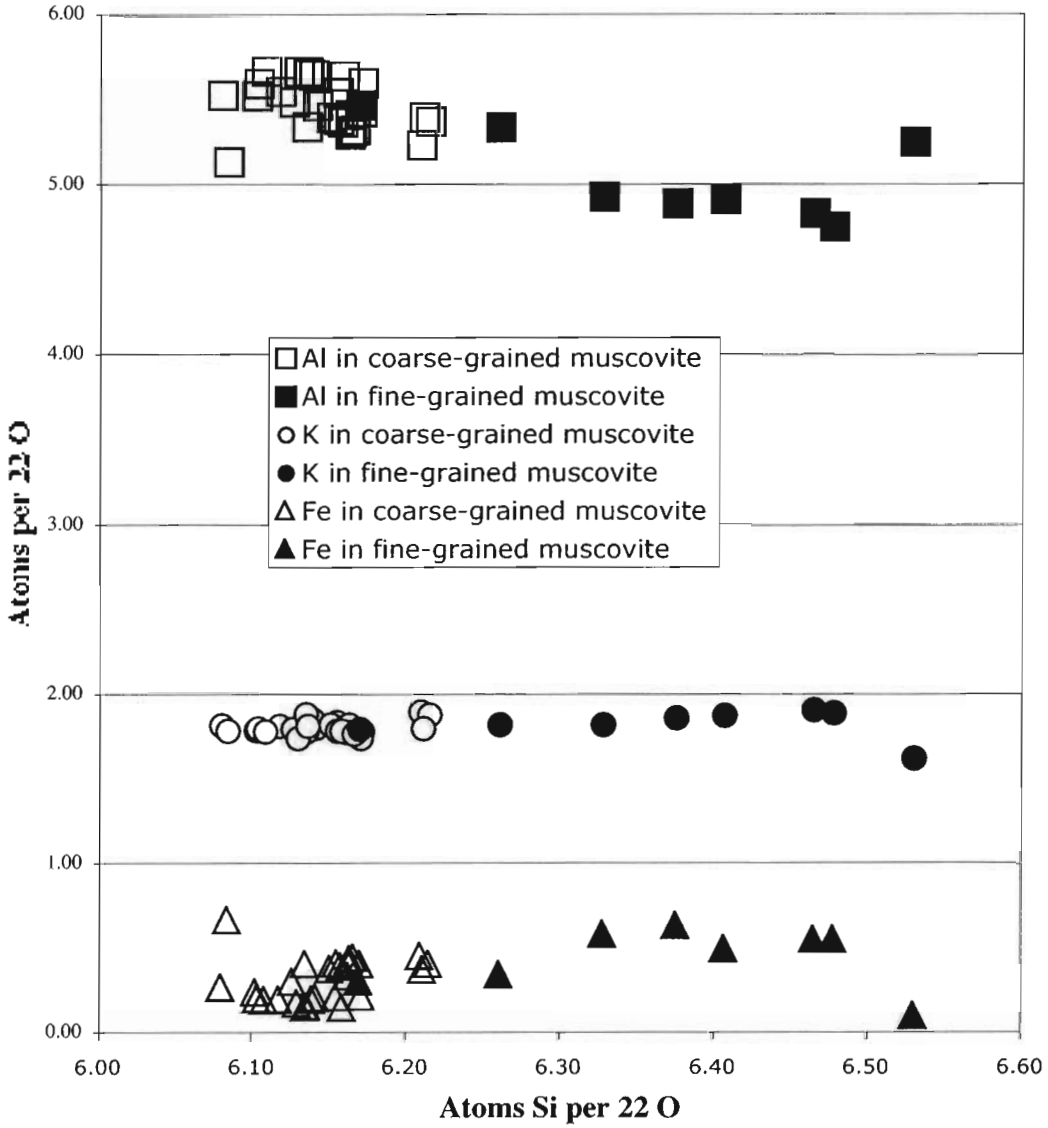

Figure 2.7 Concentration of selected elements within muscovite from across the Chain Lakes massif. Fine-grained muscovite (<100μm) measurements are from altered plagioclase or pseudomorphs. Coarse-grained muscovite measurements are from matrix grains or coarse-grained portions of pseudomorphs.

Table 2.1 Cation concentration in muscovite per 22 oxygens

	Coarse-grained (>100μm)			
Analysis	Si	Fe	K	Al
235-1-1	6.08	0.26	1.81	5.52
193-1-1	6.08	0.66	1.78	5.13
382-4-1	6.10	0.23	1.78	5.52
382-1-2	6.10	0.19	1.80	5.59
193-m-1	6.11	0.18	1.78	5.66
382-1-1	6.12	0.19	1.81	5.54
235-3-1	6.13	0.29	1.79	5.48
193-1-2	6.13	0.17	1.74	5.66
235-2-2	6.13	0.40	1.88	5.34
193-m-3	6.13	0.15	1.78	5.66
193-1-3	6.14	0.15	1.81	5.65
382-4-2	6.14	0.19	1.85	5.64
382-2-1	6.14	0.20	1.80	5.46
235-1-2	6.15	0.37	1.82	5.39
382-2-2	6.15	0.20	1.83	5.54
227-2-1	6.16	0.40	1.78	5.38
227-2-4	6.16	0.39	1.78	5.36
193-m-2	6.16	0.14	1.78	5.63
227-2-3	6.16	0.33	1.77	5.41
235-3-2	6.16	0.41	1.82	5.29
227-2-2	6.16	0.43	1.77	5.31
227-1-3	6.17	0.44	1.76	5.32
227-1-1	6.17	0.40	1.74	5.42
382-1-3	6.17	0.21	1.78	5.59
235-2-1	6.21	0.44	1.89	5.23
227-1-2	6.21	0.36	1.80	5.39
235-1-3	6.21	0.40	1.88	5.37
	Fine-grained (<100μm)			
Analysis	Si	Fe	K	Al
227-1-3	6.17	0.30	1.79	5.46
227-1-2	6.26	0.34	1.82	5.33
227-1-1	6.33	0.58	1.82	4.92
235-3-1	6.38	0.63	1.86	4.88
235-3-2	6.41	0.49	1.87	4.91
235-2-1	6.47	0.54	1.90	4.83
235-2-2	6.48	0.54	1.89	4.75
193-1-1	6.53	0.09	1.62	5.25

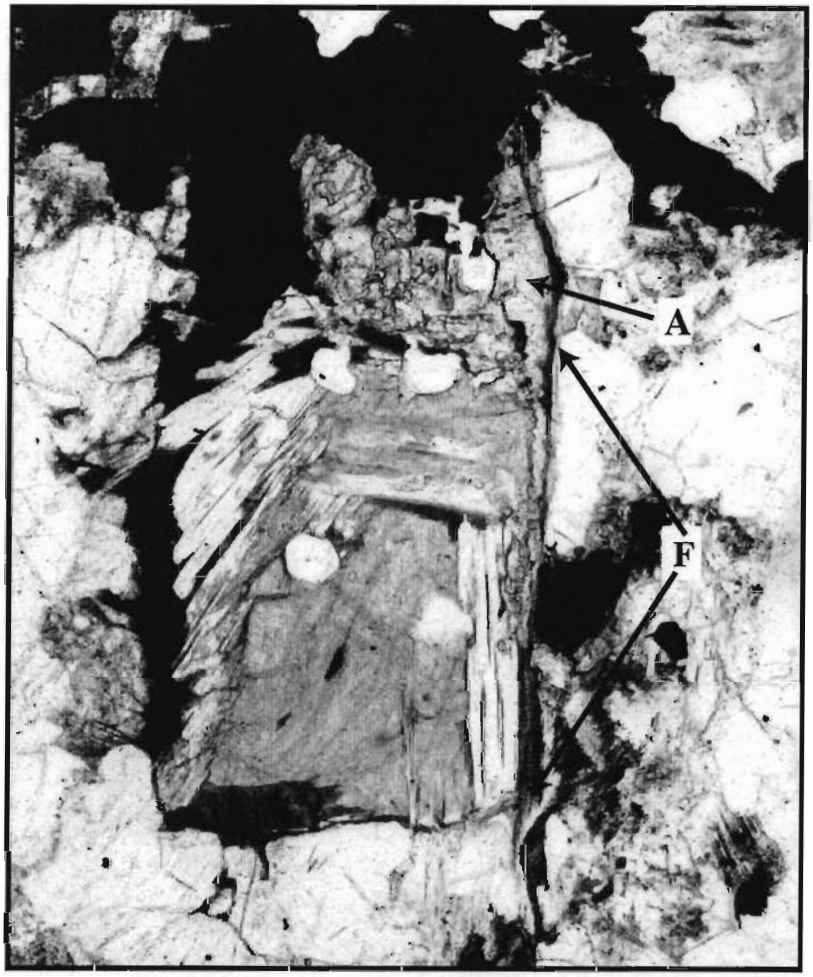

Figure 2.8 Photomicrograph of pseudomorphed andalusite. Andalusite (A) partially pseudomorphed by coarse muscovite and a fine-grained mat of intergrown chlorite and muscovite. Fibrolite (F) rims a portion of the porphyroblast.

2.5 Geochronology procedures and results

The geochronologic portion of this study involved analysis of detrital zircon from two samples and coherent age determinations from three samples. We isolated zircon and monazite using standard crushing, density, and magnetic separation techniques. Grain selection is described below, within the individual sample descriptions. After preparing a polished epoxy mount, we photographed the grains in transmitted and reflected light, and imaged each grain using cathodoluminescence (zircon) or electron backscatter (monazite). The cleaned and gold-coated mount was loaded into the U.S.G.S.-Stanford Sensitive High Resolution Ion Microprobe – Reverse Geometry (SHRIMP-RG) at Stanford University.

For zircon, we used internal standards SL13 or CZ3 for concentrations and R33 for age (419.3 ± 0.4 Ma; (Black et al. 2004)). For monazite, we used 44069B (425 ± 0.5 Ma; (Aleinikoff et al. in press)). The primary O_2^- beam operated at approximately 3 nA, sputtering a pit approximately 25-40 μm across. For analysis of detrital grains we collected data over four cycles through each mass station; for the remaining analyses we used a six-cycle data collection routine. During detrital analysis, we returned to the age standard every fifth or sixth analysis; for other analyses, we analyzed the standard after every two to three analyses of the unknown. Raw data were processed with Squid (Ludwig 2001), using the observed best-fit ln(U/Pb)/ln(U/UO) ratio for accepted standard analyses. Data presented here were plotted using Isoplot/Ex (Ludwig 2003). All results are plotted at the 2σ level of uncertainty. In the data tables, individual spot ages are listed at 1σ uncertainties, but all final age determinations are presented at 95% confidence. For consistency among all detrital grains, we corrected for common lead

assemblage represents crystallized melt plus residue. A lower grade assemblage consisted of quartz + plagioclase + muscovite + chlorite ± epidote. In both assemblages, various accessory minerals, including zircon, monazite, apatite, calcite, ilmenite, and magnetite, are present; some exist as metasTable 2.phases. Magnetite concentrations are locally high throughout the various facies, with no clear spatial or lithologic patterns. We observed no graphite or tourmaline. The amphibolite mineralogy is consistent with the metamorphic phases recognized in the quartzofeldspathic rocks.

In contrast to previous reports (e.g. Boudette 1970), we found no spatial relationship between coarse muscovite and the contact between the massif and the Boil Mountain Complex. Instead, we suggest that the relatively uniform mineral assemblages and anatectic microstructures present throughout the study area indicate the lack of a significant metamorphic gradient across the massif. Based on mineral assemblages, Trzcienski et al. (1992) argued that the northwestern part of the massif experienced lower-grade metamorphic conditions, no higher than greenschist facies. We concur that in many places the rocks contain what appears to be a muscovite-biotite-chlorite-plagioclase assemblage, but we note that in the central portions of the massif, we have observed biotite-muscovite schlieren, without evidence for sillimanite, in rocks adjacent to those containing sillimanite. We interpret the biotite-muscovite schlieren as retrograded versions of biotite-sillimanite schlieren. This implies that a lack of sillimanite in any particular location in the massif does not necessarily indicate the earlier absence of the mineral.

using measured ^{204}Pb, based on the Stacy and Kramers (1975) model. Likewise, we calculated the ages of the xenocrysts in the non-detrital samples based on measured ^{204}Pb. For the two coherent age determinations, both of Paleozoic age, we used measured ^{207}Pb as the basis for the common lead correction. All Concordia plots, however, use the ^{204}Pb correction for common Pb. Unless noted, we calculated ages younger than 1200 Ma using $^{206}Pb/^{238}U$, and ages older than 1200 Ma using $^{207}Pb/^{206}Pb$.

2.5.1 SHRIMP detrital zircon

We collected two samples, one each from the McKenney Stream (GCL327) and Sarampus Falls facies (GCL405), for detrital zircon analysis. The McKenney Stream facies sample is the same rock from which we separated monazite. Zircon grains were mounted as a poured random sample of several hundred grains. A few additional analyses were included from hand-picked zircons that were selected to determine whether metamorphic rims were present. We analyzed 66 spots on 65 grains from sample GCL405 and 68 spots on 64 grains from GCL327. Approximately half the combined population exhibits oscillatory igneous zonation (66), with the remainder exhibiting irregular, patchy metamorphic zonation (19), or ambiguous or no zonation (49). In most instances where grains exhibited a core and rim or mantle, we dated one or the other; on five grains we dated both. Mantles and rims are systematically younger than the cores, but we observed no obvious relationship between zoning type and age.

The resulting reduced data (Fig. 2.9; Table 2.2) represent the age spectrum of detrital zircon present in the two facies. Eliminated from the relative probability calculation are grains not concordant at 2σ (Fig. 2.9a,b). In addition, analysis 327-2 (448 ± 8 Ma) was eliminated because it is younger than the depositional age of the unit;

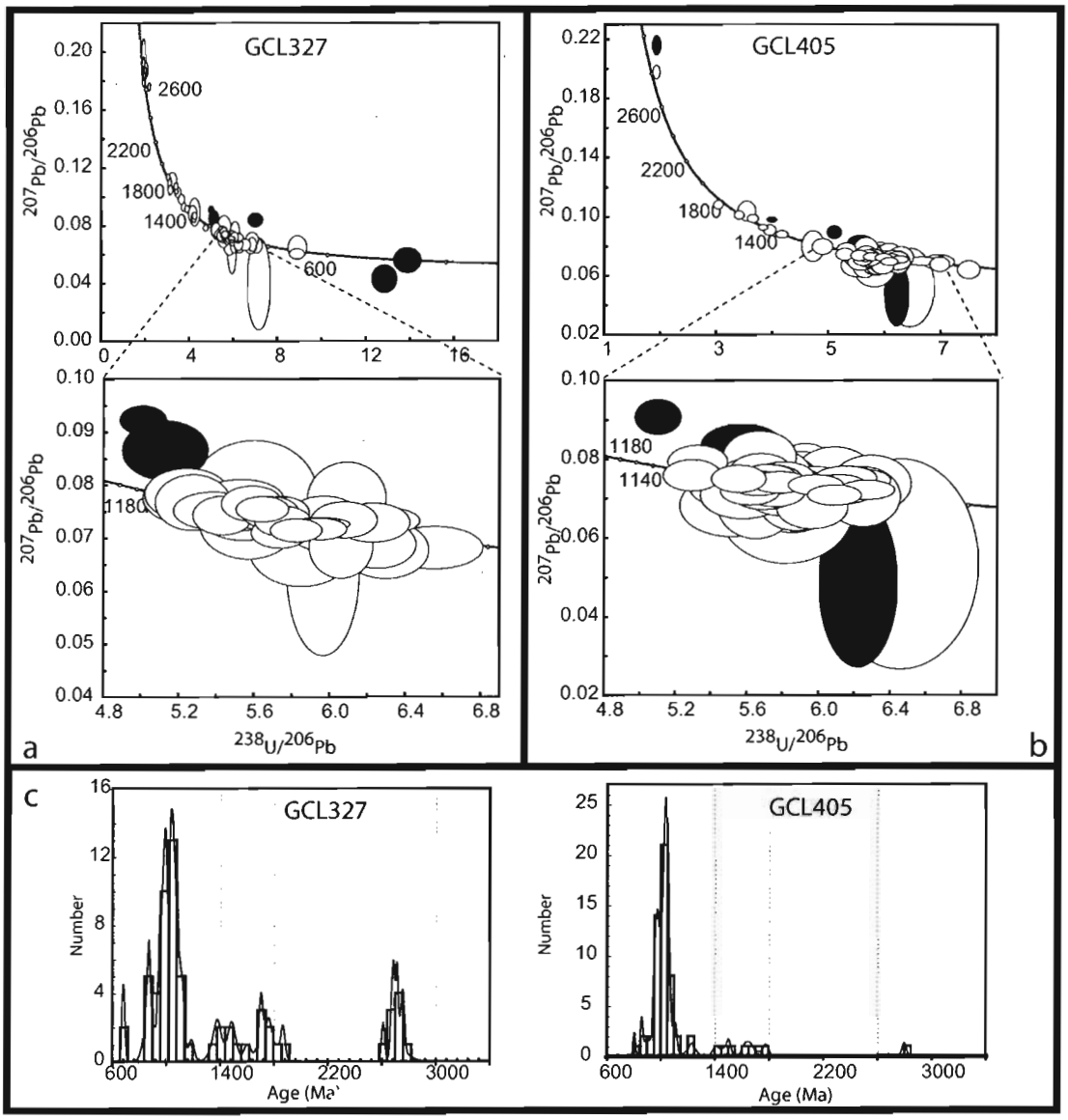

Figure 2.9 Results from detrital zircon U-Pb isotopic analyses. (a) Tera-Wasserburg plots of zircon from the McKenney Stream facies (GCL327). (b) Tera-Wasserburg plots of zircon from the Sarampus Falls facies (GCL405). Shaded error ellipses were not included in the relative probability calculation. All error ellipses shown at 2σ. (c) Relative probability age plots and histograms. Ages greater than 1200 Ma are calculated using $^{207}Pb/^{206}Pb$; younger ages are based on $^{238}U/^{206}Pb$.

Table 2.2 U-Pb SHRIMP isotopic data for detrital zircon from the Chain Lakes massif

										^{204}Pb-corrected[c]					
Spot[a]	Notes[b]		^{204}Pb /^{206}Pb	^{207}Pb /^{206}Pb	% common ^{206}Pb	U (ppm)	Th/U	^{238}U/^{206}Pb	% err	^{207}Pb /^{206}Pb	% err	^{206}Pb /^{238}U Age	1σ	^{207}Pb /^{206}Pb Age	1σ
GCL327 (UTM Zone 19T 383739 5038389)															
1	R	I	0.0000	0.1118	0.00	53	1.07	3.2486	2.58	0.1118	2.19	1730	39	1830	40
2	R	I	0.0004	0.0641	0.81	317	0.08	13.8853	1.83	0.0576	6.09	448	8	514	134
3	R	I	0.0001	0.1003	0.13	183	0.63	3.6715	1.61	0.0993	1.41	1553	22	1611	26
4	R	A	0.0000	0.0853	0.00	245	0.14	7.0110	1.96	0.0853	2.29	860	16	1323	44
5		I	0.0000	0.0761	0.00	112	0.00	5.5055	1.76	0.0761	2.45	1076	17	1098	49
6	R	I	0.0000	0.0734	0.00	377	0.39	6.2379	1.57	0.0734	1.47	959	14	1025	30
7	R	A	0.0002	0.0695	0.38	207	0.02	8.9213	1.94	0.0664	4.97	685	13	820	104
7.2	R	A	0.0000	0.0908	0.00	38	0.83	4.2573	2.40	0.0908	4.34	1360	29	1442	83
8	R	A	-0.0001	0.0704	-0.18	298	0.11	6.8669	1.72	0.0719	2.83	876	14	982	58
8.2	R	A	0.0000	0.0788	0.00	49	0.89	5.6006	2.40	0.0788	4.96	1059	23	1166	98
9		I	0.0003	0.0715	0.50	589	0.02	6.8039	1.64	0.0676	3.22	884	14	855	67
10		I	0.0000	0.0865	0.00	141	0.10	5.1303	1.81	0.0865	2.60	1148	19	1350	50
11		A	0.0000	0.0894	0.00	130	0.27	4.1852	1.84	0.0894	2.60	1381	23	1412	50
12		I	0.0003	0.0728	0.62	446	0.01	7.0462	1.62	0.0679	3.18	856	13	865	66
13	R	M	0.0001	0.0633	0.15	573	0.04	8.9033	1.61	0.0621	2.32	686	10	679	49
14	R	A	-0.0001	0.0746	-0.10	486	0.30	5.3854	1.59	0.0753	1.87	1098	16	1078	38
15		M	0.0001	0.0721	0.10	282	0.29	6.0392	1.71	0.0713	2.22	988	16	967	45
16		M	0.0000	0.1876	0.00	167	0.46	2.0472	1.74	0.1876	1.08	2564	37	2721	18
16.2		M	0.0000	0.1920	0.00	53	1.70	1.9435	2.09	0.1920	3.54	2676	46	2760	58
17		I	0.0001	0.0702	0.23	517	0.04	6.5513	1.61	0.0684	2.37	916	14	880	49
18		A	0.0000	0.1042	0.00	278	0.40	3.5043	1.67	0.1042	1.41	1618	24	1700	26
19	R	A	0.0000	0.0779	0.00	154	0.34	5.2426	1.79	0.0779	2.64	1125	18	1145	52
20		A	0.0000	0.0748	0.00	167	0.44	5.5451	1.78	0.0748	2.73	1069	18	1064	55
21		A	0.0000	0.0774	0.00	180	0.54	5.5326	1.66	0.0774	1.94	1071	16	1132	39
21.2		A	-0.0001	0.0772	-0.16	140	0.83	5.2466	1.73	0.0784	2.49	1125	18	1157	49
22		I	0.0000	0.0729	0.00	32	1.04	5.5706	1.89	0.0729	3.70	1064	19	1012	75

Table 2.2, cont.

							----------^{204}Pb-corrected[c]----------							
Spot[a]	Notes[b]	^{204}Pb /^{206}Pb	^{207}Pb /^{206}Pb	% common ^{206}Pb	U (ppm)	Th/U	^{238}U/^{206}Pb	% err	^{207}Pb /^{206}Pb	% err	^{206}Pb /^{238}U Age	1σ	^{207}Pb /^{206}Pb Age	1σ
GCL327														
23	M	0.0001	0.0752	0.09	126	0.45	5.4363	1.19	0.0744	1.99	1089	12	1054	40
24	I	0.0000	0.1846	0.00	89	1.10	1.9503	1.29	0.1846	0.98	2668	28	2695	16
25	M	0.0000	0.0750	0.00	236	0.44	5.6857	1.09	0.0750	1.61	1044	11	1069	32
26	I	0.0000	0.0742	0.01	368	0.31	5.6319	1.32	0.0741	1.19	1054	13	1045	24
27	I	0.0000	0.1840	0.00	155	0.92	1.9775	1.07	0.1840	0.66	2638	23	2689	11
28	A	0.0000	0.0934	0.07	209	0.39	3.9212	1.04	0.0928	1.10	1464	14	1484	21
29	I	0.0001	0.0880	0.11	129	0.39	4.2358	1.12	0.0872	1.64	1366	14	1364	32
30	I	0.0000	0.0754	-0.02	280	0.33	5.6452	1.01	0.0756	1.26	1051	10	1084	25
31	A	0.0000	0.1046	0.00	432	0.41	3.4399	0.93	0.1046	0.64	1645	13	1708	12
32	A	0.0002	0.0708	0.34	76	0.65	5.8522	1.93	0.0681	4.14	1017	18	873	86
33	I	0.0000	0.0886	0.04	239	0.21	4.2654	1.10	0.0883	1.17	1358	13	1388	22
34	A	0.0000	0.1920	0.05	70	0.75	1.9232	1.46	0.1916	0.97	2699	32	2756	16
35	R A	0.0000	0.0719	0.00	491	1.70	5.9502	0.96	0.0719	1.14	1001	9	983	23
36	I	0.0022	0.0748	4.04	22	1.95	7.1786	3.04	0.0416	30.82	841	24	-251	780
37	I	0.0001	0.0745	0.18	160	0.34	6.2288	1.28	0.0731	2.04	960	11	1016	41
38	A	0.0000	0.1082	0.00	187	0.60	3.4158	1.10	0.1082	0.92	1655	16	1770	17
39	I	0.0000	0.1830	0.00	123	0.74	1.9870	1.11	0.1830	0.72	2628	24	2680	12
40	I	0.0001	0.0712	0.27	85	0.93	6.2538	1.32	0.0690	2.65	956	12	900	55
41	A	0.0000	0.1872	0.01	343	0.83	2.0106	0.95	0.1871	0.46	2602	20	2717	8
42	I	0.0000	0.1056	-0.02	127	0.49	3.1630	1.25	0.1058	1.22	1771	19	1729	22
43	I	0.0000	0.0736	0.00	159	1.19	6.0777	1.17	0.0736	1.86	982	11	1030	38
44	M	0.0000	0.0717	0.06	184	0.32	5.7392	1.09	0.0712	1.64	1035	10	964	33
45	I	0.0000	0.0750	0.00	214	0.38	5.7371	1.10	0.0750	1.60	1036	10	1070	32
46	I	0.0000	0.0768	0.00	57	0.49	5.2788	1.55	0.0768	2.75	1118	16	1117	55
47	M	0.0000	0.0729	0.01	943	0.06	5.9440	1.12	0.0728	0.69	1002	10	1008	14
48	A	0.0000	0.1088	0.04	263	0.40	3.1350	1.06	0.1085	2.36	1785	16	1775	43

Table 2.2, cont.

									----------^{204}Pb-corrected[c]----------						
Spot[a]	Notes[b]		^{204}Pb /^{206}Pb	^{207}Pb /^{206}Pb	% common ^{206}Pb	U (ppm)	Th/U	^{238}U/^{206}Pb	% err	^{207}Pb /^{206}Pb	% err	^{206}Pb /^{238}U Age	1σ	^{207}Pb /^{206}Pb Age	1σ
GCL327															
49		I	0.0000	0.0798	0.00	327	0.62	4.7670	0.98	0.0798	1.04	1228	11	1193	20
50	R	I	0.0013	0.0648	2.43	778	0.00	12.8395	1.80	0.0449	8.63	483	8	-59	210
51		A	-0.0001	0.0759	-0.09	153	0.46	5.5903	1.19	0.0766	1.75	1061	12	1112	35
52		M	0.0000	0.0722	0.07	352	0.20	5.8232	0.96	0.0717	1.24	1022	9	977	25
53		I	0.0000	0.1149	0.05	195	1.04	3.0543	1.01	0.1146	0.81	1826	16	1873	15
54	R	A	0.0003	0.0725	0.50	281	0.17	6.8718	1.16	0.0685	2.84	876	9	885	59
55	R	I	0.0001	0.0941	0.25	772	0.38	5.0137	1.00	0.0922	1.18	1172	11	1471	22
56	R	I	0.0000	0.1762	0.05	151	1.82	2.2031	1.05	0.1758	0.66	2413	21	2614	11
57	R	I	0.0006	0.0777	1.14	260	0.24	6.0607	1.13	0.0686	3.48	984	10	887	72
58		I	0.0000	0.1922	0.01	120	1.78	1.9232	1.13	0.1921	0.74	2699	25	2760	12
59		M	-0.0002	0.0743	-0.43	68	1.36	6.0909	1.38	0.0777	3.45	980	13	1140	69
60		I	0.0001	0.0746	0.20	60	1.25	5.9691	1.47	0.0730	2.83	998	14	1013	57
61		M	0.0001	0.0695	0.19	66	0.79	6.2973	1.47	0.0680	3.20	950	13	868	66
62	R	I	0.0000	0.0945	0.05	144	0.90	3.7733	1.12	0.0941	1.30	1515	15	1509	25
63			0.0000	0.0728	-0.07	203	0.36	5.7532	1.05	0.0734	1.57	1033	10	1024	32
64			0.0020	0.0930	3.62	234	0.14	5.9657	1.31	0.0641	9.99	999	12	744	211
GCL405 (UTM Zone 19T 373097 5020059)															
1	R	I	0.0001	0.0763	0.14	292	0.26	5.7892	1.59	0.0752	1.66	1027	15	1074	33
2	R	I	0.0002	0.0740	0.43	200	0.37	6.9636	1.67	0.0706	2.75	865	14	946	56
3	R	I	0.0000	0.0775	0.00	133	0.36	5.8943	1.97	0.0775	2.31	1010	18	1134	46
4	R	A	0.0000	0.0713	0.00	566	0.32	6.6590	1.82	0.0713	1.58	902	15	965	32
5		I	0.0000	0.0743	0.00	336	0.36	5.6768	1.58	0.0743	1.48	1046	15	1050	30
6	R	I	0.0000	0.0759	0.09	613	0.08	5.9822	1.57	0.0752	1.56	996	14	1075	31
7	R	I	0.0000	0.0735	0.00	110	0.53	5.5335	1.90	0.0735	3.26	1071	19	1027	66
8	R	A	0.0000	0.0760	-0.04	421	0.21	5.7102	1.61	0.0764	1.84	1040	16	1104	37
9	R	A	0.0002	0.0735	0.32	276	0.32	5.5798	1.73	0.0710	3.36	1063	17	957	69

Table 2.2, cont.

Spot[a]	Notes[b]		$^{204}Pb/^{206}Pb$	$^{207}Pb/^{206}Pb$	% common ^{206}Pb	U (ppm)	Th/U	$^{238}U/^{206}Pb$	% err	$^{207}Pb/^{206}Pb$	% err	$^{206}Pb/^{238}U$ Age	1σ	$^{207}Pb/^{206}Pb$ Age	1σ
									^{204}Pb-corrected[c]						
GCL405															
10	R	A	0.0000	0.0741	0.02	585	0.23	5.9579	1.59	0.0739	1.55	1000	15	1040	31
11		I	0.0000	0.0745	0.08	126	0.25	6.0851	1.16	0.0738	1.79	981	11	1037	36
12		I	0.0000	0.0757	0.00	162	0.36	5.8063	1.20	0.0757	1.97	1024	11	1087	40
13		A	0.0004	0.0738	0.67	34	0.69	5.5136	2.12	0.0684	4.66	1074	21	882	96
14		I	0.0000	0.0751	0.01	125	0.50	5.7430	1.19	0.0749	2.00	1035	11	1067	40
15		M	0.0000	0.0927	0.06	143	0.46	3.9555	1.17	0.0922	1.49	1453	15	1472	28
16		A	0.0001	0.0903	0.13	204	0.36	4.1751	1.04	0.0893	1.21	1384	13	1411	23
17		M	0.0002	0.0739	0.29	63	0.31	5.7966	1.46	0.0716	3.29	1026	14	975	67
18		M	0.0001	0.0739	0.25	143	0.29	5.7572	1.19	0.0719	2.11	1032	11	982	43
19		I	0.0001	0.0719	0.13	145	0.31	5.6966	1.24	0.0708	1.99	1043	12	953	41
20		M	-0.0002	0.0809	-0.35	60	0.78	5.5723	1.67	0.0836	2.55	1064	16	1283	50
21		A	0.0000	0.0746	0.05	185	0.66	5.7852	1.14	0.0742	1.49	1028	11	1047	30
21.2	R	A	0.0004	0.0749	0.73	552	0.29	6.9858	1.05	0.0691	2.91	862	8	902	60
22		A	0.0000	0.0709	0.00	43	1.04	6.2192	1.61	0.0709	3.16	961	14	954	65
23		A	0.0004	0.0738	0.79	20	1.09	5.8190	2.63	0.0676	8.24	1022	25	855	171
24		A	0.0001	0.0768	0.10	96	0.59	5.2959	1.25	0.0760	2.10	1115	13	1095	42
25		I	0.0000	0.0943	0.04	386	0.48	3.8368	0.94	0.0940	0.78	1493	13	1508	15
26		M	-0.0001	0.0787	-0.25	66	0.90	5.6710	1.47	0.0807	3.24	1047	14	1214	64
27		I	0.0000	0.1047	0.00	31	0.31	3.5492	1.81	0.1047	2.57	1600	26	1710	47
28		M	0.0000	0.0756	0.00	41	0.16	5.7596	1.65	0.0756	3.16	1032	16	1086	63
29		I	0.0001	0.0802	0.10	87	0.55	5.3265	1.27	0.0794	2.10	1109	13	1183	42
30		I	-0.0002	0.0734	-0.30	58	1.17	6.0872	1.53	0.0757	3.98	981	14	1087	80
31		A	0.0000	0.0716	-0.04	125	0.44	5.6181	1.19	0.0719	1.93	1056	12	984	39
32		I	-0.0001	0.0763	-0.14	122	0.52	5.6784	1.21	0.0774	2.13	1046	12	1132	42
33		I	0.0003	0.0739	0.51	68	0.99	5.8719	1.47	0.0698	4.49	1014	14	924	92
34		A	0.0002	0.0702	0.28	72	1.06	5.9651	1.36	0.0679	3.19	999	13	867	66

Table 2.2, cont.

Spot[a]	Notes[b]	$^{204}Pb/^{206}Pb$	$^{207}Pb/^{206}Pb$	% common ^{206}Pb	U (ppm)	Th/U	$^{238}U/^{206}Pb$	% err	$^{207}Pb/^{206}Pb$	% err	$^{206}Pb/^{238}U$ Age	1σ	$^{207}Pb/^{206}Pb$ Age	1σ
							----------^{204}Pb-corrected[c]----------							
GCL405														
35	A	0.0000	0.0740	0.00	133	0.58	5.6614	1.15	0.0740	1.72	1049	11	1041	35
36	I	0.0000	0.0717	0.09	303	0.25	6.0891	1.01	0.0710	1.45	980	9	958	30
37	A	0.0000	0.0727	-0.04	159	0.26	6.1110	1.13	0.0730	1.75	977	10	1015	35
38	R A	0.0004	0.0797	0.73	245	0.30	6.2922	1.45	0.0739	3.93	951	13	1039	79
39	I	0.0001	0.0763	0.12	284	0.41	6.1514	1.14	0.0754	1.59	971	10	1078	32
40	I	0.0000	0.1026	0.07	194	0.70	3.4130	1.07	0.1020	1.14	1656	16	1662	21
41	A	0.0000	0.1000	0.00	216	0.72	3.6552	1.15	0.1000	1.11	1559	16	1623	21
42	I	-0.0001	0.2143	-0.13	47	0.66	1.9295	1.59	0.2151	1.24	2692	35	2944	20
43	I	0.0000	0.0747	0.00	267	0.19	6.2268	1.14	0.0747	1.54	960	10	1061	31
44	A	0.0000	0.1972	0.00	85	1.05	1.9315	1.30	0.1972	0.94	2690	29	2803	15
45	I	0.0000	0.0803	-0.09	60	0.65	4.8993	1.52	0.0810	2.63	1197	17	1221	52
46	I	0.0003	0.0728	0.56	63	0.75	5.6522	1.54	0.0684	4.92	1050	15	879	102
47	M	0.0001	0.0767	0.15	76	0.63	5.6325	1.41	0.0755	2.64	1054	14	1083	53
48	I	0.0000	0.0753	0.00	146	0.47	5.7184	1.17	0.0753	1.84	1039	11	1078	37
49	I	-0.0001	0.0743	-0.10	184	0.54	5.5546	1.12	0.0751	1.88	1067	11	1072	38
50	M	0.0000	0.0745	0.00	35	1.43	5.7362	1.98	0.0745	4.10	1036	19	1056	83
51	A	-0.0001	0.0720	-0.10	191	0.52	6.1432	1.20	0.0728	2.24	972	11	1008	45
52	I	0.0000	0.1090	0.00	202	0.30	3.0438	1.16	0.1090	1.08	1831	19	1782	20
53	I	0.0001	0.0745	0.11	415	0.30	5.9849	1.05	0.0736	1.42	996	10	1029	29
54	A	0.0002	0.0713	0.33	50	0.68	5.8511	1.66	0.0687	4.18	1017	16	890	86
55	M	0.0000	0.0727	0.05	256	1.11	6.2673	1.02	0.0723	1.36	954	9	994	28
56	I	0.0002	0.0784	0.44	123	1.14	5.7855	1.30	0.0749	4.10	1028	12	1066	82
57	R A	0.0003	0.0742	0.45	153	0.31	6.2486	1.35	0.0706	4.34	957	12	946	89
58	R I	0.0016	0.0726	2.89	230	0.01	6.2215	1.44	0.0490	17.53	961	13	149	411
59	R I	0.0002	0.0935	0.38	295	0.11	5.1036	1.03	0.0906	1.99	1153	11	1438	38
60	R I	0.0004	0.0708	0.67	290	0.03	7.5027	1.11	0.0655	3.72	807	8	789	78

Table 2.2, cont.

								----------^{204}Pb-corrected^{c}----------						
Spot^{a}	Notes^{b}	^{204}Pb /^{206}Pb	^{207}Pb /^{206}Pb	% common ^{206}Pb	U (ppm)	Th/U	^{238}U/^{206}Pb	% err	^{207}Pb /^{206}Pb	% err	^{206}Pb /^{238}U Age	1σ	^{207}Pb /^{206}Pb Age	1σ
GCL405														
61		I	0.0005	0.0815	0.99	91	0.38	5.9260	1.47	0.0737	5.72	1005	14	1032	116
62		M	0.0000	0.0721	0.00	50	0.50	5.6412	1.95	0.0721	3.39	1052	19	990	69
63		I	0.0001	0.0829	0.19	55	0.24	4.7308	1.73	0.0814	5.18	1236	19	1231	102
64		M	0.0011	0.0703	2.04	22	1.48	6.4569	2.76	0.0538	19.99	928	24	362	451
65	R	I	0.0001	0.1003	0.14	860	0.13	3.9935	0.93	0.0992	0.74	1441	12	1609	14

a Bold denotes spots not included in age spectrum calculation

b Location of spot on zircon grain: R=rim; C=core; no notation = core or thick mantle
Rype of zonation: I=igneous; M=metamorphic; A=ambiguous

c All results corrected for common lead using model of Stacey and Kramers (1975); * refers to radiogenic Pb

327-2 was measured on a rim that we interpret as related to metamorphism accompanying the intrusion of the nearby Attean pluton.

The McKenney Stream facies (GCL327) is dominated by detrital grains in the range ~840-~1050 Ma, with three grains younger than 800 Ma and several grains between 1350 and 1875 Ma. A large gap exists between 1875 Ma and 2600 Ma, but nine grains have ages between 2600 and 2800 Ma. In the Sarampus Falls facies, the early Neoproterozoic to late Mesoproterozoic population is more dominant, with 39 grains falling between 800 Ma and 1150 Ma. Several grains indicate the presence of age populations through 1800 Ma. A gap is present from 1800 Ma through 2800 Ma, where a single grain indicates a source with age ca. 2800 Ma. Although the magnitudes differ slightly, relative probability peaks for in both units for ages older than 800 Ma are quite similar, suggesting that the entire massif was derived from similar, albeit mixed-age, sedimentary source regions.

Within the GCL327 sample set, overgrowths on three grains have ages younger than 800 Ma and cannot be unequivocally described as detrital. These overgrowths, all of which have Th/U ratios <0.04, were dated at 686 ± 10 Ma (1σ), 685 ± 13 Ma, and 483 ± 8 Ma. Three possible interpretations exist to explain their presence: (1) the Chain Lakes massif protolith was deposited prior to ca. 685 Ma, and all three grains represent metamorphic events in the massif; (2) deposition occurred between ca. 685 Ma and ca. 483 Ma, with the older grains being detrital and the youngest being metamorphic; (3) deposition postdated ca. 483 Ma, and all three grains are detrital. Because of their low Th/U ratios, the overgrowths are most likely of metamorphic, rather than rift-related magmatic, origin (Hoskin and Schaltegger 2003). A widespread high-grade metamorphic

event affected the massif at ca. 469 Ma (see below), but it did not produce significant zircon overgrowths. The rim we dated at 483 ± 8 Ma (1σ) may have been produced in this event, but a single occurrence out of 35 rim analyses suggests that, overall, zircon was relatively unaffected by even high-grade metamorphism. In a similar way, an earlier metamorphism at ca. 685 Ma may not have produced well-developed rims of that age. The ca. 685 Ma grains are slightly rounded, lending credence to an interpretation of them as detrital. Although we could not unequivocally determine whether deposition pre- or post-dated 685 Ma, we strongly favor a post-685 Ma depositional age for the Chain lakes massif protolith.

2.5.2 SHRIMP dating of monazite

From a sample of the McKenney Stream facies (GCL327) we separated monazite for U-Pb isotopic age analysis. Monazite grains are not abundant, and many of those that were present were anhedral. Nevertheless, we were able to select a sufficient number of clear, pale yellow inclusion-free grains for analysis. The selected grains ranged in size from approximately 30 μm to 100 μm. Electron backscatter images revealed some grains with complex zoning, but the majority are homogeneous (Fig. 2.10a). We analyzed 15 spots on 15 grains; all results are concordant at 2σ (Fig. 2.10b; Table 2.3). Fourteen of the grains are subhedral with homogenous composition, and one was irregularly zoned and anhedral. Despite being concordant, the morphology and spot age of the zoned grain are sufficiently different from the others (446±6 Ma) to justify not including it in the age calculation. The $^{206}Pb/^{238}U$ weighted average age of the remaining fourteen spots is 469 ± 4 Ma (95% confidence) (Fig. 2.10c). This age could represent either the time of monazite growth or cooling through the monazite blocking temperature. Although monazite has

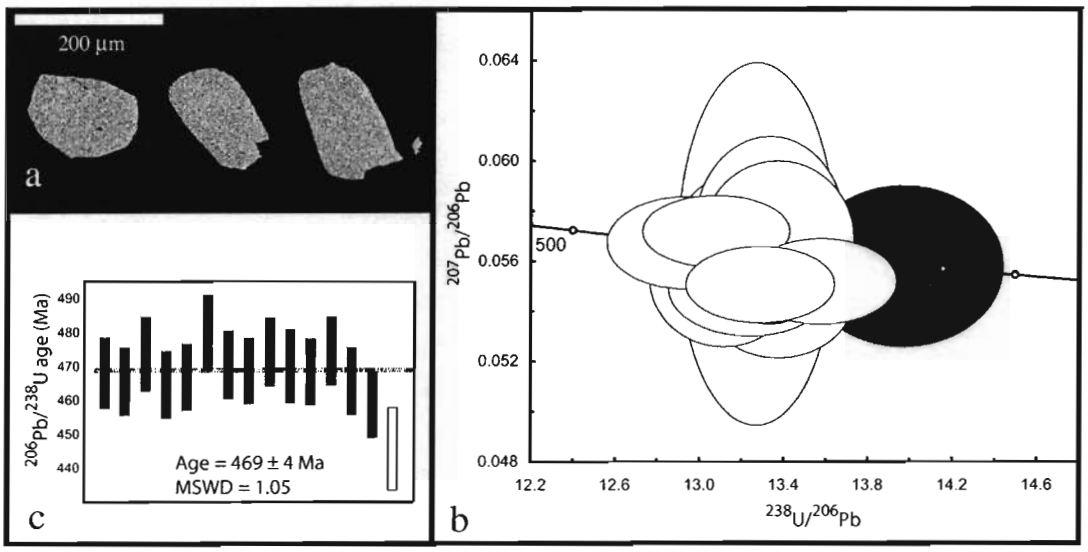

Figure 2.10 Results from U-Pb analysis of metamorphic monazite. (a) Backscatter-electron image of monazite from GCL327. The analyzed grains are relatively uniform, without compositional structure. (b) Tera-Wasserburg plot and (c) weighted average of ages from monazite in sample GCL327, from the McKenney Stream facies. The shaded error ellipse and unfilled error bar represent the only analysis not included in the age calculation. All uncertanties plotted at 2σ.

Table 2.3 U-Pb SHRIMP isotopic data for monazite from sample GCL327
(McKenney Stream facies of the Chain Lakes massif)

						^{204}Pb-corrected				^{207}Pb-corrected	
Spot	^{204}Pb /^{206}Pb	^{207}Pb /^{206}Pb	% common ^{206}Pb	U (ppm)	Th/U	^{238}U/^{206}Pb*	% err	^{207}Pb* /^{206}Pb*	% err	^{206}Pb /^{238}U Age	1σ
GCL327 (UTM Zone 19T 383739 5038389)											
1	0.0003	0.0607	0.5319	1176	88.89	13.2739	1.14	0.0567	5.13	468	5
2	0.0003	0.0587	0.2952	973	92.14	13.3790	1.11	0.0548	1.87	466	5
3	0.0001	0.0580	0.1783	1036	85.59	13.1235	1.19	0.0563	1.28	474	6
4	0.0002	0.0601	0.4627	1077	93.03	13.3743	1.10	0.0569	2.21	464	5
5	0.0002	0.0589	0.3064	1458	94.58	13.3111	1.08	0.0567	1.22	467	5
6	0.0002	0.0595	0.3474	1375	86.95	12.9347	1.18	0.0568	1.31	480	6
7	0.0003	0.0607	0.5205	1166	93.07	13.2013	1.10	0.0569	1.59	470	5
8	0.0003	0.0615	0.6262	2128	95.24	13.2473	1.07	0.0573	1.63	469	5
9	0.0003	0.0592	0.3296	1045	92.79	13.1188	1.10	0.0554	2.00	474	5
10	0.0002	0.0581	0.2009	1249	85.38	13.2443	1.20	0.0550	1.41	470	6
11	0.0001	0.0569	0.0603	1406	94.24	13.2920	1.08	0.0551	1.11	468	5
12	0.0001	0.0580	0.1812	1151	93.59	13.0823	1.09	0.0572	1.01	474	5
13	0.0006	0.0656	1.1440	1297	92.83	13.3364	1.10	0.0573	2.63	466	5
14	0.0001	0.0572	0.1246	1455	94.21	13.5800	1.08	0.0552	1.25	459	5
15C	0.0004	0.0610	0.6337	1059	73.63	13.9721	1.38	0.0559	2.31	446	6

Note: All results corrected for common lead using model of Stacey and Kramers (1975); * refers to radiogenic Pb
Bold indicates spot not included in age calculation

long been considered to have a blocking temperature of approximately 700-750°C (Parrish 1990), in recent years, that interpretation has been called into question. There is growing evidence that monazite may not undergo significant diffusional lead-loss, even at temperatures in excess of 750°C, and that any chronological information lost from monazite is more likely due to dissolution (Rubatto et al. 2001; Cherniak et al. 2002; Seydoux-Guillaume et al. 2002). The tight cluster of individual spot ages (Fig. 2.10c) indicates that if the age represents growth, then that growth did not span a significant time. If the age is a cooling age, the lack of inheritance requires complete resetting of the isotopic system. Without further information, we will treat the U-Pb monazite age as the general time of metamorphism rather than as a particular event in the metamorphic history.

2.5.3 SHRIMP dating of felsic volcanic fragment

From one of the volcanic lithic fragments within the Sarampus Falls facies (GCL203-2), we separated euhedral, clear, elongate zircon for U-Pb age determination. Cathodoluminescence imaging indicates that most grains contain fine concentric oscillatory zoning over the whole grain or a wide mantle (Fig. 2.11a). We interpret these zoned areas as having grown in magma prior to eruption. We analyzed the finely zoned portions of 14 grains and the cores of 4 grains. All analyses are concordant at 2σ (Fig. 2.11b; Table 2.4). The weighted average $^{206}Pb/^{238}U$ age of igneous zones is 479 ± 6 Ma (95% confidence) (Fig. 2.11c); we interpret that age as the time of eruption. Core $^{207}Pb/^{206}Pb$ ages are 1431 ± 18 Ma, 1338 ± 24 Ma, 1731 ± 10 Ma, and 1041 ± 17 Ma (1σ). The core ages fall within the range of the detrital zircon from the same unit (see Section 2.4.1; Fig. 2.9), so we reason that either the magma source was metasedimentary rocks

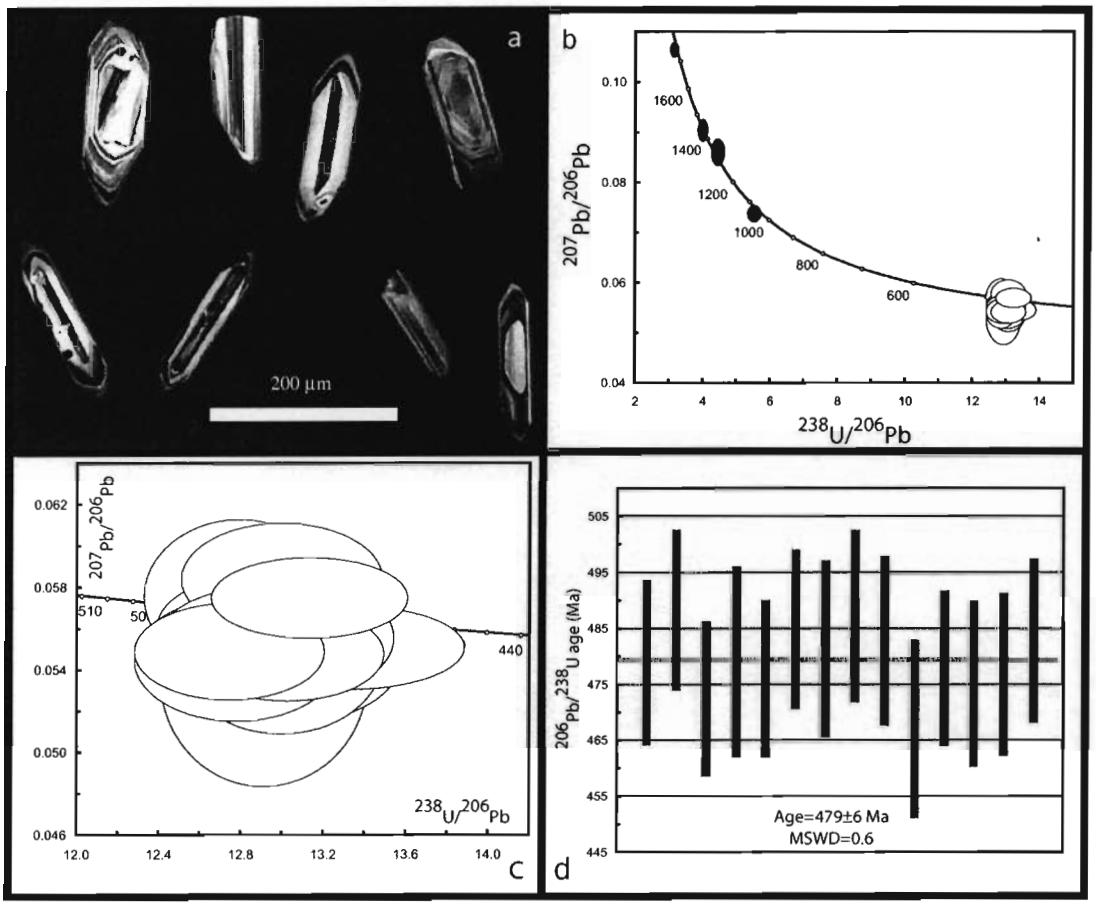

Figure 2.11 Results from U-Pb analysis of felsic metavolcanic. (a) Cathodoluminescence images of representative zircon from volcanic fragment GCL203-2. (b) Tera-Wasserburg plot of all analyzed zircon; shaded analyses represent xenocrysts and are not included in age calculation. (c) Portion of (b) showing analyses used to calculate the age of the volcanic fragment. (d) Weighted average $^{206}Pb/^{238}U$ age. All uncertainties are plotted at 2σ.

Table 2.4 U-Pb SHRIMP isotopic data for zircon in sample GCL203-2 (volcanic fragment in Sarampus Falls facies)

							^{204}Pb-corrected[c]						^{207}Pb-corrected[c]	
Spot[a]	Notes[b]	^{204}Pb /^{206}Pb	^{207}Pb /^{206}Pb	% common ^{206}Pb	U (ppm)	Th/U	^{238}U/^{206}Pb*	% err	^{207}Pb* /^{206}Pb*	% err	^{207}Pb /^{206}Pb Age	1σ	^{206}Pb /^{238}U Age	1σ
GCL203-2 (UTM 19T 382185 5037708)														
1		0.0001	0.0562	-0.0624	202	0.4068	12.9993	1.56	0.0547	2.79	478	7	479	7
2		0.0001	0.0568	-0.0084	494	0.6315	12.7415	1.49	0.0549	1.72	487	7	488	7
3		0.0000	0.0575	0.1229	443	0.4989	13.1344	1.49	0.0575	1.36	473	7	472	7
4		0.0001	0.0563	-0.0495	371	0.6235	12.9998	1.81	0.0545	2.27	478	8	479	8
5		0.0001	0.0569	0.0427	432	0.3077	13.0644	1.51	0.0556	2.06	475	7	476	7
6		0.0002	0.0611	0.5302	492	0.2167	12.7913	1.49	0.0576	2.61	485	7	485	7
7.1		0.0000	0.0561	-0.0822	218	0.4626	12.9104	1.66	0.0561	1.91	481	8	481	8
7.2	C	0.0000	0.0899	-0.0280	164	0.4922	4.0278	1.50	0.0903	0.97	1430	19	1429	21
8		0.0001	0.0567	-0.0168	323	0.7256	12.7770	1.60	0.0546	2.23	486	8	487	8
9		0.0002	0.0566	-0.0216	177	0.3477	12.9106	1.60	0.0536	3.95	481	7	483	8
10		0.0001	0.0562	-0.0263	562	0.3968	13.3275	1.73	0.0551	1.48	466	8	467	8
11		0.0002	0.0571	0.0533	628	0.2399	13.0260	1.48	0.0548	1.68	477	7	478	7
12		0.0001	0.0576	0.1286	171	0.5944	13.0922	1.59	0.0556	3.01	474	7	475	7
13		0.0000	0.0584	0.2199	218	0.3157	12.9984	1.55	0.0584	1.87	478	7	477	7
14		0.0000	0.0555	-0.1554	246	0.6354	12.8799	1.54	0.0555	1.83	482	7	483	7
15C	C	0.0000	0.0866	0.2649	133	0.4611	4.4681	1.78	0.0860	1.25	1302	21	1300	22
16C	C	0.0000	0.1062	-0.1899	416	0.4884	3.1846	1.47	0.1060	0.53	1760	23	1764	25
17C	C	0.0001	0.0748	-0.0343	415	0.8687	5.5414	1.47	0.0740	0.86	1041	17	1071	15

a Bold denotes spots not included in age calculation

b Location of spot on zircon grain: C=core; no notation = thick mantle or no growth zones in grain

c All results corrected for common lead using model of Stacey and Kramers (1975); * refers to radiogenic Pb

similar to those presently exposed in the massif or the magma assimilated zircon grains from the massif during ascent.

2.5.4 SHRIMP dating of amphibolite

Separation of zircon from an amphibolite lens within the Sarampus Falls facies (GCL371) yielded clear, equant to elongate grains with rounded edges and faces. Cathodoluminescence imaging revealed a combination of concentric, oscillatory zones and irregular patches (Fig. 2.12a). Many grains also exhibited a ring of high REE concentration, as indicated by strong cathodoluminescence, surrounded by weakly-zoned mantles. Of the 27 analyses, 21 were of these mantles. Most analyses are concordant at 2σ uncertainty, and those that are not (five analyses) are reversely discordant (Fig. 2.12b; Table 2.5). Seven spots (six cores and one mantle) have $^{206}Pb/^{238}U$ ages ranging from 874 to 1714 Ma; we consider these grains to be xenocrysts incorporated into mafic magma. The xenocryst ages are compatible with a source similar to that of the detrital zircons analyzed previously (GCL327 and GCL405).

The remaining 20 analyses are all from mantles. Cores of these mantled grains do not appear any different than those of the >850 Ma population, so we believe that all zircon grains in this sample are detrital or xenocrystic. The mantles have Neoproterozoic to Early Ordovician ages, and fall into two clusters (Fig. 2.12c; Table 2.5). The larger cluster consists of thirteen analyses concordant at 2σ, with Th/U ratios ranging from 0.15-0.28. The smaller cluster consists of seven analyses, all of which are either reversely discordant at 2σ or have unusually high uncertainties. The weighted average age of the first cluster is 486 ± 11 Ma (Fig. 2.12d), which we interpret as the time of mafic magma crystallization, probably in the form of basalt flows. The ages of the

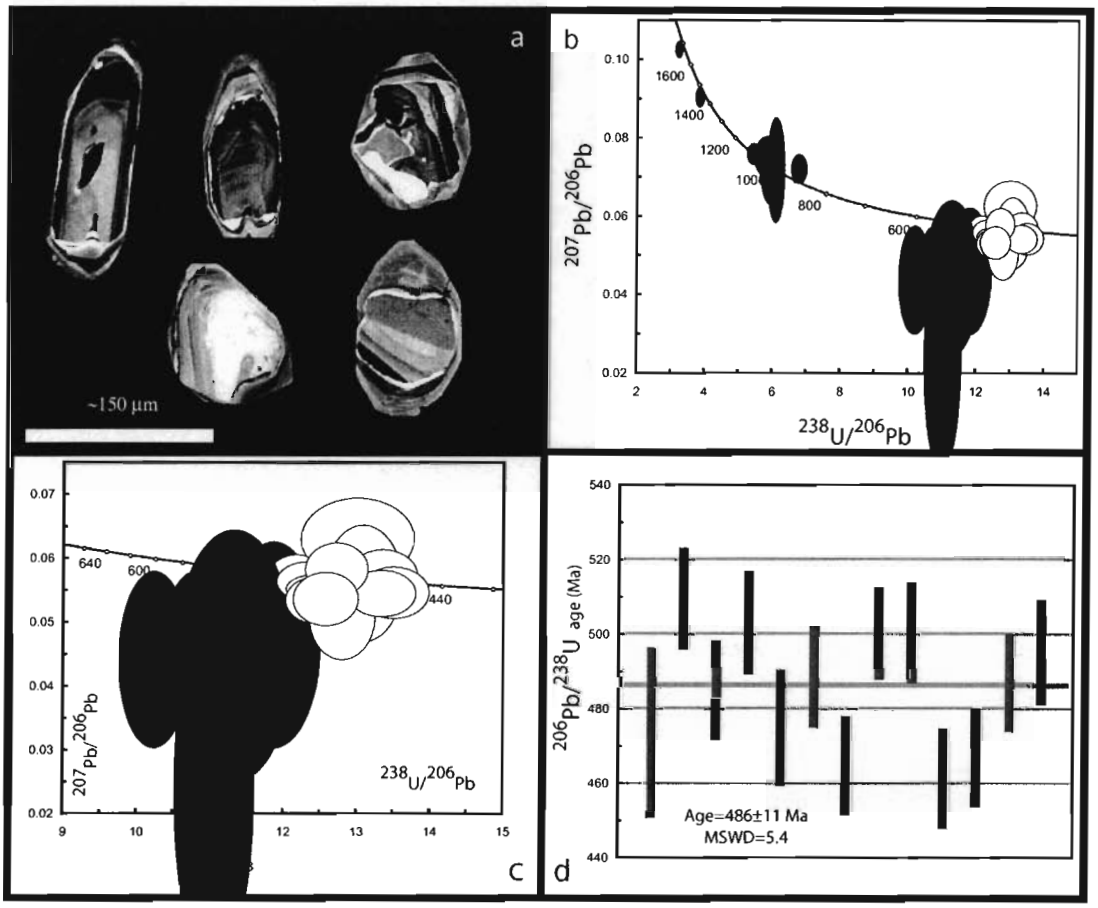

Figure 2.12 Results from U-Pb analysis of amphibolite. (a) Cathodoluminescence images of representative zircon from amphibolite (GCL371). Cores are surrounded by thin bands of highly luminescence, followed by zoned mantles. We interpret the cores as xenocrysts in a mafic melt and the mantles as having formed in that melt. (b) Tera-Wasserburg plot of all analyzed zircon; shaded analyses represent xenocrysts and are not included in age calculation. (c) Portion of (b) showing analyses used to calculate the age of zircon rims. (d) Weighted average $^{206}Pb/^{238}U$ age. All uncertainties are plotted at 2σ.

Table 2.5 U-Pb SHRIMP isotopic data for zircon in sample GCL371 (amphibolite)

							----------^{204}Pb-corrected^{c}----------						^{207}Pb-corrected^{c}	
Spot^{a}	Notes^{b}	^{204}Pb /^{206}Pb	^{207}Pb /^{206}Pb	% common ^{206}Pb	U (ppm)	Th/U	^{238}U/^{206}Pb*	% err	^{207}Pb* /^{206}Pb*	% err	^{207}Pb /^{206}Pb Age	1σ	^{206}Pb /^{238}U Age	1σ
GCL371 (UTM 19T 379970 5035633)														
M1	C	0.0000	0.0753	0.3528	44	1.1259	5.9151	2.62	0.0753	2.79	1077	56	1004	26
M2		0.0025	0.0627	0.4331	83	0.1730	11.1040	2.00	0.0247	47.24	-1804	1688	580	10
M3		0.0010	0.0588	-0.1827	228	0.1966	10.2763	1.92	0.0443	12.55	-91	308	610	11
M4		0.0000	0.0630	0.8258	136	0.2005	13.0091	2.42	0.0630	4.07	707	87	474	11
M5		0.0001	0.0582	0.0915	239	0.2041	12.1775	1.36	0.0565	2.93	472	65	509	7
M6	C	0.0000	0.0760	0.1084	146	0.7141	5.5097	1.41	0.0760	1.44	1096	29	1074	15
M7		0.0001	0.0563	-0.0637	241	0.2384	12.8211	1.40	0.0553	2.60	424	58	485	7
M8		0.0012	0.0618	0.4931	107	0.1965	11.9170	2.06	0.0447	10.53	-70	257	528	10
M9		0.0012	0.0628	0.5430	193	0.1472	11.3614	2.88	0.0448	17.78	-64	434	553	15
M10		0.0008	0.0613	0.2611	180	0.1474	10.8406	1.52	0.0490	7.45	148	175	576	8
M11		0.0000	0.0565	-0.1083	226	0.1791	12.3347	1.40	0.0565	2.18	470	48	503	7
M12		0.0003	0.0609	0.5488	100	0.1856	13.0845	1.66	0.0561	6.56	456	146	475	8
M13		0.0004	0.0566	-0.0399	264	0.1773	12.8036	1.43	0.0510	5.32	241	123	488	7
M14		0.0001	0.0590	0.3441	186	0.2405	13.3532	1.44	0.0574	2.79	507	61	465	7
M15		0.0004	0.0767	0.5677	89	0.5639	5.9916	1.77	0.0715	4.56	972	93	996	17
M16		0.0000	0.0559	-0.1711	754	0.1522	12.4285	1.28	0.0553	1.58	424	35	500	6
M17		0.0002	0.0746	0.8365	200	0.4395	6.8525	1.38	0.0723	2.07	994	42	874	12
M18		0.0004	0.0590	0.2251	238	0.2002	12.4518	1.38	0.0535	2.76	351	62	500	7
M19		0.0002	0.0581	0.2446	176	0.1993	13.5016	1.47	0.0547	2.94	399	66	461	7
I1		0.0011	0.0622	0.5440	168	0.1490	11.8928	2.20	0.0466	13.97	30	335	528	11
I2		0.0013	0.0903	2.4791	76	0.4883	6.1716	1.72	0.0720	7.49	985	153	967	16
I3	C	0.0000	0.0902	-0.2409	158	0.6037	3.9211	1.39	0.0902	1.12	1430	21	1468	20
I4		0.0008	0.0590	0.1032	225	0.2598	11.6878	1.47	0.0470	8.77	47	210	537	7
I5	C	0.0000	0.1022	-0.3738	199	0.5355	3.2965	1.35	0.1022	0.87	1665	16	1713	23
I6		0.0003	0.0590	0.3347	207	0.2821	13.3428	1.42	0.0546	2.66	394	60	467	7
I7		0.0002	0.0613	0.5693	298	0.2062	12.7260	1.36	0.0583	2.86	540	63	487	7
I8		0.0003	0.0574	0.03947	192	0.1866	12.5792	1.45	0.0537	3.12	359	70	495	7

a Bold denotes spots not included in age calculation

b Location of spot on zircon grain: C=core; no notation = thick mantle or no growth zones in grain

c All results corrected for common lead using model of Stacey and Kramers (1975); * refers to radiogenic Pb

second cluster broadly fall into the age range of Iapetan rifting (Aleinikoff et al. 1995; Cawood et al. 2001; Cawood and Nemchin 2001). Because of their discordancy, we cannot offer a firm interpretation of the source of these ages; one possibility is that these ages are from detrital grains whose magmatic overgrowths formed in a rifting episode.

2.6 Discussion

2.6.1 Protolith age

To ascertain the time of deposition of the protolith of the Chain Lakes massif, we rely on several lines of evidence. All lines are consistent with an Early Ordovician deposition.

(1) The 486 ± 11 Ma protolith of the amphibolite (Section 2.4.4) represents the minimum depositional age for the massif protolith; sediment of the massif had to be present by this time. If, as we believe, the Chain Lakes massif was a sedimentary sequence with minor volcanic input (see below), this age marks the deposition itself. Lower portions of the massif may have been deposited earlier, providing a setting into which the Boil Mountain Complex could have intruded.

(2) The age of a felsic lithic fragment (Section 2.4.3), 479 ± 6 Ma, is the same, within uncertainty, as the age of the amphibolite protolith. Again, if the massif were a sedimentary-volcanic sequence, this age records the time of deposition.

(3) The age of the youngest unequivocally detrital zircon measured in this study is ca. 800 Ma; this is the maximum age of deposition. Data from other geochronological analyses from within the massif provide further constraints. Ages of xenocrysts from the amphibolite range down to approximately 530 Ma

(Table 2.5), and a xenocryst within the Ordovician Skinner pluton – which intruded the massif – has an age of 502 ± 8 Ma (Gerbi et al. in review-c). The xenocrysts need not have come from the adjacent quartzofeldspathic parts of the massif, but a non-massif source for the xenocrysts is not evident. Finally, pre-metamorphic ages from a quartzofeldspathic sample taken from part the massif adjacent to the Boil Mountain Complex are as young as ca. 516 Ma (Gerbi et al. in review-c).

(4) The detrital age spectrum recorded in rocks of the Ordovician foreland basin in western Newfoundland (American Tickle Formation of Cawood and Nemchin, 2001) matches quite well with the detrital age spectrum for the Chain Lakes massif (Fig. 2.13). The Newfoundland data indicate that rocks of appropriate age to be the source of the massif were exposed in the region and eroding in the Early Ordovician.

Each of the above points does not on its own tightly constrain the depositional age of the massif protolith, but taken together the data support the interpretation that the Chain Lakes massif protolith was deposited in the Late Cambrian to Early Ordovician. Even if we do not accept all of the above interpretations, we are confident that the Chain lakes massif protolith was deposited between ca. 800 and 480 Ma.

2.6.2 Provenance

Despite its inclusion in several paleogeographical models, the Chain Lakes massif has not been convincingly assigned a source craton. Zen (1983) and Kusky et al. (1997) preferred a peri-Gondwanan source, but Waldron and van Staal (2001) and Moench and Aleinikoff (2003) preferred a Laurentian source. One method for resolving this

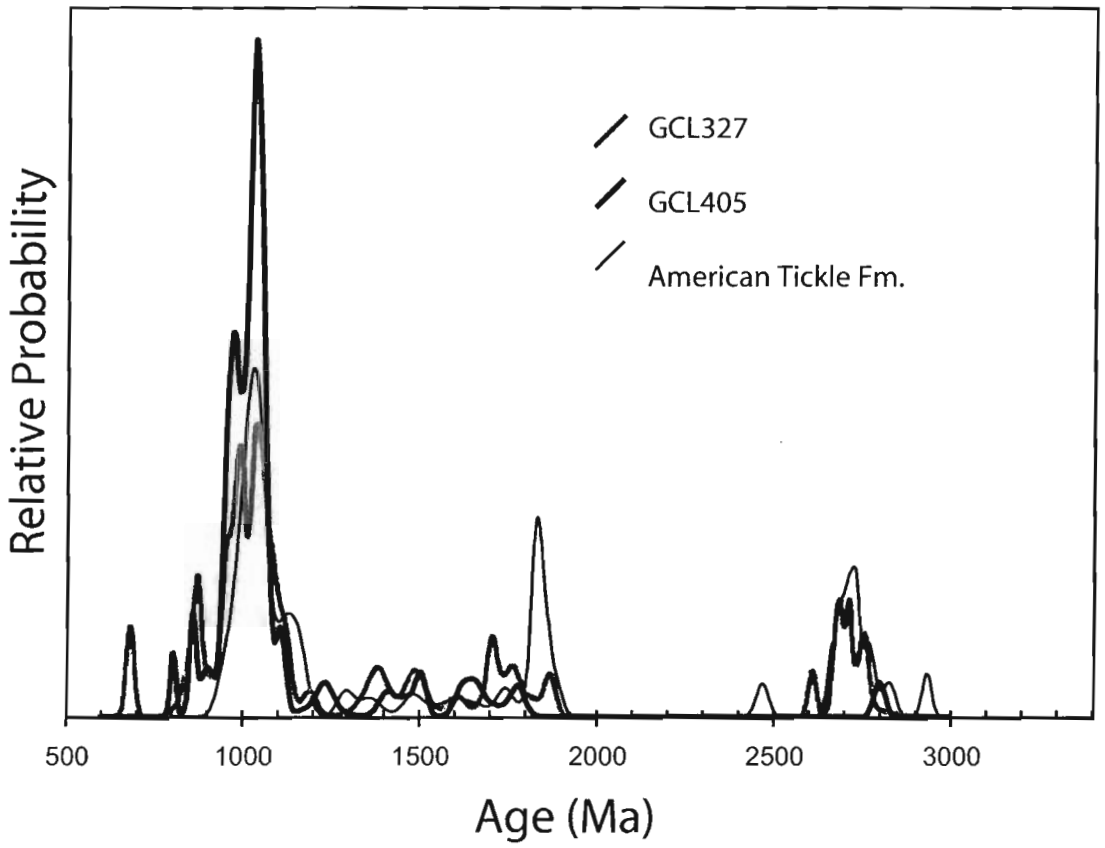

Figure 2.13 Comparison of relative probabilities of detrital zircon ages. GCL327 and GCL405 are from the Chain Lakes massif (this study); data from the American Tickle Fm., Newfoundland, are from Cawood and Nemchin (2001). Note the overall similarity of the plots. Variations such as the presence of ca. 1800 Ma grains in the American Tickle Fm. are probably due to local sources.

uncertainty is to compare the detrital age spectrum from the massif with that of the possible source areas. Age spectra of Gondwanan rocks (Avigad et al. 2003; Guiterrez-Alonso et al. 2003) contain prominent concentrations of zircon in the 750-600 Ma range. Similarly, detrital zircon from the peri-Gondwanan Gander and Avalon terranes record extensive Neoproterozoic through Cambrian activity (O'Brien et al. 1996; van Staal et al. 1996; McNicoll et al. 2002; van Staal et al. 2004). Therefore, if the Chain Lakes massif were derived from Gondwanan sources, we would expect to see an 800-500 Ma age concentration. A Laurentian provenance signature, such as one described by Cawood and Nemchin (2001), exhibits dominant age ranges of 950-1200 Ma, 1600-1900 Ma, and 2500-2800 Ma. The detrital age spectrum from the Chain Lakes massif (Fig. 2.9) matches the Laurentian age spectrum much better than that of Gondwana and the Gondwanan-derived terranes. In agreement with this, Moench and Aleinikoff (2003) and Dunning and Cousineau (1990) interpreted the limited U-Pb zircon data as consistent with derivation from Laurentia.

Nd isotopic composition of seven whole-rock samples from throughout the massif (Cheatham et al. 1989) have calculated T_{dm} model ages of 1.1-1.8 Ga. These are generally older than Avalonian model ages, but they do slightly overlap some Avalonian and Ganderian model ages (van Staal et al. 1996; Murphy and Nance 2002). However, a Grenville source (Dicken 2000) is clearly compatible with the Nd composition of the massif. With support from the detrital zircon age spectrum and the Nd data, we conclude that the Chain Lakes massif was originally deposited in a peri-Laurentian setting. These data do not allow us to determine whether the deposition occurred near the Laurentian margin or offshore along a rifted block.

2.6.3 Protolith setting

The formative environment of the Chain Lakes massif protolith has never been conclusively determined. The mesoscopic texture of the rocks, with numerous, seemingly randomly oriented, rounded lithic fragments, led others (Boudette et al. 1989; Trzcienski et al. 1992) to suggest that the original sedimentary rocks were diamictite or matrix-supported conglomerate. Such a large extent of diamictite – ~900km^2 – requires an unusual depositional environment. An alternative hypothesis, that the massif represents an impact breccia (Boudette and Boone 1982), is unlikely on several grounds, including a lack of planar deformation lamellae in quartz and any other high-pressure or high-strain-rate microstructures. If, instead, the fragments were derived by breaking up existing stratigraphy during anatexis, the protolith need not have formed in an unusual sedimentary setting. In fact, anatexis can explain the lithic fragments, the flecks, and the compositional segregations. Before completing this argument, we must demonstrate that the Chain Lakes massif was pervasively melted in place.

2.6.3.1 The case for melting

Criteria for recognizing partial melting include schlieren, veins of expelled melt, patch migmatite ("flecky" gneiss), crystal faces against former melt, and appropriate mineral assemblages (Sawyer 1999). Igneous microstructures, such as oscillatory zoning in plagioclase concordant with crystal faces and interstitial crystal development, also indicate the presence of melt (Vernon and Collins 1988). These features are all present within the Chain Lakes massif. Schlieren, defined by compositional segregations, and veins or dikes of expelled melt are present in both the Sarampus Falls and Twin Bridges

facies. Patch migmatite is present in all quartzofeldspathic facies (Fig. 2.6c). All three facies also record abundant igneous microstructures, including straight crystal faces and oscillatory zoning in plagioclase (Fig. 2.6b). A final indication of melt presence is the eutectic assemblage quartz + plagioclase + K-feldspar present in leucosomes segregated from the matrix.

The ubiquitous presence of melt evidence and the proportion of these features within all exposures indicates that much, perhaps 40%, of the Chain Lakes massif was molten. In most rocks, such extensive melting would result in significant melt loss, feeding higher-level plutons (cf. Brown 2001). Yet the preservation of the textural evidence for such widespread anatexis suggests that little melt was lost from the system.

Although we have established that melting occurred, it is more difficult to determine peak pressure-temperature conditions and the shape of the pressure-temperature-time path because of the subsequent extensive retrogression and alteration. The presence of andalusite and cordierite and a lack of higher-pressure phases limits the peak pressure to approximately 6 kb; this interpretation assumes some thickening followed andalusite formation. Pseudomorphs after garnet and cordierite suggest that both phases were part of the peak assemblage. Coexistence of these two phases with an aluminosilicate would imply that biotite dehydration melting occurred. Without chemical data indicating their coexistence, we cannot test this supposition, but it is possible that garnet was stabilized by additional components. Additional support for biotite dehydration melting comes from the intergrowths of biotite and sillimanite that could represent the retrograde reaction grt + crd + liq $\rightarrow$ bio + sil. The lack of spinel or pyroxene limits the maximum temperature to about 825°C at 6 kb (Spear et al. 1999).

Where andalusite pseudomorphs and sillimanite coexist, sillimanite rims the pseudomorphs, implying that andalusite was present first (Fig. 2.8). The above constraints are most consistent with a P-T-t path exhibiting nearly isobaric heating, perhaps with slightly increasing pressure, to peak metamorphic conditions of approximately 750-800°C at 4-5 kb (Fig. 2.14).

2.6.3.2 Origin of lithic fragments

The textural features of the Chain Lakes massif listed in Section 2.3.2, including the lithic fragments, can all be related to anatexis. Autobrecciation and consequent fragmentation of a pelitic and volcanic sedimentary sequence is a natural response to melting because: (1) volume increase associated with melting can cause fractures and initiate break-up (Clemens and Mawer 1992) and (2) disaggregation can occur as melting eliminates the solid framework (Clarke et al. 1998). The amphibolite unit did not fragment to the same degree as the more felsic parts of the massif because its higher melting point precluded substantial anatexis from occurring.

Several prominent migmatitic regions throughout the world record the transition from unmelted to melted rocks, with a documented progression from the early stages of melting, vein development, autobrecciation, and development of a diatexite. Well-documented cases include St. Malo, France (Brown 1979), Mt. Stafford, Australia (Greenfield et al. 1996), the Cooma Complex, Australia (Vernon and Johnson 2000), and the Opatica subprovince, Canada (Sawyer 1998). The Chain Lakes massif does not retain portions of unmelted protolith, but several lines of evidence suggest that these rocks followed a history broadly similar to the cases above. First, the composition of the lithic fragments is dominantly five rock types: calcsilicate, pelite, amphibolite, vein quartz, and

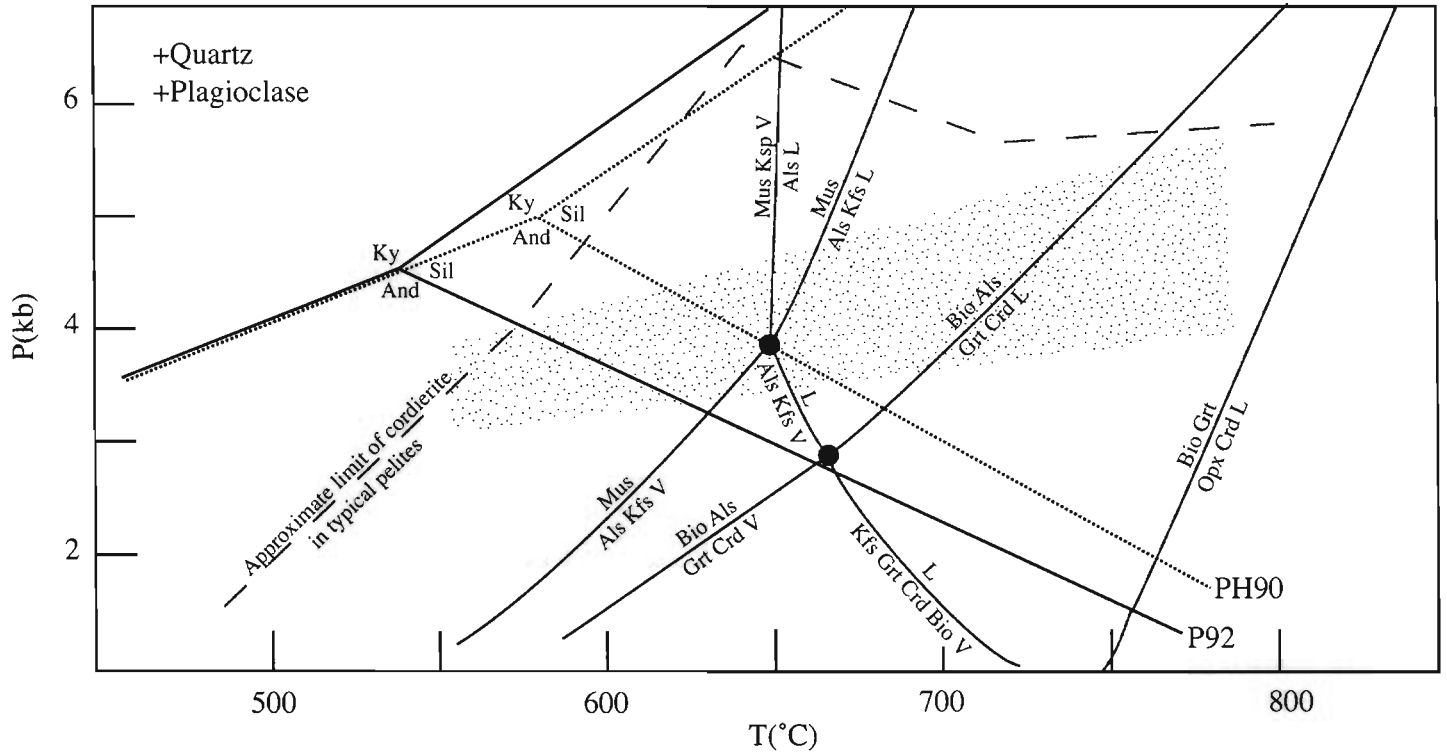

Figure 2.14 P-T history of the Chain Lakes massif. Petrogenetic grid (after Spear et al., 1999) with approximate locations of major phase reactions for a typical pelitic composition in the NaKFMASH system. Actual positions of reactions will vary with intensive parameters such as the activity of water, oxygen fugacity, and functional bulk composition. The aluminosilicate fields are those of Pattison (1992) [P92] and Powell and Holland (1990) [PH90]. Petrological data suggest that the prograde and retrograde paths of rocks from the Chain Lakes massif lie within the stippled region.

felsic volcanics. If the protolith were a diamictite, the clasts would probably have a much more varied population. In our interpretation, these clasts represent resistate, or unmelted portions of the sedimentary-volcanic protolith. Second, the extent of the massif is exceptionally large for a diamictite deposit. Both common sedimentary environments for diamictite, glacial till and alluvial fans, do not normally encompass such a large area. Third, the presence of relict pillow structures in at least some of the amphibolite units (Goldsmith 1985) suggest a protolith of subaqueous basalt that could have been part of a supracrustal sedimentary sequence. Some amphibolite regions are big enough that we can reasonably exclude their interpretation as dikes or olistoliths.

2.6.3.3 Depositional environment

At the time of the inferred Early Ordovician depositional age, the eastern margin (present coordinates) of Laurentia was undergoing a dramatic change in tectonic activity, from a passive margin to active subduction (van Staal et al. 1998). Consequently, a limited number of depositional settings are possible. Based on our interpretation that the Chain Lakes massif is a melted sedimentary sequence with minor volcanics, we suggest the following restrictions on the depositional setting. (1) The presence of widespread volcanic rocks suggests deposition near an active plate margin. Arc-related ultramafic and mafic rocks of the Boil Mountain Complex (Gerbi et al. in review-c) support this hypothesis. (2) The generally medium to fine grained, rather than conglomeratic, nature of the sediments indicates deposition distant from areas of high relief. (3) The match in detrital zircon age populations between the American Tickle Formation of Newfoundland (Cawood and Nemchin 2001) and the Chain Lakes massif may indicate a regionally consistent drainage pattern, and perhaps paleogeography, during the Neoproterozoic to

Early Ordovician. The American Tickle Formation, which represents foreland basin deposits laid down in front of an arc (Cawood and Nemchin 2001; Waldron and van Staal 2001), may therefore serve as an provenance indicator for the Chain Lakes massif protolith. The apparent lack of a syntectonic zircon age population in the Chain Lakes massif protolith sediments mirrors that seen in similar-age rocks throughout the region (McDaniel et al. 1997; Karabinos et al. 1999; Cawood and Nemchin 2001; McLennan et al. 2001). Considering the above discussion, we suggest that an arc-marginal basin, probably a forearc basin, is the most likely depositional setting for the protolith to the Chain Lakes massif (Fig. 2.15).

2.6.4 The second metamorphic episode and the lack of melt migration

As has been widely recognized, following peak metamorphism the Chain Lakes massif was pervasively altered to a lower grade metamorphic assemblage. Most studies (eg. Boudette et al. 1989) have attributed this to Acadian-age greenschist-grade metamorphism accompanying regional burial and moderate heating. This hypothesis has a few unsatisfactory requirements, including: (1) that the Lower Silurian Attean and possibly the Devonian Chain of Ponds Plutons should have been affected by this metamorphism, but they were not, and (2) that sufficient water was available and able to pervasively infiltrate the massif, as would be required by the universal sub-grain scale retrogression. Such extensive infiltration should leave microstructural evidence, including microfracturing, veins, and predominant alteration of crystal rims. We found none of these features. In addition, one compositional end member of a common "alteration" phase, fine-grained muscovite in pseudomorphs, lies at the composition of coarse-grained matrix muscovite (Fig. 2.7). Silica variation in the pseudomorphs may

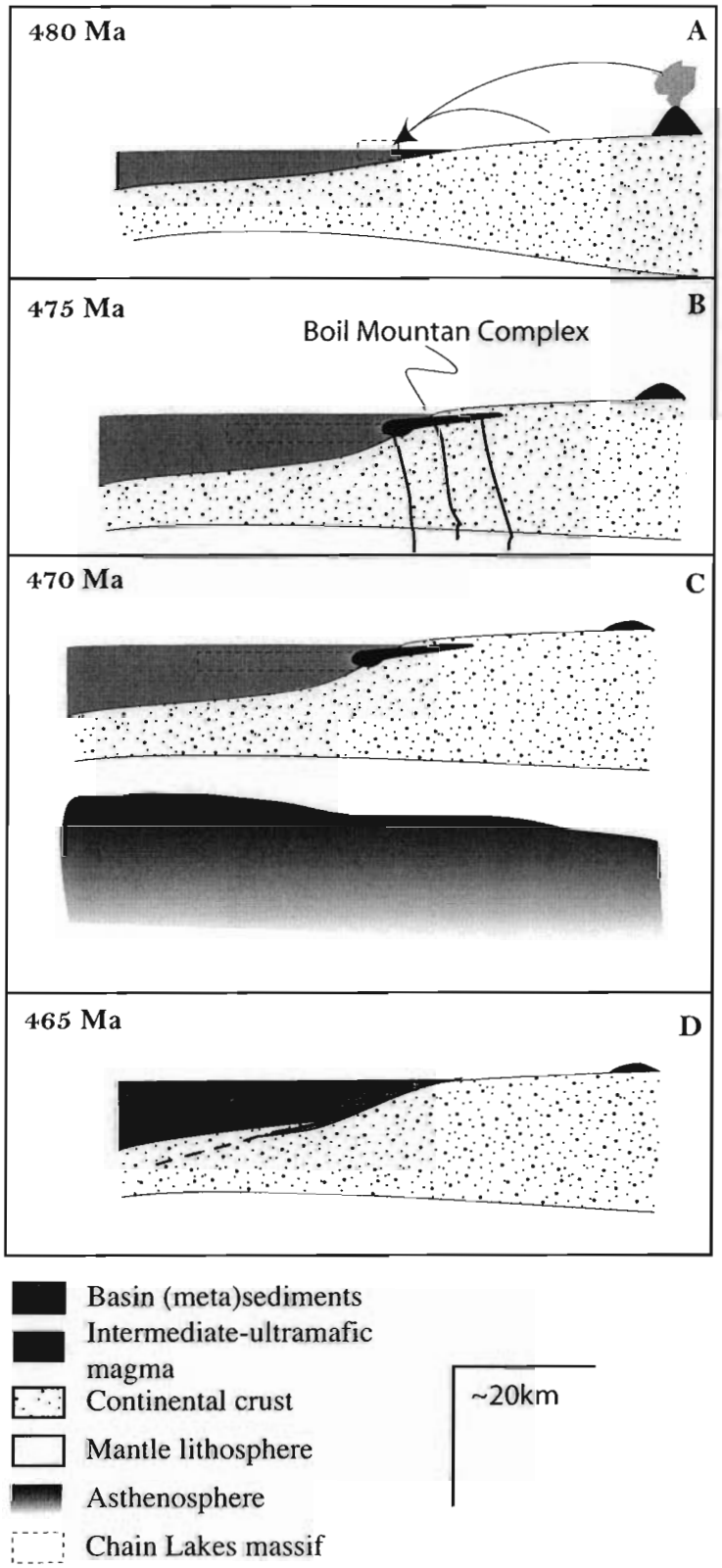

Figure 2.15 Inferred history of the Chain Lakes massif and adjacent Boil Mountain Complex. (A) Deposition of sediments eroded from Laurentia-derived microcontinent and volcanicmaterial from Notre Dame arc. (B) Intrusion of ultramafic magma that generated the Boil Mountan Complex. This is followed by intrusion of granodioritic arc-related magma into the Chain Lakes massif to form the Skinner pluton (not shown). (C) Shallow asthenosphere and perhaps associated magma (not shown) provide the heat to drive anatexis. (D) The Chain Lakes massif and Boil Mountain Complex are separated from the heat source and eroded near to the present level of exposure. See text for further details.

track muscovite formation during cooling from conditions under which the coarse laths formed. We believe that the water for retrogression could not have had an external source.

If water for the retrograde metamorphism was not externally derived in a separate metamorphic event, it must have originated within the massif. The widespread evidence for crystallized melt in the diatexite allows for the possibility that little water escaped during prograde metamorphism, but was instead dissolved in the melt. Upon cooling, the water was released from the melt and drove the production of hydrous phases (cf. Spear et al. 1999). We envision a scenario much like that described by Kohn et al. (1997) wherein crossing of the muscovite dehydration reaction during cooling, in the presence of sufficient water-rich melt, accounts for the production of muscovite. Chlorite, including that as an alteration product of biotite, would be produced in a similar fashion. In this case, the water was a vapor phase rather than dissolved in a melt. Because sillimanite is still present, the reactions clearly were not completely reversed.

2.6.5 The missing heat source

The presence of cordierite and andalusite requires a geothermal gradient much higher than is present in typical continental crust. Such an elevated geothermal gradient can occur because of local perturbation due to: (1) magmatic advection (Lux et al. 1986; Barton and Hanson 1989), (2) the presence of high heat production in the upper crust (Chamberlain and Sonder 1990; Sandiford and Hand 1998b; Sandiford et al. 1998), or (3) significantly increased heat flux from the mantle (Wickham and Oxburgh 1987; Loosveld and Etheridge 1990; Bodorkos et al. 2002). Evidence for the first mechanism would include widespread presence of synmetamorphic plutonism (e.g. De Yoreo et al. 1991),

and evidence for the second is high modern crustal heat flux and production (Sandiford et al. 1998). The third mechanism requires lithospheric thinning, evidence for which could include basaltic magmatism or crustal extension (Wickham and Oxburgh 1987). Extensive lithospheric thinning during crustal thickening can also produce high temperatures at low pressure (Loosveld and Etheridge 1990; Sandiford and Powell 1991); in this case, a pressure increase would accompany metamorphism. Widespread melting in, and consequent melt migration from, the lower crust would enhance a high conductive mantle heat flux. As such, it may be difficult to separate the effects of higher mantle heat flow from those of lower crustal magmas emplaced higher in the crust (cf. Sandiford et al. 1998).

We evaluated the likelihood that any of the above three mechanisms could account for the conditions of 750-800°C at 4-5 kb that we interpret for the Chain Lakes massif. Two of the possible magmatic heat sources for Chain Lakes massif metamorphism, the Skinner and Attean plutons (Trzcienski et al. 1992), were emplaced either before or after the massif was metamorphosed. The uncertainty in the age of the Skinner pluton does overlap the determined metamorphic age in the massif, but textures in the Skinner pluton indicate that it was present prior to the metamorphism (Gerbi et al. in review-c). Textural and geochronologic data indicate that the mafic-ultramafic Boil Mountain Complex (Boudette 1982) also intruded prior to metamorphism in the massif. In addition, the Complex is exposed only on the southern margin of the massif and is much too small to have metamorphosed the entire massif. The present-day heat flux (Decker 1987) and concentration of heat-producing elements (E.L. Boudette, unpublished data) do not suggest that the massif ever produced anomalously high heat internally.

Given present conditions, therefore, we must rule out the first two mechanisms for a high geothermal gradient. A review by Gerbi et al. (in review-b) suggests that the inferred peak pressure and temperature conditions require, in the absence of major magmatic advection, a thin or non-existent lithospheric mantle under a thin crust or a crustal scale detachment fault. To account for a lack of evidence for significant decompression and allow for heating through the andalusite field into the sillimanite field, the crust must initially be thin or heterogeneous crustal thinning must accompany lithospheric thinning. Such thinning may follow a geometry such as that described by a detachment mechanism (Lister et al. 1986b; Zen 1995b; Escuder Virute 1999). Slab breakoff or lithospheric mantle thinning by detachment or by necking would likely cause decompression melting in the mantle (McKenzie and Bickle 1988) as well as extensive melting in any crust below the present level of exposure. Because melt did not migrate out of the Chain Lakes massif, we have no *a priori* reason to expect that melt would have migrated from the lower crust as well. Without further evidence, none of the three possible heating mechanisms provides a ready explanation for anatexis. From this, we must conclude that either: (1) the Chain Lakes massif became separated from the heat source that caused widespread anatexis, or (2) the heat source is not exposed. Geophysical support is lacking for ponded mafic intrusions below the present level of exposure (Spencer et al. 1989; Stewart et al. 1993), so we believe that the massif must have been separated from its heat source.

This conclusion leaves us with no well-defined tectonic setting for metamorphism. The arguments against high internal heat production (mechanism 2) still hold, as do those against overlapping thermal aureoles of adjacent intrusions (mechanism

1) unless the intrusions were all either above or below the present level of exposure. So, we suggest that shallow asthenosphere lay below what is now the Chain Lakes massif and, through conductive heat transfer, caused the anatexis (Fig. 2.15). Detachment and subsequent emplacement of the massif over a wedge of Grenville crust (Stewart et al. 1993) separated the massif from its metamorphic heat source. The fabric in the Twin Bridges facies, indicative of strain while the rocks were partially melted, could represent a portion of the shear zone on which this separation was accomplished. We envision the asthenosphere to have welled up as slab break-off and/or lithospheric detachment were occurring in a forearc setting (Fig. 2.15). This sequence of events is similar to that proposed for the potentially correlative Dashwoods Block in Newfoundland (Pehrsson et al. 2003).

Without any orientational frame of reference for the foliation in the massif prior to disaggregation and formation of the diatexite, we cannot ascertain whether the structure preceding anatexis was more consistent with crustal thickening or thinning. The relatively flat-lying structure that developed following anatexis, defined by compositional banding, is consistent with either vertical shortening or highly non-coaxial subhorizontal shear, such as that at the base of ductile thrust sheets. Asymmetric isoclinal microfolds preserved in the schlieren of the Twin Bridges facies (Fig. 2.5b) suggest a strong non-coaxiality to the strain, so we prefer the interpretation that the deformation regime while the massif was molten was subhorizontal shear, probably associated with tectonic emplacement of the massif.

2.6.6 Is it a "massif"?

Boudette (1970) use the term "massif" because the rocks in the Chain Lakes region were relatively unaffected by later deformation events (Boudette and Boone 1976). Trzcienski et al. (1992) prefer to use the term Chain Lakes "unit", based on their interpretation that the rocks were deposited essentially in place as part of a regional stratigraphic succession.

As we have described above, the dominant fabric in the massif is a flat to low-angle compositional banding defined by the high-grade metamorphic assemblage. The lack of solid state deformation features in the fossil melt indicates that this fabric formed while melt was present, at approximately 469 Ma. Yet surrounding the Chain Lakes massif, the structural fabric is defined by regionally extensive subvertical, northeast-striking bedding and penetrative foliation (Moench et al. 1995). The ages of the regionally deformed rocks constrain this vertical fabric to Devonian time. The Chain Lakes massif was affected to some degree by this deformation: on its southern margin, weak to strong vertical penetrative foliation defined by the shape-preferred orientation of quartz and feldspar is variably developed in narrow zones (Gerbi et al. in review-c). The bulk of the massif remained undeformed during this and any later deformational events, so we concur with Boudette (1970) and Moench and Aleinikoff (2003) that "massif" is an appropriate term for these rocks.

2.6.7 Role of the Chain Lakes massif in Appalachian orogenesis

At least one active arc was present offshore of Laurentia as subduction continued to close Iapetus throughout the Ordovician. If the modern southwest Pacific serves as an analogue for the early Paleozoic Iapetus ocean (van Staal et al. 1998), there may have

been several arc systems that together appear as a single chain in the rock record. These arcs include the Notre Dame arc (van Staal et al. 1998; Waldron and van Staal 2001) of Newfoundland, the Ascot Complex of Québec, which may overlie Chain Lakes-type basement (Spencer et al. 1989), and the Shelburne Falls arc of central New England (Karabinos et al. 1998). In addition, the slightly younger Ammonoosuc volcanics of western Maine and New Hampshire could have erupted during accretion of this microcontinent (Moench and Aleinikoff 2003). If our interpretation is correct, the Chain Lakes massif, with its bimodal volcanics, low-pressure anatexis, and adjacent arc-related Boil Mountain Complex, would have developed in a segment of this arc or arc system. The basement to the arc is not exposed, but the presence of xenocrystic zircon in the felsic volcanic fragment and amphibolite (Tables 4 and 5), as well as the composition of the felsic volcanics, suggests that continental crust underlay the arc.

The above interpretations allow us to link the Chain Lakes massif to other early Paleozoic Appalachian events. Recent geochronological data and reinterpretations of stratigraphic, structural, and seismic data in Québec and Newfoundland (Cawood et al. 1995; Whitehead et al. 1996; Waldron et al. 1998; Castonguay et al. 2001; Waldron and van Staal 2001; Tremblay and Castonguay 2002; Pincivy et al. 2003) detail the timing and location of pre-Acadian deformation in the northern Appalachians. These studies suggest that deformation of the Laurentian passive margin in Québec and Newfoundland began at approximately 470 Ma, and perhaps as early as 480 Ma with ophiolite emplacement (Whitehead et al., 1995). Deformation in New England had begun by then as well (Laird et al. 1984; Karabinos et al. 1999). Prior to this time, by ca. 490 Ma, arc

plutonism had begun in an outboard, peri-Laurentian microcontinent (Waldron and van Staal 2001).

The active volcanism recorded in the Chain Lakes massif protolith, along with the adjacent 477 Ma intrusive Boil Mountain Complex, is consistent with the massif being deposited and metamorphosed near this microcontinent, which by this time also formed the axis of the Notre Dame arc. The melted and cooled massif could then have formed part of the collider that drove Ordovician deformation of the Laurentian margin.

2.7 Summary

The Chain Lakes massif has long held an uncertain role in Appalachian orogenesis, due in large part to incomplete understanding of the low-pressure high-temperature metamorphism, abundant lithic fragments, structural discordance with the adjacent terrain, provenance, and protolith. We have recognized that the metamorphism involved widespread anatexis that resulted in the disruption and fragmentation of the original volcanic-clastic sedimentary sequence. In this scenario, the lithic fragments are a consequence of melting, and the protolith was deposited in an arc-marginal sedimentary basin. Detrital and xenocrystic zircon ages indicate that the sediment was deposited in the Late Cambrian or Early Ordovician. The age of a felsic volcanic fragment in the massif and the correlation to detrital age spectra from Newfoundland support an Ordovician depositional age. The sediment source was either the Laurentian craton or a microcontinent previously rifted from the craton. A well-defined heat source for the metamorphism is lacking, but could have been high heat flux through a thin lithosphere into a heterogeneously thinned forearc crust. The anatexis did not result in significant melt migration, so microstructural evidence for fossil melt is ubiquitous. The lack of

melt segregation also permitted water to remain in the system, allowing significant retrogression of the rocks during cooling.

The available data support an interpretation of the Chain Lakes massif as being deposited in an arc-marginal setting in the Early Ordovician, probably on a rifted portion of Laurentian crust, then intruded by ultramafic to mafic rocks of the Boil Mountain Complex and the granodioritic Skinner pluton. Less than ten million years later, these units were metamorphosed, partially melted, and subsequently separated from the metamorphic heat source. Following cooling from a partially melted state, the Chain Lakes massif, Boil Mountain Complex, and Skinner pluton remained nearly undeformed as they composed part of the undoubtedly complex arc system that collided with the Laurentian passive margin to drive Ordovician deformation.

Chapter 3

EARLY PALEOZOIC DEVELOPMENT OF THE MAINE-QUÉBEC BOUNDARY MOUNTAINS REGION

3.1 Abstract

Within the Maine-Québec segment of the northern Appalachian orogen, we have investigated several pre-Silurian bedrock units that played key roles in early Paleozoic Appalachian accretionary history. We present new field, petrological, geochronological, and geochemical data to support the following interpretations. (1) The Boil Mountain Complex and Jim Pond Formation do not represent part of a coherent ophiolite. (2) The Boil Mountain Complex intruded the Chain Lakes massif at ca. 477 Ma. (3) The Skinner pluton, an arc-related granodiorite, intruded the Chain Lakes massif at ca. 473 Ma. (4) These four units formed part of the collider that deformed the Laurentian passive margin in the initial stages of Appalachian orogenesis. (5) The Attean pluton, with a reconfirmed age of ca. 443 Ma, is unrelated to Early Ordovician orogenesis. (6) The most likely timing for the juxtaposition of the Jim Pond Formation and the Boil Mountain Complex was during regional Devonian deformation. These interpretations suggest that the Boundary Mountains were once part of a series of arcs extending at least from central New England through Newfoundland.

3.2 Introduction

Accretionary orogens result from the amalgamation of multiple arcs, crustal blocks, and oceanic fragments. Although assembly of the components of an orogen may require a considerable amount of time, the individual events constituting it may be active over relatively short length and time scales (Hall 1996; van Staal et al. 1998). In

aggregate, these relatively short-lived events create complex and extensive features, such as the Lachlan (Coney 1992), Famatinian (Ramos 1988), and Appalachian (Dewey 1969; Williams 1978) orogens, as well as much of Alaska (Jones et al. 1986). Although later activity and loss of the geologic record preclude a complete reconstruction of the fine-scale kinematics in many ancient orogens, middle and lower crustal exposures provide an opportunity to examine many of the physical processes at work during their development. A thorough accounting of these physical processes, including the interplay between metamorphism, magmatism, and deformation, requires an accurate understanding of the history of the segment of the orogen in question.

In reconstructing the early Paleozoic history of the northern Appalachians, various studies have assigned mutually exclusive tectonic roles to parts of the Boundary Mountains region, which lies along the southwestern segment of the Maine-Québec border. The Boundary Mountains comprise primarily the Chain Lakes massif, Boil Mountain Complex, and Jim Pond Formation (Fig. 3.1). The Chain Lakes massif has been interpreted as a microcontinent originating from Gondwana (Zen 1983; Kusky et al. 1997) or forming near Laurentia (Zen 1983; Trzcienski et al. 1992; Kusky et al. 1997; Waldron and van Staal 2001; Moench and Aleinikoff 2003). This uncertainty bears directly on the location of the principal Iapetan suture, the Red Indian Line (Williams et al. 1988). Although its location in Maine is not yet resolved (Moench and Aleinikoff 2003), the Red Indian Line most likely passes through the Boundary Mountains region (van Staal et al. 1998). Moreover, the Boil Mountain Complex and Jim Pond Formation, which have in the past been described as an ophiolite sequence (Boudette 1982), have been interpreted both as unrelated (Boone and Boudette 1989) and related (Pinet and

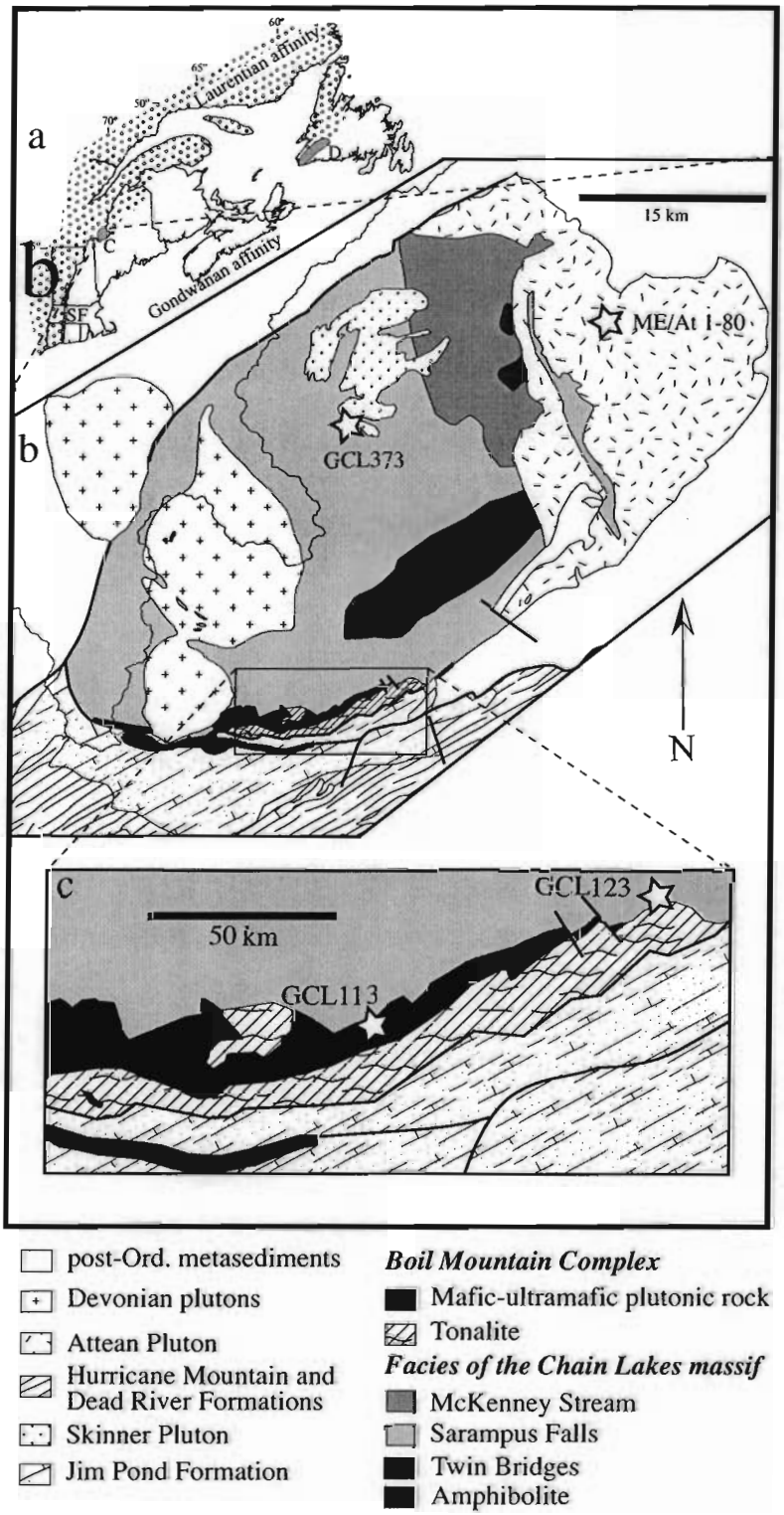

Figure 3.1 Geology of the study area. (a) Selected tectonic elements of the northern Appalachians. Shaded areas correspond to terranes possibly correlative with the Chain Lakes massif. C = Chain Lakes massif; D = Dashwoods subzone (Waldron and van Staal, 2001); SF = Shelburne Falls arc (Karabinos et al., 1998). (b) Bedrock geologic map of the Chain Lakes massif and surrounding area. Heavy lines mark faults; dotted line represents the international border. Stars and labels refer to geochronologic sample locations. (c) Bedrock map showing relationships between the Boil Mountain Complex, Jim Pond Formation, and Chain lakes massif. After Albee and Boudette (1972), Goldsmith (1985), Osberg et al. (1985) Boudette (1991), Moench et al. (1995).

Tremblay 1995) to the Thetford Mines ophiolite, which lies along the principal line of Appalachian ophiolites. By resolving these problems and further describing the geologic development of the region, we provide a framework for ongoing syntheses of Appalachian development and the processes that control accretionary orogenesis.

3.3 Regional setting

The main exposure of pre-Silurian bedrock units in western Maine lies in a northeast-trending belt that separates the Siluro-Devonian Connecticut Valley-Gaspé and Central Maine troughs (Fig. 3.1). Our study area, part of the Boundary Mountains anticlinorium (Albee 1961), straddles a wide array of bedrock units in the belt. The Boundary Mountains are cored by the migmatitic Chain Lakes massif (Gerbi et al. in review-a) (Fig. 3.1). The Silurian Attean quartz monzonite intruded the eastern margin of the massif (Lyons et al. 1986). Two plutons intruded the interior of the massif: the previously undated granodioritic Skinner pluton (Goldsmith 1985), and the 373 ± 2 Ma Chain of Ponds pluton (Heizler et al. 1988). No contact aureole has been described around the Skinner pluton, but an aureole is present around the Chain of Ponds pluton (Harwood 1973; Biederman 1984).

To the south of the massif lies the Boil Mountain Complex (Boudette 1982), a unit of mixed ultramafic and mafic plutonic rocks accompanied by extensive tonalite. The Boil Mountain Complex is, in turn, bordered to the south by the dominantly volcanic and volcanogenic Jim Pond Formation. To the northeast and southwest, pre-Silurian units consist mainly of bimodal volcanics and sediments, black shale mélange, and slate to schist; respectively, the Jim Pond, Hurricane Mountain, and Dead River Formations (Osberg et al. 1985; Moench et al. 1995). Exposed farther to the southwest are the

intermediate to mafic Ordovician Ammonoosuc volcanics (Moench et al. 1995). The Hurricane Mountain Formation is a tectonic mélange (Boone et al. 1989), and the Dead River Formation represents a flysch carapace over the mélange (Boone 1973).

These Paleozoic units of the Boundary Mountains appear to be allochthonous or parautocthonous on Grenville basement at a depth of approximately 4 km (Stewart et al. 1993). Grenville basement continues northwestward under the Connecticut Valley-Gaspé trough, and either it or Chain Lakes massif-like basement underlies the Ascot-Weedon volcanics and the Notre Dame mountains of Québec (Spencer et al. 1989). Farther to the northwest, allochthonous metasediments, mélange, and ophiolitic material make up the Humber zone, a belt of early Paleozoic Laurentian nappes that allochthonously overlie Grenville basement and autochthonous cover (St. Julien and Hubert 1975). The nearest autochthonous basement is more than 100 km northwest of the study area. Basement southeast of the study area comprises thinned Grenville crust and peri-Gondwanan material of the Ganderian microcontinent (Stewart et al. 1993). Although this basement is entirely concealed beneath the Central Maine Belt, a southeastward change in pluton chemistry suggests Ganderia's presence (Ayuso 1986; Dorais and Paige 2000; Tomascak et al. 2005).

3.4 Unit descriptions

3.4.1 Rocks of the Chain Lakes massif

The Chain Lakes massif (Boudette 1970) has long been enigmatic, largely because of a lack of detailed mapping and first-order structural and petrological analyses. Parts of the Chain Lakes massif have been described previously (Boudette 1970; Albee and Boudette 1972; Harwood 1973; Boudette and Boone 1976; Burroughs 1979;

Biederman 1984; Goldsmith 1985; Boudette et al. 1989; Cheatham et al. 1989; Boudette 1991; Trzcienski et al. 1992; Moench et al. 1995; Moench et al. 1999; Moench and Aleinikoff 2003; Gerbi et al. in review-a), but until recently there had been no systematic mapping and interpretation of the entire massif. The Chain Lakes massif is predominantly a diatexitic (Gerbi et al. in review-a) quartzo-feldspathic terrain with minor amphibolite (Boudette 1970). The entire massif is exposed in a broad arch about a northeast-trending hinge line (Boudette 1970; Biederman 1984), with compositional banding in the massif dipping shallowly away from this hinge. A younger, nearly vertical penetrative foliation is superimposed in places near the contact with the Boil Mountain Complex. No unaltered porphyroblasts are present in the massif, but widespread pseudomorphs after andalusite, cordierite, and garnet indicate their former presence (Trzcienski et al. 1992; Gerbi et al. in review-a). With andalusite relics and pseudomorphs wrapped by fibrolite, the massif records a prograde metamorphic path from the andalusite to sillimanite field. Peak metamorphism apparently reached biotite dehydration melting, but sufficient water was present in the *in-situ* melt to allow abundant growth of retrograde muscovite and chlorite as the magmatic portion of the diatexite crystallized (cf. Kohn et al. 1997). The widespread presence of fossil melt features and retrograde minerals suggests that little melt migrated out of the system. Abundant lithic and quartz fragments, diagnostic of the massif, are present throughout. Previously interpreted as either a protolith of diamictitic sediment (e.g. Trzcienski et al. 1992) or impact breccia (Boudette and Boone 1982), the lithic fragments are more likely the result of anatectic disaggregation of pre-existing sedimentary-volcanic layering (Gerbi et al. in review-a).

Following Gerbi et al. (in review-a), we interpret the Chain Lakes massif protolith as a sedimentary sequence with volcanic input deposited adjacent a Laurentian-derived microcontinent. Subsequently, the sequence was metamorphosed and melted in place at approximately 470 Ma (Dunning and Cousineau 1990; Gerbi et al. in review-a).

At the contact between the northeastern end of the Boil Mountain Complex and the Chain Lakes massif, Boudette et al. (1989) and Holtzman et al. (1996) described a body of "tonalite" different from that in the Boil Mountain Complex (see below). This "tonalite" is medium grained, unfoliated, and consists of quartz, plagioclase, and biotite. As it appears to include xenoliths of the Chain Lakes massif and the Boil Mountain Complex, Holtzman et al. (1996) interpreted the "tonalite" to stitch the contact. Our study of this unit indicates that it is texturally similar to the main body of the Chain Lakes massif, and we could not map any discrete boundary between this unit and the massif. The "tonalite" lacks the retrograde chlorite and muscovite common to the massif, but it does contain similar euhedral plagioclase crystals and a range of lithic fragments. Although its origin is in part igneous, we prefer to label the rock as a diatexite, belonging to the massif, and we consider any textural differences from the massif to be a result of pre-anatectic contact metamorphism accompanying the emplacement of the adjacent Boil Mountain Complex. Geochronologic data supporting this interpretation are described below.

3.4.2 Boil Mountain Complex

The Boil Mountain Complex (Boudette 1978, 1982) is exposed along the southern margin of the Chain Lakes massif in an elongate northeast striking lens (Fig. 3.1). In

agreement with Boudette (1982), we consider much of the Complex to be a heterogeneous mix of metamorphosed ultramafic rocks, gabbro, and minor diorite, with the ultramafic rocks more dominant to the northwest, along the contact with the Chain Lakes massif. Fine-grained plagiogranite makes up a minor portion of the unit and most commonly occurs as dikes up to 3 m wide near the contact with the Chain Lakes massif (Eisenberg 1982; this study). Quartz-porphyritic tonalite, approximately equal in areal exposure to the mafic and ultramafic rocks, makes up the southeastern edge of the Complex.

The ultramafic rocks are dominantly websterite and clinopyroxenite, and consist of coarse (5-12 mm) grains, in places exhibiting a cumulate texture (Fig. 3.2a), with smaller interstitial clinopyroxene or altered orthopyroxene. Recrystallization products include aggregates of equant clinopyroxene and amphibole. The amphibole, hornblende and actinolite, grew mimetically over the pyroxene texture. In places, the pryoxenites are 100% recrystallized to amphibole (Boudette et al. 1989), some of it due to uralitization. To the west, the ultramafic rocks experienced from 10-100% serpentization; Boudette (1982) inferred the original presence of dunite and harzburgite. Although we observed no olivine in any sample, we recognized possible pseudomorphs after olivine in the serpentinite.

Metagabbro exhibits a wide range of textures, including medium-grained foliated rock, pegmatite, and autobreccia. In the autobreccia, coarse-grained quartzo-feldspathic veins separate angular blocks of medium to coarse-grained metagabbro. The majority of the metagabbro consists of patches of highly variable and gradational grain size. The mineralogy is dominantly hornblende, plagioclase, and epidote group minerals, with the

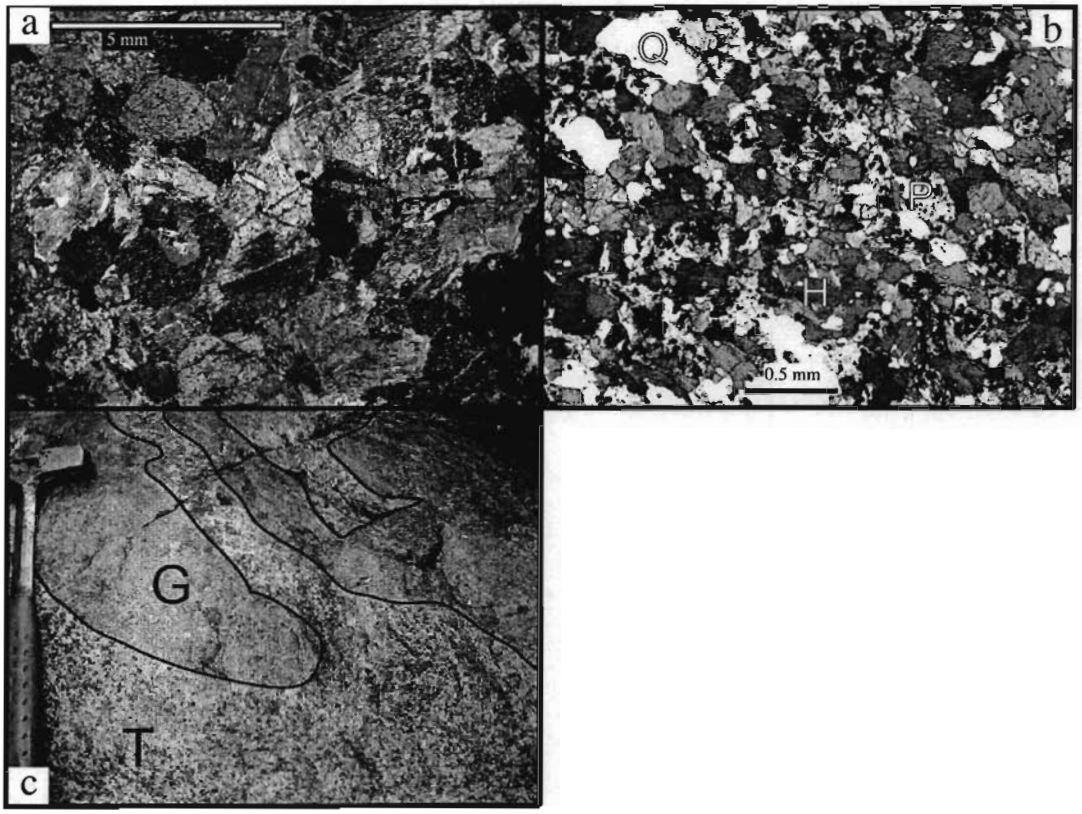

Figure 3.2 Textures and relationships in the Boil Mountain Complex. (a) Relict igneous microstructure of a clinopyroxenite cumulate. (b) Recrystallized portion of gabbro, with hornblende (H), plagioclase (P), and quartz (Q). (c) Outcrop-scale mingling of gabbro (G) and tonalite (T).

plagioclase commonly altered (Fig. 3.2b). Textures vary widely, from isotropic with euhedral plagioclase and straight hornblende boundaries in autobrecciated zones to well-foliated with anhedral, elongate plagioclase and hornblende. Igneous ophitic or poikiloblastic textures are absent.

The tonalite is coarse- to very coarse-grained, leucocratic, quartz porphyritic, and weathers light brown to pale orange. Equant quartz crystals are reasonably uniform in size, approximately 6-10 mm across. The matrix consists of interlocking crystals of quartz and plagioclase, with minor alteration to epidote group minerals. Estimated modes are approximately 50% quartz and 50% plagioclase, with trace amounts of accessory minerals. The tonalite texture is nearly uniform throughout the body, with only minor (meter-scale) equigranular, medium-grained patches. Numerous exposures exhibit a cm-scale mingling of tonalite and metagabbro with gradational contacts (Fig. 3.2c). Based on U-Pb thermal ionization mass spectrometry (TIMS) analysis of zircon, Kusky et al. (1997) determined a crystallization age of 477 ± 1 Ma for the tonalite.

The nature of the contact between the Boil Mountain Complex and the Chain Lakes massif – intrusive or structural – is of primary importance in the tectonic reconstructions of the region. Citing evidence for ductile faulting, most previous interpretations conclude that the contact is structural (e.g. Boudette 1982). We observed that much but not all of the contact is defined by narrow, <3 m wide, zones of intense mylonitization (Fig. 3.3a,b). These shear zones crosscut the contact in places and also occur within thin zones of plagiogranite that exist near and parallel to the contact (<10 m into the Boil Mountain Complex). Within the Chain Lakes massif, the mylonitic zones contain mica fish, brittlely milled feldspar, and abundant intrafolial chlorite. High-strain

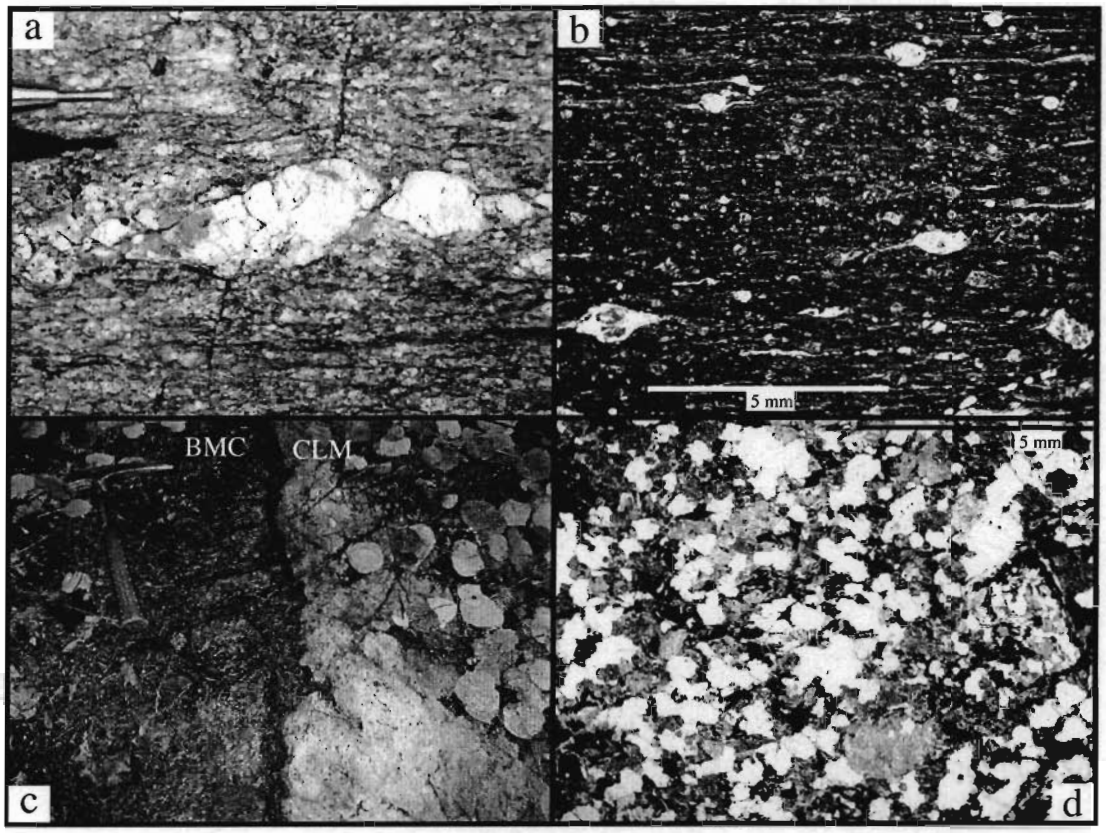

Figure 3.3 Fabric at and near the contact between the Chain Lakes massif and the Boil Mountain Complex. (a) Feldspar porphyroclast within a shear zone < 2m from contact. (b) Photomicrograph from same location, illustrating the mylonitic texture of the shear zone. (c) Contact between Boil Mountain Complex (left) and Chain Lakes massif (right). Contact lacks a shear zone in this location. (d) Photomicrograph from the massif < 2m from contact in the vicinity of (c), illustrating non-mylonitic texture similar to that found throughout the interior of the massif.

zones within the Boil Mountain Complex exhibit cataclasized hornblende, commonly altered to actinolite (Boudette et al. 1989). Those portions of the contact that are not mylonitized do not exhibit any evidence of macro- or microscale ductile or brittle deformation (Fig. 3.3c,d). Instead, the textures along the sharp lithologic boundary are indistinguishable from internal textures in the units.

3.4.3 Jim Pond Formation

The Jim Pond Formation (Boudette 1982) is an internally conformable sequence of volcanic and sedimentary rocks that experienced greenschist facies metamorphism. Regionally, the formation continues far to both the northeast and southwest, well beyond the extent of the Boil Mountain Complex.

As described by Boudette (1978; 1982) and Coish and Rogers (1987), the unit consists of alternating units of mafic and felsic volcanic rocks, covered by metasiltstone and metasandstone. The volcanic rocks are in places intimately interlayered, and in places separated by conglomeratic to shaly horizons. Overall, there are two dominant bands each of mafic and felsic flows. The felsic rocks are rhyolitic to dacitic; the basalt locally contains pillow structures but primarily consists of massive flows. Although the two bands of mafic volcanic rocks are superficially similar, their chemistries differ. Nevertheless, Coish and Rogers (1987) proposed a suprasubduction zone setting for both bands of mafic volcanics. Minor gabbro occurs within the lower lavas. This gabbro contains ophitic feldspar laths and euhedral clinopyroxene and is texturally and mineralogically distinct from the metagabbro of the Boil Mountain Complex.

Currently, the mafic volcanic rocks are greenstone (Boudette 1970), with a metamorphic mineralogy of actinolite, chlorite, albite, and epidote (Coish and Rogers

1987). No textures or relic minerals indicate that the metamorphic grade ever exceeded the greenschist facies. The composition of the felsic volcanic rocks precluded growth of similarly diagnostic metamorphic assemblages. Moench et al. (2000), dating zircon in the upper layer of felsic volcanic rocks by the U-Pb sensitive high resolution ion microprobe (SHRIMP) method, determined a crystallization age of 484 ± 5 Ma.

3.4.4 Other relevant units

The eastern border of the Chain Lakes massif was intruded by the Attean pluton (Fig. 3.1). This unfoliated hornblende-bearing quartz monzonite was dated at 443 ± 4 Ma (Lyons et al. 1986), but recent work has called that age into question (Trzcienski et al. 1992; van Staal et al. 1998). The Attean pluton exhibits an igneous texture, with poikiloblastic hornblende accompanying interlocking quartz, K-feldspar, and euhedral plagioclase (Albee and Boudette 1972). Although some minor shear zones are present, the pluton does not exhibit a penetrative solid-state fabric that would be consistent with it being present during docking of the Boundary Mountains with Laurentia. A new confirmation of the crystallization age is presented below.

In the northern half of the Chain Lakes massif, the biotite-bearing granodioritic Skinner pluton crops out with an irregular pattern (Fig. 3.1). This pattern led Goldsmith (1985) to suggest that the pluton is barely unroofed. This interpretation in turn led Trzcienski et al. (1992) to suggest the Skinner pluton as a candidate for the Chain Lakes massif metamorphism. The Skinner pluton contains a typical interlocking igneous texture, with euhedral plagioclase, subhedral K-feldspar, and interstitial quartz. Biotite and the two feldspars have been extensively altered to chlorite and fine-grained white mica, respectively. The pervasive microscale alteration is quite similar to that in the

Chain Lakes massif, indicating that the Skinner pluton was present prior to retrogression of the massif.

3.5 Analytical methods and results

3.5.1 Geochronology

The lack of accurate geochronological data has hampered efforts to reconstruct the tectonic events that shaped the early Appalachians, particularly in the Maine-Québec segment. For this study, we dated three units whose ages have direct bearing on the early Paleozoic tectonic history. All minerals dated were separated using standard density and magnetic techniques. For the TIMS analysis, zircon was abraded, then dissolved in HF. The solution was then passed through ion exchange columns and the separate metals were loaded onto a filament and thermally ionized in a Finnigan MAT 262V TI mass spectrometer at the Memorial University of Newfoundland.

Preparation for SHRIMP analyses for the non-detrital zircon included sieving to between 100 and 150 μm, followed by hand-picking appropriate grains. These were then mounted in epoxy, photographed, and imaged using cathodoluminesence. Grains for detrital analysis were poured onto the mount in order to obtain a random population sample. Monazite grains were picked, mounted, and imaged in backscatter. Unless otherwise noted, we carried out U-Pb isotopic analysis using the U.S.G.S.-Stanford SHRIMP-RG. We set the primary O_2^- ion beam set to a nominal diameter of ~25μm at current of 3 nA and used $^{206}Pb/^{238}U$ standard R33 (Black et al. 2004). For monazite we used standard 44069 (Aleinikoff et al. in press). We used Squid (Ludwig 2001) for data reduction, based on and the observed ln(Pb/U)-ln(UO/U) ratio.

3.5.1.1 U-Pb TIMS age of Boil Mountain Complex gabbro

We separated zircon from the autobrecciated portion of gabbro within the Boil Mountain Complex. Analysis of five fractions of between 2 and 8 grains (Table 3.1) yielded a mix of concordant and discordant results. A chord calculated through the three most precise points (Z3, Z4, Z5) yields an upper intercept age of 477 +7/-5 Ma and a lower intercept age of 71 ± 71 Ma (Fig. 3.4). Including fraction Z2 in the age calculation shifts the upper intercept only slightly, to 478 Ma, but due to its large uncertainty, we have excluded it. Also not included in the age calculation is fraction Z1, concordant at 457 Ma; this point lies well outside the main trend and may indicate the existence of another magmatic episode involving injection into the gabbro. We interpret the age of 477 +7/-5 Ma (95% confidence) as the crystallization age of the gabbro. This age is identical to that of the 477 ± 1 Ma tonalitic portion of the Complex (Kusky et al. 1997), supporting the field evidence for a cogenetic relationship between the metagabbro and tonalite.

3.5.1.2 U-Pb SHRIMP age of contact metamorphism in the Chain Lakes massif

From a portion of the Chain Lakes massif adjacent to the Boil Mountain Complex, we sought to evaluate the effects of any contact metamorphism. The rock we analyzed was previously considered tonalite (Boudette et al. 1989; Holtzman et al. 1996), but we recognize it as diatexite of the massif. We separated zircon from a characteristic medium-grained, nonfoliated outcrop using the same techniques as above. We hand-picked approximately 60 clear grains with smooth faces and pyramidal terminations. The cathodoluminescence imaging identified, in many grains, cores, mantles, and rims of variable thickness (Fig. 3.5a). Cores and mantles exhibit a wide range of zoning patterns,

Table 3.1 U-Pb TIMS isotopic data for zircon in sample GCL113 (Boil Mtn. Complex gabbro)

										----------Corrected atomic ratios*----------					--Age (Ma)--		
Frac.	# grains		Weight (mg)	U (ppm)	Pb* (ppm)	Measured total common Pb (pg)	^{206}Pb $/^{204}Pb$	^{208}Pb $/^{206}Pb$	^{207}Pb $/^{235}U$	unc	^{206}Pb $/^{238}U$	unc	^{207}Pb $/^{206}Pb$	unc	^{206}Pb $/^{238}U$ Age	^{207}Pb $/^{235}U$ Age	^{207}Pb $/^{206}Pb$ Age
Z1	2	clr brn	0.005	940	68.9	1	16089	0.1060	0.5680	0.0026	0.07340	0.00040	0.05612	0.00018	457	457	457
Z2	8	clr tabular	0.010	331	25.4	1	12660	0.1437	0.5816	0.0054	0.07432	0.00082	0.05676	0.00034	462	465	482
Z3	4	equant sml brn	0.005	982	73.9	1	15722	0.1030	0.5882	0.0026	0.07545	0.00040	0.05655	0.00018	469	470	474
Z4	2	lrg clr brn euh	0.015	2205	158.0	30	4969	0.0947	0.5645	0.0026	0.07240	0.00034	0.05655	0.00006	451	454	474
Z5	4	sml clr lt brn euh	0.010	4099	287.7	9	20067	0.1088	0.5453	0.0024	0.07003	0.00032	0.05647	0.00004	436	442	471

Notes: Atomic ratios corrected for fractionation, spike, laboratory blank and 2 picograms total common lead at the age of the sample calculated from Stacey and Kramers (1975) and 1 picogram U blank.

Two sigma uncertainties are reported after the ratios.

Abbreviations: clr = clear, brn = brown, sml = small, lrg = large, lt = light, euh = euhedral.

* radiogenic Pb

Sample location UTM 19T E376818 N5014613

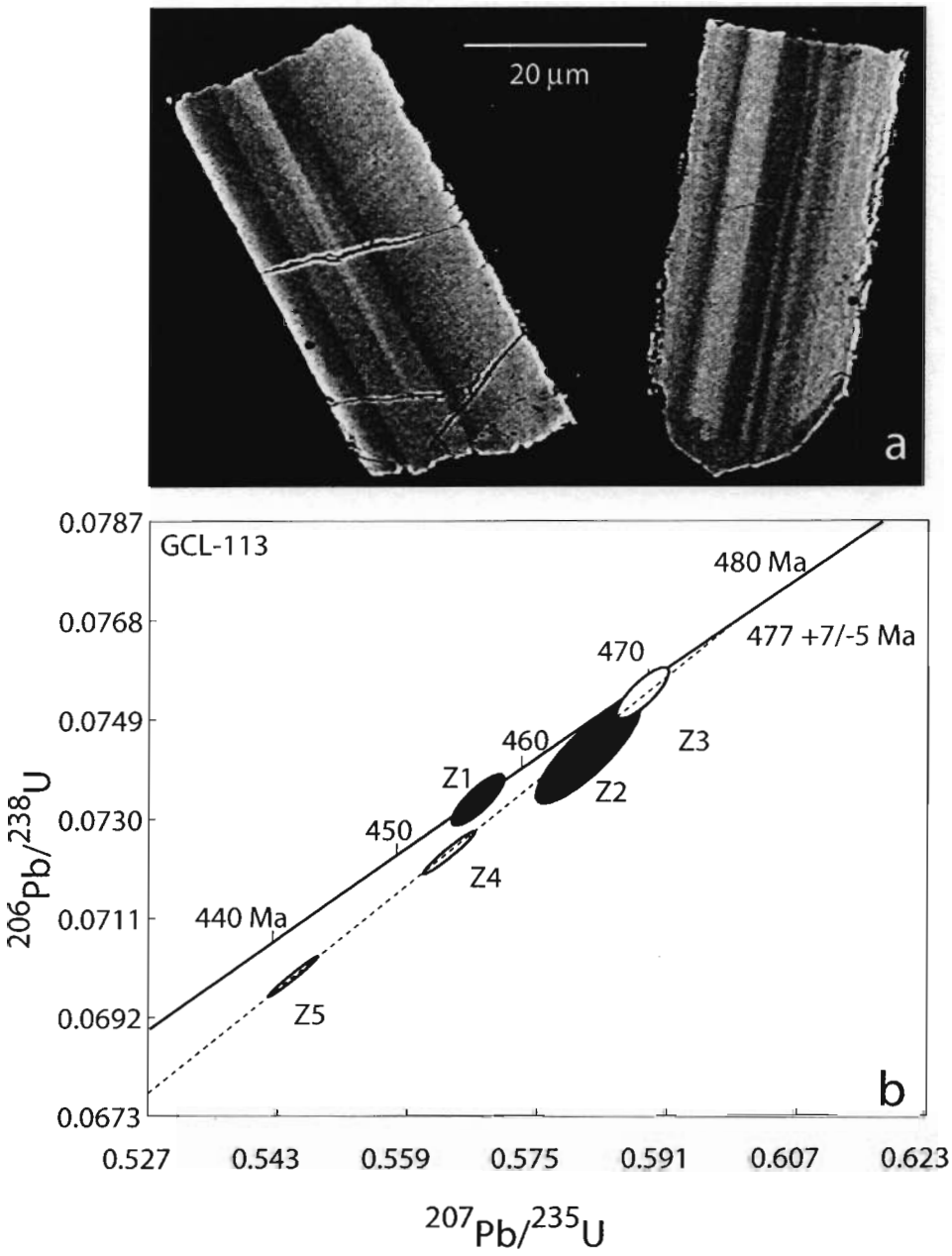

Figure 3.4 Results from U-Pb analysis of gabbro. Backscatter electron images of zircon from gabbro of the Boil Mountain Complex (GCL113). (b) Concordia plot showing results of U-Pb isotopic analysis of five zircon fractions. Chord (dotted) through points Z3, Z4, and Z5 has an upper intercept of 477 +7/-5 Ma and a lower intercept of 71 ± 71 Ma. We interpret the upper intercept as the time the gabbro crystallized.

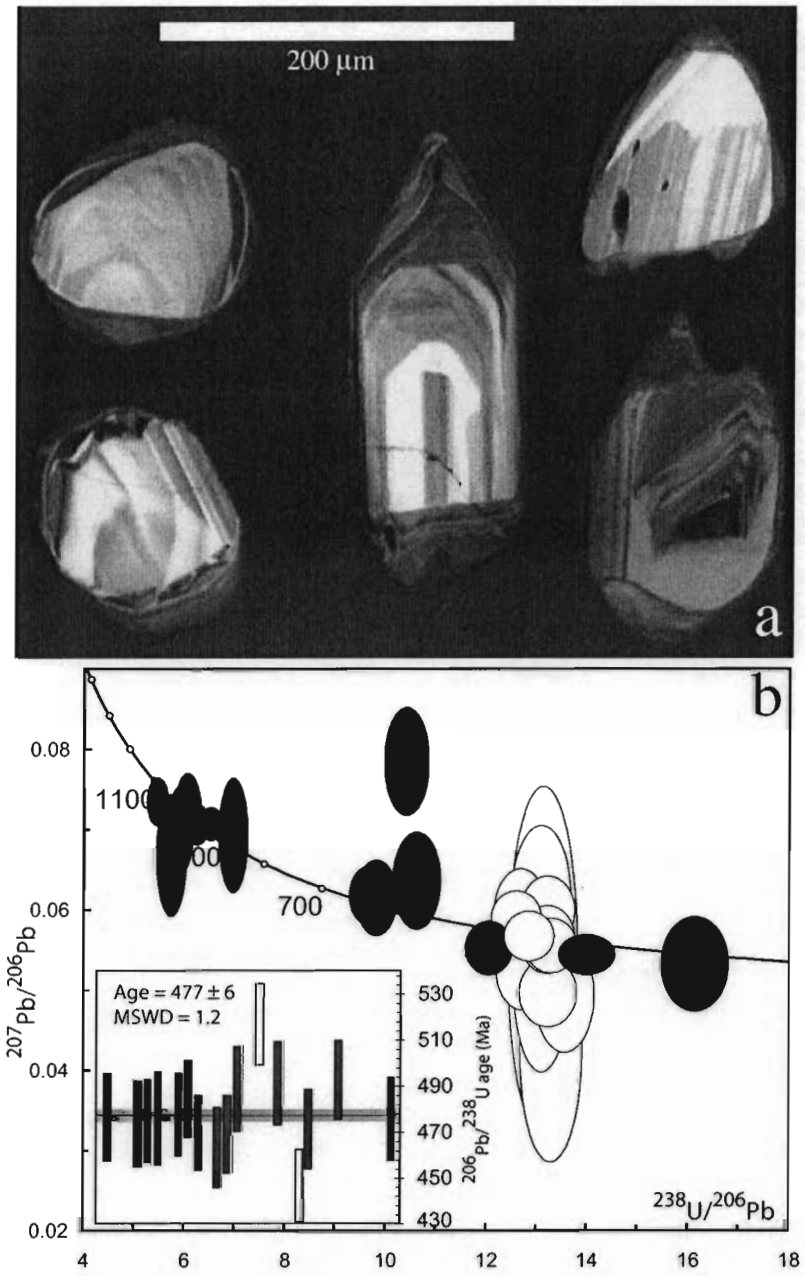

Figure 3.5 Results from U-Pb analysis of zircon in Chain Lakes massif. (a) Cathodoluminescence images of zircon from GCL123, sample of the Chain Lakes massif adjacent to the Boil Mountain Complex. (b) Tera-Wasserburg plus weighted average age plot (inset) for zircon from sample GCL123. In 20 of the 29 spots, rims of the zircon grains were analyzed; the remaining analyses were thick mantles or cores. Shaded ellipses and open bars (inset) indicate analyses excluded from the age calculation; these represent either detrital grains or inferred younger metamorphic overgrowths. All symbols are plotted at 2σ. Shaded horizontal bar marks uncertainty in the calculated age. We interpret the weighted average age, 477 ± 6 Ma, to represent the time of contact metamorphism due to the intrusion of the Boil Mountain Complex.

but rims are commonly thin, homogeneous, and dark in cathodoluminscence. We determined U-Pb isotopic ages in 20 thin rims, 7 thick mantles, and 2 cores. All ages are reported using $^{206}Pb/^{238}U$ ratios (Table 3.2).

Morphological divisions of spot locations into core, mantle and rim do not necessarily correlate with age. Core ages ranged between 1049 Ma and 960 Ma, mantle ages between 1092 Ma and 477 Ma, and rim ages between 1013 Ma and 446 Ma (Fig. 3.5b, Table 3.2). Post-SHRIMP imaging indicates that ages for spots GCL123-11, -15, and -26 probably represent analyses of multiple age domains; these analyses have been excluded from our interpretation. Ages younger than 500 Ma cluster in a distinct Ordovician population with two outliers. The two youngest analyses (GCL123-4 and –10; 388 ± 6 Ma and 446 ± 7 Ma, respectively) are not included in the age calculation because they fall well outside the coherent cluster. These ages probably represent growth due to later fluid infiltration. The Attean Pluton, dated at 443 ± 3 Ma (see below), could be the source of one of those ages. The fourteen analyses that form a coherent group have a weighted average age of 477 ± 6 Ma (95% confidence) (Fig. 3.5b). Th/U ratios in this age cluster are low, averaging approximately 0.01, typical of a metamorphic origin (Hoskin and Schaltegger 2003). Moreover, the weighted average age is identical to that of the Boil Mountain Complex. Therefore, we consider the Ordovician rims grown on these zircon grains as a metamorphic response to the intrusion of the adjacent Boil Mountain Complex.

The remaining ages span ca. 516 Ma to 1092 Ma. This spread of ages is consistent with a detrital paragenesis, from sediments derived from sources similar to those for the massif as a whole (cf. Gerbi et al. in review-a). Spot GCL123-14, 516 ± 8

Table 3.2 U-Pb SHRIMP isotopic data for zircon in sample GCL123 (Chain Lakes massif near Boil Mountain Complex)
Sample location UTM Zone 19T E384102 N5017652

							----------^{204}Pb-corrected^{c}----------						^{207}Pb-corrected^{c}	
Spot^{a}	Notes^{b}	^{204}Pb /^{206}Pb	^{207}Pb /^{206}Pb	% common ^{206}Pb	U (ppm)	Th/U	^{238}U/^{206}Pb*	% err	^{207}Pb* /^{206}Pb*	% err	^{207}Pb /^{206}Pb Age	1σ	^{206}Pb /^{238}U Age	1σ
GCL123 (UTM 19T 384102 5017652)														
GCL123-1	R	0.0003	0.0579	0.1673	197	0.0658	13.1329	1.75	0.0532	5.07	339	115	475	8
GCL123-2	M	0.0000	0.0727	0.0716	121	0.5290	6.0337	1.76	0.0727	2.56	1005	52	988	17
GCL123-3	R	0.0000	0.0621	0.1483	269	0.1777	9.6446	1.66	0.0621	2.39	677	51	635	10
GCL123-4	R	0.0004	0.0600	0.6938	909	0.0105	16.1181	1.71	0.0537	4.44	357	100	388	6
GCL123-5	M	0.0000	0.0709	0.1398	596	0.0521	6.4962	1.54	0.0709	1.17	956	24	922	14
GCL123-6	R	0.0000	0.0595	0.3031	463	0.0933	12.5690	1.61	0.0595	2.20	585	48	492	8
GCL123-7	M	-0.0001	0.0702	-0.3123	249	0.3452	5.9047	1.61	0.0722	1.94	992	40	1009	16
GCL123-8	M	0.0000	0.0737	-0.2620	332	0.4486	5.4335	1.58	0.0737	1.67	1032	34	1092	17
GCL123-9	R	0.0000	0.0567	0.0241	226	0.0766	13.1989	1.71	0.0567	3.00	478	66	471	8
GCL123-10	R	0.0001	0.0557	-0.0134	1077	0.0122	13.9795	1.62	0.0548	1.84	405	41	446	7
GCL123-10.2	C	0.0000	0.0709	-0.0232	660	0.2704	6.2297	1.59	0.0709	1.48	954	30	960	15
GCL123-11	R	0.0002	0.0653	0.5718	209	0.1225	9.7869	1.70	0.0618	3.10	668	66	626	10
GCL123-12	R	0.0003	0.0582	0.1534	249	0.1551	12.6930	1.71	0.0535	4.18	350	94	491	8
GCL123-13	R	0.0004	0.0754	0.9075	239	0.1875	6.9439	1.72	0.0695	4.16	914	86	866	14
GCL123-14	R	0.0002	0.0582	0.0648	641	0.0097	12.0246	1.58	0.0556	2.43	437	54	516	8
GCL123-15	M	0.0000	0.0639	0.5662	146	0.0841	10.5954	1.81	0.0639	3.84	739	81	578	10
GCL123-16	R	-0.0001	0.0581	0.1469	233	0.0237	12.6602	1.74	0.0599	3.78	599	82	488	8
GCL123-17	R	-0.0001	0.0591	0.3272	347	0.1763	13.2034	1.65	0.0602	2.90	612	63	468	8
GCL123-18	R	0.0006	0.0589	0.3196	273	0.1304	13.5487	1.77	0.0497	5.73	183	134	463	8
GCL123-19	R	0.0002	0.0732	0.0296	181	0.3125	5.8973	1.68	0.0698	2.91	924	60	1013	16
GCL123-20	R	0.0002	0.0582	0.2235	825	0.0147	13.2653	1.58	0.0559	2.46	449	55	469	7
GCL123-21	M	0.0000	0.0571	0.0334	459	0.0096	12.8329	1.60	0.0571	2.19	494	48	484	8
GCL123-22	M	0.0008	0.0649	1.0175	260	0.1609	13.0804	1.83	0.0530	9.75	329	221	477	8
GCL123-23	R	0.0011	0.0697	1.6167	274	0.0610	13.1090	2.18	0.0542	16.09	380	362	475	9
GCL123-24	R	0.0002	0.0533	-0.3947	1001	0.0068	13.2069	1.78	0.0501	3.42	200	79	474	8
GCL123-25	R	-0.0003	0.0577	0.1469	289	0.1072	13.0645	1.88	0.0614	6.20	653	133	473	9
GCL123-25.2	C	0.0002	0.0697	-0.5436	99	0.7690	5.7079	2.15	0.0671	4.59	840	96	1049	22
GCL123-26	R	0.0001	0.0803	2.5674	447	0.0364	10.3832	1.76	0.0786	3.49	1162	69	579	10
GCL123-27	R	0.0011	0.0592	0.3208	314	0.0349	13.2717	1.94	0.0432	13.17	-156	327	476	9

a Bold denotes spots not included in age calculation

b Location of spot on zircon grain: C = core; M = thick mantle; R = thin rim or tip

c All results corrected for common lead using model of Stacey and Kramers (1975); * refers to radiogenic Pb

Ma, is worth considering carefully, for it is on the youngest grain we interpret as detrital and therefore could provide a constraint on the depositional age of the Chain Lakes massif. This spot is wholly located on a wide rim that is texturally discordant from an irregularly zoned core (Fig. 3.6). The age is concordant, with a Th/U ratio of 0.01. At the 2σ level of uncertainty, this analysis is well outside the uncertainty associated with the clustered analyses discussed above (Fig. 3.5b). Therefore, the rim in question could have formed either: (1) after deposition of the Chain Lakes massif, in a massif-wide metamorphic event that is not reflected in any other analyses, or (2) outside the massif. If the rim grew outside the massif, then the entire grain would be detrital. Because of the lack of evidence for a massif-wide metamorphic event at ca. 516 Ma, we prefer the latter interpretation that the grain is detrital. Nevertheless, the former interpretation cannot be ruled out.

3.5.1.3 U-Pb SHRIMP age of Skinner pluton

We hand-selected approximately 60 colorless, clear, euhedral zircon grains for SHRIMP analysis. Cathodoluminescence imaging reveals that nearly all selected grains exhibit a fine oscillatory concentric zoning across either the entire grain or a wide mantle (Fig. 3.7a) which we interpret as igneous in origin. Some grains contain an inherited core with variable zoning texturally discordant to the mantle. We analyzed the finely zoned portions of 15 grains and the cores of 4 grains. Reduced data illustrate that all finely zoned portions of the grains are concordant (Fig. 3.7b,c) and represent a coherent weighted-average $^{206}Pb/^{238}U$ age of 474 ± 7 Ma (95% confidence) (Fig. 3.7d, Table 3.3). We interpret this age as the crystallization age of the Skinner Pluton. Core $^{207}Pb/^{206}Pb$ ages are 2561 ± 12 Ma, 1082 ± 36 Ma, 911 ± 56 Ma, and 2712 ± 8 Ma (Table 3.3). We

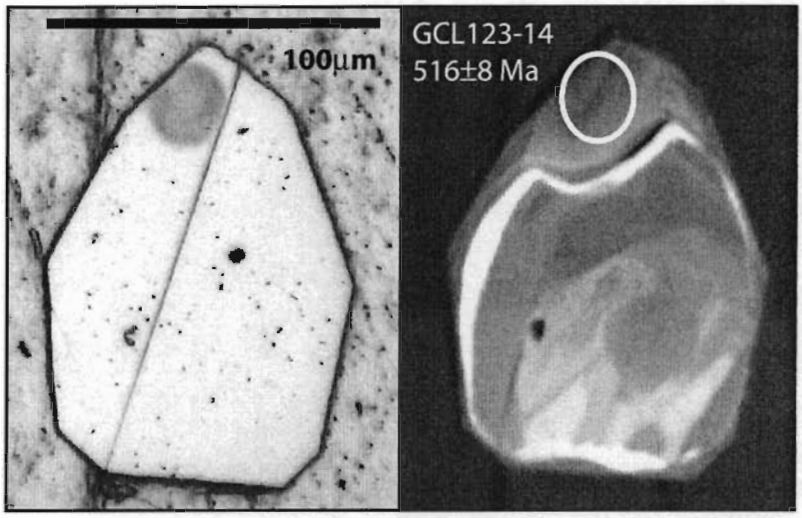

Figure 3.6 Details of spot GCL123-14. (a) Reflected light post-SHRIMP image of spot GCL123-14. We consider this grain to be the youngest analyzed zircon of detrital origin. (b) Location of SHRIMP analysis overlain on cathodoluminesence image. The spot appears to have sampled only a single age domain.

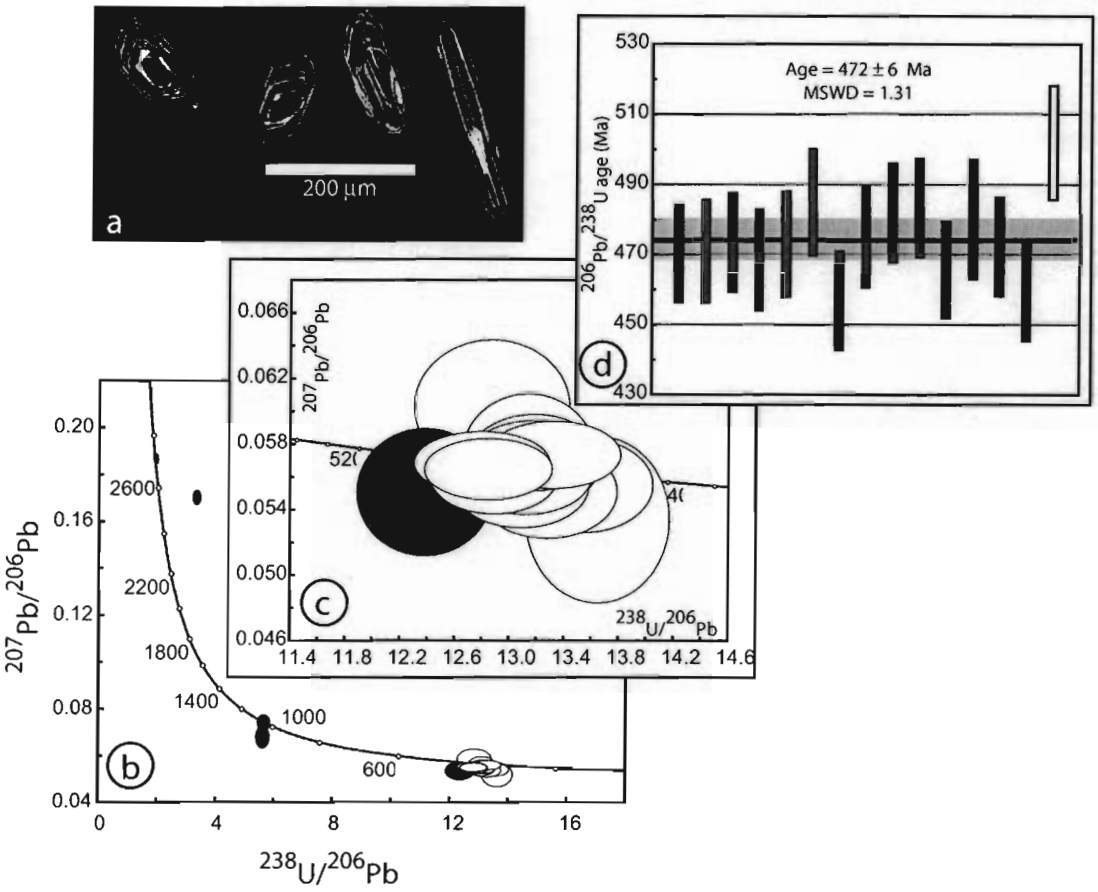

Figure 3.7 Results from U-Pb analysis of the Skinner pluton. (a) Cathodoluminescence images of representative zircon from the granodioritic Skinner pluton (GCL373). Cores in the leftmost two grains are similar to those that yielded ages >1000 Ma. (b) Tera-Wasserburg plot of all analyzed points; shaded analyses represent xenocrysts and are not included in age calculation. (c) Portion of (b) showing analyses used to calculate the age of the granodiorite; shaded analysis excluded. (d) Weighted average $^{206}Pb/^{238}U$ age. Unshaded bar corresponds to shaded ellipse in (b) and is not included in age determination. Lightly shaded band indicates the 95% confidence of the age, which we interpret as the time of crystallization.

Table 3.3 U-Pb SHRIMP isotopic data for zircon in GCL373 (Skinner pluton).
Sample loc. UTM ZONE 19T E377357 N5039340

						^{204}Pb-corrected[b]						^{207}Pb-corrected[b]	
Spot[a]	^{204}Pb /^{206}Pb	^{207}Pb /^{206}Pb	% common ^{206}Pb	U (ppm)	Th/U	^{238}U/^{206}Pb*	% err	^{207}Pb* /^{206}Pb*	% err	^{207}Pb /^{206}Pb Age	1σ	^{206}Pb /^{238}U Age	1σ
1	0.0000	0.0574	0.1107	352	0.5013	13.1954	1.51	0.0574	1.51	505	33	470	7
2	0.0000	0.0569	0.0487	170	0.4599	13.1869	1.58	0.0569	2.15	486	47	471	7
3	0.0000	0.0562	-0.0406	304	0.5243	13.1244	1.51	0.0562	1.74	461	39	474	7
4	0.0000	0.0552	-0.1542	198	0.4582	13.2835	1.57	0.0552	2.07	419	46	469	7
5	0.0000	0.0566	0.0147	223	0.4266	13.1334	1.62	0.0566	1.87	478	41	473	8
5C	0.0000	0.1703	8.5912	563	0.1240	3.3489	1.68	0.1703	0.73	2561	12	1556	30
6	0.0000	0.0569	0.0127	392	0.5679	12.8027	1.59	0.0569	1.35	489	30	485	8
7C	0.0003	0.0580	0.2380	190	0.8633	13.6540	1.57	0.0535	3.83	350	86	457	7
8	0.0001	0.0571	0.0675	263	0.7752	13.0919	1.54	0.0555	1.83	432	41	475	7
9	0.0001	0.0583	0.1890	327	0.7000	12.8931	1.50	0.0562	1.73	462	38	482	7
10	0.0000	0.0565	-0.0291	400	0.5040	12.8498	1.49	0.0565	1.34	474	30	483	7
11	0.0000	0.0574	0.1319	377	0.4794	13.3280	1.50	0.0574	1.44	507	32	466	7
12	-0.0002	0.0575	0.0950	249	0.5943	12.8743	1.81	0.0603	2.70	616	58	480	8
13	0.0001	0.0593	0.3501	279	0.4441	13.1409	1.52	0.0574	2.65	506	58	472	7
13C	0.0000	0.0556	-0.0764	178	0.3266	13.5361	1.57	0.0556	2.10	435	47	460	7
14C	0.0002	0.0578	0.0717	161	0.3436	12.3858	1.64	0.0552	2.84	419	64	502	8
15C	-0.0001	0.0747	0.0651	139	0.4611	5.6688	1.58	0.0755	1.82	1082	36	1046	16
16C	0.0002	0.0730	-0.2046	101	0.3001	5.6313	1.73	0.0694	2.73	911	56	1060	18
17C	0.0000	0.1865	1.0507	173	0.6237	1.9674	1.48	0.1865	0.48	2712	8	2626	43

a Bold denotes spots not included in age calculation; C denotes core analyzed

b All results corrected for common lead using model of Stacey and Kramers (1975); * refers to radiogenic Pb

interpret the core ages as inherited either from the source area or the host rock; the core ages are well-represented in the detrital age spectrum of the surrounding Chain Lakes massif (Gerbi et al. in review-a).

3.5.1.4 U-Pb SHRIMP-II age of Attean pluton

From zircon concentrate separated from the same sample of the quartz monzonitic Attean pluton analyzed by Lyons et al. (1986), we selected approximately 60 colorless, clear, euhedral grains. Zircons are euhedral, prismatic (length-to-width ratios of 2-5), and tan. Most grains display fine concentric oscillatory zoning in cathodoluminescence. Many grains contain elongate fluid inclusions parallel the c-axis. Analyzed locations are near the tips of grains, within areas of fine oscillatory zoning (interpreted as igneous in origin), to avoid possible complications in core regions that might contain inherited material. Reduced data illustrate that all analyses are concordant (Fig. 3.8). We interpret the weighted average $^{206}Pb/^{238}U$ age of 443 ± 3 Ma (95% confidence) (Fig. 3.8, Table 3.4) for zircon as the time of crystallization age of the Attean pluton.

3.5.2 Whole-rock geochemistry – Boil Mountain Complex

We selected eight samples from the Boil Mountain Complex to help constrain the tectonic setting in which it formed; and to provide a test for cogenetic relationships with locally occurring lavas (Jim Pond Formation). For most samples, major, trace, and rare earth element concentrations were determined at Activation Laboratories; samples GCL89 and GCL112b were analyzed at the Institut National de la Recherche Scientifique Laboratories in Québec City (Table 3.5). We also considered data on cumulate rocks from Coish and Rogers (1987). There are some significant differences between the rocks analyzed in the three laboratories. Notably, most of the samples analyzed at Activation

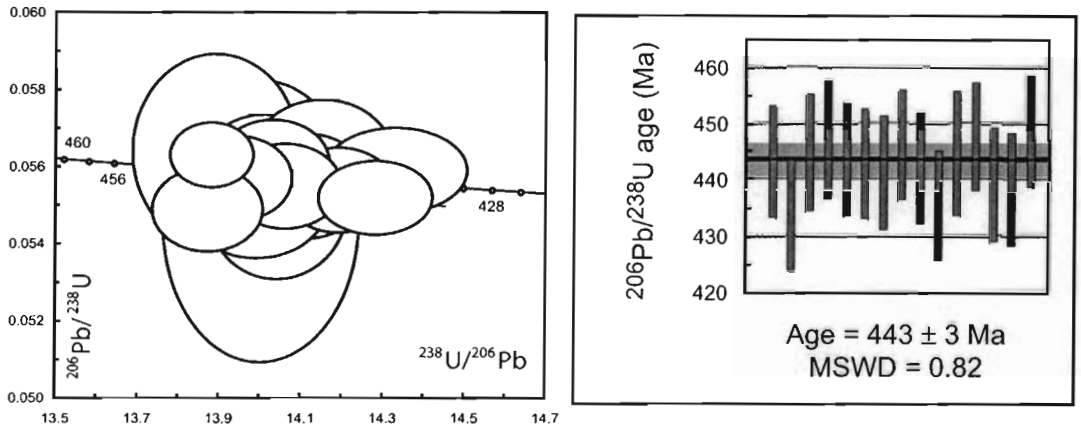

Figure 3.8 Results from U-Pb analysis of the Attean pluton. (a) Tera-Wasserburg plot of all analyzed zircon from the quartz monzonitic Attean pluton (ME/At 1-79). All analyses are included in age calculation. (b) Weighted average $^{206}Pb/^{238}U$ age. We interpret the age as the time of crystallization.

Table 3.4 U-Pb SHRIMP-II isotopic data for zircon in Attean pluton
Sample ME-At1-79 location UTM Zone 19T E397901 N5046550

						----------^{204}Pb-corrected[b]---------		^{207}Pb-corrected[b]			
Spot[a]	^{204}Pb /^{206}Pb	^{207}Pb /^{206}Pb	% common ^{206}Pb	U (ppm)	Th/U	^{238}U/^{206}Pb *	%err (1σ)	^{207}Pb* /^{206}Pb*	%err (1σ)	^{206}Pb /^{238}U Age	err (1σ)
1.1	0.0001	0.0559	0.0200	431	1.8500	14.0400	0.50	0.0550	1.40	444	5
2.1	---	0.0557	0.0200	397	2.6000	14.3300	0.50	0.0559	0.80	435	5
3.1	0.0000	0.0551	---	358	2.1800	13.9900	0.50	0.0550	1.00	446	5
4.1	---	0.0552	---	301	0.7300	13.8900	0.60	0.0564	1.80	448	5
5.1	0.0000	0.0562	0.0400	355	1.0800	14.0100	0.50	0.0557	1.20	445	5
6.1	---	0.0559	0.0100	596	0.9200	14.0300	0.40	0.0561	0.80	444	5
7.1	0.0000	0.0561	0.0500	322	0.8200	14.1000	0.50	0.0555	1.00	442	5
8.1	0.0000	0.0560	0.0200	529	1.1800	13.9400	0.40	0.0557	0.80	447	5
9.1	---	0.0552	---	433	0.7600	14.0600	0.40	0.0555	0.80	443	5
10.1	---	0.0550	---	544	1.0700	14.2800	0.40	0.0552	0.70	436	5
11.1	0.0001	0.0557	---	175	0.3500	14.0000	0.70	0.0546	2.70	445	5
12.1	---	0.0559	0.0000	919	1.0200	13.8800	0.30	0.0563	0.60	448	5
13.1	0.0000	0.0563	0.0800	350	0.7500	14.1500	0.50	0.0562	1.10	440	5
14.1	0.0000	0.0555	---	522	1.1400	14.1900	0.40	0.0554	0.80	439	5
15.1	0.0000	0.0551	---	459	0.7400	13.8700	0.40	0.0549	0.80	449	5

a Zircon analyzed during April 2004 on SHRIMP II at Australian National University

b All results corrected for common lead using model of Stacey and Kramers (1975); * refers to radiogenic Pb

Table 3.5 Whole-rock chemistry from the Boil Mountain Complex

	GCL-412	GCL-413	GCL-419	GCL-131A	GCL-411	GCL-407	GCL-112b	GCL-89
	Olivine gabbro /Norite	Harzburgite /Dunite	Websterite	Websterite	Harzburgite /Dunite	Olivine gabbro /Norite	Websterite	Websterite
SiO_2	41.8	42.5	34.0	50.3	36.2	44.7	50.7	45.6
Al_2O_3	12.7	0.74	7.77	1.58	1.42	16.3	3.33	6.22
Fe_2O_3	10.7	13.1	7.81	8.21	12.8	12.3	6.3	12.5
MnO	0.16	0.2	0.19	0.15	0.1	0.18	0.13	0.27
MgO	18.2	31.0	9.49	22.4	36.1	7.98	17.3	13.8
CaO	9.52	3.78	20.0	12.4	0.46	11.9	17.7	14.7
Na_2O	0.79	0.06	0.17	0.14	nd	1.69	0.17	0.48
K_2O	0.13	nd	nd	nd	nd	0.03	0.01	0.02
TiO_2	0.22	0.03	0.22	0.06	0.03	0.63	0.11	0.36
P_2O_5	nd	nd	nd	0.01	nd	0.05	< 0.013	< 0.013
LOI	5.54	7.98	19.3	4.71	12.9	2.91	2.23	3.84
TOTAL	99.7	99.3	98.9	99.9	100.0	98.6	98.0	97.8
Ba	16	9	4	14	2	12.0		
Sr	21	5	55	48	1	327.		
Y	5	1	4	2	nd	13.0		
Sc	47	26	79	42	6	53.0	58	104
Zr	4	4	5	nd	nd	9.		
Be	nd	nd	nd	nd	nd	nd		
V	128	47	202	87	nd	365.		
V	135.	58.3	206.	93.0	8.25	347.	173.	256.
Cr	249.	686.	751.	1470.	6950.	22.4	2796.	1613.
Co	85.2	126.	41.2	68.4	158.	23.4	42.5	51.1
Ni	148.	434.	110.	374.	2060.	27.4	152.	120.
Cu	221.	74.7	335.	16.3	103.	30.7	19.2	105.
Zn	76.9	65.5	50.3	37.2	79.5	73.8	36.6	74.3
Ga	7.57	1.04	6.95	1.89	2.59	15.4		
Ge	1.56	2.27	nd	2.4	1.44	2.32		
As	nd	16.5	nd	30.3	15.6	nd	< 38.4	< 38.6
Rb	nd	nd	nd	nd	nd	nd	0.21	0.5
Sr	21.7	4.81	53.9	46.0	nd	317.	4.43	18.9
Y	5.03	nd	4.56	1.94	nd	14.2	2.83	16.9
Zr	nd	5.73	6.89	5.59	6.85	13.7	1.12	4.34
Nb	6.17	4.17	1.67	3.61	2.28	2.89	0.03	0.03
Mo	nd	nd	12.2	nd	nd	nd		
Ag	nd	nd	0.65	nd	nd	nd		
In	nd	nd	nd	nd	nd	nd		
Sn	nd	1.42	nd	nd	nd	nd		
Sb	nd	nd	nd	nd	0.66	nd		
Cs	nd	nd	nd	nd	nd	nd	< 0.008	0.03
Ba	15.5	7.5	nd	8.62	nd	13.1	1.4	13.9

Table 5, continued

	GCL-412 Olivine gabbro /Norite	GCL-413 Harzburgite /Dunite	GCL-419 Websterite	GCL-131A Websterite	GCL-411 Harzburgite /Dunite	GCL-407 Olivine gabbro /Norite	GCL-112b Websterite	GCL-89 Websterite
Sm	0.49	0.12	0.42	0.17	nd	1.31	0.17	1.41
Eu	0.18	nd	0.1	0.06	nd	0.57	0.09	0.41
Gd	0.72	0.14	0.66	0.2	nd	1.88	0.34	2.39
Tb	0.16	nd	0.14	nd	nd	0.38	0.06	0.43
Dy	0.95	0.14	0.89	0.29	nd	2.46	0.47	3.13
Ho	0.2	nd	0.19	nd	nd	0.54	0.1	0.68
Er	0.59	nd	0.6	0.23	nd	1.75	0.32	2.02
Tm	0.08	nd	0.09	nd	nd	0.28	0.05	0.28
Yb	0.48	nd	0.55	0.27	nd	1.71	0.31	1.83
Lu	0.08	nd	0.08	0.04	nd	0.28	0.05	0.28
Hf	0.87	0.45	0.22	0.32	0.27	0.84	0.05	0.19
Ta	nd	nd	nd	nd	nd	nd	< 0.003	< 0.003
W	nd	1.08	nd	nd	nd	nd		
Tl	nd	nd	nd	nd	nd	nd		
Pb	nd	nd	11.3	nd	nd	nd	0.77	0.92
Bi	nd	1.34	nd	nd	nd	nd		
Th	nd	nd	nd	nd	nd	nd	< 0.03	< 0.03
U	nd	nd	nd	nd	0.11	0.13	< 0.008	< 0.008
Cd							< 10.2	10.7
S							0.0001	0.00008

Notes

Major elements and those in italics by ICP-ES; all others by ICP-MS. nd=below detection limits

GCL-112b and GCL-89 analyzed at the Institut Nationanal de la Recherche Scientifique; other samples analyzed at Activation Laboratories

Laboratories show prominent positive Nb-Hf anomalies, which we tentatively interpret to be analytical artifacts. In contrast, similar rocks analyzed at INRS show prominent negative Nb anomalies, and show coherent Zr-Hf behavior, commonly with negative Zr-Hf anomalies. Data from Coish and Rogers (1987) are more difficult to interpret because the profiles are incomplete, but Zr appears to be anomalously enriched. Because of these uncertainties, we will not base our interpretation on the presence or absence of high field strength cation anomalies, but rather on the rare earth elements (REE), which show much more coherent behavior, with smooth profiles.

Although igneous minerals are rarely preserved, we will omit the "meta-" prefix, with the understanding that all these rocks are now metamorphic. Based on normative mineralogy and interpretation of pseudomorphic textures in thin section, four of our samples of the Boil Mountain Complex can be classified as websterites (GCL-419, 89, 131, 112b), two as olivine gabbro-norite (GCL-412 and 407), and two as harzburgite or dunite (GCL-411 and 413). Most of the cumulate rocks from Coish and Rogers (Coish and Rogers 1987) are melagabbros, with two websterites (83-70 and 83-32) and one harzburgite (83-148). Based on major element chemistry, we interpret most samples as cumulate rocks (high MgO in harzburgites, dunites and websterites; high Al_2O_3 in gabbros). This inference is supported by the generally very low abundances of incompatible trace elements, with the exception of Sr (compatible in plagioclase), which is typically enriched in the cumulate gabbros. Gabbros GCL-407 and 412 exhibit an interlocking rather than a cumulate texture, and we suspect they may not be cumulates.

Using the equilibrium distribution method of Bédard (1994; 2001), we calculate the trace element concentrations of the magmas from which the rocks crystallized for

different assumed trapped melt fractions; and then compared these to the upper and lower mafic volcanic suites of the overlying and possibly correlative Jim Pond Formation (Coish and Rogers 1987), and the average primitive low-Ti Betts Cove boninite (Bédard 1999). The objective is to test whether a cogenetic cumulate/lava relationship is plausible, and to gain insight into the tectonic affinities of the different magmas from which these rocks crystallized. Our interpretations are constrained principally by the behavior of the least-mobile elements, such as the REE. Nevertheless, the entire geochemical profile is shown, despite the known mobility of certain elements during metamorphism and hydrothermal alteration. We note simply that the behavior of the mobile elements is generally consistent with inferences drawn from the relatively immobile elements.

Calculation of the model liquid requires the whole-rock trace element compositions, a mineralogical mode, and accurate mineral/liquid distribution coefficients (see Appendix D). Modes were approximated from a corrected CIPW norm, by a method similar to that outlined in Bédard (2001), with additional insight being provided from the interpretation of pseudomorphic textures and assemblages in thin section. Error propagation calculations (Bédard 1994) imply that small errors in the modal estimates have little impact on the compositions of the calculated liquids. Variations in the assumed trapped melt fraction affect the overall abundance of trace elements in the liquid, but the relative concentrations, i.e. the profile shape, is less affected. Partition coefficients for olivine and orthopyroxene (Bédard in press, in review-a) are fully parameterized against liquid MgO content. We estimated MgO content by comparison of whole-rock FeO/MgO with the Jim Pond volcanic suites for samples with inferred tholeiitic affinities, and with the Betts Cove boninitic suite (Bédard 1999) for those which resemble boninites. We

assumed FeO/MgO exchange coefficients of 0.3, 0.27 and 0.23 for olivine, orthopyroxene and clinopyroxene respectively, and weighted the calculation according to the estimated mode at the assumed trapped melt fraction of interest. The calculated liquid MgO content was corrected for the trapped melt affect by a method similar to that of Barnes (1986), using the FeO vs MgO trend derived from the Jim Pond lavas for tholeiitic samples, and by comparison with Betts Cove lavas for samples with inferred boninitic affinities. A minimum liquid MgO content of 4 wt% was assumed. Partition coefficients for clinopyroxene were parameterized against the Al^{iv} content (cf. Lundstrom et al. 1994; Gaetani and Grove 1995), assuming a typical tholeiitic value of Cpx Al^{iv} = 0.125 for tholeiitic rocks and 0.075 for boninitic rocks. Plagioclase D values were parameterized against temperature and An-content (cf. Bindeman et al. 1998). The An-content was estimated from the norm calculation, and linked to MgO and temperature from a compilation of experimental data for melts with H_2O contents <1 wt% (Bédard, in preparation).

The trace element patterns of model liquid from rocks of the Boil Mountain Complex indicate the presence of at least two, and perhaps three magmatic suites.

SUITE 1. The first suite comprises samples GCL-112b, 131a, 411, 413, 83-148 and 83-27 (Figs. 3.9a,b). These samples show generally depleted incompatible element abundances, with LREE and HREE being enriched relative to MREE. Abundances of large-ion lithophile elements and Pb are typically enriched, as is Sr in most samples. However, little reliance can be placed in the LILE-Pb-Sr abundances because of the known mobility of these elements. In samples analyzed at INRS, model liquids show prominent negative Nb-Zr-Hf anomalies. Despite the uncertainties about the significance

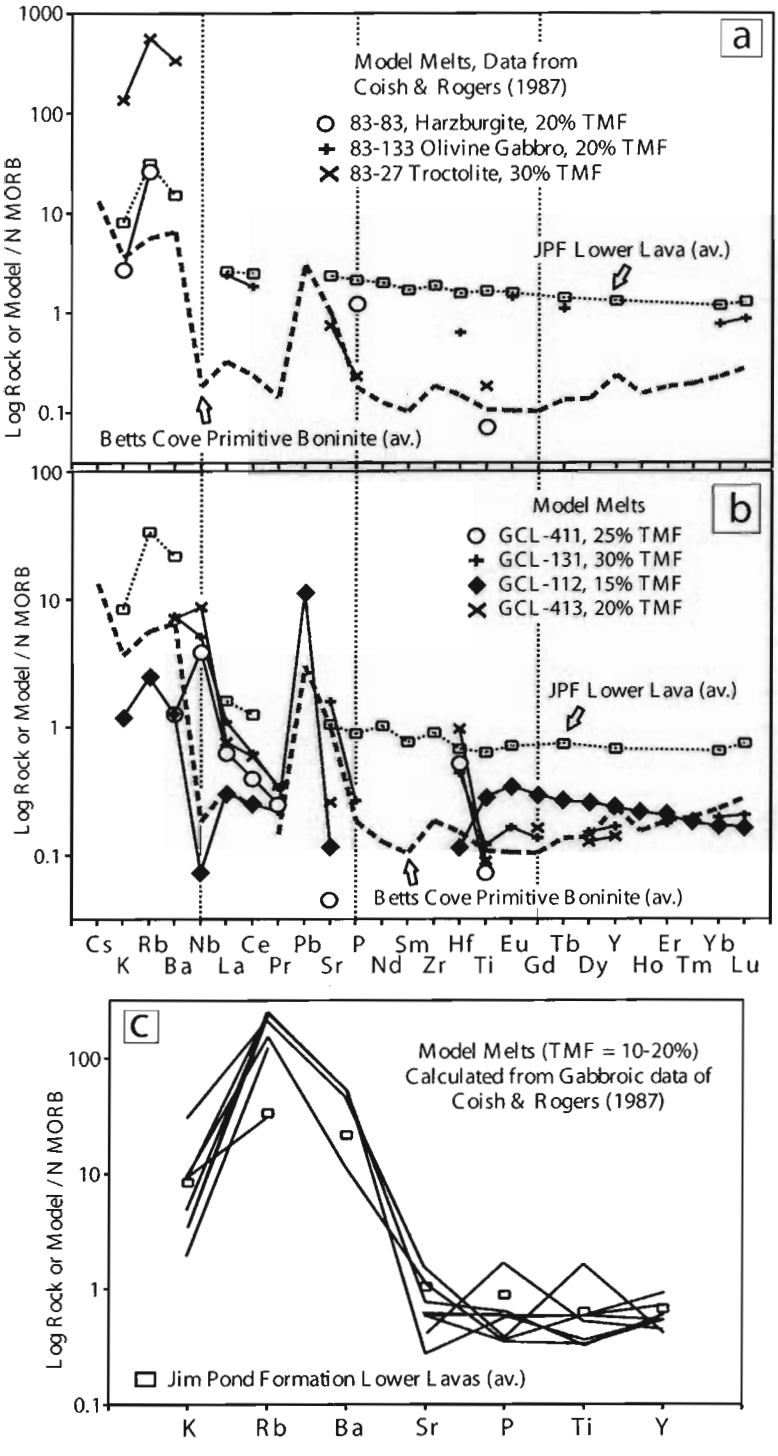

Figure 3.9 Calculations of model melts from whole-rock composition. See text for method. Normalization factors from Sun and McDonough (1989). TMF=trapped melt fraction. (a) Model melts calculated from data of Coish and Rogers (1987). Melts calculated for gabbro 83-133 closely resembles Jim Pond Fm. lower lavas, while melts calculated from troctolite 83-27 and harzburgite 83-148 more closely resemble typical Betts Cove boninites. (b) Model melts calculated from data obtained in this study. Models show a close resemblance to typical Betts Cove boninites and do not resemble Jim Pond Fm. lavas. Note that sample GCL-112, analyzed at INRS shows negative Nb-Hf anomalies, whilst samples analysed at Actlabs (GCL-411, 131 and 413) have positive Nb-Hf anomalies. (c) Model melts calculated from gabbroic data of Coish and Rogers (1987) assuming 10-20% trapped melt fractions.

of these HFSC anomalies, the REE profiles show coherent behaviour and their interpretation is less ambiguous. The model REE profiles from the of these samples closely resemble those of Betts Cove low-Ti boninites, and cannot be fit to Jim Pond Fm lavas at any assumed trapped melt fraction or mode. To summarize, these five samples display geochemical signatures that strongly suggest a boninitic affinity.

SUITE 2. The second suite comprises most of the gabbro data from Coish and Rogers (1987), including 83-133 (Figs. 3.9a,c). Normalized trace element profiles of these model melts are relatively flat, with slight to moderate large-ion lithophile element enrichment, and have REE-Y abundances that are much higher than those of boninitic melts, precluding a consanguineous relationship with rocks of the first suite. The model melts extracted from the data of Coish and Rogers (1987) are generally very similar to typical Jim Pond lower lavas, and we suggest that these gabbros may have formed from the same feeder system as the lavas.

SUITE 3. The third suite consists of samples GCL-89 (Fig. 3.10a) and GCL-407 (Fig. 3.10b). Websterite sample GCL-89 (analysed at INRS) shows prominent negative Nb-Zr-Hf-Ti anomalies, of uncertain origin and significance, possibly the result of ilmenite fractionation, but shows coherent, LREE-depleted profiles. Abundances of LREE are slightly depleted relative to typical Jim Pond upper lavas. Model melts from gabbro GCL-407 are very different from typical Jim Pond lavas, with high abundances and slight LREE-depletion. However, the gabbro itself has a slightly LREE-depleted profile only slightly below those of average Jim Pond Lower lavas. We suspect that this rock may be a quasi-liquid, with only a minor cumulate (phenocryst) component. However, a model melt calculated assuming that the rock contains 10% plagioclase and

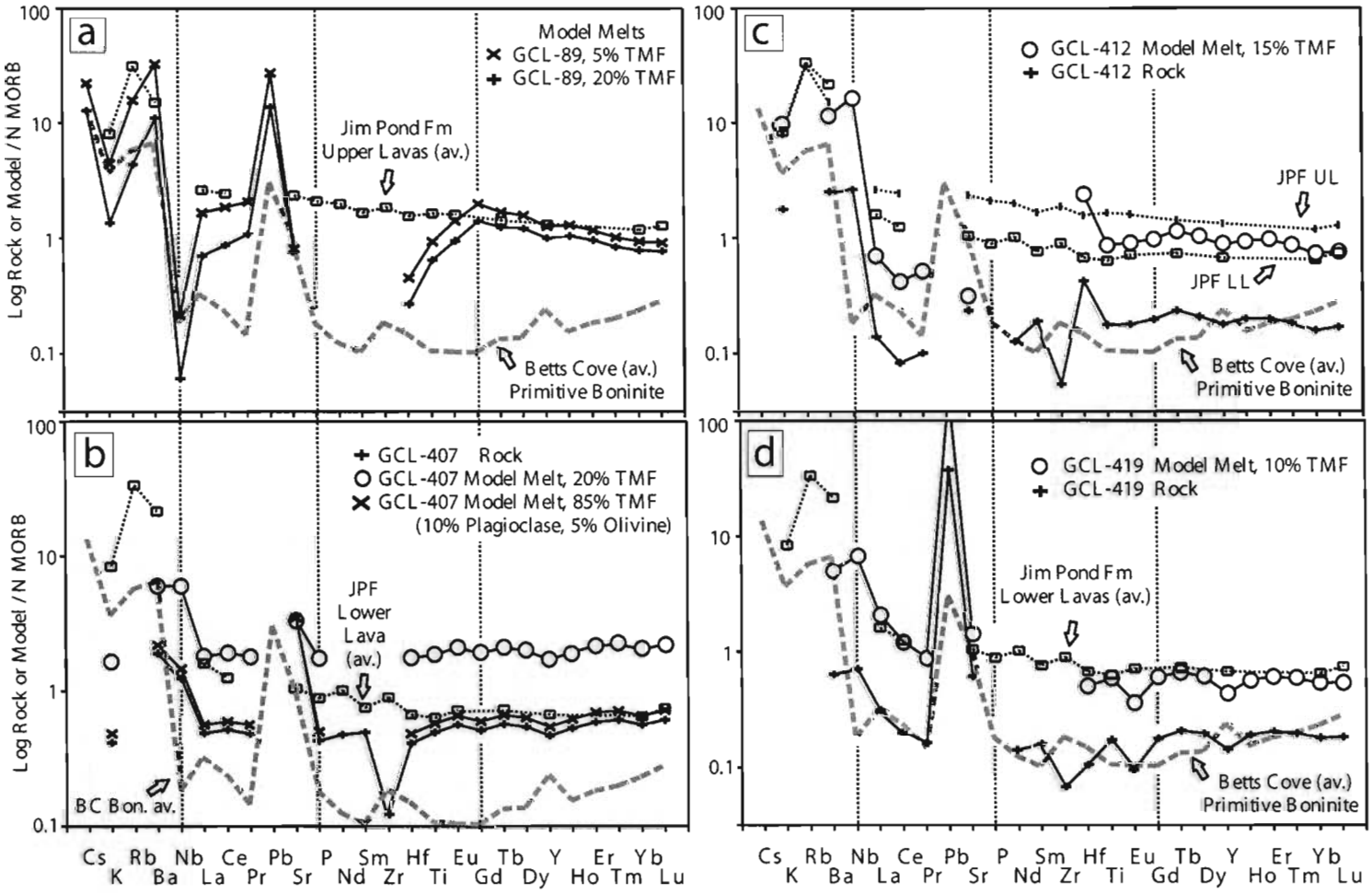

Figure 3.10 Rock chemistry and model melts calculated for additional samples. (a) GCL-89, (b) GCL-407, (c) GCL-412, and (d) GCL-419. See text for method. Normalization factors from Sun and McDonough (1989). TMF=trapped melt fraction

5% olivine phenocrysts yields a profile that is still markedly different from typical Jim Pond lavas. Taken at face value, the models suggest that these two samples formed from melts that were significantly less LREE-enriched than typical Jim Pond lavas. However, loss of a small amount of late-stage trapped melt might account for some of the LREE depletion, and so we cannot conclusively exclude the possibility that these two samples are related to the Jim Pond Formation.

The analyses of olivine gabbro-norite GCL-412, and websterite GCL-419 are remarkably similar to the average Betts Cove boninite (Fig. 3.10c and 10d). In the case of sample GCL412, model liquids exhibit unusual humped patterns that do not resemble those of Jim Pond Fm lavas, but show some resemblance to the model melts from GCL-89. We suspect that this sample (GCL-412) is only weakly cumulate in character, and may represent a boninitic meta-dyke or meta-lava. Alternatively, it may be a cumulate related to the third suite. Sample GCL-419, on the other hand, yields model liquids that are very similar to typical Jim Pond Formation lower lavas. Thus, the attribution of an affinity to sample GCL-419 hinges on whether this rock is a cumulate or a quenched liquid.

3.6 Discussion

3.6.1 Unit origins and histories

3.6.1.1 Boil Mountain Complex

One of the factors complicating interpretation of the Boil Mountain Complex and Jim Pond Formation is that for more than twenty years, these two units were considered part of an ophiolite sequence (Boudette 1982). Based on the arguments presented below,

we believe that the Boil Mountain Complex and Jim Pond Formation are serendipitously juxtaposed. The Boil Mountain Complex comprises metamorphosed intrusive ultramafic rocks, gabbro, and tonalite. Although the gabbro and ultramafic rocks are in places separable at map scale, in many locations they are intimately distributed at the outcrop scale (Boudette and Boone 1976). As such, we interpret the gabbro and ultramafic rocks as comagmatic. The cm-scale mixed occurrence of the gabbro and tonalite leads us to infer either an intrusive relationship of the tonalite into the gabbro or a cogenetic origin. Although any relationship between the tonalite and the rest of the Complex is speculative, Chow (1995) indicated that it is chemically permissible for the tonalite to be derived from a partial melt of the gabbro. Available trace element data do not permit a detailed assignment of tectonic setting for the Boil Mountain Complex, but the similarity of the various suites with Betts Cove and Jim Pond Formation rocks suggests that the Boil Mountain Complex formed in an active arc environment.

Textures of rocks within the Complex, principally the pyroxenite and tonalite, indicate an igneous origin overprinted by high-grade metamorphism. Igneous structures are well-preserved in the tonalite and consist primarily of cumulate textures in pyroxenite (Fig. 3.2a). To varying degrees throughout the Complex, hornblende has replaced clinopyroxene. Some websterite contains <5% hornblende whereas in the gabbroic portions of the Complex, hornblende is the only Fe-Mg silicate (Fig. 3.2b). In the absence of sufficiently unaltered plagioclase, we cannot perform quantitative thermometry. Nevertheless, the presence of metamorphic hornblende indicates that the Boil Mountain Complex reached pressure-temperature conditions in the amphibolite facies, well beyond those experienced by the Jim Pond Formation and overlying rocks

(Osberg et al. 1985). In contrast, amphibolite facies or higher metamorphic conditions are fully consistent with those experienced by the diatexitic Chain Lakes massif.

3.6.1.2 Jim Pond Formation

The bimodal nature of the volcanism and the range of mafic volcanic compositions, including between the upper and lower mafic units (Coish and Rogers 1987), can be found in rift or arc settings. Evidence for subaqueous deposition, including pillow lavas and sedimentary beds between volcanic layers, suggests a marine origin. These observations support chemical interpretations (Coish and Rogers 1987) that place the Jim Pond Formation in a suprasubduction zone setting, probably within a dynamic arc environment. In agreement with Moench and Aleinikoff (2003), we believe that such an arc formed near the Laurentian margin.

The chemical similarity between one suite in the Boil Mountain Complex and the lower mafic lavas of the Jim Pond Formation raises the possibility that these two units may have had a common source for some portion of their development. If this were the case, then, as argued below, the Boil Mountain Complex and the Jim Pond Formation must have formed in different regions of a single arc and were later structurally juxtaposed.

At some time following eruption and deposition, deformation rotated the flows and bedding within the Jim Pond Formation to vertical, synchronous with vertical foliation development, and at no time did metamorphic conditions ever exceed greenschist facies. The timing of deformation and metamorphism is undetermined, but their nature matches the tectonism that affected Silurian and early Devonian rocks in the area (Bradley et al. 2000). With a lack of evidence for multiple deformations, we infer

that the Jim Pond Formation remained at high crustal levels throughout its history, becoming penetratively deformed and metamorphosed only in the Devonian.

3.6.2 Timing and style of juxtaposition

3.6.2.1 Chain Lakes massif and Boil Mountain Complex

Much has been hypothesized about the timing and style by which the Boil Mountain Complex arrived in its present position (Boudette 1970; Boudette and Boone 1976; Zen 1983; Boone and Boudette 1989; Boudette et al. 1989; Trzcienski et al. 1992; Kusky et al. 1997; Moench and Aleinikoff 2003). The basis for the interpretation that the Chain Lakes massif and the Boil Mountain Complex were tectonically juxtaposed lies in the observed high strain zones along and near the contact between the two units. However, the sub-amphibolite facies metamorphic conditions associated with the deformation indicate that the shear zones developed after the high grade metamorphism of both the Chain Lakes massif and the Boil Mountain Complex. The lack of ubiquitous high (or even moderate) strain features along the entire contact suggests that these shear zones could not have been the primary mode of juxtaposition. In particular, the deformational effects are too weak to suggest that the contact represents an obduction surface related to the emplacement of an ophiolite as originally proposed (Boudette et al. 1989).

As an alternative, we propose that the Boil Mountain Complex-Chain Lakes massif contact represents an initially intrusive contact that has since been modified twice (Figs. 3.11, 3.12). Intrusion of Boil Mountain Complex magma occurred at ca. 477 Ma. The first modification of the contact came during the high grade metamorphic event at ca. 470 Ma (Gerbi et al. in review-a) that affected both the Chain Lakes massif and the Boil

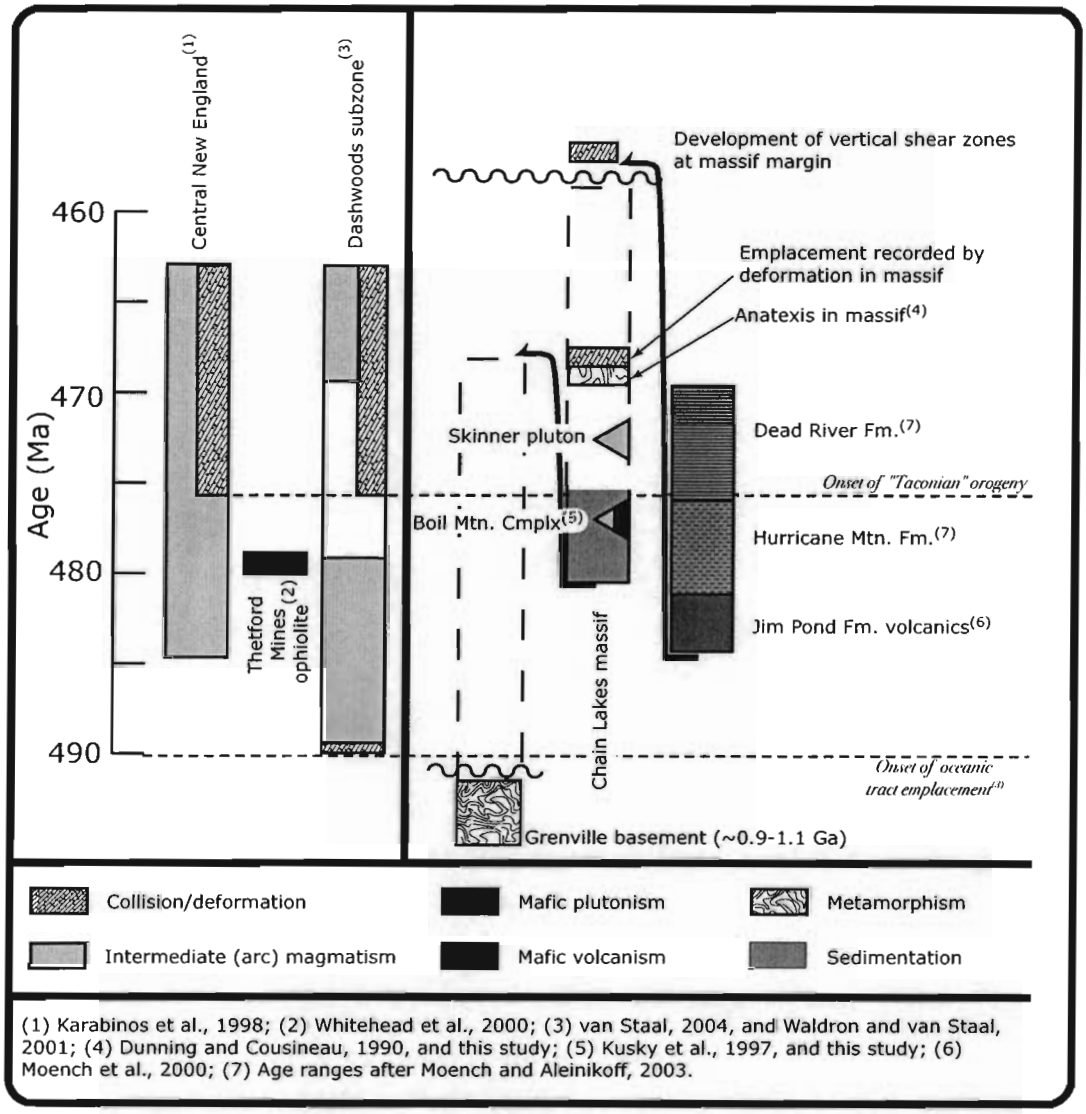

Figure 3.11 Schematic history of the pre-Silurian bedrock units. The Boundary Mountains region (right) is compared with potentially correlative Appalachian segments in central New England and Newfoundland (left). In our interpretation, the Chain Lakes massif represents an arc-marginal basin formed in the Early Ordovician that was then intruded by the arc-related Boil Mountain Complex and Skinner pluton. The entire package was metamorphosed and deformed at high temperature then emplaced northwestward over Grenville basement. Later, following intrusion of the Attean pluton (not shown) and exhumation of the Chain Lakes massif in the Silurian, the Jim Pond Formation and overlying Hurricane Mountain mélange and Dead River flysch were juxtaposed against the Boil Mountain Complex.

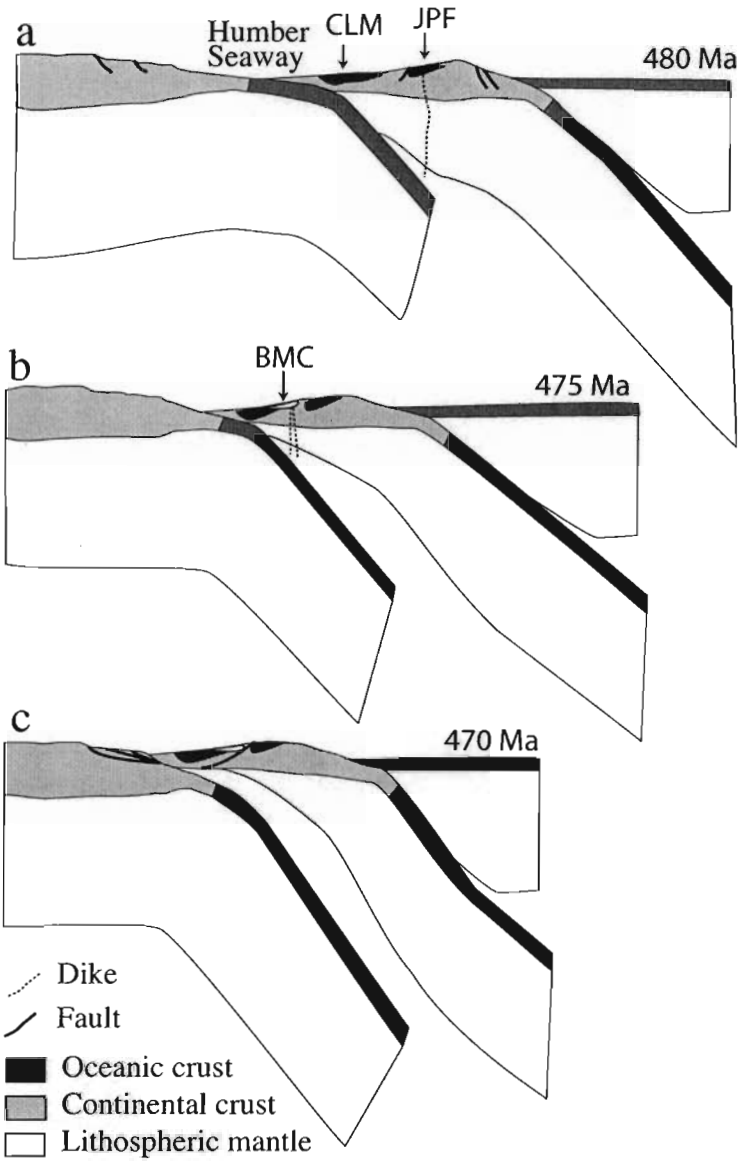

Figure 3.12 Inferred history of the Boundary Mountains region. Compare with fig. 3 of Waldron and van Staal (2001). (a) Intra-Iapetan subduction ceases as a Laurentian-derived microcontinent fails to subduct. Subduction steps cratonward, closing the Humber Seaway. The Jim Pond Formation (JPF) and Chain Lakes massif (CLM) are developing about this time. (b) Subduction continues to close the Humber Seaway while mafic and ultramafic magma of the Boil Mountain Complex (BMC) propagates to the mid-crust, perhaps generated in part by rising asthenosphere. (c) With the Humber Seaway closed, contraction is taken up by the Laurentian margin and by the outboard margin of the microcontinent. Prior to displacement of the Chain Lakes massif, it was metamorphosed and melted. The heat source may have been a combination of shallow asthenosphere and magmatism (not shown) induced by lithospheric thinning.

Mountain Complex. Partial melting in the massif largely eliminated textural (i.e., contact metamorphic) evidence of the original intrusive relationship. In the small portion of the massif previously considered a separate tonalitic intrusion (Holtzman et al. 1996), anatexis in the Chain Lakes massif is recorded by zircon rim growth. The second modification produced the observed mylonitic shear zones, which are oriented parallel to regional Devonian structures. This modification probably took place during the regional Devonian deformation that also affected the Jim Pond Formation.

3.6.2.2 Boil Mountain Complex and Jim Pond Formation

Before discussing the juxtaposition of the Boil Mountain Complex and the Jim Pond Formation, we must first demonstrate that these two units do not represent part of an ophiolite sequence (cf. Boudette 1982). Although they may have formed in the same arc at different crustal levels, several lines of evidence suggest Boil Mountain Complex and Jim Pond Formation actually are unrelated igneous units that have been serendipitously juxtaposed to suggest a false, cogenetic affinity.

(1) Whereas the Boil Mountain Complex underwent solid-state metamorphism in the amphibolite facies, the Jim Pond Formation never experienced conditions greater than greenschist facies.

(2) Some chemical similarities exist between the Boil Mountain Complex and the mafic lower lavas of the Jim Pond Formation (Section 3.4.2), but the felsic volcanic sequences in the Jim Pond Formation have no counterpart in the Boil Mountain Complex and some components of the Boil Mountain Complex have no counterparts in the Jim Pond Formation.

(3) The abundance of tonalite is atypical of ophiolites but is more typical of arc terranes.

(4) Although the ages of the units (Jim Pond Formation: 484 ± 5 Ma; gabbro of Boil Mountain Complex: 477 +7/-5 Ma) overlap at 95% confidence, the tonalite (477 ± 1 Ma) is statistically younger than the Jim Pond volcanics. If the gabbro and the tonalite were cogenetic, as textures suggest, the volcanic rocks must also be older than the gabbro, and by extension, older than at least some of the ultramafic rocks in the Boil Mountain Complex.

(5) Tonalite of the Boil Mountain Complex is measurably younger than the Jim Pond Formation, so if the Boil Mountain Complex and Jim Pond Formation formed in their presently adjacent locations, the tonalite must also have intruded the Jim Pond Formation, presumably leaving some evidence of contact metamorphism near the contact. Although the contact between the tonalite and the Jim Pond Formation is not directly exposed, we observed no evidence of thermal perturbation approaching the contact.

(6) Gabbro in the Jim Pond Formation is texturally and mineralogically distinct from gabbro in the Boil Mountain Complex.

(7) No tectonized harzburgite or sheeted dikes are present in either the Boil Mountain Complex or Jim Pond Formation.

(8) One argument used to support the notion of an ophiolite sequence is that the Boil Mountain Complex is now vertical and faces south, in parallel with the Jim Pond Formation. However because the Complex lacks any paleohorizontal indicators, the true structural orientation of the Complex is unknown.

(9) The Boil Mountain Complex is limited in extent to the southern margin of the Chain Lakes massif, but the Jim Pond Formation extends hundreds of kilometers along strike. If the two were once a continuous sequence, we would expect to see at least sporadic occurrences of Boil Mountain Complex rocks along more of the length of the Jim Pond Formation.

Given this evidence, we conclude that the Boil Mountain Complex and the Jim Pond Formation do not represent an ophiolite sequence. The problem now becomes determining the nature and timing of their juxtaposition.

Chemical, structural, petrologic, and geochronologic evidence supports the interpretation that the Boil Mountain Complex and Jim Pond Formation formed at slightly different times, at different structural levels, but likely within the same arc environment. Given the additional constraint that the Boil Mountain Complex intruded the Chain Lakes massif prior to the ca. 470 Ma high-grade metamorphism, the Jim Pond Formation must have been juxtaposed against these two units more recently than 470 Ma. The Silurian Hardwood Mountain Formation was unconformably deposited over the Chain Lakes massif and Boil Mountain Complex, but no similar unconformity is reported over the Jim Pond Formation. As such, there is no direct upper constraint on the timing of the Jim Pond Formation and Boil Mountain Complex juxtaposition, and we believe that it need not have occurred prior to the Devonian deformation that affected the region. No evidence exists for multiple deformational or metamorphic episodes within the Jim Pond Formation, and the deformational and metamorphic style of the formation matches well with that of nearby Silurian and Devonian rocks (Boudette 1991), suggesting a

Devonian age of deformation. Final juxtaposition of the Jim Pond Formation and the Boil Mountain Complex could have occurred along segments of the regionally extensive Squirtgun Fault (mapped by Boudette 1991; Moench et al. 1995).

3.6.3 Scenario for the development of the Boundary Mountains terrane

Based on past studies and our present work, we envision the following stages as the most likely history for the development and juxtaposition of the pre-Silurian bedrock in the Boundary Mountains region (Figs. 3.11, 3.12).

Earliest Ordovician After a period of quiescence following Iapetan rifting and passive margin development (Cawood et al. 2001), east-dipping subduction (following Waldron and van Staal 2001) commenced as Iapetus began to close. After aborted subduction of a microcontinent, subduction stepped westward, closing the Humber Seaway that separated Laurentia from the offshore microcontinent. The microcontinent served as the nucleus for an arc in which rocks of the Jim Pond Formation, and possibly the Ammonoosuc sequence, formed. In addition, an forearc basin began to receive Laurentian-derived sediment.

Late-Early to Early-Middle Ordovician Ongoing accumulation into the forearc basin of juvenile arc-derived tuffs and lavas, and voluminous Laurentian-derived sediments, constitute the Chain Lakes massif protolith. Concurrently, the arc generated Boil Mountain Complex magmas that rose and intruded the Chain Lakes massif. Some Boil Mountain Complex tholeiites were similar to those of the slightly older Jim Pond Formation. Later, more mature arc-related magmatism produced the Skinner granodiorite. At or about this time, the Hurricane Mountain Formation, a black shale tectonic mélange (Boone et al. 1989), developed over the Jim Pond Formation.

Deposition of the Dead River Formation flysch followed cessation of mélange growth (Boone 1973).

Middle Ordovician Deposition of the Dead River Formation (> 469 Ma; Moench and Aleinikoff, 2003) marks a tectonically quiet period in the upper crustal Section 3.of the Boundary Mountains region. Likely, erosion produced a slow exhumation of the arc. Meanwhile, low-pressure–high-temperature metamorphism affected the Chain Lakes massif and Boil Mountain Complex. The Chain Lakes massif partially melted at this time, becoming a diatexite, and the Boil Mountain Complex was metamorphosed in the amphibolite facies. As the Chain Lakes massif cooled but while it was still partially molten, the massif and the Boil Mountain Complex were thrust northwestward over the Laurentian margin. The allochthonous relationship persists today (Stewart et al. 1993), but the suture is buried under younger sediments.

Late Ordovician-Silurian Continued closure of Iapetus resulted in continued arc activity in the region, marked by the Quimby sequence of Moench and Aleinikoff (2003). The Early Silurian Attean pluton was part of the Highlandcroft plutonic series and probably associated with Ganderia docking. Following this stage of Appalachian orogenesis, the Chain Lakes massif, Boil Mountain Complex and Attean pluton were exhumed and nonconformably overlain by Silurian sediment. Coeval erosion appears to have occurred in the separate lithologic sequence of Jim Pond Formation through Ammonoosuc sequence (Moench and Aleinikoff 2003), though the erosive surface did not reach into the Jim Pond Formation. It is possible that the Jim Pond Formation and succeeding rocks were juxtaposed against the Chain Lakes-Boil Mountain suite at or by this time, but no direct evidence constrains this.

Devonian In the middle Paleozoic, deformation and magmatism once again affected the Boundary Mountains region. The deformation front passed through the area at approximately 400 Ma (Bradley et al. 2000), producing a northeast-southwest-striking, subvertical fabric in most of the units. The deformation is best recorded in the Silurian-Devonian sediments deposited during the tectonic hiatus following early Silurian magmatism, but it also affected the pre-Silurian units. The fabric of the Jim Pond Formation probably developed at this time, as did the subvertical shear zones near and crossing the contact between the Chain Lakes massif and the Boil Mountain Complex. The regionally extensive Squirtgun fault was active at this time (e.g. Boudette 1991); we suspect that the Boil Mountain Complex and Jim Pond Formation were juxtaposed along a strand of that fault system.

3.6.4 Relationship to northern Appalachian tectonic evolution

The results presented here invite broader consideration of the nature of the early Ordovician eastern Laurentian margin. The presence of at least four different series of arc-related magmas, represented by the Jim Pond Formation, Boil Mountain Complex, Skinner pluton, and Attean pluton, supports the assertion of van Staal et al. (1998) that the region contained a complex and rapidly evolving series of subduction zones and arcs. We have no direct evidence that the Chain Lakes massif represents a microcontinent rifted from the Laurentian margin as has been suggested for the Dashwoods subzone of Newfoundland (Waldron and van Staal 2001), but the presence of the quartzofeldspathic rocks within the massif, rhyolitic magma in the Jim Pond Formation, and the granodioritic Skinner pluton indicates that at least some continental material existed outboard of the Laurentian margin at that time.

The Shelburne Falls (Karabinos et al. 1998) and Notre Dame (van Staal et al. 1998) arcs of New England and Newfoundland range in age from early to late Ordovician. This age range compares favorably with that of the arc-related rocks of western Maine. Although we cannot directly link these three geographically separated segments (Fig. 3.1), their ages and positions relative to the craton strongly suggest that they were once part of a continuous or segmented arc developed over intraoceanic subduction zones near the Laurentian margin.

Recent studies by Karabinos et al. (1998), van Staal et al. (1998), Pehrsson et al. (2003), and van Staal (2004), among others, have demonstrated arc collision as the driving force for deformation in Newfoundland and central New England, but no comparable structure had been identified in Maine or Québec. Boone and Boudette (1989) and Moench and Aleinikoff (2003) hypothesized that the Chain Lakes massif represented part of a microcontinent that served as the Ordovician collider, but they did not consider it as part of an active arc. The evidence presented here and by Gerbi et al. (in review-a) indicate that arc collision is indeed a viable mechanism for deforming the Ordovician Laurentian passive margin in the Maine-Québec segment of the northern Appalachian orogen.

In light of these new interpretations, a more complete picture of the pre-Silurian evolution of the western Maine bedrock awaits further investigation into the origin of the Hurricane Mountain and Dead River Formations and their relationship to the Jim Pond Formation, Boil Mountain Complex, and Chain Lakes massif.

3.7 Summary

Synthesizing field, petrologic, geochronologic, and geochemical data, we have revised previous interpretations of the Boil Mountain Complex, Skinner pluton, and Jim Pond Formation, as well as developed new interpretations of the timing and nature of their juxtaposition with each other and with the Chain Lakes massif. These units, which make up the majority of the pre-Silurian bedrock exposure in western Maine, play a key role in tectonic reconstructions of the early stages of Appalachian growth. In contrast to considering the Boil Mountain Complex and Jim Pond Formation as part of an ophiolite, we prefer to consider them genetically separate units. Their different ages, chemistry, and metamorphic and structural history preclude adjacent development. Instead, these two units formed in separate but probably related arc environments off the Laurentian margin in the early Ordovician. They were most likely juxtaposed during a Devonian deformational episode that affected the entire region.

The Boil Mountain Complex does, however, share a history with the adjacent quartzofeldspathic Chain Lakes massif. After the volcanic-sedimentary protolith of the Chain Lakes massif developed in an arc-marginal environment, the mafic and ultramafic Boil Mountain Complex intruded the depositional sequence at approximately 477 Ma. Later, at approximately 473 Ma, the granodioritic Skinner pluton also intruded the massif. A few million years later, an amphibolite-grade or higher metamorphic event affected the Boil Mountain Complex and partially melted the massif. This composite block was part of the complex arc system that existed at that time off the Laurentian margin. The Chain Lakes massif, Boil Mountain Complex, Skinner pluton, and Jim Pond

Formation likely formed part of the collider that deformed the Laurentian passive margin, initiating the Appalachian orogeny.

Chapter 4

CONTROLS ON LOW-PRESSURE ANATEXIS

4.1 Abstract

Widespread low-pressure anatexis, whereby rocks melt in place after passing through the andalusite stability field, develops under more restricted conditions than does low-pressure metamorphism. Our review of published work and use of one-dimensional thermal modeling indicates that the following mechanisms may induce anatexis in typical pelitic rocks: (1) magmatic advection by percolative flow, (2) crustal-scale detachment faulting, (3) removal of the lithospheric mantle during crustal thinning, and (4) the presence of a high heat producing layer. Of these, only magmatic advection by percolative flow and crustal-scale detachment faulting are shown quantitatively to provide sufficient heat to cause widespread melting. Combinations of the above mechanisms with each other or with pluton-scale magmatic advection provide additional means of developing suitably high temperatures at shallow crustal levels to generate low-pressure anatexis.

4.2 Introduction

The thermal structure of the crust plays a major role in numerous geologic processes, including deformation and metamorphism, erosion patterns and magnitudes, fluid flow, and magma generation. Moreover, accurate descriptions of the thermal structure of the crust are prerequisites for understanding large-scale rheology and the relationship between surficial features and geodynamic processes (e.g., Koons et al. 2002). Fortunately, well-established heat transfer relationships (Carslaw and Jaeger 1959) and advances in numerical modeling have allowed Earth scientists to predict

temperature patterns at local through lithospheric scales (cf. Jamieson et al. 1998) in a variety of settings. In this contribution, we consider the origin of thermal conditions in continental crust sufficient to melt rocks at depths less than 15 km.

Stable continental geotherms produce temperatures of 400°-500°C at 15 km depth, but many orogenic belts contain mid- to upper-crustal rocks heated to over 600°C. Some perturbation must have occurred to generate such high temperatures. Low-pressure metamorphic belts, which record these high temperatures, are common in orogens throughout the world and therefore must represent transient conditions in Earth's crust that readily develop in active tectonic settings. Because of the widespread presence of these belts, the causes of low-pressure metamorphism have received significant attention (Lux et al. 1986; Wickham and Oxburgh 1987; Hanson and Barton 1989; Loosveld 1989; De Yoreo et al. 1991; Sandiford and Powell 1991; Sandiford and Hand 1998a; Sandiford et al. 1998; Escuder Virute 1999; Bodorkos et al. 2002; Miyazaki 2004). Many of these studies discuss, if not model, anatexis at lower crustal levels in the context of generating magma that then propagates upward to provide additional heat to the upper levels of the crust. Consideration of anatexis at low pressures, however, has received comparatively little attention.

Even though low-pressure anatexis can be considered an extension of low-pressure metamorphism, there can be a temperature difference of 200°C between when conditions for low-pressure metamorphism develop and when low-pressure anatexis occurs (Fig. 4.1). We sought to determine the extent to which proposed low-pressure metamorphism-causing mechanisms could also drive anatexis. For the purposes of this paper, we define low-pressure anatexis as the progression in pressure-temperature space

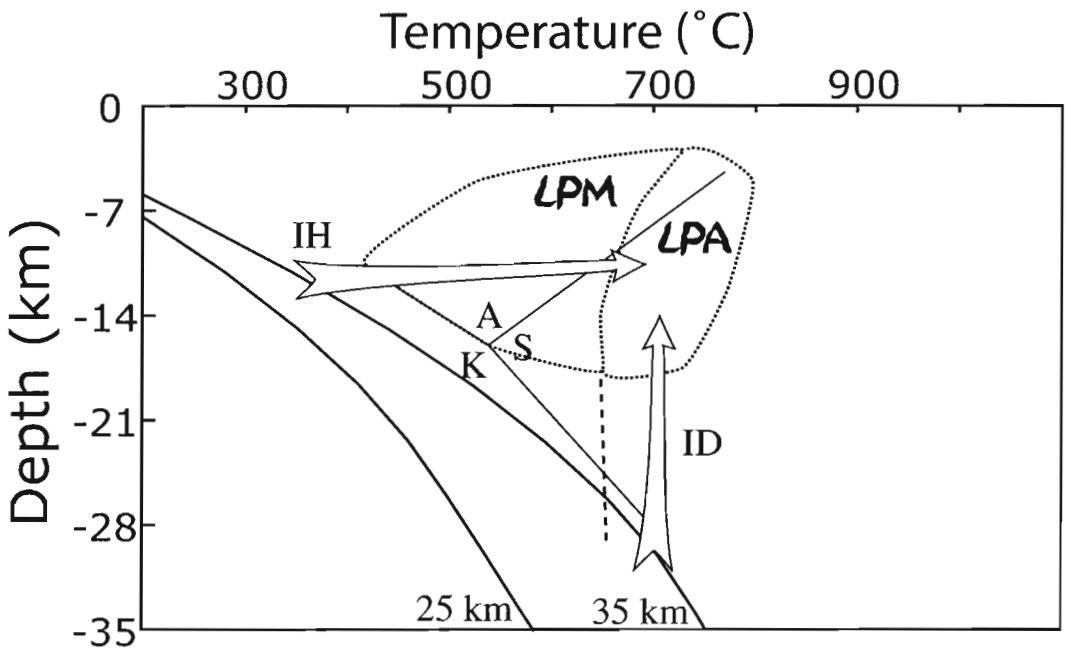

Figure 4.1 Stable geotherms and pressure-temperature paths leading to low-pressure anatexis. Depth-temperature space illustrating typical geotherms for stable continental crust of 25 km and 35 km thickness (labeled solid lines) and pressure-temperature paths that can lead to anatexis at low pressure (arrows: IH = isobaric heating; ID = isothermal decompression). Also shown are the aluminosilicate phase boundaries (A = andalusite; S = sillimanite; K = kyanite) and the wet pelite melting curve (dashed) after Spear and others (1999). LPM = field of low-pressure metamorphism; LPA = field of conditions appropriate for low-pressure anatexis.

through the andalusite field, into the sillimanite field, and across a melt-producing reaction (Fig. 4.1). Our goal was to determine the solution space in which the crust can achieve temperatures in excess of 650°C at less than 5 kb without undergoing substantial decompression. Although we present much of the discussion in the context of pelite melting, the thermal conditions can easily be generalized. We use the widely cited wet pelite melting curve (Spear et al. 1999) because it is the lowest temperature melting reaction for common rock types, and it is one of the dominant crustal melting reactions.

Excluded from this analysis is anatexis due to (near-)isothermal decompression. Such decompression allows deeper crustal material to approach the surface, carrying heat with it. If the decompression is fast enough, rocks can enter melting fields at low pressures (Fig. 4.1). Numerous examples of this style of low-pressure melting exist around the world, including in areas where the decompression is caused by erosion (Zeitler et al. 1993). Melting at low pressure because of isothermal decompression is readily explicable by well-known crustal kinematics, and at the same time has a fundamentally different cause than low-pressure anatexis in rocks that passed through the andalusite field.

As discussed below, several mechanisms are capable of generating low-pressure anatexis. In some areas, field relations allow easy determination of the heat source, but in many places clear evidence for the causative agents is lacking or ambiguous. For example, the Pyrenees contain several Hercynian massifs whose low-pressure metamorphic signatures have been ascribed to heat related to both extension (Wickham and Oxburgh 1987; Gibson 1991) and transpression accompanied by magmatism (Druguet 2001; Olivier et al. 2004). The Cooma and Glenelg River Complexes in

Australia underwent low-pressure anatexis, but the heat source remains unresolved (Cooma: Johnson 1999; Richards and Collins 2002) or unidentified (Glenelg: Gray et al. 2002). In the Chain Lakes massif of the Maine Appalachians, anatexis occurred without voluminous plutonism, leading Gerbi et al. (in review-a) to conclude that the massif was displaced from its heat source following metamorphism. By placing tighter kinematic constraints on the general causes of low-pressure anatexis, we limit the possible mechanisms relied upon in field investigations to explain anatectic terrains. Determining geodynamic settings for anatexis is particularly relevant, given the recent progress in relating crustal rheology to the presence of melt (Rutter 1997; Renner et al. 2000; Brown 2001; Takeda and Obata 2003).

4.3 Numerical model

4.3.1 Background

We designed a one-dimensional numerical model to evaluate the relationship among deformation, lithospheric mantle removal, sedimentation or erosion, and the thermal structure of the crust. One-dimensional models necessarily simplify the structure of the lithosphere, but they also provide information about fundamental processes that may be obscured by two-dimensional complexities. One-dimensional models are not appropriate when investigating the effects of magma transport (Hanson and Barton 1989; De Yoreo et al. 1991; Pedersen et al. 1998; Ryan and Soper 2001) or inclined shear zones (Buck et al. 1988; Sandiford and Powell 1991; Escuder Virute 1999), but they are appropriate for studying homogeneous deformation. The model we constructed follows the same principles employed by others (Loosveld and Etheridge 1990; Sandiford and

Hand 1998a; Bodorkos et al. 2002), and we include it here to allow direct comparison of different heat transfer mechanisms.

One-dimensional models do not allow for lateral variation in lithospheric or crustal structure, as is commonly found in collisional and extensional settings. In an extensional setting, for example, necking of the lithospheric mantle would allow upwelling asthenosphere to approach the base of the crust across a narrow zone. Although such a geometry cannot be modeled in one dimension, the center of the necking zone can be represented in one dimension by ignoring lateral heat transfer. Clearly in such a region lateral heat transfer may be important, but heat flow will be away from the hotter, central portion of the model. As a result, the one-dimensional model represents the most conservative approach to determining the thermal structure of the crust. For example, Bodorkos et al. (2002) examined the two-dimensional relationship between heating and the width of a mantle anomaly and quantitatively demonstrated that the narrower the anomaly, the cooler all parts of the crust are.

4.3.2 One-dimensional transient model

Geometrically, this model consists of continental crust and lithospheric mantle underlain by asthenosphere (Fig. 4.2). Each layer has uniform properties, is 100 km in the x-direction (parallel to extension or contraction) and infinite in the y-direction . The vertical extent of the model, z, varies. The upper boundary of the model represents Earth's surface and had a fixed temperature of 0°C. The lower boundary of the model is the lithosphere-asthenosphere boundary, assigned a constant temperature of 1400°C. Parameters include layer thickness, density, crustal heat production, heat capacity, thermal conductivity, and asthenosphere temperature (Tables 4.1 and 4.2). We began

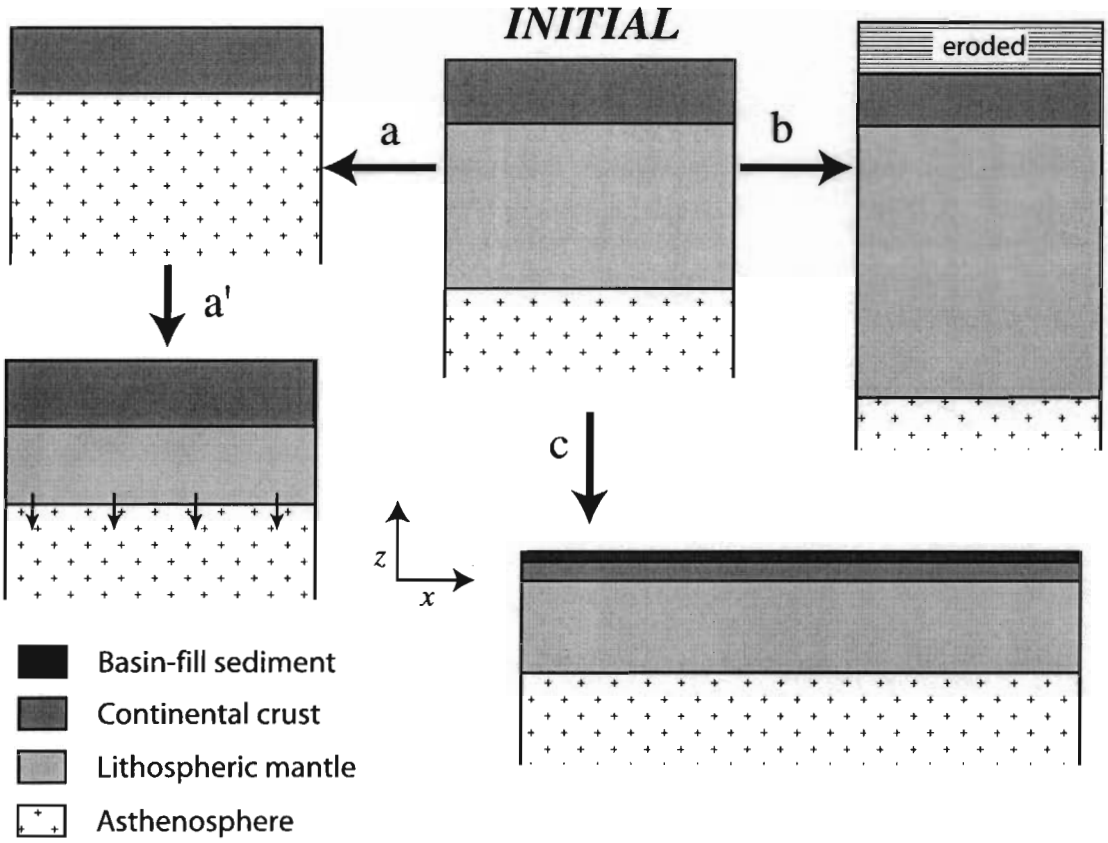

Figure 4.2 End-member geometries of one-dimensional numerical model. (a) Without deforming the crust, the lithospheric mantle is removed and replaced by constant-temperature asthenosphere. Additional parameters include erosion, whereby the crust may erode to maintain isostatic balance with the initial conditions, and when the lithospheric mantle begins to reform by conductive cooling (a'). No mechanism for removal of the lithospheric mantle is implied. (b) The initial two-layer lithosphere contracts horizontally at a prescribed rate and thickens vertically. The extent of erosion is a parameter in the model. (c) The initial lithosphere extends and thins at a prescribed rate. The degree of sedimentation is a model parameter. Variations (b) and (c) may be coupled with removal of the lithospheric mantle.

Table 4.1 Model parameters

Parameters and variables	Symbol and units	Units	Value or Range
Temperature	T	°C	n.a.
Depth (positive upwards)	z	m	n.a.
Basal heat flow	Q_d	W m^{-2}	n.a.
Heat production	A	W m^{-3}	2 10^{-6} to 4 10^{-6}
Thermal conductivity	k	W m^{-1} °C^{-1}	2.5
Crustal thickness	d_c	m	25,000 to 35,000
Lithospheric mantle thickness	d_m	m	120,000
Crustal density	ρ_c	kg m^{-3}	2800
Lithospheric mantle density	ρ_m	kg m^{-3}	3400
Asthenosphere density	ρ_a	kg m^{-3}	3300
Basin sediment density	ρ_s	kg m^{-3}	2300
Sedimentation or erosion factor	γ	--	0 to 1
Heat capacity	C_p	J kg^{-1}°C^{-1}	1000
Asthenosphere temperature	T_d	°C	1400
Maximum erosion rate	$\overline{v}$	m y^{-1}	0.001
Block edge velocity (extension positive)		m y^{-1}	-0.002 to 0.05

Table 4.2 Varied parameters for model runs discussed in text

	Standard geotherm		Geotherm with high heat production	Removal of lithospheric mantle without erosion		Removal of lithospheric mantle with erosion		Removal of lithospheric mantle with reformation commencing after 1 Ma		Crustal thickening with erosion	
Figure	1	1	3	4	4	4	4	4	4	5	5
Prescribed											
Crustal thickness (m)	25000	35000	35000	25000	35000	25000	35000	25000	35000	25000	35000
A ($\mu W\ m^{-3}$)	2	2	4	2	2	2	2	2	2	2	2
Edge velocity ($m\ y^{-1}$)	na	na	na	0	0	0	0	0	0	-0.002	-0.002
γ	na	na	na	0	0	1	1	0	0	1	1
Max. erosion rate ($mm\ yr^{-1}$)	na	na	na	na	na	0.1	0.1	na	na	0.1	0.1
Time to reformation of the lithospheric mantle (Ma)	na	na	na	na	na	na	na	1	1	na	na
Calculated											
Final time (Ma)	na	na	na	5.9	11.8	5.9	7.4	11.8	11.8	14.8	14.8
Sediment thickness or (amount eroded) (m)	na	na	na	0	0	(5906)	(7383)	0	0	(2515)	(7546)
Initial Q_d ($W\ m^{-2}$)	0.024	0.019	0.009	0.024	0.019	0.024	0.019	0.024	0.019	0.024	0.019
Final Q_d ($W\ m^{-2}$)	na	na	na	0.096	0.074	0.143	0.125	0.054	0.042	0.019	0.019
Final crustal thickness (m)	na	na	na	25000	35000	19094	27618	25000	35000	32966	42127

Table 4.2, continued

	Crustal thickening without erosion		Crustal thickening with erosion and removal of lithospheric mantle		Crustal thickening without erosion and with removal of lithospheric mantle		Crustal thickening with removal of lithospheric mantle and reformation after 1 Ma		Crustal thinning with deposition	
Figure	5	5	5	5	5	5	5	5	6	6
Prescribed										
Crustal thickness (m)	25000	35000	25000	35000	25000	35000	25000	35000	25000	35000
A ($\mu W\ m^{-3}$)	2	2	2	2	2	2	2	2	2	2
Edge velocity ($m\ y^{-1}$)	-0.002	-0.002	-0.002	-0.002	-0.002	-0.002	-0.002	-0.002	0.05	0.05
γ	0	0	1	1	0	0	0	0	1	1
Max. erosion rate ($mm\ yr^{-1}$)	na	na	0.1	0.1	na	na	na	na	0.1	0.1
Time to reformation of the lithospheric mantle (Ma)	na	na	na	na	na	na	1	1	na	na
Calculated										
Final time (Ma)	14.8	14.8	5.9	8.9	3.0	5.9	7.4	14.8	5.9	3.0
Sediment thickness or (amount eroded) (m)	0	0	5906	(8860)	0	0	0	0	2241	2954
Initial Q_d ($W\ m^{-2}$)	0.024	0.019	0.024	0.019	0.024	0.019	0.024	0.019	0.024	0.019
Final Q_d ($W\ m^{-2}$)	0.017	0.013	0.136	0.108	0.120	0.083	0.056	0.025	0.091	0.036
Final crustal thickness (m)	35481	49674	22444	33680	26570	53579	29332	49674	8564	17084

Table 4.2, continued

	Crustal thinning without erosion or deposition		Crustal thinning without erosion and with removal of lithospheric mantle		Crustal thinning with erosion and removal of lithospheric mantle		Crustal thinning with removal of lithospheric mantle and reformation after 1 Ma	
Figure	6	6	6	6	6	6	6	6
Prescribed								
Crustal thickness (m)	25000	35000	25000	35000	25000	35000	35000	25000
A ($\mu W\ m^{-3}$)	2	2	2	2	2	2	2	2
Edge velocity ($m\ y^{-1}$)	0.05	0.05	0.05	0.05	0.05	0.05	0.05	0.05
γ	0	0	0	0	1	1	0	0
Max. erosion rate ($mm\ yr^{-1}$)	na	na	na	na	0.1	0.1	na	na
Time to reformation of the lithospheric mantle (Ma)	na	na	na	na	na	na	1	1
Calculated								
Final time (Ma)	5.9	3.0	5.9	3.0	3.0	3.0	3.0	3.0
Sediment thickness or (amount eroded) (m)	0	0	0	0	(2952)	(2952)	0	0
Initial Q_d ($W\ m^{-2}$)	0.024	0.019	0.024	0.019	0.024	0.019	0.019	0.024
Final Q_d ($W\ m^{-2}$)	0.100	0.047	0.149	0.189	0.181	0.237	0.109	0.141
Final crustal thickness (m)	6323	14130	6323	14130	7141	11178	14130	10093

each model run by calculating an equilibrium geotherm for the assigned geometry using Equations (4.1) and (4.2), modified from (Fowler 1990). The temperature profile of the crust follows the rule:

$$T = -\frac{A}{2k}z^2 - \frac{Q_d + Ad_c}{k}z \tag{4.1}$$

And the lithospheric mantle temperature is:

$$T = -\frac{Q_d}{k}z + \frac{Ad_c^{\,2}}{2k} \tag{4.2}$$

where T is temperature, A is heat production, k is thermal conductivity, z is depth, Q_d is the heat flux from the asthenosphere, and d_c is crustal thickness. Depth (z) is positive upwards and T=0°C at z=0.

We apply constant horizontal velocities to the edge of the block (Fig. 4.2), with the mantle and crustal velocities being independent. Interior horizontal and vertical velocities are calculated to maintain a constant area within each layer, and deformation within each layer is homogeneous. Upon extension or contraction, the model may accept sediment or erode to maintain isostatic balance with the initial geometry. At each timestep, we calculate the temperature at 32 nodes initially evenly spaced throughout the lithosphere. The initial temperature at each node is taken as the value of the stable geotherm at that point, and at each timestep, the temperature changes according to the solution of:

$$\frac{\partial T}{\partial t} = \frac{k}{\rho_c C_p}\frac{d^2T}{dz^2} - \bar{v}\frac{dT}{dz} + \frac{A}{\rho_c C_p} \tag{4.3}$$

where ρ is density, C_p is heat capacity, t is time, and $\bar{v}$ is erosion or sedimentation rate (e.g., Stuwe 2002). Because we employ a Lagrangian reference frame, the advective term of the heat flow equation relates to exhumation or burial rather than to the absolute particle velocity. We can approximate the change in temperature with time for any given rock particle by:

$$\Delta T = \left(\frac{k}{\rho_c C_p}\frac{d^2T}{dz^2} - \bar{v}\frac{dT}{dz} + \frac{A}{\rho_c C_p} \right)\Delta t \tag{4.4}$$

for sufficiently small time steps. We approximate the spatial derivatives using central differences except at the boundaries, where we use forward or reverse differences as appropriate.

Some studies fix the heat flux from the mantle (e.g., England and Thompson 1984), but we chose instead to prescribe a constant temperature to the mantle during each model run. With a constant asthenosphere temperature, the heat flux through the lithosphere-asthenosphere boundary varies as the lithosphere thickens or thins. The mantle heat flux, Q_d, used in calculating the initial geotherm, is the flux required to achieve the assigned asthenospheric temperature, T_d,at the base of the lithosphere:

$$Q_d = k\frac{\frac{Ad_c^{\,2}}{2k} - T_d}{d_m + d_c} \tag{4.5}$$

where d_m is the initial thickness of the lithospheric mantle.

The extent of sedimentation or erosion in the lithospheric column follows the rule:

$$d_s = \gamma\frac{(\rho_c - \rho_a)\left(d_c - \frac{d_c}{\beta_c}\right) + (\rho_m - \rho_a)\left(d_m - \frac{d_m}{\beta_m}\right)}{(\rho_s - \rho_a)} \tag{4.6}$$

where ρ_m is lithospheric mantle density, ρ_a is asthenospheric density, ρ_c is crustal density, and γ is a prescribed constant. The value of γ indicates the fraction of sedimentation or erosion modeled compared with that needed to maintain isostatic balance: a value of zero indicates no deposition or erosion, whereas a value of unity produces complete isostatic compensation relative to the original geometry. We can also prescribe a maximum erosion rate.

We considered heat production to be uniform throughout the crust and absent in the mantle. Different distributions of heat production would certainly affect the temperature profiles (Chamberlain and Sonder 1990; Sandiford and Hand 1998a), but such variability is outside the scope of this contribution. Thermal conductivity is assumed constant throughout the lithosphere. In detail this is not the case (Clauser and Huenges 1995), but the average conductivity probably does not vary greatly from the values we use. For similar reasons, density is assumed constant for each compositional zone. We chose not to include the latent heat of fusion or thermal expansion. Although it

plays a vital role in buffering the maximum temperatures achieved, the latent heat of fusion is lithology-dependent and therefore introduces uncertainty that may obscure the fundamental concepts we wish to investigate. Moreover, we are interested in determining factors that lead to fusion, rather than the thermal evolution following fusion. We do not use the coefficient of thermal expansion in our calculation. Including thermal expansion affects the total subsidence (McKenzie 1978), but other calculations we conducted indicate that the temperature at a given depth is only minimally affected.

To simulate the effects of lithospheric delamination, we varied the model as follows: without stretching the crust, we instantaneously change the temperature of the asthenosphere to T_d, simulating separation of the lithosphere from the crust. At any time following the detachment event, we can allow the lithosphere to conductively cool and thicken.

4.4 Evaluation of possible driving mechanisms

Geotherms that reach the andalusite field are not realized in undeforming, cratonic lithosphere (Fig. 4.1). Therefore, perturbation is necessary to produce low-pressure metamorphism, let alone low-pressure anatexis. These perturbations may be combinations of advection, heat production, and conduction, with advection comprising the three subtypes of magma, rock, and fluid movement. In the following sections, we evaluate whether these heat transfer mechanisms are sufficient to cause low-pressure anatexis.

Our modeling results bear on the effects of removal of the lithospheric mantle, homogeneous crustal thickening, and homogeneous crustal thinning. As our results verify and extend the work of others with regard to the possiblility that any of these heat

transfer mechanisms can cause low-pressure anatexis, we integrate the discussion of the numerical modeling results with the overall evaluation of the driving mechanisms (Sections 4.4.4 to 4.4.6).

4.4.1 Magmatic advection

Magma advects heat as it rises through cooler rock. At its site of emplacement, the cooling magma transfers heat to the surrounding crust by conduction or hydrothermal convection. In numerous sites worldwide, such magmatic activity has heated host rocks through the andalusite and into the sillimanite fields, locally causing anatexis. Such heating is isobaric or nearly so (e.g. 1991), owing to the rapid rate of conduction relative to regional deformation. In several orogens, including the Sierra Nevada (Barton and Hanson 1989) and Appalachians (Lux et al. 1986), voluminous plutonism accompanied low-pressure metamorphism of regional extent. For areas where plutons make up more than 50% of the exposure, magmatically advected heat can explain regional low-pressure metamorphism into the sillimanite field (Barton and Hanson 1989; Hanson and Barton 1989) because the heat brought into the crust serves both to raise the background temperature of the surrounding area and cause localized prograde metamorphism (De Yoreo et al. 1991). Nevertheless, even for such high plutonic volume, the host rocks between the plutons do not warm enough to melt or, with some geometries, even to enter the sillimanite field from the andalusite field (see figs. 7 and 11 of Hanson and Barton 1989). For lesser plutonic volumes, regional contact aureoles cannot be fully explained by heat from magmatic advection because anatexis is restricted to the immediate pluton vicinity. So although heat transferred to the middle and upper crust by rising magma can produce low-pressure metamorphic conditions and localized low-pressure anatexis,

magmatic advection in the form of plutons does not appear to be sufficient to generate widespread low-pressure anatexis. Recognizing this, Miyazaki (2004) proposed that pervasive flow of melt, producing migmatites, could raise the temperature of a region to conditions suitable for low-pressure metamorphism and low-pressure anatexis. Thermal modeling in support of this suggestion indicates that temperatures of 600-800°C at 15 km depth are attainable (Miyazaki 2004). In this case, if magmatic advection were the primary or sole cause of widespread low-pressure anatexis, the anatectic region should comprise extensive injected magma as well as anatectic magma.

4.4.2 Fluid advection

In some environments, circulating fluid drives advective heat transfer. On the continents, one of the best documented examples is the Taupo Volcanic Zone in New Zealand (Bibby et al. 1995). There, convection cells up to 8 km deep assist in producing a surface heat flow of 0.7 Wm^{-2}. The temperature at 15 km depth, interpreted to be the base of the crust, could be over 1000°C (Bibby et al. 1995). Although the present environment is quite conducive to large-scale heat transfer by fluids, the development and maintenance of the hydrothermal convection cell required an initial temperature gradient of approximately the present value. So, rather than initiating a thermal perturbation, advective fluid flow can only enhance an already-anomalous thermal pattern. Moreover, although the fluids certainly assist in the heat transfer from the mantle to the crust, the base of the convecting cell in Taupo is too cool (350°C) for melting to occur there. Any melting must necessarily occur in the non-convective region below 8 km.

4.4.3 Heat production

Independent of advection, unusually high heat production in the crust can generate low-pressure metamorphism (Chamberlain and Sonder 1990; Sandiford and Hand 1998a; Sandiford et al. 1998). As with a magmatic advection heat source, a layer of high heat production should leave evidence in the geologic record. If, for example, 25 km thick crust within a 120 km thick lithosphere were to produce heat on the order of 4 μWm^{-3} , the geotherm would pass through the andalusite field, and the base of the crust would be approximately 780°C (Fig. 4.3). Although these conditions would generate a metamorphic field gradient indicative of a high geothermal gradient, high heat production would not, on its own, drive low-pressure anatexis. Thickening of a high heat-producing crust may produce pressure-temperature paths that pass from the andalusite field across the pelite melting reaction, but in doing so, the base of the crust would heat to well over 1000°C (cf. Sandiford and Hand 1998a).

Recognizing the unrealistic nature of the whole crust having high heat production and the attendant geologic complications, Sandiford et al. (1998) showed that rapid burial of a layer of high heat-producing sediments can have a first-order effect on the temperature profile of the crust. For example, crust at 15 km depth may heat to approximately 600°C with a layer of high heat production and a thick (250 km) lithosphere. This geometry appears to explain the heat flow and metamorphic patterns observed in the Mt. Painter region of the Australian Flinders Ranges. Sandiford et al. (1998) did not address low-pressure anatexis directly, but their model results did not generate conditions appropriate for low-pressure anatexis. Nevertheless, based on this work, Goscombe and Hand (2000) hypothesized that anatexis in the Greater Himalayan

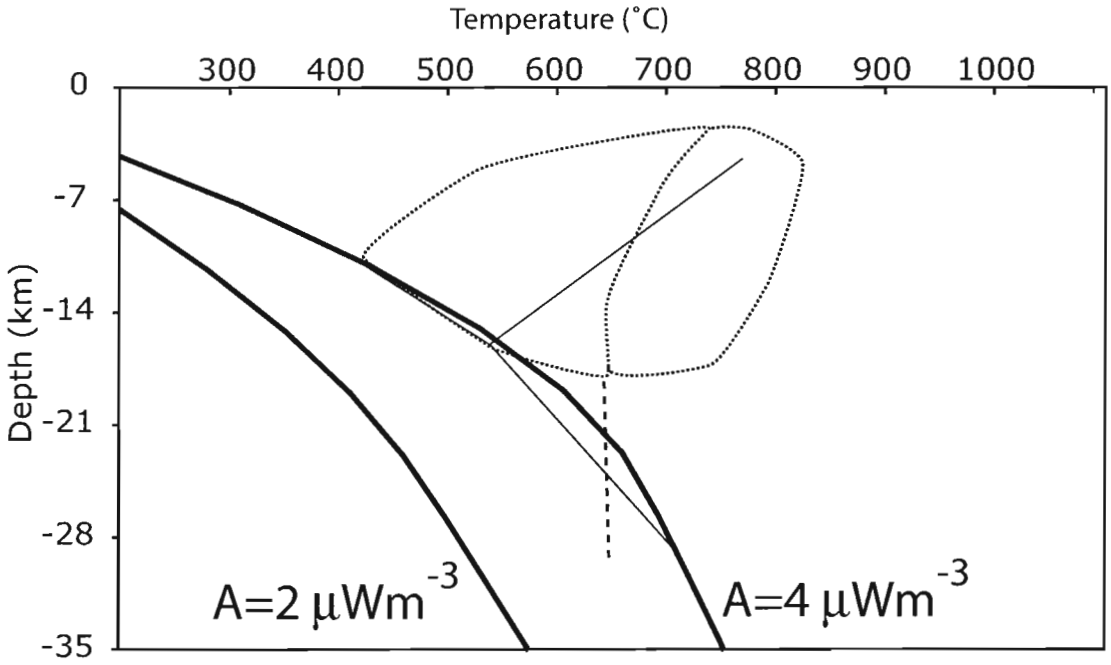

Figure 4.3 Effect of high heat production on stable geotherm. Heat production is uniformly distributed and crust is 25 km thick crust. Different distributions of heat-producing elements would yield different temperature distributions (labeled solid lines), but would not, on their own, produce low-pressure anatexis. Symbols and fields as in Figure 4.1.

Sequence of Eastern Nepal may be due to high heat production. In Eastern Nepal, the high heat-producing rocks are leucogranites. Goscombe and Hand (2000) indicate that heat from the melt itself was not sufficient to generate the anatexis, but the long term cumulative effect of the U- and K-rich leucogranites may been more substantial. The suggestion that a high heat producing layer can cause anatexis has not yet been demonstrated quantitatively.

4.4.4 Lithospheric mantle removal

During or following crustal thinning or thickening, the lithospheric mantle may become unstable. The primary mechanisms proposed for replacement of part or all of the lithospheric mantle with asthenosphere are convective thinning (Houseman et al. 1981; Molnar et al. 1998) and delamination between the crust and the mantle (Bird 1979; Schott and Schmeling 1998). Herein, we do not consider the causes or likelihood of such an event; rather, we are concerned with the consequences. In this section, we discuss crust-mantle delamination operating alone, and in subsequent sections we discuss delamination accompanying crustal thinning and thickening.

The initial consequence of the asthenosphere rising to or near the base of the crust is a dramatic heating of the lower crust. Bodorkos et al. (2002) investigated the thermal consequences of complete lithospheric mantle removal without surface erosion, and concluded that conditions for low-pressure metamorphism (550-600°C at 17 km) may develop within 35 km-thick crust if the asthenosphere remains at the base of the crust. Our modeling produced similar results. The thermal anomaly propagates upwards to the middle and upper crust, generating low-pressure metamorphism but not anatectic conditions at pressures less than that of the aluminosilicate triple point in 35 km thick

crust (Fig. 4.4). The shorter length scale in 25 km-thick crust allows anatectic conditions to develop at 10 km and below (Fig. 4.4), but for this to occur, the base of the crust must remain hotter than 1000°C for several million years.

Bodorkos et al. (2002) did not incorporate erosion due to isostatic uplift; our calculations indicate that erosion can have a significant effect on the pressure-temperature paths of rocks originating in the middle to upper crust. Although we considered mantle delamination to occur instantaneously, we set a maximum erosion rate of 1 mm yr^{-1}. We justify the simplification of instantaneous delamination because it represents the maximum possible heating effect on the crust; slower delamination would produce only cooler conditions in the crust. With the erosion constraint, exhumation in the upper crust dominates, producing nearly isothermal decompression (Fig. 4.4). As the middle crustal rocks approach the surface, they cool. The warming effects of the shallow asthenosphere are limited to the base of the crust if uplift and erosion accompanies removal of most or all of the lithospheric mantle. Incorporating erosion into the model for 25 km thick crust allows the middle crust to develop conditions appropriate for low-pressure anatexis, but only over an unrealistically hot lower crust (Fig. 4.4).

The above discussion is predicated on asthenosphere remaining near the base of the crust throughout the experiment. If cooling and reformation of the lithospheric mantle commences immediately following its removal, conditions suitable for low-pressure anatexis do not develop. For both 25 and 35 km thick crust, the asthenospheric heat source decays too rapidly to infuse sufficient heat into the crust to generate melt, even low-pressure metamorphism occurs (Fig. 4.4).

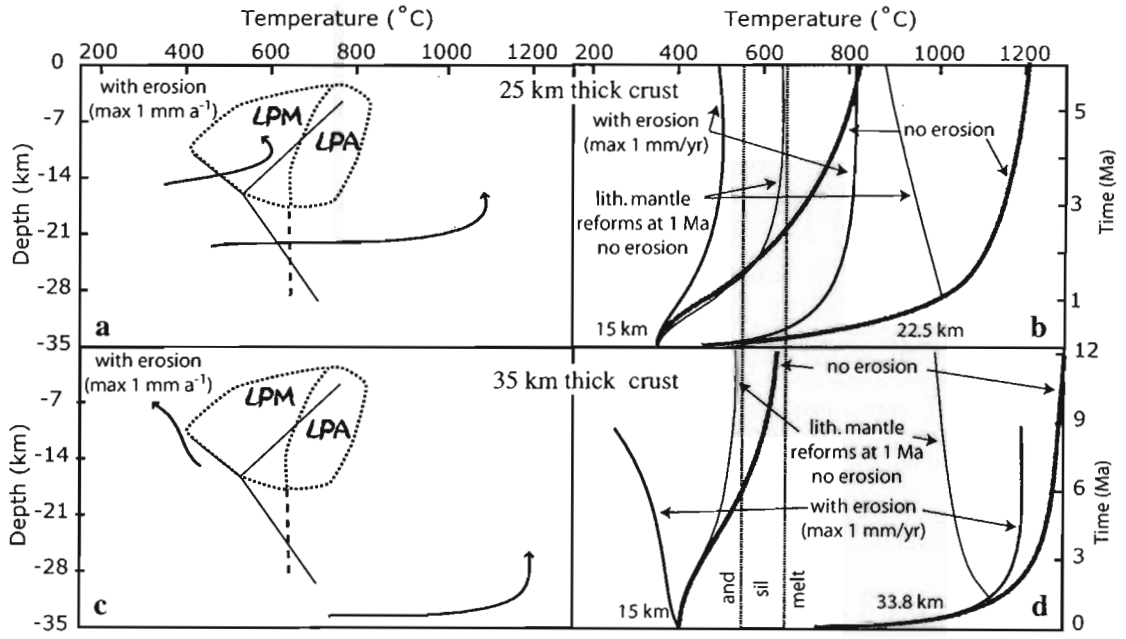

Figure 4.4 Effects of removing the lithospheric mantle. Temperature-time and temperature-depth paths for rocks starting at 15 km depth and near the base of the crust following removal of the lithospheric mantle. (a) and (c) Temperature-depth paths incorporating erosion up to 1 mm a^{-1}. Fields as in Fig. 4.1. (b) and (d) Temperature-time paths at depths of 15 km and near the base of the crust following removal of the lithospheric mantle. Labels indicate which paths represent results with and without erosion and with and without reformation of the lithospheric mantle. Vertical lines mark the sillimanite stability field at 15 km depth. See Table 4.2 for model parameters.

4.4.5 Crustal thickening

Convergent orogens are well-known sites of metamorphism and crustal melting (e.g., England and Thompson 1986; Jamieson et al. 1998). Homogeneous thickening of the lithosphere results in downward bowing of isotherms in the crust, and heating of individual rocks (Fig. 4.5, curves E and N; England and Thompson, 1984). The trajectories of crustal pressure-temperature paths (i.e., $\frac{dP}{dT}$) depend on the relative rates of thickening and conduction: faster thickening, and hence higher vertical velocities, produces steeper pressure-temperature paths; slower thickening and slower vertical velocities produce shallower paths. Thompson (1989) proposed that slow thickening of thinned lithosphere may have produced the conditions for low-pressure metamorphism in the Slave Province, Canada. However, his model is not universally applicable due to the long timescales involved (on the order of 80 Ma). Nevertheless, because of the nearly isobaric heating required for pressure-temperature paths that pass from the andalusite field to the muscovite breakdown reaction, crustal thickening must occur slowly if low-pressure anatexis is to develop. After quantitatively exploring this relationship, Loosveld (1989) and Sandiford and Powell (1991) concluded that homogeneous lithospheric thickening alone is insufficient to generate rock trajectories suitable for even low-pressure metamorphism. Moreover, rather than heating, rocks in the upper levels of the crust may cool with homogeneous lithospheric thickening if we incorporate syn-thickening erosion in the model. The exact locus of rocks neither heating nor cooling depends on the relative density and thicknesses of the crust and lithospheric mantle.

Although low-pressure metamorphism cannot occur solely due to homogeneous lithospheric thickening, it may accompany crustal thickening if the lithospheric mantle

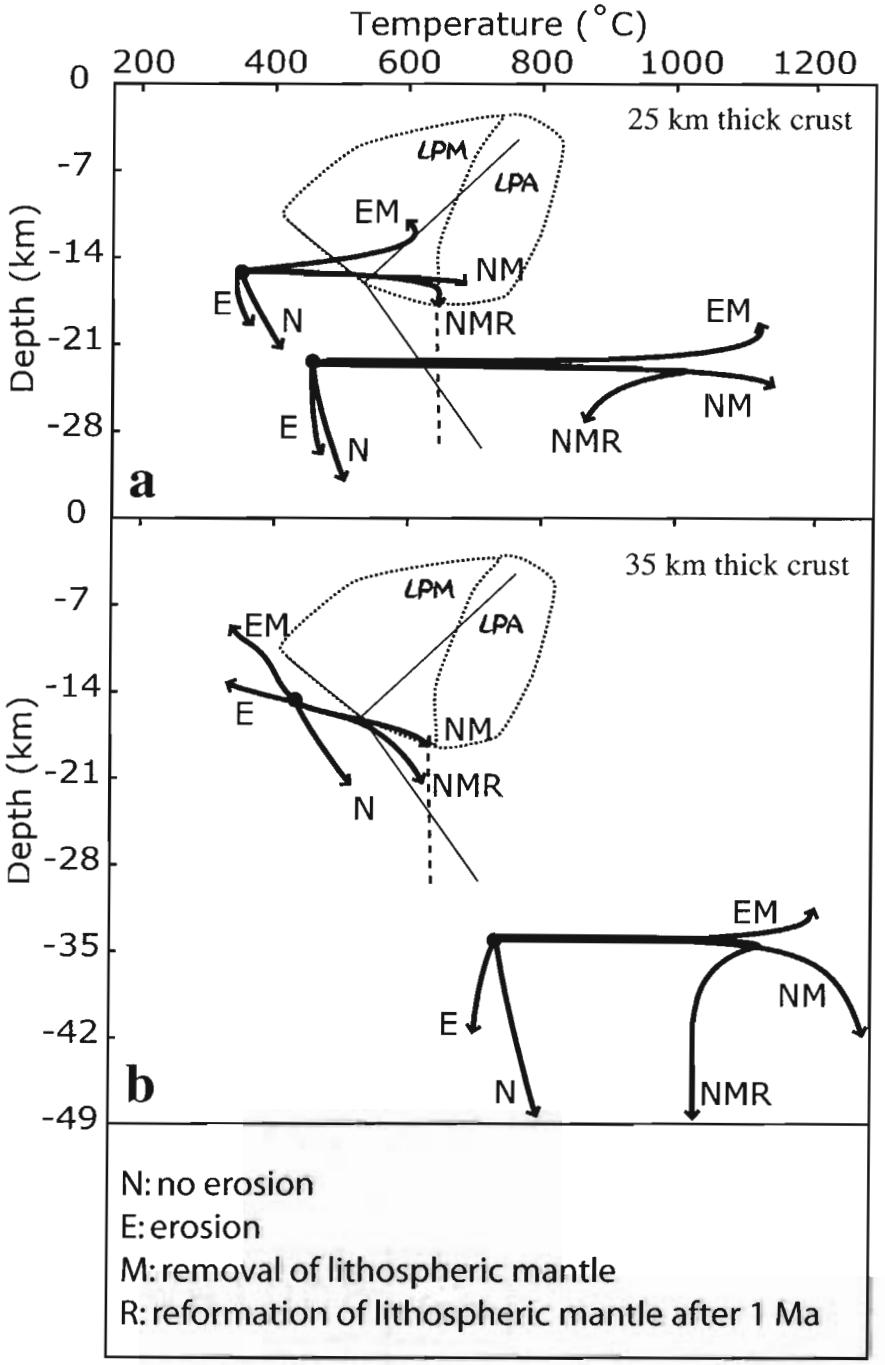

Figure 4.5 Effects of crustal thickening. Temperature-depth paths resulting from model runs for crust initially (a) 25 km and (b) 35 km thick. Varied parameters are listed by letter; three runs include removal of lithospheric mantle. In (a), paths are shown for rocks starting at 15 km and 22.5 km depth; in (b), paths shown for rocks starting at 15 km, and 33.8 km depth. Other symbols as in Figure 4.1. See Table 4.2 for complete parameters.

thins substantially or is removed (Loosveld 1989; Sandiford and Powell 1991). Thermal modeling by Loosveld (1989) and Loosveld and Etheridge (1990) suggests that peak temperatures during slow crustal thickening and removal of the lithospheric mantle may reach 550°C at the depth of the aluminosilicate triple point. Subsequently, Sandiford and Powell (1991) predicted temperatures up to 700°C at approximately 20 km depth during thickening of 35 km thick crust if no lithospheric mantle is present; they predict cooler temperatures the slower the lithospheric mantle thins. Our calculations support the above conclusions: without accounting for erosion, rocks at all levels of thickening crust over a thinned mantle lithosphere will warm (Fig. 4.5, curve NM). Incorporating even minimal erosion (max of 1 mm/yr) at a shortening rate of –0.002 my^{-1}, the loss of the mass of the dense lithospheric slab overcomes burial due to shortening, so rocks are exhumed while warming (Fig. 4.5, curve EM). Low-pressure metamorphism conditions may develop in 35 km thick crust. With 25 km thick crust, some mid-crustal rocks may melt after passing through the andalusite field, but the lower crust is heated to over 1100°C (Fig. 4.5, curve NM).

In search of causes of low-pressure metamorphism that do not require removal of the lithospheric mantle, Huerta et al. (1998; 1999) proposed that much low-pressure metamorphism in collisional orogens may be a product of accretion of heat-producing material. Based on a lithosphere-scale thermal model, Huerta et al. (1998) calculated that temperatures >700°C could occur at 20 km depth in the crust if the heat-producing wedge were >50 km thick and heat production were >2.5 $\mu W/m^3$. As in the cases of lithospheric delamination described above, the thermal model of Huerta et al. (1998) produces low-

pressure metamorphism, but not low-pressure anatexis. In fact, pressure-temperature paths based on this model do not even transect the andalusite field (Huerta et al. 1999).

In summary, low-pressure anatexis does not appear possible during lithospheric thickening without additional heat sources such as advected magma. Although individual rocks heat, no thermal models produce pressure-temperature paths that sequentially cross the andalusite-sillimanite and melting reactions. Thermal models of crustal thickening accompanied by lithospheric thinning can generate low-pressure metamorphism, but even these models do not predict sufficiently high temperatures in the middle to upper crust to generate melt.

4.4.6 Crustal thinning

In much of the crust, conduction is the dominant heat transfer mechanism, carrying heat from the convecting asthenosphere to the surface. Crustal thinning reduces the length scale of conductive heat transfer and allows high basal heat flow to more quickly influence middle to upper crustal temperatures. With that in mind, lithospheric thinning accompanying crustal thinning has long been considered a driving force for low-pressure metamorphism and possibly low-pressure anatexis. Wickham and Oxburgh (1985; 1987), based on their work in the Trois Signieurs massif in the Pyrenees, concluded that shallow asthenosphere was a major component driving metamorphism there. Other studies in Scotland (Ryan and Soper 2001), Norway (Pedersen et al. 1998), Antarctica (Smith 1997), and Spain (Cesare and Gomez-Pugnaire 2001), ascribed the observed metamorphic grade in large part to high heat flow from the mantle brought on by lithospheric thinning.

Homogeneous thinning of the lithosphere universally produces cooling paths in the crust if deposition does not occur (Fig. 4.6, curve N). If the basin produced by subsidence accompanying extension (cf. McKenzie 1978) fills with sediment, most of the crust cools, but the uppermost crust warms – it is in effect insulated by the sediment (fig. 1 of Sandiford et al., 1998). Reasonable variations in any of the parameters in our calculations, including crustal thickness, lithopheric thickness, and strain rate, do not result in heating even into the andalusite field. As in the case of crustal thickening, low-pressure metamorphism can develop only if the lithosphere thins inhomogeneously, with the lithospheric mantle thinning much more than the crust (Loosveld 1989; De Yoreo et al. 1991). Conditions for low-pressure anatexis are of course even more restrictive. Unlike homogeneous lithospheric thinning, during inhomogeneous thinning, when the lithospheric mantle thins more rapidly than the crust, parts of the crust can warm. Taken to its extreme, heterogeneous thinning would result in the lithospheric mantle being replaced by asthenosphere.

As discussed above, removal of lithospheric mantle on its own can generate low-pressure metamorphism, but low-pressure anatexis appears unattainable without also inducing wholesale melting of the lower crust. Here we describe quantitative results from combining lithospheric mantle removal and crustal thinning. With no erosion, an original crustal thickness of 25 km, lithospheric thickness of 120 km, and an extension rate of 0.05 m/y, rocks in the thinning crust rise from 15 km to 6 km while heating from 354°C to 778°C over the course of 3.5 Ma (Fig. 4.6). Conditions such as these can induce low-pressure anatexis, but this anatexis would be accompanied by extensive melting in the lower crust (which warms to nearly 1200°C). If the crust begins 35 km thick, rocks

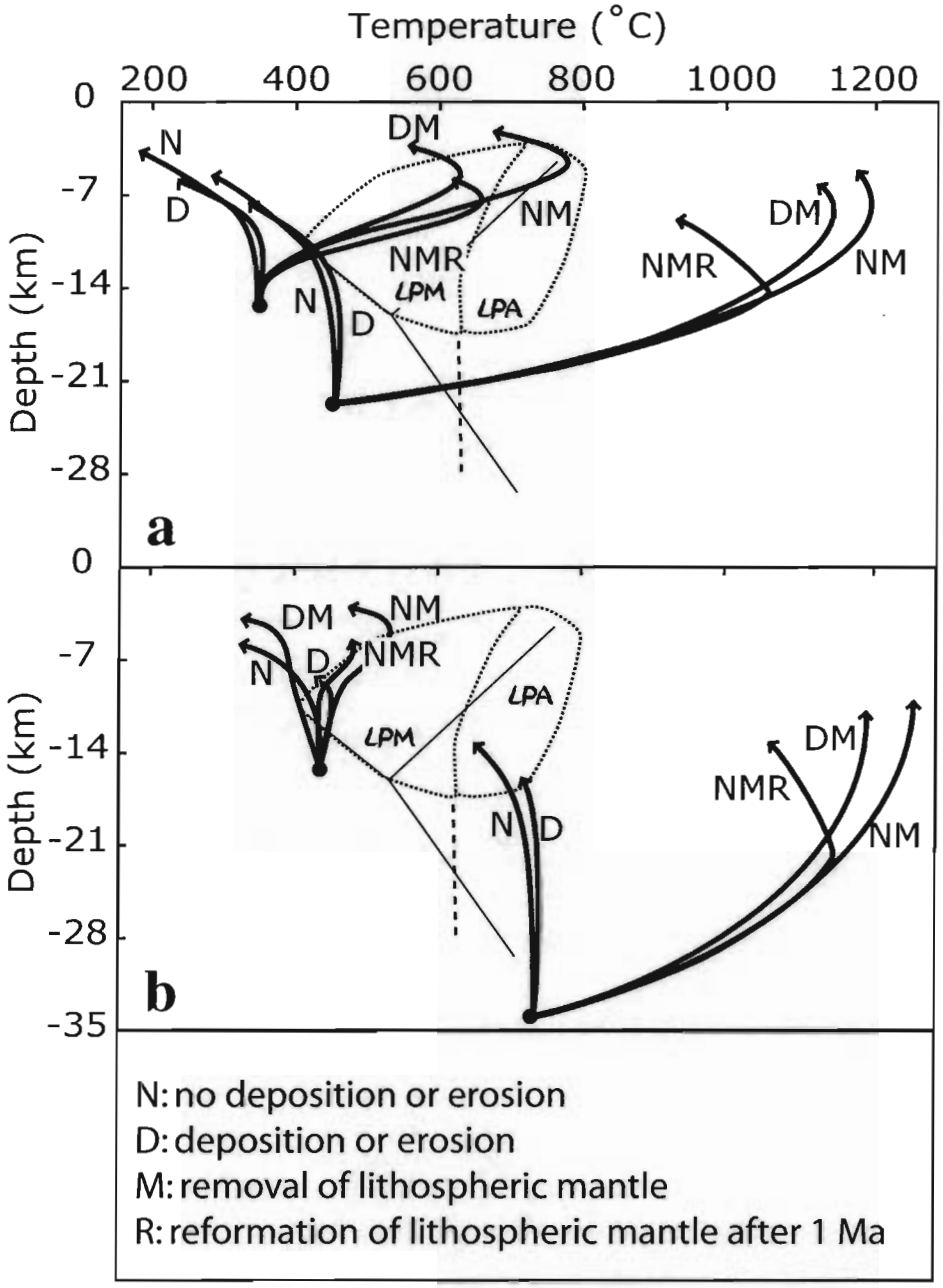

Figure 4.6 Effects of crustal thinning. Temperature-depth paths resulting from crustal thinning model runs for crust initially (a) 25 km and (b) 35 km thick. Varied parameters are listed by letter. In (a), paths are shown for rocks starting at 15 km and 22.5 km depth; in (b), paths shown for rocks starting at 15 km and 33.8 km depth. Other symbols as in Figure 4.1. See Table 4.2 for complete parameters.

starting at 15 km depth may heat to 532°C (Fig. 4.6), enough to cause low-pressure metamorphism but not low-pressure anatexis. The lower temperature is a result of the longer length scale for conduction. Slower strain rates produce less decompression over time, but can allow more time for conduction before the crust becomes unreasonably thin. For example, extending 25 km-thick crust at a rate of 0.01 m/y produces maximum temperatures of 811°C, but again the lowermost crust should melt extensively. Without incorporating erosion, other combinations of stretching rates and initial conditions produce fundamentally the same results as above.

Including erosion results in somewhat different pressure-temperature paths. Rocks that began at 15 km depth within 25 km-thick crust extending 0.05 m/y over replaced lithospheric mantle and eroding up to 1 mm/y may warm to 702°C, roughly 75°C less than without erosion (Fig. 4.6). More significantly, the lower part of the crust achieves only a slightly lower maximum temperature, 1170°C (compared with 1185°C without erosion). Other experiments we ran, varying extension rate, crustal thickness, and erosion rate, yielded similar results. From this we conclude that incorporating erosion into our model of crustal thinning accompanied by replacement of the lithospheric mantle only serves to cool the upper crust, reducing the solution space for low-pressure anatexis to occur. Moreover, erosion does little to alleviate the problem of wholesale melt-inducing temperatures at the crust-mantle boundary.

Another kinematic scenario for inhomogeneous lithospheric thinning involves inhomogeneous thinning in the crust itself, in the form of a dipping shear zone or detachment fault (Wernicke 1985; Lister et al. 1986a). Extensional activity along this shear zone drops cooler upper crustal rocks onto warmer lower crustal rocks or even on

the mantle; the upper plate rocks then heat nearly isobarically. Escuder Virute (1999) modeled such a two-dimensional geometry, with extension occurring at approximately 25 km depth within 70 km thick crust, and concluded that for a shear zone dipping 45° and instantaneous extension, the upper plate could readily develop temperatures greater than 500°C. He showed that temperatures much greater than 600°C, however, were not possible in the upper plate. Zen (1995a) developed a one-dimensional model to evaluate total crustal melting during detachment-style extension, with detachment at between 22 and 32 km depth within 60 km thick crust. This one-dimensional conductive model neglects magma transport following fusion in the middle crust, a feature that may dramatically affect hanging wall temperatures. Overall, Zen (1995a) modeled higher basal heat flow and greater extension than did Escuder Virute (1999), which allowed the upper crust to drop onto warmer footwall crust and therefore allowed the hanging wall to heat more. For this mechanism to produce low-pressure anatexis, footwall temperatures must be sufficiently hot to warm the down-dropped hanging wall into the melting field. This would require either thickened crust, as modeled by Zen (1995a), or a juxtaposition of middle- to upper-crustal rocks against the upper mantle. Without thickened crust, temperatures at the base of the crust would likely not exceed 700-750°C. Zen's (1995a) model achieves a basal heat flux of 60 mW m^{-2} or greater, and even with that high basal heat flow, anatexis does not occur at depths shallower than 14 km. Anatexis at 14 km requires heat production of 2 to 3 μW m^{-3} throughout the crust, a basal heat flow up to 75 mW m^{-2}, and detachment level of 22 km depth. Four of the five models run by Zen (1995a) that produce anatexis at 14 km depth require more than 30 Ma for rocks to undergo prograde metamorphism from the andalusite field to the sillimanite field and

continue on to cross the muscovite dehydration melting reaction. Although the solution space is limited, Zen's (1995a) model does quantitatively predict that low-pressure anatexis is possible along a crustal-scale detachment fault. A shallower level of detachment or detachment faulting in normal thickness crust would produce warmer temperatures at shallower crustal levels and may more readily produce conditions for low-pressure anatexis; this geometry awaits testing.

4.5 Discussion

4.5.1 Solution space

For low-pressure anatexis to occur under geologically reasonable conditions, two primary criteria must be met: (1) during heating, the middle to upper crust must have low $\frac{dP}{dT}$, and (2) while the middle to upper crust heats to melting conditions, the lower crust must stay cool enough not to melt extensively. Qualitatively, the first criterion exists because the geotherm in a tectonically stable region (i.e., before orogenesis and consequent perturbation) lies outside the andalusite field. For a rock to heat through the andalusite field and cross melting reactions in pressure-temperature space, the slope must be sufficiently shallow to allow the rock to remain at a pressure lower than that of the aluminosilicate triple point (~4.5 kbar) as it heats past 550°C (triple point of Pattison 1992).

Conditions suitable for generating low-pressure metamorphism may develop by each of several proposed mechanisms: (1) magmatic advection (Lux et al. 1986; Hanson and Barton 1989; De Yoreo et al. 1991; Miyazaki 2004), (2) heat production (Chamberlain and Sonder 1990; Sandiford et al. 1998), (3) removal of the lithospheric

mantle (Loosveld 1989; Loosveld and Etheridge 1990; Sandiford and Powell 1991; Bodorkos et al. 2002), and (4) crustal extension a long detachment faults (Zen 1995a; Escuder Virute 1999). In the original studies, little or no discussion was devoted to whether low-pressure anatexis could develop as well. After evaluating each of those mechanisms, we conclude that five mechanisms could generate widespread low-pressure anatexis (Table 4.3): migration of melt by percolation, presence of a high-heat producing layer, crustal thickening or thinning accompanied by removal of the lithospheric mantle, and crustal extension along a major detachment fault. Of these, crustal thickening or thinning accompanied by removal of the lithospheric mantle may not be geologically reasonable due to the high temperatures attained in the lower crust. Moreover, replacement of the lithospheric mantle by upwelling asthenosphere should induce mantle melting at levels shallower than 40 km (McKenzie and Bickle 1988). The mantle melts could propagate upward and preheat the crust (Bodorkos et al. 2002). So although mathematically possible, crustal thickening or thinning accompanied by removal of the lithospheric mantle probably cannot produce low-pressure anatexis on its own.

Each of the three remaining mechanisms we consider as viable sole sources of low-pressure anatexis should leave different evidence in the rock record. Evidence for a high heat-producing layer could include high modern heat flow and/or exposed high heat-producing rocks (Goscombe and Hand 2000). If low-pressure anatexis was generated by detachment faulting, the anatectic rocks should lie within a few kilometers of a detachment zone. And if low-pressure anatexis was caused by percolative flow (Miyazaki 2004), both anatectic and injected magmas should be present.

Table 4.3 Summary of heat transfer mechanisms

Mechanism	Can cause low-pressure anatexis?	Notes	Reference
Plutonism	Locally	Widespread low-pressure metamorphism only if plutons constitute >50% of the exposure	Hanson and Barton (1989); DeYoreo et al. (1991)
Pervasive melt migration	Yes	Need sufficient flux; both injected and anatectic migmatitic material exposed	Miyazaki (2004)
Fluid advection	No		
High heat production	Possibly*	High surface heat flow, high heat-producing rocks exposed	Sandiford et al. (1998); Goscombe and Hand (2000)
Removal of lithospheric mantle alone	Yes	Crust must be less than 35 km thick Should also induce significant mantle and lower crustal melting	Bodorkos et al. (2002)
Crustal thickening	No		Loosveld (1989); Loosveld and Etheridge (1990); Sandiford and Powell (1991)
Crustal thickening and removal of lithospheric mantle	Yes	Should also induce significant mantle and lower crustal melting	Loosveld (1989); Loosveld and Etheridge (1990); Sandiford and Powell (1991)
Crustal thinning (homogeneous)	No		
Crustal thinning (homogeneous) and removal of lithospheric mantle	Yes	Should also induce significant mantle and lower crustal melting	This paper
Crustal thinning along major dipping shear zone	Yes	Successfully modeled for thick crust	Zen (1995); Escuder Virute (1999)

*Qualitative extrapolation of the thermal models done to date suggest this possibility, but quantitative determination has yet to be performed.

4.5.2 Multiple mechanisms

As in most Earth systems, multiple processes operate simultaneously and affect tectonic environments conducive to low-pressure anatexis. Thermal modeling during case studies in Scotland (Ryan and Soper 2001), the Pyrenees (Wickham and Oxburgh 1987), and Australia (Bodorkos et al. 2002) led to the broad conclusion that a combination of advected heat from mafic magma and high basal heat flow, such as is generated by thinning or removal of the lithospheric mantle, is necessary and sufficient to cause anatexis. The work of Ryan and Soper (2001) models melt generation below triple point depths, but the locus of anatexis is largely controlled by the position of the injected magma. Therefore, we are confident that by varying only the magma emplacement geometry, they could describe conditions for low-pressure anatexis. In some locations, extension or lithospheric removal may precede magmatism (Wickham and Oxburgh 1987; Ryan and Soper 2001), and in others, the magmatism may come first (Bodorkos et al. 2002). Whichever mechanism operates first, it effectively serves to "preheat" the crust and raise the thermal profile well above the position of the stable geotherm. A secondary heat source is then sufficient to warm the crust nearly isobarically to generate low-pressure anatexis.

Combinations of mechanisms that may produce low-pressure anatexis are not restricted to high basal heat flow. For example, if crustal extension along a detachment fault were sufficient to generate widespread low-pressure metamorphism (Zen 1995a; Escuder Virute 1999), emplacement of magma could induce low-pressure anatexis. Similarly, if appropriate-age plutons had intruded the Mt. Painter province of the Flinders

Ranges, Australia, the crust that was already quite warm from the extremely high heat production (Sandiford et al. 1998) would likely have melted in place.

4.6 Summary

Although not as common as low-pressure metamorphism, low-pressure anatexis has occurred present in many orogenic belts. We have evaluated whether the primary heat transfer mechanisms proposed and modeled for low-pressure metamorphism are suitable for generating low-pressure anatexis. The mechanisms we considered are: (1) magmatic advection by plutons, (2) magmatic advection by percolative flow, (3) fluid advection, (4) high heat production, (5) removal of the lithospheric mantle, (6) crustal thickening, and (7) crustal thinning. Of these mechanisms, magmatic advection by percolative flow (Miyazaki 2004) and detachment faulting (Zen 1995a) are the only ones quantitatively shown to produce widespread, regional anatexis without wholesale melting in the lower crust. Removal of the lithospheric mantle during crustal thinning can generate conditions suitable to melt rocks in the middle and upper crust, but in most models the base of the crust must therefore heat to over 1100°C. One other single mechanism, the presence of a high heat producing layer (Goscombe and Hand 2000), may also generate low-pressure anatexis, but this has not been demonstrated quantitatively.

Although single mechanisms may cause melting below the aluminosilicate triple point, low-pressure anatexis is most likely to develop when two heat transfer mechanisms operate in concert. The probable combinations involve magmatic advection. The magma can serve to preheat the middle to upper crust, allowing a later and larger-scale thermal perturbation, such as is generated either during lithospheric thinning or by the presence of

rocks with moderate to high heat production, to provide the additional heat necessary to cause anatexis.

Chapter 5

IMPLICATIONS OF RAPID, DIKE-FED PLUTON GROWTH FOR HOST-ROCK STRAIN RATES AND EMPLACEMENT MECHANISMS

5.1 Abstract

Dikes must maintain a critical width and flow velocity in order to propagate several kilometers from source to sink without freezing; consequently, they must support a high volumetric magma flow rate. This in turn implies that plutons fed by dikes must fill rapidly. In an effort to predict host-rock strain rates required by dike-fed growth, we employ a three-dimensional geometric model consisting of concentric shells to track instantaneous strain rates in a homogeneously deforming aureole around spheroidal plutons with a range of aspect ratios. Using published values for magma and host-rock parameters appropriate for mid-crustal levels, we calculate, for example, a minimum instantaneous strain rate of approximately 10^{-10} s^{-1} in the deformation aureole of a 1 km radius spherical pluton. Aureole strain rates, which range upward to greater than 10^{-4} s^{-1}, are primarily a function of position in the aureole, pluton size, and filling rate; pluton shape plays only a secondary role. Although preservation of evidence for high strain rates may be rare, and although multiple mechanisms probably operate simultaneously, we expect that deformation this rapid in the middle crust would be accommodated primarily by brittle mechanisms.

5.2 Introduction

Silicic magmatism plays a major role in crustal growth and evolution, but the relative importance of various mechanisms, such as diapirs and dikes, by which magma moves from its source region to a magma chamber remains unresolved (e.g. Clemens et

al. 1997; Clemens 1998; Miller and Paterson 1999). Magma transport is only one of many mass transfer processes that operate within the crust, and the movement of molten material is intimately coupled to crustal rheology as well as strain and strain rate patterns both near and far from a pluton (Paterson and Fowler 1993). Therefore, to evaluate the efficacy of different magma transport mechanisms, we must consider how the crust responds to the movement and collection of magma.

In recent years, attention has focused on dikes as an efficient method for rapidly moving large quantities of silicic magma through the crust. Some studies have considered the physical conditions required for fracture propagation (Clemens and Mawer 1992; Rubin 1995), whereas others have addressed questions related to the flow rate of magma through dikes (Bruce and Huppert 1990; Petford 1996; Petford et al. 2000). Despite some concerns about the likelihood of dike propagation (Rubin 1995), these studies raise the possibility of generating a 6000 km^3 dike-fed mid-crustal pluton in less than 400 years (Petford et al. 1993). Although magma transport and emplacement have been considered somewhat independent processes (e.g. Clemens et al. 1997), some degree of in-situ expansion must accompany dike-fed pluton growth. To permit such growth, wall rocks must be able to deform sufficiently fast to accommodate the high volumetric fluxes associated with dikes. Addressing this point, Clemens et al. (1997, p. 157) stated that "Given the various forces applied to potential host rocks by the magma, spaces should be able to open relatively rapidly – so magma supply is most likely to provide the overriding rate-limit." However, only a few studies have quantitatively evaluated the rates at which space-making mechanisms must operate. Some examples include those by Nyman et al. (1995), who inferred that the aureole around the Papoose

Flat pluton deformed at a finite rate of approximately 10^{-12} s^{-1}, and Fernandez and Castro (1999), who suggested rates as high as 10^{-10} s^{-1} in rocks surrounding parts of the Extremadura batholith. Using a geometrical approach, Johnson et al. (2001) calculated finite strain rates ranging upward from approximately 10^{-10} s^{-1}, with the exact value depending on pluton size and filling rate.

To provide additional constraints on instantaneous strain rates associated with emplacement of silicic magma, we have constructed a three-dimensional geometrical model to evaluate the rates of homogeneous host-rock deformation during in-situ expansion of spheroidal dike-fed plutons. We use rock and magma parameters applicable to mid-crustal levels and a geometrical construction similar to that employed in other pluton aureole strain studies (e.g. Holder 1979; Ramsay 1989; Tikoff et al. 1999). Our results indicate that instantaneous strain rates fall in the range of $10^{-7.5}$ s^{-1} to 10^{-11} s^{-1} for most rocks within the deformation aureole of a dike-fed pluton up to 5 km in radius. These strain rates are too fast to be measured with standard geochronological techniques, but host-rock microstructures may record strain rates of this magnitude. After presenting the model and the results, we discuss the microstructures likely to be indicative of these strain rates and assess the potential for their preservation. This study should not be construed either as supporting or disputing dike-fed pluton growth; our intention is to present some consequences of in-situ expansion of a dike-fed pluton.

5.3 Model parameters

5.3.1 Derivation of strain rate in the general spheroidal case

We use a three-dimensional, isovolumetric shell as the basis for calculating strain rates around an expanding pluton (Fig. 5.1). This geometrical model considers a spheroidal pluton fed by a dike of 1 km plan length. All near-field mass transfer accommodating the growing pluton occurs by homogeneous deformation in isotropic host rock. Around an expanding sphere, all deformation is symmetric and accomplished by coaxial deformation (Fig. 5.1a). In the general case, noncoaxial deformation occurs in most locations around an expanding spheroid, but for this work we have restricted our calculations to the loci of coaxial deformation along the principal axes of the spheroid (Fig. 5.1b). Our model does not explicitly incorporate surface uplift, far-field return flow to the source area, or discrete faults and shear zones.

As a model spheroidal pluton expands, a concentric shell with pre-pluton thickness τ^o will thin to τ and increase its radius to maintain a constant volume (Fig. 5.1). In all expressions, the superscript o refers to the initial state. Because volume remains constant, shell thickness is coupled to the shell radius; this is the starting point for the following derivation using the instantaneous rate of thinning to calculate strain rate.

To determine the radius of the deforming shell, we must consider the original shell size and the added pluton volume. The original volume contained inside the shell is:

$$V_{in}^{o} = \frac{4}{3}\pi r_{in}^{o^3} \tag{5.1}$$

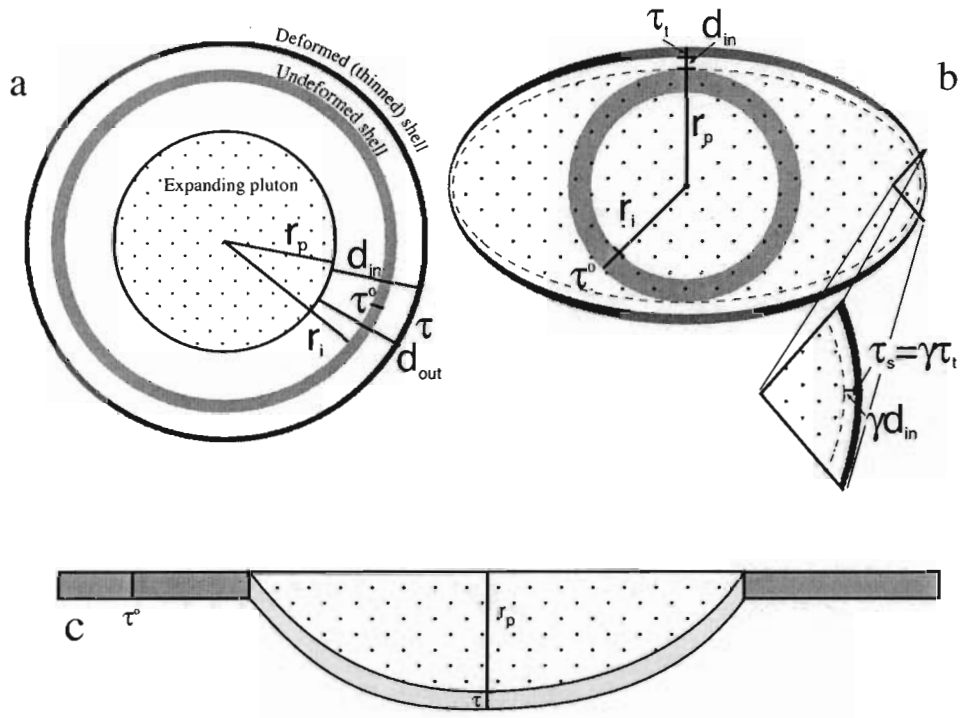

Figure 5.1 Model geometry. Vertical central cross-sections illustrating the geometric bases for models of an in-situ expanding spheroidal pluton. See text for explanation of variables. (a) As a spherical pluton expands from a point source, a spherical shell of wall rocks deforms symmetrically, expanding and thinning. Light gray represents the initial, undeformed shell; the dark gray shell corresponds to the instance where a pluton of radius r_p has intruded. (b) In the more general case of a spheroidal pluton, the deforming shell has either a uniform thickness, or thins more at the ends. We define the shell thickness ratio, $\gamma=\tau_s/\tau_t$. This ratio also applies to the distance between the pluton and the shell of interest (d_{in}). (c) A pluton inflating from a sill to a hemisphere by floor subsidence drives uniform thinning of model host-rock layer (light gray) beneath the expanding pluton with a fixed horizontal dimension. This geometry also applies, if inverted, to a laccolith geometry.

where r^o_{in} is the initial inner radius of the shell. With emplacement of a spheroidal pluton, the deforming shell will develop a spheroidal shape, but we always begin with a spherical shell because a spherical initial shell geometry is independent of the final pluton shape and thus allows comparisons between all models, and because we assume the host rock is isotropic and has no inherent shape-preferred structure. The volume inside the shell will change with the addition of a pluton by:

$$V_{in} = V^o_{in} + V_p \tag{5.2}$$

where the subscript p refers to the pluton. In radius notation, the volume of the pluton and the volume inside the shell are (Fig. 5.1):

$$V_p = \frac{4}{3}\pi\alpha^2 r_p^3 \tag{5.3a}$$

$$V_{in} = \frac{4}{3}\pi\left(r_p + d_{in}\right)\left(\alpha r_p + \gamma d_{in}\right)^2 \tag{5.3b}$$

where d_{in} is the distance between the edge of the pluton and the inside of the shell, α is the pluton aspect ratio, defined as the ratio of the lengths of the horizontal to vertical axes of the spheroid; the two horizontal axes of the spheroid are equal. The shell thickness ratio, γ, allows for different degrees of shortening at the top and sides of the shell (Fig. 5.1b). We define the shell thickness ratio as:

$$\gamma = \frac{\tau_s}{\tau_t} \tag{5.4}$$

where the subscripts s and t refer to the side and top (or bottom) of the expanding pluton. Both α and γ are imposed conditions, and we can assign them to be constant or vary with pluton radius. Substituting Eqs. (5.1) and (5.3) into Eq. (5.2):

$$\frac{4}{3}\pi\left(r_p + d_{in}\right)\left(\alpha r_p + \gamma d_{in}\right)^2 = \frac{4}{3}\pi r^{o3}_{in} + \frac{4}{3}\pi\alpha^2 r_p^3 \tag{5.5a}$$

The volume contained by the outer edge of the shell, d_{out}, follows similarly:

$$\frac{4}{3}\pi\left(r_p + d_{out}\right)\left(\alpha r_p + \gamma d_{out}\right)^2 = \frac{4}{3}\pi\left(r_{in}^o + \tau^o\right)^3 + \frac{4}{3}\pi\alpha^2 r_p^3 \tag{5.5b}$$

We define the shell thickness as (Fig. 5.1):

$$\tau = d_{out} - d_{in} \tag{5.6}$$

Solving Eqs. (5.5a) and (5.5b) for d_{in} and d_{out} allows us to calculate τ as a function of r_p (see Mathematical Note). The strain rate related to the thinning shell, $d\tau/dt$ (derived below), is thus a function of the change in pluton radius with respect to time.

The derivative of Eq. (5.3a) with respect to r_p, recalling that α is either constant or a function of r_p, is:

$$\frac{dV_p}{dr_p} = \left(4\pi\alpha^2 r_p^2\right) + \frac{8}{3}\pi\alpha r_p^3 \frac{d\alpha}{dr_p} \tag{5.7a}$$

The volume rate of change of the pluton is equivalent to the filling rate, Q:

$$\frac{dV_p}{dt} = Q \tag{5.7b}$$

Combining Eqs. (5.7a) and (5.7b):

$$\frac{dr_p}{dt} = \frac{dr_p}{dV_p}\frac{dV_p}{dt} = \frac{Q}{\left(4\pi\alpha^2 r_p^2\right) + \frac{8}{3}\pi\alpha r_p^3 \frac{d\alpha}{dr_p}} \tag{5.7c}$$

Multiplying the derivative of τ with respect to r_p by Eq. (5.7c) yields:

$$\frac{d\tau}{dr_p}\frac{dr_p}{dt} = \frac{d\tau}{dt} \tag{5.8}$$

The instantaneous strain rate for a deforming shell is then:

$$\dot{\varepsilon} = \frac{d\tau/dt}{\tau} \tag{5.9}$$

5.3.2 Floor subsidence and roof doming

To consider the possibility that a pluton may grow by inflation from a sill into a laccolith or lopolith geometry by roof doming (Corry 1988; Morgan et al. 1998) or floor subsidence (Cruden 1998; Wiebe and Collins 1998; Cruden and McCaffrey 2001), we constructed another model geometry using a constant horizontal width. To do so, we constantly change the aspect ratio as the pluton expands. The final geometry of this model is a hemisphere with a 5 km radius (Fig. 5.1c). As the circumference of the pluton increases, the shells in this model stretch uniformly either underneath the deforming floor, as shown in Fig. 5.1 (c), or over the roof of the pluton. Because we assume that no surface uplift occurs, roof doming is mathematically equivalent to floor subsidence.

5.3.3 Filling rate

The strain rate in our model depends strongly on the pluton filling rate, or the magma flux through the feeder dike. We calculated the volumetric flux through a single dike using published values for the various parameters that determine critical dike widths and flow rates (Bruce and Huppert 1990; Petford et al. 1993; Clemens et al. 1997; Cruden 1998). The magmatic flux, Q, is the product of the dike width, flow rate, and plan length. We use a dike plan length of 1 km. The critical width, w, necessary to prevent a dike from freezing depends on the viscosity, η, thermal diffusivity, κ, density contrast between the magma and host rock, $\Delta\rho$, acceleration due to gravity, g, latent heat of solidification, L, specific heat, C, vertical dike length, H, initial magma temperature, T_m, effective magma freezing temperature, T_w, and far field temperature of the host rock, T_∞ (Bruce and Huppert 1990; Petford et al. 1993):

$$w = 1.5\left(\frac{C(T_w - T_\infty)^2}{L(T_m - T_w)}\right)^{\frac{3}{4}}\left(\frac{\eta\kappa H}{g\Delta\rho}\right)^{\frac{1}{4}} \tag{5.10}$$

Using the width from Eq. (5.10), the velocity, v, assuming buoyancy-driven flow, is:

$$v = \frac{g\Delta\rho w^2}{12\eta} \tag{5.11}$$

Using a range of physical magma parameters suggested by Clemens and Petford (1999), we calculated a range of volumetric flow rates of 5.62 m^3/s to 179 m^3/s (Table 5.1). These flow rates are based on a mid-crustal emplacement level (far-field temperature of 450°C). The slow rate is for a relatively dry tonalite melt with viscosity 10^7 Pa s, initial temperature of 950°C, and density difference between host rock and magma of 200 kg/m^3. The fast rate is for a wet granitic melt with viscosity 10^4 Pa s, initial temperature of 850°C, and density difference between host rock and magma of 400 kg/m^3. Other combinations of viscosity, magma temperature and density difference between the above values yield intermediate volumetric flow rates. These flow rates are for dikes at the critical, or minimum, width to prevent freezing; dikes could be wider and therefore have higher flow rates. Thus, given the above conditions, we regard the flow rate of 5.62 m^3/s as the minimum filling rate for a pluton fed by a dike 1 km in plan length.

The geometry of our model does not explicitly assume a mid-crustal pluton emplacement level. However, because the parameters we used to calculate magma flow rates are based on values most consistent with the middle crust, the strain rates we derive are most applicable to those levels. Higher temperatures deeper in the crust reduce the critical magma flow rate, perhaps to approximately 10^{-5} m^3/s. At such low flow rates, a pluton should expand much more slowly and require much lower host-rock strain rates.

Table 5.1 Magma parameters and calculated volumetric flow rates in dikes*

CONSTANTS		
Thermal diffusivity, κ (m^2/s)	$8\ 10^{-7}$	
Latent heat of solidification, L (J/kg)	$3\ 10^5$	
Specific heat, C (J/kg/°C)	$1.2\ 10^3$	
Acceleration due to gravity, g (m/s^2)	9.8	
Vertical dike length, H (m)	$2\ 10^4$	
Effective magma freezing temp., T_{wo} (°C)	750	
Horizontal dike length (m)	10^3	
Far field host rock temperature, T_∞ (°C)	450	
VARIABLES	**FOR LOW FLUX**	**FOR HIGH FLUX**
Initial magma temperature, T_m, (°C)	950	850
Density contrast, $\Delta\rho$ (kg/m^3)	200	400
Viscosity, η (Pa s)	10^7	10^4
OUTPUT		
Dike width, w (m)	7.01	1.76
Magma velocity, ν (m/s)	0.0008	0.101
Volumetric flux, Q (m^3/s)	5.62	179

*Input values, except horizontal dike length, from the range of permissible values given by Bruce and Huppert (1990), Petford et al. (1993), and Clemens and Petford (1999).

5.4 Results

To evaluate the host-rock strain-rates associated with a range of pluton growth histories, we employed various values for filling rate, pluton aspect ratio, and shell thickness ratio (Table 5.2). Filling rates were 5.62 m^3/s and 179 m^3/s, and pluton aspect ratios were 1, 2, 5, and a size-dependent function calculated from McCaffrey and Petford (1997):

$$\alpha=2.34r_p^{1.67} \tag{5.12}$$

where r_p is the vertical pluton radius. All shells initially have a uniform thickness (γ=1), so for a different shell thickness ratio to develop after a pluton grows, the shell thickness ratio must vary with r_p. For those cases, we chose functions (Table 5.2) so that the ratio between the thickness at the side and at the top of the shell was approximately 0.5 at the end of the model run. The ratio of 0.5 is an arbitrary value, but represents a reasonable estimate of differential strain around a pluton. In all model runs, strain rates in shells surrounding an expanding pluton decrease monotonically with both r_p and distance from the pluton (Figs. 5.2 and 5.3a). Additional runs, not described here, indicated that results were not sensitive to initial shell thickness, so for all runs we discuss, the initial shell thickness is 1 m. We chose the plan length of 1 km as a reasonable estimate for dikes feeding plutons on the order of 5 km in radius. As shown by Johnson et al (2001), a different plan length, even one that grows as the pluton expands, has little effect on the modeled strain rates.

5.4.1 Range of permissible strain rates

Around a 1 km pluton, rocks in the aureole deform at rates higher than 10^{-10} s^{-1} (Figs. 5.2 and 5.3). Considering all modeled geometries and different observation

Table 5.2 Parameters for model runs

Run[a]	Q (m^3/s)	r_i (m)	α_p	γ	r_p (m)	Δr (m)
	Magma flux	Initial inner shell radius	Pluton aspect ratio	Shell thickness ratio	Vertical pluton radius	Initial shell thickness
1	5.62	0	1	1	-	1
2	5.62	1000	1	1	-	1
3	179	0	1	1	-	1
4	179	1000	1	1	-	1
5	5.62	500	2	1	-	1
6	5.62	500	5	1	-	1
7	5.62	500	$2.34\ r_p^{5/3}$ [b]	1	-	1
8	5.62	500	5	$-0.5/(r_p/1000)^2+1$	-	1
9	5.62	-	1	1	1000	1
10	179	-	1	1	1000	1
11	5.62	-	5	$-0.5/(r_p/1000)^2+1$	200	1
12[c]	5.62	500	$5/r_p$	1	-	1
13[c]	179	500	$5/r_p$	1	-	1

[a]For runs 1-8, see Fig. 5.2; for 9-11, see Fig. 5.3
[b]Calculated from McCaffrey and Petford (1997)
[c]Models a pluton with a constant 5 km radius inflating from a sill (see Fig. 5.4).

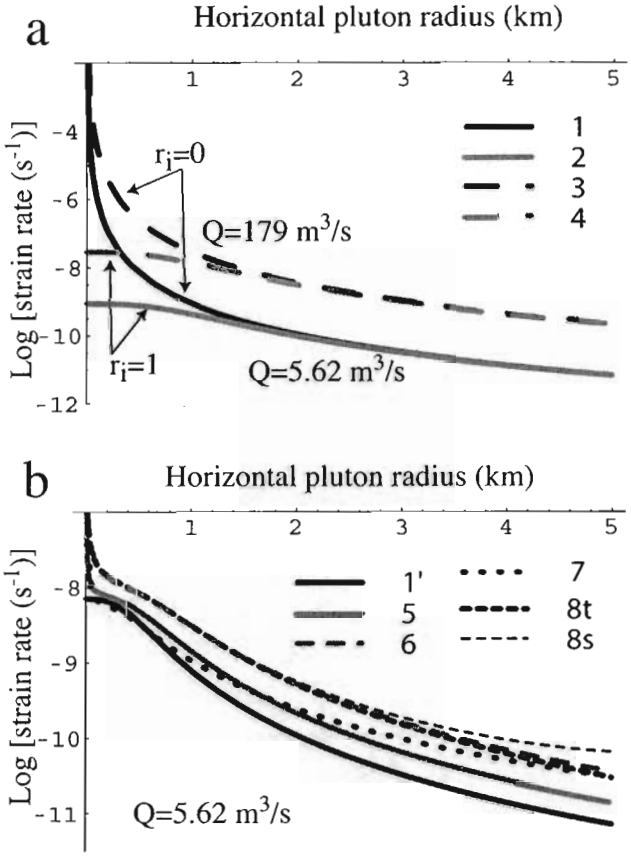

Figure 5.2 Change in strain rate through time. (a) Results from model runs 1 through 4 (legend refers to Table 5.2), showing dependence of strain rate on initial shell radius (r_i) and on filling rate (Q). (b) Results from runs 5 through 8 (Table 5.2) and from a run with a sphere for comparison (labeled 1': parameters as run 1 (Table 5.2) except that r_i = 500 m for comparison with runs 5 through 8). Postscripts t and s refer to top and side, respectively, of the deforming shell (Fig. 1b). Runs 5 through 8, which are based on the minimum filling rate, represent the lowest predicted strain rates for dike-fed pluton expanding in-situ.

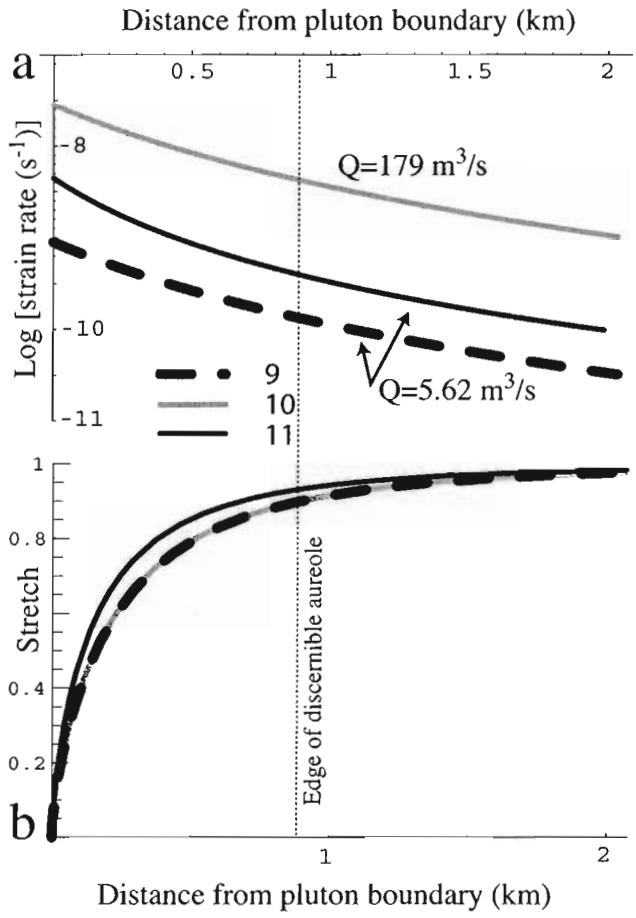

Figure 5.3 Snapshot of strain rate throughout aureole. Results of model runs 9 through 11 (Table 5.2). (a) Snapshot of horizontal instantaneous strain rates and stretch distributions across deformation aureoles surrounding a 1 km horizontal radius pluton. (b) The finite strain gradient, shown as the change in stretch (ratio of final to initial length) with distance from the edge of the pluton. We arbitrarily define the edge of the aureole as the locus of 10% shortening, or stretch of 0.9, which occurs at approximately one pluton radius from the pluton boundary.

positions in the aureole, we calculate instantaneous strain rates that range from 10^{-11} s^{-1} to greater than 10^{-4} s^{-1}. The calculated strain rates depend primarily on the size of the pluton, the original shell distance from the pluton center (i.e., where in the aureole the strain rate is measured), and the filling rate, such that greater distance from the pluton contact, larger pluton radius, and lower dike flow rate contribute to lower strain rates. A uniform shell thickness around a spherical pluton (Fig. 5.2b, Run 1') produces lower strain rates than other geometries, but the effect of pluton shape and deformation shell uniformity is of secondary importance (Fig. 5.2b).

As a pluton expands at a constant volumetric rate, the instantaneous strain rate everywhere in the aureole diminishes (Fig. 5.2), with the very high rates for rocks adjacent to the pluton boundary decaying rapidly (Fig. 5.2a). As an example, a shell that started 1 km from the center of a spherical pluton 1 km in radius deforms at $10^{-7.5}$ s^{-1} to 10^{-9} s^{-1}, depending on filling rate (Fig. 5.2a). As the pluton grows to 5 km radius, the strain rates decrease to a range of $10^{-9.5}$ s^{-1} to 10^{-11} s^{-1}. Results are similar for the non-spherical cases. Except during the earliest stages of growth (r_p<~750 m), the instantaneous strain rate varies less than an order of magnitude across the aureole (Figs. 5.2a and 5.3).

For the floor subsidence and roof doming model, strain rates are nearly constant, decreasing by less than an order of magnitude as the pluton inflates (Fig. 5.4). Recall that this strain rate measures the thinning of a shell under a sinking floor or over a doming roof, and does not incorporate any lateral expansion; the pluton is assumed to inflate vertically from a sill. As in the original model, strain rates are highly sensitive to filling rate, being approximately $10^{-9.3}$ s^{-1} to $10^{-10.8}$ s^{-1} for the fast and slow filling rates,

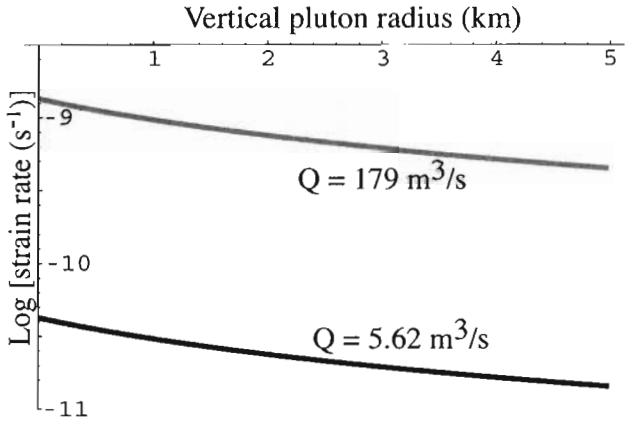

Figure 5.4 Effects of floor subsidence. Results of model runs 12 and 13 (Table 5.2): instantaneous strain rates associated with floor subsidence or roof doming around a spheroidal pluton with a constant horizontal radius of 5 km as it inflates from a sill. Initial shell radius is 500 m.

respectively. These rates are initially lower than those for the expanding spheroid (Fig. 5.2), but become equal or higher as the pluton grows.

5.4.2 Effect of varying initial shell radius

The initial shell radius, or the distance a shell originated from the incipient pluton center, strongly affects the calculated strain and strain rate (Fig. 5.2), but it does not affect the strain or strain-rate fields. In effect, the initial shell radius identifies which shell we track through the model: a shell with initial radius of 0 km (Runs 1 and 3; Fig. 5.2a) represents the rocks at the pluton margin, whereas a shell with initial radius of 1 km (Runs 2 and 4; Fig. 5.2a) represents rocks that started 1 km from the pluton center. Because of thinning and translation associated with pluton growth, rocks that began 1 km from the pluton center end up 1.261 km from the center, and only 261 m from the boundary, of a 1 km radius pluton. Shells closer to the pluton center (lower r_i) predictably experience a higher initial strain rate as they rapidly thin to accommodate the growing pluton (Fig. 5.2a, Runs 1 and 3). However, shells starting at $r_i = 0$ and $r_i = 1$ km will experience different strain rates only until the pluton is approximately 1 km in radius (Fig. 5.2a). Intermediate values of r_i contour smoothly between these curves. To allow comparison among other variables, we discuss our remaining results for a shell that started 500 m from the pluton center.

5.4.3 Effect of varying filling rate

Wall-rock strain rate is highly sensitive to the pluton filling rate. The filling rates used here are based on theoretical and experimental determinations of magma characteristics and flow dynamics (Bruce and Huppert 1990; Petford et al. 1993; Clemens et al. 1997; Cruden 1998) relevant to mid-crustal levels. Rocks surrounding a pluton

filling at the lower end of the flux range will experience strain rates nearly 1.5 orders of magnitude lower than those around a pluton filling at the higher rate (Fig. 5.2a). Because the difference between the minimum and maximum filling rates is also approximately 1.5 orders of magnitude, we can consider the strain rate to scale approximately linearly with the filling rate.

5.4.4 Effect of varying aspect ratio and shell thickness ratio

Compared to a uniform shell thickness surrounding a spherical pluton, shell thickness ratio, γ, and pluton aspect ratio, α, have less than an order of magnitude effect on the strain rate (Table 5.2; Figs. 5.2b and 5.3a). Similarly, the difference in strain rate at the top and sides of a non-spherical pluton is less than an order of magnitude (Fig. 5.2b, Runs 8s and 8t). Because we model the non-spherical plutons as oblate bodies, the sides of those plutons always experience strain rates greater than the top for a shell thickness ratio $\gamma < 1$.

5.5 Corollary calculations

5.5.1 Stoping

Stoping has long been recognized as an efficient mechanism for removing inner portions of a deformation aureole (Buddington 1959; Paterson et al. 1996). With that in mind, we modified our model to determine the effects of stoping on the instantaneous strain rate and finite strain distribution around a pluton with aspect ratios of 1 and 2, and consisting of 0%, 20%, and 50% stoped blocks by volume. In this model, stoping is assumed to operate uniformly around the spheroidal pluton (Fig. 5.5a). The fundamental difference between this model and those previously described is that the pluton radius

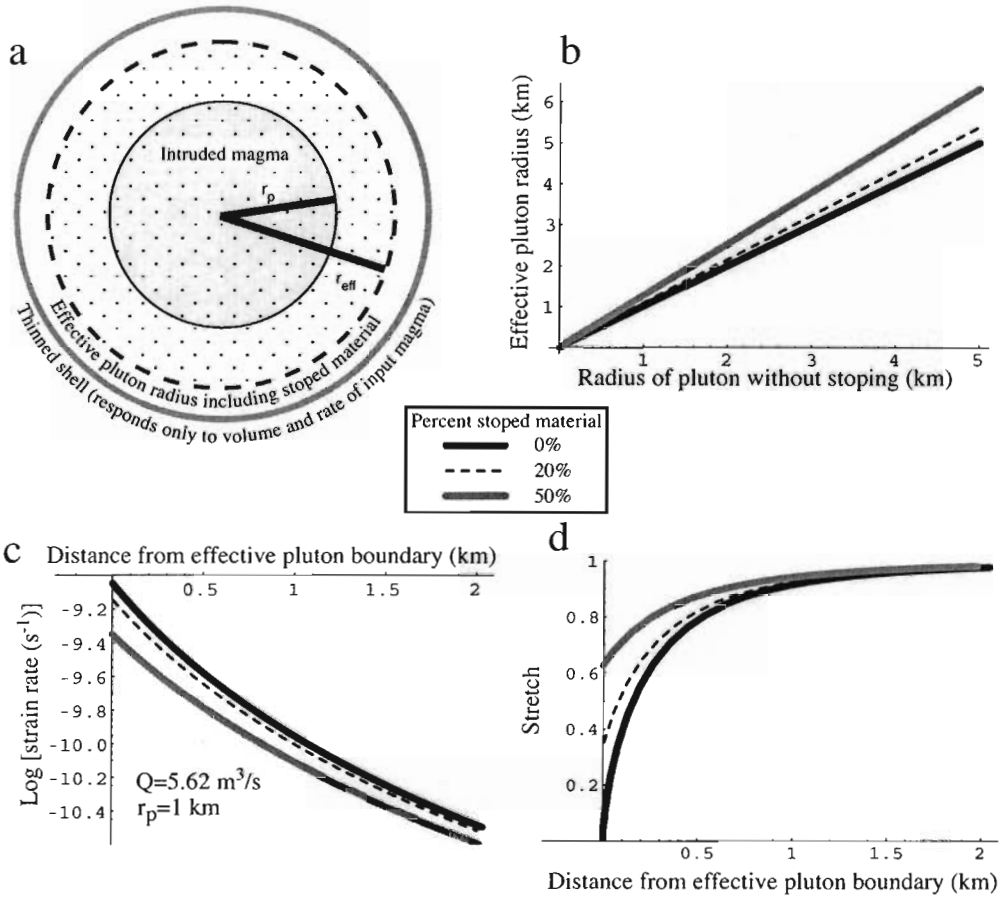

Figure 5.5 Effects of stoping. (a) Central cross-section of a spherical pluton that incorporates stoped blocks. If some fraction of the pluton consists of stoped material, the effective pluton radius, reff, will be larger than the pluton radius, r_p, to which the deforming shells are responding. Stoping removes the high strain portion of the inner aureole and decreases the bulk strain across the remainder of the aureole. For clarity, the undeformed shell is not shown, but it is the same as in Fig. 1(a). (b) Relationship between the effective pluton radius and the radius of the emplaced magma (not including stoped blocks), which we model as a sphere at the center of the pluton. (c) Instantaneous strain rate distribution, for different degrees of stoping, across the deformation aureole surrounding a 1 km radius pluton filled at the minimum rate. (d) Stretch distribution, for different degrees of stoping, across the deformation aureole surrounding a 1 km radius pluton. Because stoping uniformly removes the high strain inner portion of the aureole, with higher degrees of stoping, rocks immediately adjacent to the effective pluton boundary are less strained.

includes volume of both the magma added and the stoped blocks. Because stoped blocks constitute a portion of the pluton, the *effective* pluton radius for a given volume of dike-fed magma is larger than it would be without stoping (Fig. 5.5b).

Because the response of the rocks outside the effective radius of the pluton depends only on the volume added to the system (Eq. 5.2), the degree of stoping does not influence deformation of rocks in the aureole. Although strain rate and finite strain distributions around plutons with stoped material (Figs. 5.5c and 5.5d) appear to be sensitive to the degree of stoping when viewed in relation to the *edge* of the pluton, if the same strain-rate curves are plotted in relation to the *center* of the pluton, they are identical. Therefore we expect that, given the same volumetric magma flux, aureoles around plutons with high degrees of stoping deform at strain rates equivalent to those around plutons with no stoping.

Although it does not significantly affect predicted strain rates, stoping does affect the finite strain distribution in the aureole. In particular, because the pluton has incorporated the inner, high-strain portion of the aureole, rocks adjacent to the pluton have a lower finite strain with increased degree of stoping (Fig. 5.5d; Table 5.3). This in turn affects the bulk strain of the aureole. If we define the edge of the deformation aureole at 10% shortening, equivalent to a stretch of 0.9, and consider a central section through a spherical pluton, we can calculate, for different degrees of stoping, the aureole width normalized to the pluton radius and the percentage of the pluton radius accounted for by the linear shortening in the aureole (Table 5.3). Normalized aureole widths range from 0.9 for no stoping and an aspect ratio of 1, to 0.39 for 50% stoping and an aspect ratio of 2. Homogeneous shortening accounts for only 32% and 13% of the pluton radius

Table 5.3 Strain-related calculations for different degrees of stoping

Stoping (% total pluton volume)	Pluton aspect ratio	Aureole width normalized to pluton radius	Horizontal radial accommodation*	Maximum shortening (at pluton margin)
0%	1	0.9	90%	> 99%
20%	1	0.76	32%	66%
50%	1	0.50	13%	37%
0%	2	0.75	74%	>99%
20%	2	0.63	30%	68%
50%	2	0.39	17%	39%

* Percentage of pluton radius accommodated by bulk shortening across the aureole

at 20% and 50% stoping, respectively, as compared to 90% with no stoping. The maximum observable shortening at the pluton boundary around spherical plutons with 20% and 50% stoping are 66% and 37%, respectively. The modeled aureole widths and radial accommodation values incorporating stoping are in agreement with those determined by Paterson and Fowler (1993) for six natural plutons.

5.5.2 Tectonic accommodation

Based on field mapping and analogue modeling, several studies have proposed dilational sites associated with faults, such as those in pull-apart basins or along normal faults, as locations where plutons can develop (e.g. Hutton 1982; Guineberteau et al. 1987; Hutton 1988b; Tikoff and Teyssier 1992; Ferre et al. 1995; Benn et al. 1998). For this mechanism to accommodate an inflating pluton, the dilation rate must at least equal the rate at which the walls of the pluton diverge (twice the rate at which the pluton radius grows). The pluton radial growth rate depends on the magmatic flux and pluton geometry. We can use Eq. 5.7(c) to calculate those rates for a central section of a spherical pluton:

$$2\frac{dr_p}{dt} = 2\frac{Q}{4\pi r_p^{\,2}} = \frac{Q}{2\pi r_p^{\,2}} \qquad (13)$$

Around a 1 km radius pluton filled at the slowest permissible rate (Table 5.1), the host-rock walls must diverge at approximately 28 m/yr (Fig. 5.6), faster than the rate calculated by Fernandez and Castro (1999) for a pluton in the Central Extremadura batholith. Plutons growing in pull-apart basins would probably have an aspect ratio

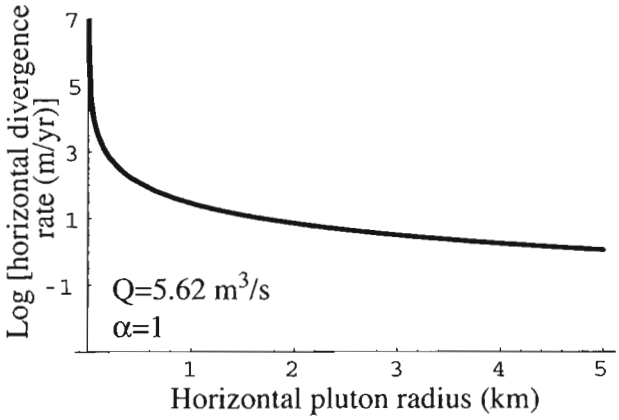

Figure 5.6 Wall-rock divergence rate. Horizontal divergence rates of wall rocks necessary to accommodate the central section of a spherically expanding pluton fed by a dike with our minimum filling rate. Based on the geometries we have described, this curve represents the minimum divergence rate for the walls around the center of a spherical dike-fed pluton.

closer to 2, but rotated so the short axis is horizontal and the two long axes lie in the vertical fault plane. Walls around the short axis of such a spheroid will diverge one quarter as fast as in the spherical case.

5.6 Discussion

5.6.1 Accommodating predicted strain rates

Although near-field and far-field material transfer processes together accommmodate magma transfer (e.g. Hutton 1988a; Paterson and Fowler 1993), we have modeled only the near-field effects of a single intrusion driving homogeneous deformation in the host rock. Other near-field processes that may make space for magma, including regional tectonic strain, roof uplift, and floor subsidence, must also occur at rates sufficient to allow pluton growth in accordance with proposed filling rates (Paterson and Fowler 1993; Cruden and McCaffrey 2001). Below, we address the likelihood that these mechanisms can operate at sufficient rates to accommodate dike-fed pluton growth. Host-rock volume loss is another proposed space-making mechanism, but it is likely to be too slow to be significant at these strain rates (e.g. Marsh 1989; Yoshinobu and Girty 1999). As shown in Sec. 4.1, stoping does not affect the strain rates in the aureole, so we do not discuss that mechanism further here.

5.6.1.1 Regional tectonic accommodation

Rates of bulk regional deformation are usually quoted in the range of 10^{-13} to 10^{-15} s^{-1} (Pfiffner and Ramsay 1982; Paterson and Tobisch 1992; Dunlap et al. 1997; Foster and Gray 1999; Muller et al. 2000). Although some workers have proposed that discrete

zones, such as kink folds and shear zones, within tectonically active areas can deform much faster than the regional strain rate, strain rates at these local sites are suggested to be no greater than 10^{-9} s^{-1} (e.g. Schmid 1989; White and Mawer 1992; Fernandez and Castro 1999). In some instances, it appears that shear zones or kink folds may deform fast enough to accommodate strain rates required by dike-fed pluton expansion, but shear strain rates associated with shear zones are not directly comparable to strain rates predicted by our model.

Perhaps a better measure for the ability of regional tectonic activity to make space for plutons would be the divergence rate of faults, such as in pull-apart basins. Divergent plate boundaries probably set the upper limit for making space by faulting (Paterson and Tobisch 1992), with part of the East Pacific rise recognized as the fastest spreading center at 0.15 m/yr (Hey et al. 1995). This rate is two orders of magnitude lower than around the slowest-growing modeled spherical pluton (Section 4.2), much too slow to accommodate a pluton inflating in a single pulse at the lowest calculated filling rate.

5.6.1.2 Translation and rotation

Several recent models and interpretations of natural plutons have invoked variations of translation and rotation as accommodation mechanisms for expanding plutons (e.g, Cruden 1998; Morgan et al. 1998; Wiebe and Collins 1998; Tikoff et al. 1999; Cruden and McCaffrey 2001). Without significant strain in the host rocks, translation and rotation must result in surface uplift, Moho depression, far-field plastic or brittle deformation, or downward transfer of material to the depleted pluton source (Paterson and Fowler 1993). Surface uplift has been documented for plutons and

laccoliths in the upper crust (e.g. Acocella and Mulugeta 2001) and postulated for those in the middle crust (Saint-Blanquat et al. 2001). Brown and McClelland (2000) suggested that Moho depression accommodated magmatic growth in the Coast Plutonic Complex.

Translation accompanying a penetratively thinning shell can be an accommodating factor (Tikoff et al. 1999), but rocks within and outside that shell must deform at high instantaneous strain rates ($>10^{-10}$ s^{-1}) during at least early stages of the deformation. In general, however, translation and rotation by themselves do not involve penetrative deformation, so structures at the boundaries of translating and rotating blocks must accumulate strain. In order to accommodate our modeled 1 km radius spherical pluton, translation or rotation must open space at a rate of at least 28 m/yr. This requires that rocks in zones bounding areas of rotation or translation must deform at equivalently high strain rates. Cruden (1998) has suggested that shear zones bounding a subsiding pluton floor (or a doming roof) must deform at shear strain rates greater than 10^{-10} s^{-1}.

5.6.2 Applying the model to natural settings

Our model uses a simple geometry to predict instantaneous strain rates in the deformation aureole of a spheroidal pluton as it expands concentrically in a single pulse. As such, it falls short of describing many naturally occurring plutons. Nevertheless, several studies, including reinterpretations of well-studied plutons, have argued for some degree of in-situ expansion during emplacement (e.g. Papoose Flat (Morgan et al. 1998), Flamanville (Brun et al. 1990), Ardara (Molyneux and Hutton 2000), San José (Johnson et al. in press-b)). The composition and size of the Flamanville, San José, and Ardara plutons are appropriate for our model. If the in-situ expansion of these plutons was

driven by an influx of dike-fed magma, the surrounding deformation may preserve microstructural evidence (see below) of instantaneous strain rates within the range suggested by our results.

5.6.2.1 Pluton evolution and episodic construction

Regardless of how a long-lived plutonic magma chamber eventually grows, it must initiate with a critical volume to prevent freezing. A smaller initial volume of magma is necessary in warmer host rock, as could develop if the host rock were preheated by a series of intrusions. If a pluton were fed by small, temporally spaced dike-fed injections, early injections would cool below their solidus before the next injection occurred, likely resulting in a sheeted complex, at least on the margins (Yoshinobu et al. 1998). Therefore, unless stoping or remelting removed the evidence, plutons with no sheeted margins probably originated as a substantial pulse of magma, whether or not they continued to grow episodically.

For plutons growing episodically, even though a single filling event may be fast, the long-term average magma supply rate can be low due to the time interval between injections. In an ideal system, the non-elastic host-rock strain rates during each filling event should be a function of the pluton size, shape, and filling rate, and thus be predicted by our model. Natural systems, however, may vary from the ideal in several important ways. For example, if hundreds of small injections intrude a large chamber (such as in the mafic-silic systems described by Wiebe and Collins, 1998), the host rock may have the capacity to absorb the additional volume elastically, or the small strains could be taken up by episodic faulting. Alternatively, magma entering the chamber from the bottom could induce an eruption or transfer of magma to a higher level chamber, thereby

keeping the pluton volume approximately constant and eliminating any need for host-rock strain.

Some plutons that grow episodically do so with the intrusion of only a few discrete pulses. Johnson et al. (in press) described a multiple pulse tonalite pluton in the Peninsular Ranges of México. The initial pulse of this pluton apparently had time to undergo extensive crystallization at its margins before being intruded by a second pulse of tonalite magma. The partly crystallized outer shell of the pluton was deformed, at rates estimated by Johnson et al. (in press-a) to lie between approximately 10^{-8} s^{-1} to 10^{-11} s^{-1}, during the emplacement of the second pulse. The partly crystallized carapace behaved mechanically as part the host rock into which the magma intruded, so our model may be applicable to this type of system.

5.6.2.2 Field and microstructural evidence for high instantaneous strain rates

Obtaining strain-rate information from pluton aureoles is difficult, owing principally to the poor calibration of structures and microstructures to the dominantly transient thermal and dynamic conditions that existed in these environments. But under certain conditions, aureole rocks can record and retain evidence for high strain rates. Our above modeled strain rates are based on pluton filling rates calculated for a background temperature of 450°C, and although not part of the calculations, this temperature might reasonably correspond to the upper middle crust, depending on geothermal gradients. Under these conditions, rocks straining at rates in excess of 10^{-10} s^{-1} are unlikely to flow, at least initially, by dislocation or diffusion creep processes. Therefore, around rapidly-filling plutons, we might expect widespread evidence for grain-scale brittle deformation

regardless of the dominant mineralogy. In addition, the following observations are compatible with high strain rates (Johnson et al. 1999).

1. Brittle features such as radiating fracture sets oriented perpendicular to the direction of minimum compressive stress, local or extensive zones of brecciation, and extensive fracturing of minerals that were present prior to emplacement may be common. Gradients in the development of these features may be present, with the most intense development near the pluton margin.
2. Contact metamorphism will completely postdate the emplacement-related deformation, owing to the slow rate of heat transfer relative to the rate of pluton growth.
3. Synplutonic dikes may be isoclinally folded in the magmatic state prior to cooling below their solidus temperature.

At background temperatures higher than those used in our model, creep mechanisms may play an active role in accommodating deformation, but at mid-crustal levels, creep will not be a dominant mechanism (Albertz et al. 2002). The minimum strain rate we would predict at elevated background temperature would necessarily be lower because the minimum filling rate would be lower. In the early stages of pluton grown, however, strain rates would still be well above 10^{-10} s^{-1}. Where creep is active, it may be possible to use experimentally derived flow laws to evaluate aureole strain rates. The principal difficulty with this approach is extrapolating experimental results, on either mono- or polymineralic rocks, to an environment where steady state thermal and dynamic conditions almost certainly never prevailed. Because strong and weak minerals will partition the strain and strain rate (e.g. Bons and Cox 1994; Goodwin and Tikoff 2002; Ji

and Xia 2002; Johnson et al. in press-a), microstructures of the entire rock would have to be characterized in any attempt to determine the bulk strain rate.

Preservation of microstructures diagnostic of high strain rates in a pluton aureole requires certain conditions. If the pluton is large, with a large associated thermal flux into the aureole, evidence for microfracturing may be destroyed by recrystallization. Similarly, if the pluton is "syntectonic" , then continued accumulation of regional strain and associated differential stress may also affect the emplacement related microstructures. In general, the preservation of syn-emplacement microstructures should be favored by a rapid drop in temperature, differential stress and strain rate after emplacement (e.g. Knipe 1989; Prior et al. 1990; White and Mawer 1992; Handy et al. 2001; Johnson et al. in press-a). These conditions are probably best met around relatively small post-tectonic plutons (e.g. radius < 5 km) that formed from a single "pulse" of magma.

5.7 Conclusion

Our three-dimensional model of homogeneous deformation in host rocks surrounding dike-fed, in-situ expanding plutons predicts, for example, instantaneous strain rates greater than 10^{-10} s^{-1} in the deformational aureole of a 1 km radius pluton. If all deformation is homogeneous, whether brittle or plastic, structures within the aureole should reflect those strain rates. With the operation of other material transfer processes, such as rigid block translation and rotation, structures bounding the blocks must themselves accommodate deformation at comparably high strain rates. Microstructures provide the best opportunity to record strain rates of this magnitude, provided they are not overprinted by later thermal or deformational events. The presence of evidence for

high strain rates in deformation aureoles, whether the deformation is penetrative or in discrete zones, would be consistent with in-situ dike-fed pluton expansion as a magma emplacement mechanism.

5.8 Mathematical Note

We derived the function relating the shell thickness to the pluton radius using the *Solve* function in Mathematica 4.0, by Wolfram Research, Inc. The explicit solution for shell thickness, τ, determined by solving Eq. 5.5 for d_{in} and d_{out} and substituting the results into Eq. (5.6), is

$$\tau = \frac{1}{2^{\frac{2}{3}}3\gamma^2}\left(\frac{-2r_p^2\gamma^2(\alpha-\gamma)^2}{\left(2\alpha^3\gamma^3r_p^3+27\gamma^4r_i^3+21\alpha^2\gamma^4r_p^3+6\alpha\gamma^5r_p^3-2\gamma^6r_p^3+3\sqrt{3\left(\gamma^7\left(r_i^3+\alpha^2r_p^3\right)\left(4\alpha^3r_p^3+27\gamma r_i^3+15\alpha^2\gamma r_p^3+12\alpha\gamma^2r_p^3-4\gamma^3r_p^3\right)\right)}\right)^{\frac{1}{3}}}-\right.$$
$$\left(4\alpha^3\gamma^3r_p^3+54\gamma^4r_i^3+42\alpha^2\gamma^4r_p^3+12\alpha\gamma^3r_p^3-4\gamma^6r_p^3+6\sqrt{3\left(\gamma^7\left(r_i^3+\alpha^2r_p^3\right)\left(4\alpha^3r_p^3+27\gamma r_i^3+15\alpha^2\gamma r_p^3+12\alpha\gamma^2r_p^3-4\gamma^3r_p^3\right)\right)}\right)^{\frac{1}{3}}+$$
$$\frac{-2r_p^2\gamma^2(\alpha-\gamma)^2}{\left(2\alpha^3\gamma^3r_p^3+27\gamma^4\left(r_i+\tau^o\right)^3+21\alpha^2\gamma^4r_p^3+6\alpha\gamma^5r_p^3-2\gamma^6r_p^3+\sqrt{\gamma^6\left(-4r_p^6(\alpha-\gamma)\right)^6+\left(2\alpha^3r_p^3+21\alpha^2\gamma r_p^3+6\alpha\gamma^2r_p^3+\gamma\left(27\left(r_i+\tau^o\right)^3-2\gamma^2r_p^3\right)^2\right)}\right)^{\frac{1}{3}}}+$$
$$\left.2^{\frac{1}{3}}\left(2\alpha^3\gamma^3r_p^3+27\gamma^4\left(r_i+\tau^o\right)^3+21\alpha^2\gamma^4r_p^3+6\alpha\gamma^5r_p^3-2\gamma^6r_p^3+\sqrt{\gamma^6\left(-4r_p^6(\alpha-\gamma)\right)^6+\left(2\alpha^3r_p^3+21\alpha^2\gamma r_p^3+6\alpha\gamma^2r_p^3+\gamma\left(27\left(r_i+\tau^o\right)^3-2\gamma^2r_p^3\right)^2\right)}\right)^{\frac{1}{3}}\right)$$

WORKS CITED

Acocella, V. and Mulugeta, G. 2001. Surface deformation induced by pluton emplacement: The case of Amiata (Italy). Physics and Chemistry of the Earth (A), **26**: 355-362.

Albee, A. 1961. Boundary Mountain anticlinorium, west-central Maine and northern New Hampshire. United States Geological Survey Professional Paper 424-C.

Albee, A. L. and Boudette, E. L. 1972. Geology of the Attean Quadrangle. United States Geological Survey Bulletin 1297.

Albertz, M., Paterson, S. R., and Okaya, D. 2002. Strain rates during pluton emplacement: Extremely rapid host rock deformation or aureole displacement at background strain rates? Eos (Transactions of the American Geophysical Union), Fall Meeting Supplement, **83**: Abstract T51A-1122.

Aleinikoff, J. N., Zartman, R. E., Walter, M., Rankin, D. W., Lyttle, P. T., and Burton, W. C. 1995. U-Pb ages of metarhyolites of the Catoctin and Mount Rogers Formations, Central and Southern Appalachians: Evidence for two phases of Iapetan rifting. American Journal of Science, **295**: 428-454.

Aleinikoff, J. N., Schenk, W. S., Plank, M. O., Srogi, L., Fanning, C. M., Kamo, S. L., and Bosbyshell, H. in press. Deciphering igneous and metamorphic events in high grade rocks of the Wilmington Complex, Delaware: Morphology, CL and BSE zoning, and SHRIMP U-Pb geochronology of zircon and monazite. Geological Society of America Bulletin.

Avigad, D., Kolodner, K., McWilliams, M., Persing, H., and Weissbrod, T. 2003. Origin of northern Gondwana Cambrian sandstone revealed by detrital zircon SHRIMP dating. Geology, **31**: 227-230.

Ayuso, R. A. 1986. Lead-isotopic evidence for distinct sources of granite and for distinct basements in the northern Appalachians, Maine. Geology, **14**: 322-325.

Barnes, S. J. 1986. The effect of trapped liquid crystallization on cumulus mineral compositions in mayered intrusions. Contributions to Mineralogy and Petrology, **93**: 524-531.

Barton, M. D. and Hanson, R. B. 1989. Magmatism and the development of low-pressure metamorphic belts: Implications from the western United States and thermal modeling. Geological Society of America Bulletin, **101**: 1051-1065.

Bédard, J. H. 1994. A procedure for calculating the equilibrium distribution of trace elements among the minerals of cumulate rocks, and te concentration of trace elements in the coexisting liquids. Chemical Geology, **118**: 143-153.

Bédard, J. H. 1999. Petrogenesis of boninites from the Betts Cove ophiolite, Newfoundland, Canada: identification of subducted source components. Journal of Petrology, **40**: 1853-1889.

Bédard, J. H. 2001. Parental magmas of the Nain Plutonic Suite anorthosites and mafic cumulates: a trace element modelling approach. Contributions to Mineralogy and Petrology, **141**: 747-771.

Bédard, J. H. in press. Partitioning coefficients between olivine and silicate melts. Lithos.

Bédard, J. H. in review-a. Trace element partitioning coefficients between silicate melts and orthopyroxene: Parameterizations of D variations. Chemical Geology.

Bédard, J. H. in review-b. Trace element partitioning coefficients between clinopyroxene and silicate melts: Parameterizations of D variations. Chemical Geology.

Benn, K., Odonne, F., and de Saint-Blanquat, M. 1998. Pluton emplacement during transpression in brittle crust: New views from analogue experiments. Geology, **26**: 1079-1082.

Bibby, H. M., Caldwell, T. G., Davey, F. J., and Webb, T. H. 1995. Geophysical evidence on the structure of the Taupo Volcanic Zone and its hydrothermal circulation. Journal of Volcanology and Geothermal Research, **68**: 29-58.

Biederman, J. L. 1984. Petrology of the Chain Lakes massif along Route 27 in central western Maine: A Precambrian high grade terrane. M.S. Thesis, University of Maine, Orono.

Bindeman, I. N., Davis, A. M., and Drake, M. J. 1998. Ion microprobe study of plagioclase-basalt partition experiments at natural concentration levels of trace elements. Geochimica and Cosmochimica Acta, **62**: 1175-1193.

Bird, P. 1979. Continental delamination and the Colorado Plateau. Journal of Geophysical Research, **84**: 7561-7571.

Black, L. P., Kamo, S. L., Allen, C. M., Davis, D. W., Aleinikoff, J. N., Valley, J. W., Mundil, R., Campbell, I. H., Korsch, R. J., Williams, I. S., and Foudoulis, C. 2004. Improved $^{206}Pb/^{238}U$ microprobe geochronology by the monitoring of a trace-element-related matrix effect; SHRIMP, ID–TIMS, ELA–ICP–MS and oxygen isotope documentation for a series of zircon standards. Chemical Geology, **205**: 115-140.

Bodorkos, S., Sandiford, M., Oliver, N. H. S., and Cawood, P. A. 2002. High-T, low-P metamorphism in the Palaeoproterozoic Hall's Creek Orogen, northern Australia: the middle crustal response to a mantle-related thermal pulse. Journal of Metamorphic Geology, **20**: 217-237.

Bons, P. D. and Cox, S. J. D. 1994. Analogue experiments and numerical modeling on the relation between microgeometry and flow properties of polyphase materials. Materials Science and Engineering, **A175**: 237-245.

Boone, G. M. 1973. Metamorphic stratigraphy, petrology, and structural geology of the Little Bigelow Mountain map area. Maine Geological Survey Bulletin 24.

Boone, G. M. and Boudette, E. L. 1989. Accretion of the Boundary Mountains terrane within the northern Appalachian orthotectonic zone. *In* Mélanges and olistostromes of the U.S. Appalachians, Geological Society of America Special Paper 228. *Edited by* J.W. Horton and N. Rast. pp. 17-42.

Boone, G. M., Doty, D. T., and Heizler, M. T. 1989. Hurricane Mountain Formation mélange: Description and tectonic significance of a Penobscottian accretionary complex. *In* Studies of Maine Geology. *Edited by* R.G. Marvinney and R.D. Tucker. Maine Geological Survey. pp. 33-83.

Boudette, E. L. 1978. Stratigraphy and Structure of the Kennebago Lake Quadrangle, central western Maine. Ph.D. Thesis, Dartmouth College, Hanover, NH.

Boudette, E. L., 1991. Geologic map of the Kennebago Lake quadrangle, Franklin County, Maine, United States Geologic Survey Miscellaneous Investigation I-2058.

Boudette, E. L. 1970. Pre-Silurian rocks in the Boundary Mountains anticlinorium, northwestern Maine. *In* New England Intercollegiate Geological Conference Guidebook. *Edited by* G.M. Boone. pp. C1-C21.

Boudette, E. L. 1982. Ophiolite assemblage of early Paleozoic age in central western Maine. *In* Major structural zones and faults of the northern Appalachians. *Edited by* P. St.-Julien and J. Béland. Geological Association of Canada Special Paper 24. pp. 209-230.

Boudette, E. L. and Boone, G. M. 1982. Diamictite of the Chain Lakes massif of Maine: a possible metasuevite. Geological Society of America Abstracts with Program, **14**: 448.

Boudette, E. L. and Boone, G. M. 1976. Pre-Silurian stratigraphic succession in central western Maine. *In* Contributions to the Stratigraphy of New England, Geological Society of America Memoir 148. *Edited by* L.R. Page. pp. 79-96.

Boudette, E. L., Boone, G. M., and Goldsmith, R. 1989. The Chain Lakes massif and its contact with a Cambrian ophiolite and a Caradocian granite. *In* New England Intercollegiate Geological Conference Guidebook. *Edited by* A.W. Berry. pp. 98-121.

Bradley, D. C., Tucker, R. D., Lux, D. R., Harris, A. G., and McGregor, D. C. 2000. Migration of the Acadian orogen and foreland basin across the northern Appalachians. Professional Paper 1624. United States Geological Survey.

Brown, E. H. and McClelland, W. C. 2000. Pluton emplacement by sheeting and vertical ballooning in part of the southeast Coast Plutonic Complex, British Columbia. Geological Society of America Bulletin, **112**: 708-719.

Brown, M. 1979. The petrogenesis of the St. Malo migmatite belt, Armorican Massif, France, with particular reference to the diatexites. Neues Jahrbuch Fur Mineralogie Abhandlungen, **135**: 48-74.

Brown, M. 2001. Orogeny, migmatites and leucogranites: a review. Proceedings of the Indian Academy of Sciences (Earth and Planetary Sciences), **110**: 313-336.

Brown, M. and Solar, G. S. 1999. The mechanism of ascent and emplacement of granite magma during transpression: a syntectonic granite paradigm. Tectonophysics, **312**: 1-33.

Bruce, P. M. and Huppert, H. E. 1990. Solidification and melting along dykes by the laminar flow of basaltic magma. *In* Magma Transport and Storage. *Edited by* M.P. Ryan. John Wiley & Sons, New York. pp. 87-101.

Brun, J. P., Gapais, D., Cogne, J. P., Ledru, P., and Vigneresse, J.-L. 1990. The Flamanville granite (northwest France): an unequivocal example of a syntectonically expanding pluton. Geological Journal, **25**: 271-286.

Buck, W. R., Martinez, F., Steckler, M. S., and Cochran, J. R. 1988. Thermal consequences of lithospheric extension: pure and simple. Tectonics, **7**: 213-234.

Buddington, A. F. 1959. Granite emplacement with special reference to North America. Geological Society of America Bulletin, **70**: 671-747.

Burroughs, W. A. 1979. Geologic report to accompany the preliminary bedrock geologic map of the Spencer Lake 15' quadrangle, Maine. Maine Geological Survey, Augusta, Maine.

Carslaw, H. S. and Jaeger, J. C. 1959. Conduction of Heat in Solids. Clarendon, Oxford, UK.

Castonguay, S., Ruffet, G., Tremblay, A., and Feraud, G. 2001. Tectonometamorphic evolution of the southern Quebec Appalachians; $^{40}Ar/^{39}Ar$ evidence for Middle Ordovician crustal thickening and Silurian-Early Devonian exhumation of the internal Humber Zone. Geological Society of America Bulletin, **113**: 144-160.

Cawood, P. A. and Nemchin, A. A. 2001. Paleogeographic development of the east Laurentian margin: Constraints from U-Pb dating of detrital zircons in the Newfoundland Appalachians. Geological Society of America Bulletin, **113**: 1234-1246.

Cawood, P. A., McCausland, P. J. A., and Dunning, G. R. 2001. Opening Iapetus: Constraints fron the Laurentian margin in Newfoundland. Geological Society of America Bulletin, **113**: 443-453.

Cawood, P. A., van Gool, J. A. M., and Dunning, G. R. 1995. Collisional tectonics along the Laurentian margin of the Newfoundland Appalachians. *In* Current perspectives in the Appalachian-Caledonian system. *Edited by* J.P. Hibbard, et al. Geological Association of Canada, St. John's. pp. 283-301.

Cesare, B. and Gomez-Pugnaire, M. T. 2001. Crustal melting in the Alboran domain: Constraints from xenoliths of the Neogene volcanic province. Physics and Chemistry of the Earth (A), **26**: 255-260.

Chamberlain, C. P. and Sonder, L. J. 1990. Heat-producing elements and the termal and baric patterns of metamorphic belts. Science, **250**: 763-769.

Cheatham, M. L., Olszewski, W. J., and Gaudette, H. E. 1989. Interpretation of the regional significance of the Chain Lakes massif, Maine based on preliminary

isotopic studies. *In* Studies in Maine Geology. *Edited by* R.G. Marvinney and R.D. Tucker. Maine Geological Survey. pp. 125-137.

Cherniak, D. J., Watson, E. B., Grove, M., and Harrison, T. M. 2002. Pb diffusion in monazite. *In* Abstracts with Programs - Geological Society of America. *Edited by* Geological Society of America (GSA), Boulder. pp. 311.

Chow, J. S. 1995. Origin of tonalites in the Boil Mountain Ophiolite Complex, northwest Maine, and tectonic implications. M.S. Thesis, Boston University, Boston, MA.

Clarke, D. B., Henry, A. S., and White, M. A. 1998. Exploding xenoliths and the absence of 'elephants' graveyards' in granite batholiths. Journal of Structural Geology, **20**: 1325-1343.

Clauser, C. and Huenges, E. 1995. Thermal conductivity of rocks and minerals. *In* Rock Physics and Phase Relations: A Handbook of Physical Constants. AGU Reference Shelf. pp. 105-126.

Clemens, J. D. 1998. Observations on the origins and ascent mechanisms of granitic magmas. Journal of the Geological Society, London, **155**: 843-851.

Clemens, J. D. and Mawer, C. K. 1992. Granitic magma transport by fracture propagation. Tectonophysics, **204**: 339-360.

Clemens, J. D., Petford, N., and Mawer, C. K. 1997. Ascent mechanisms of granitic magmas: causes and consequences. *In* Deformation-enhanced Fluid Transport in the Earth's Crust and Mantle. *Edited by* M.B. Holness. Chapman & Hall, London. pp. 144-171.

Coish, R. A. and Rogers, N. W. 1987. Geochemistry of the Boil Mountain ophiolite complex, northwest Maine, and tectonic implications. Contributions to Mineralogy and Petrology, **97**: 51-65.

Coney, P. J. 1992. The Lachlan belt of eastern Australia and Circum-Pacific tectonic evolution. Tectonophysics, **214**: 1-25.

Corry, C. E., 1988. Laccoliths: mechanics of emplacement and growth. In: *Geological Society of America Special Paper*, pp. 110.

Cousineau, P. A. 1991. The Riviere des Plante ophiolitic mélange: tectonic setting and mélange formation in the Québec Appalachians. Journal of Geology, **99**: 81-96.

Cruden, A. R. 1998. On the emplacement of tabular granites. Journal of the Geological Society, London, **155**: 853-862.

Cruden, A. R. and McCaffrey, K. J. W. 2001. Growth of plutons by floor subsidence: Implications for rates of emplacement, intrusion spacing, and melt-extraction mechanisms. Physics and Chemistry of the Earth (A), **26**: 303-315.

De Yoreo, J. J., Lux, D. R., and Guidotti, C. V. 1991. Thermal modelling in low-pressure/high-temperature metamorphic belts. Tectonophysics, **188**: 209-238.

Decker, E. R. 1987. Heat flow and basement radioactivity in Maine: First-order results and preliminary interpretations. Geophysical Research Letters, **14**: 256-259.

Dewey, J. 1969. Evolution of the Appalachian-Caledonian orogen. Nature, **222**: 124-129.

Dicken, A. P. 2000. Crustal formation in the Grenville Province: Nd-isotope evidence. Canadian Journal of Earth Sciences, **37**: 165-181.

Dorais, M. J. and Paige, M. L. 2000. Regional geochemical and isotopic variations of northern New England plutons: Implications for magma sources and for Grenville

and Avalon basement-terrane boundaries. Geological Society of America Bulletin, **112**: 900-914.

Druguet, E. 2001. Development of high geothermal gradients by coeval transpression and magmatism during the Variscan orogeny: insights from the Cap de Creus (Eastern Pyrenees). Tectonophysics, **332**: 275-293.

Dunlap, W. J., Hirth, G., and Teyssier, C. 1997. Thermomechanical evolution of a ductile duplex. Tectonics, **16**: 983-1000.

Dunning, G. R. and Cousineau, P. A. 1990. U/Pb ages of single zircons from Chain Lakes massif and a correlative unit in ophiolitic mélange in Québec. Geological Society of America Abstracts with Programs, **22**: 13.

Eisenberg, R. A. 1982. Chronostratigraphy and lithogeochemistry of lower Paleozoic rocks from the Boundary mountains, west-central Maine. Ph.D. Thesis, University of California, Berkeley.

England, P. C. and Thompson, A. B. 1984. Pressure-temperature-time paths of regional metamorphism I. Heat transfer during the evolution of regions of thickened continental crust. Journal of Petrology, **25**: 894-928.

England, P. C. and Thompson, A. B. 1986. Some thermal and tectonic models for crustal melting in continental collision zones. *In* Collision Tectonics, Geological Society of London Special Publication 19. *Edited by* M.P. Coward and A.C. Ries. pp. 83-94.

Escuder Virute, J. 1999. One- and two-dimensional thermal modeling of orogenic crustal extension in the Tormes Gneissic Dome, NW Iberian Massif, Spain. International Journal of Earth Sciences, **88**: 444-457.

Fernandez, C. and Castro, A. 1999. Pluton accommodation at high strain rates in the upper continental crust. The example of the Central Extremadura batholith, Spain. Journal of Structural Geology, **21**: 1143-1149.

Ferre, E., Glezizes, G., Bouchez, J.-L., and Nnabo, P. N. 1995. Internal fabric and strike-slip emplacement of the Pan-African granite of the Solli Hills, northern Nigeria. Tectonics, **14**: 1205-1219.

Foster, D. A. and Gray, D. R. 1999. Deformation rates and timing of deformation in the western Lachlan orogen, eastern Australia. Geological Society of America Abstracts with Program, **31**: 301.

Fowler, C. M. R. 1990. The Solid Earth. Cambridge University Press, Cambridge, UK.

Gaetani, G. A. and Grove, T. L. 1995. Partitioning of rare earth elements between clinopyroxene and silicate melt: Crystal-chemical controls. Geochimica and Cosmochimica Acta, **59**: 1951-1962.

Gehrels, G. E., DeCelles, P. G., Martin, A., Ojha, T. P., Pinhassi, G., and Upreti, B. N. 2003. Initiation of the Himalyan Orogen as an Early Paleozoic thin-skinned thrust belt. GSA Today, **13**: 4-9.

Gerbi, C., Johnson, S. E., and Paterson, S. R. 2004. Implications of rapid, dike-fed pluton growth for host-rock strain rates and emplacement mechanisms. Journal of Structural Geology, **26**: 583-594.

Gerbi, C., Johnson, S. E., and Aleinikoff, J. N. in review-a. Origin and orogenic role of the Chain Lakes massif, Maine and Québec. Canadian Journal of Earth Sciences.

Gerbi, C., Johnson, S. E., and Koons, P. O. in review-b. Controls on low-pressure anatexis.

Gerbi, C., Johnson, S. E., Aleinikoff, J. N., Dunning, G. R., Bédard, J., and Fanning, C. M. in review-c. Early Paleozoic development of the Maine-Québec Boundary Mountains region.

Gibson, R. L. 1991. Hercynian low-pressure-high-temperature regional metamorphism and subhorizontal foliation development in the Canigou massif, Pyrenees, France - Evidence for crustal extension. Geology, **19**: 380-383.

Goldsmith, R., 1985. Reconnaissance Geologic Map of the Skinner-Lowelltown Area, Somerset and Franklin Counties, Maine, United States Geological Survey Open-File Report 86-136.

Goodwin, L. B. and Tikoff, B. 2002. Competency contrast, kinematics, and the development of foliations and lineations in the crust. Journal of Structural Geology, **24**: 1065-1085.

Goscombe, B. and Hand, M. 2000. Contrasting P-T paths in the eastern Himalaya, Nepal: inverted isograds in a paired metamorphic mountain belt. Journal of Petrology, **41**: 1673-1719.

Gray, C. M., Kemp, A. I. S., Anderson, J. A. C., Bushell, D. J., Ferguson, D. J., Fitzherbert, J., and Stevenson, M. D. 2002. Delamerian Glenelg tectonic zone, western Victoria: geology and metamorphism of stratiform rocks. Australian Journal of Earth Sciences, **49**: 187-200.

Greenfield, J. E., Clarke, G. L., Bland, M., and Clark, D. J. 1996. In-situ migmatite and hybrid diatexite at Mt Stafford, central Australia. Journal of Metamorphic Geology, **14**: 413-426.

Guidotti, C. V. and Johnson, S. E. 2002. Pseudomorphs and associated microstructures of western Maine, USA. Journal of Structural Geology, **24**: 1139-1156.

Guineberteau, B., Bouchez, J.-L., and Vigneresse, J.-L. 1987. The Mortagne granite pluton (France) emplaced by pull-apart along a shear zone: Structural and gravimetric arguments and regional implications. Geological Society of America Bulletin, **99**: 763-770.

Guiterrez-Alonso, G., Fernandez-Suarez, J., Jeffries, T. E., Jenner, G. A., Tubrett, M. N., Cox, R., and Jackson, S. E. 2003. Terrane accretion and dispersal in the northern Gondwana margin. An Early Paleozoic analogue of a long-lived active margin. Tectonophysics, **365**: 221-232.

Hall, R. 1996. Reconstructing Cenezoic South-East Asia. *In* Tectonic Evolution of Southeast Asia. *Edited by* R. Hall and D.J. Blundell. pp. 153-184.

Handy, M. R., Mulch, A., Rosenau, M., and Rosenberg, C. L. 2001. The role of fault zones and melts as agents of weakening, hardening and differentiation of the continental crust: a synthesis. *In* The nature and tectonic significance of fault zone weakening. Geological Society of London Special Publication. *Edited by* R.E. Holdsworth, R.A. Strachan, J.F. Magloughlin and R.J. Knipe. pp. 305-332.

Hanson, R. B. and Barton, M. D. 1989. Thermal development of low-pressure metamorphic belts: results from two-dimensional numerical models. Journal of Geophysical Research, **94**: 10363-10377.

Harwood, D. S. 1973. Bedrock geology of the Cupsuptic and Arnold Pond quadrangles, west-central Maine. United States Geological Survey Bulletin 1346.

Heizler, M., Lux, D. R., and Decker, E. R. 1988. The age and cooling history of the Chain of Ponds and Big Island plutons and Spider Lake granite, west-central Maine and Quebec. American Journal of Science, **288**: 925-952.

Hey, R. N., Johnson, P. D., Martinez, F., Korenaga, J., Somers, M. L., Huggett, Q. J., LeBas, T. P., Rusby, R. I., and Naar, D. F. 1995. Plate boundary reorganization at a large-offset, rapidly propagating rift. Nature, **378**: 167-170.

Holder, M. T. 1979. An emplacement mechanism for post-tectonic granites and its implications for theri geochemical features. *In* Origin of Granite Batholiths - Geochemical Evidence. *Edited by* M.P. Atherton and J. Tarney. Shiva, Orpington, UK. pp. 116-128.

Holtzman, B., Trzcienski, W., and Gromet, L. P. 1996. New tectonic constraints on the Boil Mountain complex/Chain Lakes unit contact, central western Maine. Geological Society of America Abstracts with Programs, **28**: 65.

Hoskin, P. W. O. and Schaltegger, U. 2003. The composition of zircon and igneous and metamorphic petrogenesis. *In* Zircon. Reviews in Mineralogy and Geochemistry. *Edited by* J.M. Hanchar and P.W.O. Hoskin. Mineralogical Society of America. pp. 27-62.

Houseman, G. A., McKenzie, D. P., and Molnar, P. 1981. Convective instability of a thickened boundary layer and its relevance for the thermal evolution of continental convergent belts. Journal of Geophysical Research, **86**: 6115-6132.

Huerta, A. D., Royden, L. H., and Hodges, K. V. 1998. The thermal structure of collisional orogens as a response to accretion, erosion, and radiogenic heating. Journal of Geophysical Research, **103**: 15287-15302.

Huerta, A. D., Royden, L. H., and Hodges, K. V. 1999. The effects of erosion, accretion, and heat production on the metamorphic evolution of collisional orogens. Journal of Metamorphic Geology, **17**: 349-366.

Hutton, D. H. W. 1982. A tectonic model for the emplacement of the main Donegal granite. Journal of the Geological Society, London, **139**: 615-631.

Hutton, D. H. W. 1988a. Granite emplacement mechanisms and tectonic controls: inferences from deformation studies. Transactions of the Royal Society of Edinburgh, Earth Sciences, **79**: 245-255.

Hutton, D. H. W. 1988b. Igneous emplacement in a shear zone termination: the biotite granite at Strontian, Scotland. Geological Society of America Bulletin, **100**: 1392-1399.

Jamieson, R. A., Beaumont, C., Fullsack, P., and Lee, B. 1998. Barrovian regional metamorphism: Where's the heat? *In* What Drives Metamorphism and Metamorphic Reactions? Geological Society of London Special Publication 138. *Edited by* P.J. Treloar and P.J. O'Brien. pp. 23-51.

Ji, S. and Xia, B. 2002. Rheology of Polyphase Earth Materials. Polytechnic International Press, Montréal.

Johnson, S. E. 1999. Deformation and possible origins of the Cooma Complex, southeastern Lachlan Fold Belt, New South Wales. Australian Journal of Earth Sciences, **46**.

Johnson, S. E., Paterson, S. R., and Tate, M. C. 1999. Structure and emplacement history of a multiple-center, cone-sheet-bearing ring complex: The Zarza Intrusive

Complex, Baja California, México. Geological Society of America Bulletin, **111**: 607-619.

Johnson, S. E., Albertz, M., and Paterson, S. R. 2001. Growth rates of dike-fed plutons: Are they compatible with observations in the middle and upper crust? Geology, **29**: 727-730.

Johnson, S. E., Vernon, R. H., and Upton, P. in press-a. Initiation of microshear zones and progressive strain-rate partitioning in the crystallizing carapace of a tonalite pluton: microstructural evidence and numerical modeling. Journal of Structural Geology.

Johnson, S. E., Fletcher, J. M., Fanning, C. M., Vernon, R. H., Paterson, S. R., and Tate, M. C. in press-b. Structure, emplacement and in-situ expansion of the San José tonalite pluton, Peninsular Ranges batholith, Baja California, México. Journal of Structural Geology.

Johnson, T. E., Brown, M., and Solar, G. S. 2003. Low-pressure subsolidus and suprasolidus phase equilibria in the MnNCKFMASH system: Constraints on conditions of regional metamorphism in western Maine, northern Appalachians. American Mineralogist, **88**: 624-638.

Jones, D. L., Silberling, N. J., and Coney, P. J. 1986. Collision tectonics in the Cordillera of western N America; examples from Alaska. *In* Collision Tectonics, Gelogical Society of London Special Publication 19. *Edited by* M.P. Coward and A.C. Ries. pp. 367-387.

Karabinos, P., Aleinikoff, J. N., and Fanning, C. M. 1999. Distinguishing Grenvillian basement from pre-Taconian cover rocks in the northern Appalachians. American Journal of Science, **299**: 502-515.

Karabinos, P., Samson, S. D., Hepburn, J. C., and Stoll, H. M. 1998. Taconian orogeny in the New England Appalachians: Collision between Laurentia and the Shelburne Falls arc. Geology, **26**: 215-218.

Knipe, R. J. 1989. Deformation mechanisms - recognition from natural tectonites. Journal of Structural Geology, **11**: 127-146.

Kohn, M. J., Spear, F. S., and Valley, J. W. 1997. Dehydration melting andfluid recycling during metamorphism: Rangeley Formation, New Hampshire, USA. Journal of Petrology, **38**: 1255-1277.

Koons, P. O., Zeitler, P. K., Chamberlain, C. P., Craw, D., and Meltzer, A. S. 2002. Mechanical links between erosion and metamorphism in Nanga Parbat, Pakistan Himalaya. American Journal of Science, **302**: 749-773.

Kusky, T. M., Chow, J. S., and Bowring, S. A. 1997. Age and origin of the Boil Mountian ophiolite and Chain Lakes massif, Maine: implications for the Penobscottian orogeny. Canadian Journal of Earth Sciences, **34**: 646-654.

Laird, J., Lanphere, M. A., and Albee, A. L. 1984. Distribution of Ordovician and Devonian metamorphism in mafic and pelitic schists from northern Vermont. American Journal of Science, **284**: 376-413.

Lister, G. S., Etheridge, M. A., and Symonds, P. A. 1986a. Detachment faulting and the evolution of passive continental margins. Geology, **14**: 246-250.

Lister, G. S., Etheridge, M. A., and Symonds, P. A. 1986b. Detachment faulting and the evolution of passive continental margins. Geology, **14**: 246-250.

Loosveld, R. J. H. 1989. The synchronism of crustal thickening and low-pressure facies metamorphism in the Mount Isa inlier, Australia 2. Fast convective thinning of mantle lithosphere during crustal thickening. Tectonophysics, **165**: 191-218.

Loosveld, R. J. H. and Etheridge, M. A. 1990. A model for low-pressure facies metamorphism during crustal thickening. Journal of Metamorphic Geology, **8**: 257-267.

Ludwig, K. R. 2001. Squid. Special Publication No. 2. Berkeley Geochronology Center. Berkeley, CA.

Ludwig, K. R. 2003. Isoplot/Ex. Special Publication No. 4. Berkeley Geochronology Center. Berkeley, CA.

Lundstrom, C. C., Shaw, H. F., Ryerson, F. J., Phinney, D. L., Gill, J. B., and Williams, Q. 1994. Compositional controls on the partitioning of U, Th, Ba, Pb, Sr and Zr between clinopyroxene and haplobasaltic melts: Implications for uranium series disequilibria in basalts. Earth and Planetary Science Letters, **128**: 407-423.

Lux, D. R., de Yoreo, J. J., Guidotti, C. V., and Decker, E. R. 1986. Role of plutonism in low-pressure metamorphic belt formation. Nature, **323**: 794-797.

Lyons, J. B., Aleinikoff, J. N., and Zartman, R. E. 1986. Uranium-thorium-lead ages of the Highlandcroft plutonic suite, northern New England. American Journal of Science, **286**: 489-509.

Marleau, R.-A. 1968. Woburn-East Megantic-Armstrong area, Frontenac and Beauce Counties. Quebec Department of Natural Resources, Geological Report 131.

Marsh, B. D. 1989. Magma chambers. Annual Reviews in Earth and Planetary Sciences, **17**: 439-474.

McCaffrey, K. J. W. and Petford, N. 1997. Are granitic intrusions scale invarient? Journal of the Geological Society, London, **154**: 1-4.

McDaniel, D. K., Sevigny, J. H., Hanson, G. N., and McLennan, S. M. 1997. Grenvillian provenance for the amphibolite-grade Trap Falls Formation: implications for early Paleozoic tectonic history of New England. Canadian Journal of Earth Sciences, **34**: 1286-1294.

McKenzie, D. 1978. Some remarks on the devleopment of sedimentary basins. Earth and Planetary Science Letters, **40**: 25-32.

McKenzie, D. and Bickle, M. J. 1988. The volume and composition of melt generated by extension of the lithosphere. Journal of Petrology, **29**: 625-679.

McLennan, S. M., Bock, B., Compston, W., Hemming, S. R., and McDaniel, D. K. 2001. Detrital zircon geochronology of Taconian and Acadian foreland sedimentary rocks in New England. Journal of Sedimentary Research, **71**: 305-317.

McNicoll, V. J., van Staal, C. R., Lentz, D., and Stern, R. 2002. Uranium-lead geochronology of Middle River rhyolite: implications for the provenance of basement rocks of the Bathurst mining camp, New Brunswick. Geological Survey of Canada Current Research Report 15.

Miller, R. B. and Paterson, S. R. 1999. In defense of magmatic diapirs. Journal of Structural Geology, **21**: 1161-1173.

Miyazaki, K. 2004. Low-P–high-T metamorphism and the role of heat transport by melt migration in the Higo Metamorphic Complex, Japan. Journal of Metamorphic Geology, **22**: 793-809.

Moench, R. H. and Aleinikoff, J. N. 2003. Stratigraphy, geochronology, and accretionary terrane settings of two Bronson Hill arc sequences, northern New England. Physics and Chemistry of the Earth, **28**: 113-160.

Moench, R. H., Boudette, E. L., and Bothner, W. A., 1999. Tectonic lithofacies, geophysical, and mineral-resource appraisal maps of the Sherbrooke-Lewiston area, Maine, New Hampshire, and Vermont, United States and Québec, Canada, United States Geologic Survey Miscellaneous Investigation I-1898-E.

Moench, R. H., Aleinikoff, J. N., and Boudette, E. L. 2000. Revised Early Ordovician age for the ophiolitic Jim Pond Formation, NW Maine: Tectoinic history reappraised. Geological Society of America Abstracts with Program, **32**: 60.

Moench, R. H., Boone, G. M., Bothner, W. A., Boudette, E. L., Hatch, N. L., Hussey, A. M., and Marvinney, R. G., 1995. Geologic map of the Sherbrooke-Lewiston Area, Maine, New Hampshire, and Vermont, United States and Québec, Canada, United States Geologic Survey Miscellaneous Investigation I-1898-D.

Molnar, P., Houseman, G. A., and Conrad, C. P. 1998. Rayleigh-Taylor instability and convective thinning of mechanically thickened lithosphere: effects of non-linear viscosity decreasing exponentially with depth and of horizontal shortening of the layer. Geophysical Journal International, **133**: 568-584.

Molyneux, S. J. and Hutton, D. H. W. 2000. Evidence for significant granite space creation by the ballooning mechanism: The example of the Ardara pluton, Ireland. Geological Society of America Bulletin, **112**: 1543-1558.

Morgan, S. S., Law, R. D., and Nyman, M. W. 1998. Laccolith-like emplacement model for the Papoose Flat pluton based on porphyroblast-matrix analysis. Geological Society of America Bulletin, **110**: 96-110.

Muller, W., Aerden, D., and Halliday, A. N. 2000. Isotopic dating of strain fringe increments: Duration and rates of deformation in shear zones. Science, **288**: 2195-2198.

Murphy, J. B. and Nance, R. D. 2002. Sm-Nd isotopic systematics as tectonic tracers: an example from West Avalonia in the Canadian Appalachians. Earth Science Reviews, **59**: 77-100.

Naylor, R. S., Boone, G. M., Boudette, E. L., Ashenden, D. D., and Robinson, P. R. 1973. Pre-Ordovician rocks in the Bronson Hill and Boundary Mountain Anticlinoria, New England, U.S.A. *In* EOS, Transactions of the American Geophysical Union, Supplement, pp. 495.

Nyman, M. W., Law, R. D., and Morgan, S. S. 1995. Conditions of contact metamorphism, Papoose Flat Pluton, eastern California, USA: implications for cooling and strain histories. Journal of Metamorphic Geology, **13**: 627-643.

O'Brien, S. J., O'Brien, B. H., Dunning, G. R., and Tucker, R. D. 1996. Late Neoproterozoic Avalonian and related peri-Gondwanan rocks of the Newfoundland Appalachains. *In* Avalonian and Related Peri-Gondwanan

Terranes of the North Atlantic. *Edited by* R.D. Nance and M.D. Thompson. Geological Society of America, Boulder, CO

Olivier, P., Gleizes, G., and Paquette, J. L. 2004. Gneiss domes and granite emplacement in an obliquely convergent regime: new interpretation of the Variscan Agly Massif; eastern Pyrenees, France. *In* Gneiss domes in orogeny, Geological Society of America Special Paper 380. *Edited by* D.L. Whitney, C. Teyssier and C.S. Siddoway. Geological Society of America, Boulder, CO. pp. 229-242.

Osberg, P. H., Hussey, A. M., II, and Boone, G. M., 1985. Bedrock Geologic Map of Maine, Maine Geological Survey.

Parrish, R. R. 1990. U-Pb dating of monazite and its application to geological problems. Canadian Journal of Earth Sciences, **27**: 1435-1450.

Paterson, S. R. and Tobisch, O. T. 1992. Rates of processes in magmatic arcs: implications for the timing and mature of pluton emplacement and wall rock deformation. Journal of Structural Geology, **14**: 291-300.

Paterson, S. R. and Fowler, T. K. 1993. Re-examining pluton emplacement processes. Journal of Structural Geology, **15**: 191-206.

Paterson, S. R., Fowler, T. K., and Miller, R. B. 1996. Pluton emplacement in arcs: a crustal-scale exchange process. Transactions of the Royal Society of Edinbugh: Earth Sciences, **87**: 115-123.

Pattison, D. 1992. Stability of andalusite and sillimanite and the Al2SiO5 triple point: Constraints from the Ballachulish aureole, Scotland. Journal of Geology, **100**: 423-446.

Pedersen, T., Heeremans, M., and van der Beek, P. 1998. Models of crustal anatexis in volcanic rifts: applications to southern Finland and the Oslo Graben, southeast Norway. Geophysical Journal International, **132**: 239-255.

Pehrsson, S. J., van Staal, C. R., Herd, R., and McNicoll, V. J. 2003. The Cormacks Lake Complex, Dashwoods Subzone: A window into the deeper levels of the Notre Dame Arc. Current Research - Newfoundland Department of Mines and Energy.

Petford, N. 1996. Dykes or diapirs? Transactions of the Royal Society of Edinburgh: Earth Sciences, **87**: 105-114.

Petford, N., Kerr, R. C., and Lister, J. R. 1993. Dike transport of granitoid magmas. Geology, **21**: 845-848.

Petford, N., Cruden, A. R., McCaffrey, K. J. W., and Vigneresse, J.-L. 2000. Granite magma formation, transport and emplacement in the Earth's crust. Nature, **408**: 669-673.

Pfiffner, O. A. and Ramsay, J. G. 1982. Constraints on geological strain rates: Arguments from finite strain states of naturally deformed rocks. Journal of Geophysical Research, **87**: 311-321.

Pincivy, A., Malo, M., Ruffet, G., Tremblay, A., and Sacks, P. E. 2003. Regional metamorphism of the Appalachian Humber Zone of Gaspe Peninsula; $^{40}Ar/^{39}Ar$ evidence for crustal thickening during the Taconian Orogeny. Canadian Journal of Earth Sciences, **40**: 301-315.

Pinet, N. and Tremblay, A. 1995. Tectonic evolution of the Québec-Maine Appalachians: from oceanic spreading to obduction and collision in the northern Appalachians. American Journal of Science, **295**: 173-200.

Powell, R. and Holland, T. 1990. Calculated mineral equilibria in the pelitic system, KFMASH (K_2O-FeO-MgO-Al_2O_3-SiO_2-H_2O). American Mineralogist, **75**: 367-380.

Prior, D. J., Knipe, R. J., and Handy, M. R. 1990. Estimates of the rates of microstructural changes in mylonites. *In* Deformation Mechanisms, Rheology and Tectonics. Geological Society of America Special Publication. *Edited by* R.J. Knipe and E.H. Rutter. pp. 309-319.

Ramos, V. A. 1988. Late Proterozoic-early Paleozoic of South America - A collisional history. Episodes, **11**: 168-174.

Ramsay, J. G. 1989. Emplacement kinematics of a grainite diapir: The Chindamora batholith, Zimbabwe. Journal of Structural Geology, **11**: 191-209.

Rast, N. 1989. The evolution of the Appalachian chain. *In* The Geology of North America - An overview. *Edited by* A.W. Bally and A.R. Palmer. Geological Society of America, Boulder, CO. pp. 323-348.

Renner, J., Evans, B., and Hirth, G. 2000. On the rheologically critical melt fraction. Earth and Planetary Science Letters, **181**: 585-594.

Richards, S. W. and Collins, W. J. 2002. The Cooma Metamorphic Complex, a low-P, high-T (LPHT) regional aureole beneath the Murrumbidgee Batholith. Journal of Metamorphic Geology, **20**: 119-134.

Rubatto, D., Williams, I. S., and Buick, I. S. 2001. Zircon and monzite response to prograde metamorphism in the Reynolds Range, central Australia. Contributions to Mineralogy and Petrology, **140**: 458-468.

Rubin, A. M. 1995. Getting granitic dikes out of the source region. Journal of Geophysical Research, **100**: 5911-5929.

Rutter, E. H. 1997. The influence of deformation on the extraction of crustal melts: a consideration of the role of melt-assisted granular flow. *In* Deformation-induced Fluid Transport in the Earth's Mantle and Crust, The Mineralogical Society Series 8. *Edited by* M.B. Holness. Chapman and Hall, London. pp. 82-110.

Ryan, P. D. and Soper, N. J. 2001. Modelling anatexis in intra-cratonic rift basins: an example from the Neoproterozoic rocks of the Scottish Highlands. Geological Magazine, **138**: 577-588.

Saint-Blanquat, M. d., Law, R. D., Bouchez, J.-L., and Morgan, S. S. 2001. Internal structure and emplacement of the Papoose Flat pluton: An integrated structural, petrographic, and magnetic susceptability study. Geological Society of America Bulletin, **113**: 976-995.

Sandiford, M. and Powell, R. 1991. Some remarks on high-temperature - low-pressure metamorphism in convergent orogens. Journal of Metamorphic Geology, **9**: 333-340.

Sandiford, M. and Hand, M. 1998a. Australian Proterozoic high-temperature, low-pressure metamorphism in the conductive limit. *In* What Drives Metamorphism and Metamorphic Reactions? Geological Society of London Special Publication 138. *Edited by* P. Treloar and P. O'Brien.

Sandiford, M. and Hand, M. 1998b. Australian Proterozoic high-temperature, low-pressure metamorphism in the conductive limit. *In* What Drives Metamorphism

and Metamorphic Reactions? Geological Society of London Special Publication 138. *Edited by* P. Treloar and P. O'Brien. pp. 109-120.

Sandiford, M., Hand, M., and McLaren, S. 1998. High geothermal gradient metamorphism during thermal subsidence. Earth and Planetary Science Letters, **163**: 149-165.

Sawyer, E. S. 1998. Formation and evolution of granite magmas during crustal reworking: the significance of diatexites. Journal of Petrology, **39**: 1147-1167.

Sawyer, E. S. 1999. Criteria for the recognition of partial melting. Physics and Chemistry of the Earth, **24**: 269-279.

Schmid, S. M. 1989. Episodes in Alpine orogeny. Geological Society of America Abstracts with Program, **21**: 28.

Schott, B. and Schmeling, H. 1998. Delamination and detachment of a lithospheric root. Tectonophysics, **296**: 225-247.

Seydoux-Guillaume, A.-M., Paquette, J.-L., Wiedenbeck, M., Montel, J.-M., and Heinrich, W. 2002. Experimental resetting of the U-Th-Pb systems in monazite. *In* Chemical Geology. *Edited by* F. Poitrasson, U. Schaltegger and J.M. Hanchar. Elsevier, Amsterdam. pp. 165-181.

Smith, C. E. 1997. Mid-crustal processes during Cretaceous rifting, Fosdick Mountains, Marie Byrd Land. *In* The Antarctic Region: Geological Evolution and Processes. *Edited by* C.A. Ricci. Terra Antarctica Publications, Siena, Italy. pp. 313-320.

Spear, F. S., Kohn, M. J., and Cheney, J. T. 1999. P-T paths from anatectic pelites. Contributions to Mineralogy and Petrology, **134**: 17-32.

Spencer, C., Green, A., Morel-a-l'Huisser, P., and Milkereit, B. 1989. The extension of Grenville basement beneath the northern Appalachians: Results from the Quebec-Maine seismic reflection and refraction surveys. Tectonics, **8**: 677-696.

St. Julien, P. and Hubert, C. 1975. Evolution of the Tectonic orogen in the Quebec Appalachians. American Journal of Science, **275-A**: 337-362.

Stacey, J. and Kramers, J. 1975. Approximation of terrestrial lead isotope evolution by a two-stage model. Earth and Planetary Science Letters, **26**: 207-226.

Stewart, D. B., Wright, B. E., Unger, J. D., Phillips, J. D., and Hutchinson, D. R. 1993. Global Geoscience Transect 8: Québec-Maine-Culf of Maine transect, southeastern Canada, northeastern United States of America. United States Geological Survey Miscellaneous Publication I-2329.

Stuwe, K. 2002. Geodynamics of the lithosphere. Springer, Berlin.

Sun, S. S. and McDonough, W. F. 1989. Chemical and isotopic systematics of oceanic basalts: implications for mantle compositions and processes. *In* Magmatism in the ocean basins - Geological Society of London Special Publication. *Edited by* A.D. Saunders and M.J. Norry. pp. 313-345.

Takeda, Y.-T. and Obata, M. 2003. Some comments on the rheologically critical melt percentage. Journal of Structural Geology, **25**: 813-818.

Thompson, P. H. 1989. Moderate overthickening of thinned sialic crust and the origin of granitic magmatism and regional metmaorphism in low-P-high-T terranes. Geology, **17**: 520-523.

Tikoff, B. and Teyssier, C. 1992. Crustal-scale, en echelon 'P-shear' tensional bridges: A possible solution to the batholithic room problem. Geology, **20**: 927-930.

Tikoff, B., Saint-Blanquat, M. d., and Teyssier, C. 1999. Translation and the resolution of the pluton space problem. Journal of Structural Geology, **21**: 1109-1117.

Tomascak, P. B., Brown, M., Solar, G. S., Becker, H. J., Centorbi, T. L., and Tian, J. 2005. Source contributions to Devonian granite magmatism near the Laurentian border, New Hampshire and western Maine, USA. Lithos, **80**: 75-99.

Tremblay, A. and Castonguay, S. 2002. Structural evolution of the Laurentian margin revisited (southern Quebec Appalachians); implications for the Salinian Orogeny and successor basins. Geology, **30**: 79-82.

Trzcienski, W. E., Rogers, J., and Guidotti, C. V. 1992. Alternative hypothesis for the Chain Lakes "massif," Maine and Québec. American Journal of Science, **292**: 508-532.

Tucker, R. D., Osberg, P. H., and Berry, H. N., IV 2001. The geology of a part of Acadia and the nature of the Acadian orogeny across central and eastern Maine. American Journal of Science, **301**: 205-260.

van Staal, C., Dewey, J., MacNiocaill, C., and McKerrow, W. 1998. The Cambrian-Silurian tectonic evolution of the northern Appalachians and British Caledonides: history of a complex, west and southwest Pacific-type segment of Iapetus. *In* Lyell: the Past is the Key to the Present: Geological Society, London, Special Publications. *Edited by* D.J. Blundell and A.C. Scott. pp. 199-242.

van Staal, C., McNicoll, V. J., Valverde-Vaquero, P., Barr, S. M., Fyffe, L. R., and Reusch, D. N., 2004. Ganderia, Avalonia, and the Salinic and Acadian orogenies. In: *Geological Society of America Abstracts with Program*, pp. 128.

van Staal, C. R. 2004. Vendian – Silurian crustal evolution of the Laurentian margin of the Northern Appalachians: from the break-up of Rodinia to the onset of the Devonian Acadian Orogeny. *In* 17th International Basement Tectonics Association Conference: 4–D Framework of Continental Crust, Oak Ridge, TN, pp.

van Staal, C. R., Sullivan, R. W., and Whalen, J. B. 1996. Provenance and tectonic history of the Gander Zone in the Caledonian/Appalachian orogen: Implications for the origin and assembly of Avalon. *In* Avalonian and Related Peri-gondwanan Terranes of the Circum-North Atlantic, Geological Society of America Special Paper 304. *Edited by* R.D. Nance and M.D. Thompson. pp. 347-367.

Vernon, R. H. and Collins, W. J. 1988. Igneous microstructures in migmatites. Geology, **16**: 1126-1129.

Vernon, R. H. and Johnson, S. E. 2000. Transition from gneiss to migmatite and the relationship of leucosome to peraluminous granodiorite in the Cooma Complex, SE Australia. *In* Stress, Strain, and Structure, A volume in honour of W D Mean. Journal of the Virtual Explorer. *Edited by* M.W. Jessel and J.L. Urai.

Waldron, J. F. and van Staal, C. R. 2001. Taconian orogeny and the accretion of the Dashwoods block: A peri-Laurentian microcontinent in the Iapetus Ocean. Geology, **29**: 811-814.

Waldron, J. W. F., Anderson, S. D., Cawood, P. A., Goodwin, L. B., Hall, J., Jamieson, R. A., Palmer, S. E., Stockmal, G. S., and Williams, P. F. 1998. Evolution of the Appalachian Laurentian margin: Lithoprobe results in western Newfoundland. Canadian Journal of Earth Sciences, **35**.

Wernicke, B. 1985. Uniform-sense normal simple shear of the continental lithosphere. Canadian Journal of Earth Sciences, **22**: 108-125.

West, D. P., Guidotti, C. V., and Lux, D. R. 1995. Silurian orogenesis in the western Penobscot Bay region, Maine. Canadian Journal of Earth Sciences, **32**: 1845-1858.

White, J. C. and Mawer, C. K. 1992. Deep-crustal deformation textures along megathrusts from Newfoundland and Ontario: implications for microstructural preservation, strain rates, and strength of the lithosphere. Canadian Journal of Earth Sciences, **29**: 328-337.

Whitehead, J., Reynolds Peter, H., and Spray John, G. 1996. $^{40}Ar/^{39}Ar$ age constraints on Taconian and Acadian events in the Quebec Appalachians. Geology, **24**: 359-362.

Wickham, S. M. and Oxburgh, E. R. 1985. Continental rifts as a setting for regional metamorphism. Nature, **318**: 330-333.

Wickham, S. M. and Oxburgh, E. R. 1987. Low-pressure regional metamorphims in the Pyrenees and its implications for the thermal evolution of rifted continental crust. Philosophical Transactions of the Royal Society of London A, **321**: 219-242.

Wiebe, R. A. and Collins, W. J. 1998. Depositional features and stratigraphic sections in granitic plutons; implications for the emplacement and crystallization of granitic magma. Journal of Structural Geology, **20**: 1273-1289.

Williams, H. and Hatcher, R. D. 1983. Appalachian suspect terranes. *In* Contribution to the tectonics and geophysics of mountain chains, Geological Society of America Memoir 158. *Edited by* R.D. Hatcher, H. Williams and I. Zietz. pp. 33-53.

Williams, H., Coleman-Sadd, S., and Swinden, H. S. 1988. Tectonic-stratigraphic divisions of central Newfoundland. Current Research, **Part B**: 91-98.

Williams, H., Dehler, S. A., Grant, A. C., and Oakey, G. N. 1999. Tectonics of Atlantic Canada. Geoscience Canada, **26**: 51-70.

Williams, H. W., 1978. Tectonic lithofacies map of the Appalachian orogen, Memorial University of Newfoundland.

Yoshinobu, A. S. and Girty, G. H. 1999. Measuring host rock volume changes during magma emplacement. Journal of Structural Geology, **21**: 111-116.

Yoshinobu, A. S., Okaya, D. A., and Paterson, S. R. 1998. Modeling the thermal evolution of fault-controlled magma emplacement models: implications for the solidification of granitoid plutons. Journal of Structural Geology, **20**: 1205-1218.

Zeitler, P. K., Chamberlain, C. P., and Smith, H. A. 1993. Synchronous anatexis, metamorphism, and rapid denudation at Nanga Parbat (Pakistan Himalaya). Geology, **21**: 347-350.

Zen, E.-A. 1995a. Crustal magma generation and low-pressure high-temperature regional metamorphism in an extensional environment; possible application the the Lachlan Belt, Australia. American Journal of Science, **295**: 851-874.

Zen, E.-a. 1995b. Crustal magma generation and low-pressure high-temperature regional metamorphism in an extensional environment; possible application to the Lachlan Belt, Australia. American Journal of Science, **295**: 851-874.

Zen, E.-a. 1983. Exotic terranes in the New England Appalachians - limits, candidates, and ages: A speculative essay. *In* Contribution to the tectonics and geophysics of

mountain chains, Geological Society of America Memoir 158. *Edited by* R.D. Hatcher, H. Williams and I. Zietz. pp. 55-81.

APPENDICES

Appendix A

BEDROCK GEOLOGIC MAP OF THE JIM POND 7.5 MINUTE QUADRANGLE, MAINE

(see back pocket)

Appendix B

FIELD DATA

Table B.1 Field data, organized by station location

Location	Easting[a]	Northing[a]	Map unit[b]	Unit measured (if different)[b]	Data type[c]	Trend or Dip direction	Plunge or Dip
1	381630	5012044	ojg				
2	381623	5011896	ojg				
3	381513	5011858	ojg				
4	381853	5011891	oj				
5	381922	5011802	oj				
6	382061	5011815					
7	382135	5012090	ojg				
8	382002	5012202	ojg				
9	381633	5012626	ojg				
10	379890	5012746	ojf		p	162	51
11	380031	5012609	ojf		p	345	42
12	382269	5014846	t2				
13	381995	5014734	t2		p	445	74
14	381922	5014962	obt				
15	381813	5015063	obt				
16	381832	5015055	ojg	ojk	b	315	55
					b	322	61
					b	337	75
17	381628	5015004	ob				
18	381616	5015081	ojk				
19	381727	5015291	ojg		b	339	70
20	381657	5015529	obt				
21	381619	5015698	obt				
22	380535	5013552	ojg				
23	380536	5013482	obt				
24	380207	5013505	ojf		b	192	87
25	380131	5013431	ojf				
26	380143	5013653	ojk				
27	379952	5014057	ojk		p	150	78
					b	150	78
					b	175	73
28	379835	5014154	ojk		p	175	80
29	379868	5014244	d				
30	379840	5014407	ojk				
31	379797	5014524	ojg				
32	379750	5014771	obt		p	148	87
33	379549	5014914	obt				
35	376016	5015305	sf				
36	375989	5015281	sf		p	318	88
					l	45	57
37	377560	5015528	ob				
38	377402	5015934	sf		p	152	75
					l	77	42
39	383437	5018044	sf		f	121	79

Table B.1 continued

Location	Easting[a]	Northing[a]	Map unit[b]	Unit measured (if different)[b]	Data type[c]	Trend or Dip direction	Plunge or Dip
40	383958	5017803	obt				
41	384137	5017745	obt				
42	384072	5017690	obt				
43	382700	5017208	sf		f	240	70
					f	261	63
44	382893	5016996	sf				
45	381001	5016009					
46	380800	5017174	sf		f	239	79
47	378816	5017971	sf				
48	378574	5017990	sf		f	115	59
49	379052	5017539	sf		f	113	56
50	379012	5014354	obt				
51	379192	5014041	obt				
52	379133	5013929	ojg				
53	378756	5014270	obt				
54	378575	5014107	ojk				
55	378196	5014184	oqp				
56	378270	5013986	ojg				
57	378224	5013902	ojg				
58	377366	5014352	obt		x	141	89
59	376556	5015069	ob		x	444	68
60	376713	5014856	ob				
61	376832	5014809	ob				
62	377893	5013423	ojg		p	158	74
					b	329	87
63	378287	5013340	ojk		p	155	76
64	378114	5013466	ojk				
65	378200	5013345	ojk		p	170	85
					b	170	85
					l	255	62
66	377995	5015849	sf		p	162	80
67	378123	5015803	ob		p	5	78
68	378306	5015876	sf		p	135	77
					l	181	72
69	378361	5015884	sf		p	313	65
					l	11	48
					p	330	62
70	377787	5015765	ob				
71	377743	5016037					
72	378002	5016200	sf				
73	376858	5015617	sf		p	163	87
74	376451	5015101	ob				
75	376434	5015159	ob		p	340	57
76	380046	5012441	ojf				

Table B.1 continued

Location	Easting[a]	Northing[a]	Map unit[b]	Unit measured (if different)[b]	Data type[c]	Trend or Dip direction	Plunge or Dip
77	379978	5012340	ob		x	224	73
					xl	140	19
					x	224	73
					xl	292	51
78	376016	5015152	c		p	99	88
				sf	p	109	81
					p	114	88
					p	155	84
					p	337	88
					l	65	57
79	380908	5016126	obt		x	250	75
					xl	167	24
					j	187	81
80	380852	5016011	obt				
81	380558	5015793	obt				
82	380404	5015768	obt				
83	380323	5015519	obt				
84	380104	5015673	obt		p	149	82
85	379915	5015885	obt				
86	379936	5016004	obt				
87	379945	5016060	obt				
88	380200	5016129	obt		p	158	82
					p	336	81
89	378139	5015777	ob				
90	378251	5015796	sf		p	157	85
					p	331	83
					l	43	69
91	378470	5015800	c		p	312	88
					x	234	61
					xl	250	60
					x	272	61
					xl	182	0
92	378654	5015836	ob	sf	p	311	73
93	379129	5015952	sf				
94	382608	5015724	obt				
95	381758	5015932	obt				
96	381727	5016021	sf				
97	381838	5016132	sf				
98	381742	5015856	oqp				
99	380590	5016969	sf		f	445	64
100	380491	5016804	sf		f	318	88
101	380298	5016752	sf				
102	379206	5011802	ojg				

Table B.1 continued

Location	Easting[a]	Northing[a]	Map unit[b]	Unit measured (if different)[b]	Data type[c]	Trend or Dip direction	Plunge or Dip
103	378959	5011842	ojf		p	176	75
					b	176	75
104	378518	5012495	ojg				
105	378214	5012635	ojg				
106	377342	5013066	ojg		p	334	86
					b	334	86
107	377226	5012781	ojk		p	132	75
108	377275	5012823	ojg		p	143	79
109	377322	5012782					
110	377119	5013360	oqp		p	138	87
111	376960	5013562	oqp				
112	376278	5015011	ob				
113	376818	5014613	ob				
114	378514	5015883	sf				
115	378560	5015864	c		p	151	85
					p	335	89
					l	63	64
116	378619	5015964	sf		p	328	88
117	378637	5015934	ob				
118	378831	5016107	sf				
119	380812	5016737	sf		f	335	88
120	380741	5016558	sf				
121	380723	5016511	sf				
122	380666	5016410	obt				
123	384102	5017652	obt				
124	374538	5014119	c	ob	p	141	81
					p	148	83
					l	65	48
					p	157	72
					p	158	78
125	374368	5014050	c		p	148	64
					l	73	28
					p	166	56
					l	96	27
					p	187	49
					p	210	41
126			shm?				
127	374381	5014246	sf		p	180	77
					l	118	64
128	374398	5014180	sf		p	159	66
					l	176	65
129	374339	5014107	c	sf	p	224	64
				sf	l	164	46
					p	424	77

Table B.1 continued

Location	Easting[a]	Northing[a]	Map unit[b]	Unit measured (if different)[b]	Data type[c]	Trend or Dip direction	Plunge or Dip
130	374296	5014085	c		p	182	77
131	374187	5014169	c		p	154	76
					l	101	67
				sf	p	162	61
132	373940	5014004	ob				
133	373753	5014137	sf		p	169	64
					l	98	33
					p	173	71
134	374071	5014457	sf		p	144	62
					l	200	46
135	376011	5015198	sf		p	281	85
136	376007	5015237	sf		p	430	77
137	374897	5014767	sf		p	107	72
					l	177	47
138	374985	5014666	sf		p	119	75
					p	134	89
139	375029	5014600	c		p	161	88
					p	300	82
					p	317	83
					l	21	74
140	374985	5014493	sf		p	136	66
141	374954	5014464	ob	c	p	116	74
				sf	p	127	77
					p	164	36
					p	324	88
					l	52	42
					p	325	86
142	374624	5014166	c		p	311	78
					l	32	37
143	375649	5014970	ob		p	180	81
145	386302	5051925	ms				
146	384429	5051370	ms				
147	383707	5049364	ms				
148	382263	5050986	ms				
149	382486	5051741	ms				
150	358399	5011814	ob				
151	358193	5011996	ob				
152	357840	5012528	sf				
153	357543	5012482					
154	355102	5012764	sf				
155	354971	5012221	ojg				
156	355730	5012120	ob				
157	356036	5012053	ob				
158	356121	5011922	ojg				

Table B.1 continued

Location	Easting[a]	Northing[a]	Map unit[b]	Unit measured (if different)[b]	Data type[c]	Trend or Dip direction	Plunge or Dip
159	358149	5012223	sf				
160	355844	5010951	ojf		p	164	87
161	377440	5012525	ojg				
162	376940	5012513	ojk				
163	376777	5012529	ojk		p	148	83
164	376874	5012587	ojg				
165	376844	5012679	ojg		p	162	80
166	376602	5012795	ojg		p	150	85
167	376419	5012801	ojg				
168	375916	5012983	ojg		p	142	83
					j	142	83
169	375859	5013213	ojk				
170	375857	5013301	obt				
171	375805	5013220	obt				
172	376009	5014093	obt				
173	373330	5012677	obt				
174	373032	5012297	obt				
175	373701	5011786	ojg				
176	373748	5011960	obt				
177	374120	5013176	ob				
178	374080	5013237	obp				
179	374080	13325	obt		p	176	72
180	373644	5013551	obp				
181	373535	5013539	obp				
182	373434	5013777	sf				
183	383230	5017589	sf				
184	383303	5017801	sf		f	287	82
					f	270	70
185	384200	5017725	sf				
186	377725	5025274	sf		j	184	90
187	377571	5025343	sf		f	2	25
188	377714	5019538	sf		f	150	25
					j	178	65
189	377824	5019363	sf				
190	377813	5019306	sf		f	184	28
					j	199	61
					f	190	15
					f	125	25
					f	158	35
191	377830	5019200	sf		f	178	14
					f	186	35
192	377932	5019052	sf		f	142	35
193	378029	5018835	sf		f	150	18
					f	142	35

Table B.1 continued

Location	Easting[a]	Northing[a]	Map unit[b]	Unit measured (if different)[b]	Data type[c]	Trend or Dip direction	Plunge or Dip
194	378044	5018793	sf		f	148	62
195	378089	5018719	sf		j	129	85
					j	348	76
					j	239	89
196	378135	5018165					
197	379381	5020893	sf		f	96	16
198	379176	5030630	sf				
199	371972	5037831					
200	371972	5038922	sf				
201	374564	5038552	sf				
202	382158	5037656	sf				
203	382185	5037708	sf		p	272	39
					l	308	32
204	377201	5019569	sf		f	257	42
					l	310	28
205	377034	5019600	sf				
206	377029	5019631	amph				
207	376875	5019614	amph	amph	p	344	21
208	376867	5019541	amph				
209	376714	5019519	sf				
210	376523	5019591	amph				
211	376447	5019643	sf				
212	376280	5019948	tb		f	180	20
213	376042	5020227	tb				
214	375997	5020227	tb				
215	375816	5020385	tb				
216	375978	5021146	tb				
217	376022	5021424	tb				
218	376316	5021566	sf				
219	375272	5024446					
220	373795	5022001	sf		j	227	76
					j	286	78
221			sf				
222	373702	5021733	sf		f	306	59
223	373710	5021619	sf				
224	373700	5021500	sf				
225	373671	5021489	gabbro				
226	373658	5021265	sf		x	320	73
227	373628	5021223	sf				
228	373625	5021169	sf		f	118	10
229	373274	5020299	sf				
230	373239	5020238	sf				
231	373180	5020190	sf		x	310	82
232	373162	5020163	sf		f	320	35

Table B.1 continued

Location	Easting[a]	Northing[a]	Map unit[b]	Unit measured (if different)[b]	Data type[c]	Trend or Dip direction	Plunge or Dip
233	373138	5020008	sf	dike	d	43	90
				dike	d	310	90
234	373127	5019939	sf		f	350	35
235	372923	5019544	sf		f	330	35
236	376996	5023927	tb		f	357	21
237	377040	5023475	tb		f	324	40
					f	318	30
238	379904	5023274	tb		f	328	34
239	376753	5023227	tb		f	340	30
240	376533	5023270	tb		f	328	30
241	376241	5023028	tb		f	14	10
242	376367	5022670	tb		f	342	5
243	376288	5022593	tb		f	356	29
244	376360	5022105	tb				
245	377029	5022524	tb				
246	383327	5017744	sf				
247	383965	5017794	sf				
248	374471	5016490	sf		p	146	41
					l	120	40
249	374410	5016352	sf		p	167	71
250	374478	5016163	sf		f	166	65
251	374465	5016062	sf				
252	374349	5016007	sf		l	155	71
					p	155	71
253	373738	5016205	sf				
254	373518	5016360	sf		p	150	49
255	373554	5016507	sf				
256	373545	5016574	sf		f	150	48
257	374205	5018668	sf		f	348	14
258	366870	5011296	obt				
259	366808	5011718	ob				
260	366872	5011749	obt				
261	366755	5011791	ob				
262	366607	5011869	ob				
263	366533	5011922	obt				
264	366475	5011929	ob				
265	366417	5011878	ob		p	336	72
266	367251	5012317	obt				
267	366194	5013366					
268	366507	5013088	ob				
269	386211	5029310	tb		f	300	25
270	386187	5026580	tb		f	146	10
271	386047	5027688	tb				
272	387960	5026403	tb		f	94	50

Table B.1 continued

Location	Easting[a]	Northing[a]	Map unit[b]	Unit measured (if different)[b]	Data type[c]	Trend or Dip direction	Plunge or Dip
273	375996	5016439	sf				
274	375974	5016547	sf		p	146	73
275	375824	5016556	sf				
276	375606	5016650	sf		f	120	30
277	376010	5017126	sf				
278	376115	5016945	sf				
279	376068	5016452	sf				
280	375929	5017806	sf				
281	376653	5018263	amph				
282	377284	5017643	sf				
283	376682	5016396	sf		f	140	67
284	382060	5014843	t2				
285	382019	5015031	t2				
286	381849	5015027	t2				
287	378968	5016702	sf		f	150	20
288	378899	5016781	sf		x	135	70
289	378863	5016829	sf				
290	378698	5017004	sf				
291	378398	5017388	sf				
292	378254	5017962	sf		f	150	30
293	380216	5020385	sf				
294	380189	5020468	sf		f	115	20
					f	126	30
295	380099	5020643	tb				
296	380100	5020766	tb		f	94	20
297	379625	5021281	tb				
298	379576	5021302	tb		f	127	21
299	379001	5021359					
300	378920	5021405	tb		f	196	14
301	378522	5021930	tb		f	3	21
302	378467	5022293	tb		f	2	21
303	380869	5020628	sf		p	144	7
					l	146	7
304	377465	5025326	sf		f	58	25
305	377345	5025368	sf				
306	377206	5025444	sf		f	40	25
307	374079	5019052	sf				
308	374053	5019583	sf				
309	374094	5019749	sf				
310	374256	5019786	sf		f	228	18
311	374324	5019892	tb		f	28	24
312	374439	5019917	sf				
313	374704	5019893	sf				
314	375159	5020151	tb		f	120	7

Table B.1 continued

Location	Easting[a]	Northing[a]	Map unit[b]	Unit measured (if different)[b]	Data type[c]	Trend or Dip direction	Plunge or Dip
315	375639	5019817	sf				
316	375698	5019745	sf				
317	375817	5019561	sf		f	202	15
318	381698	5024560	tb		f	22	24
					l	170	21
					h	203	7
319	381786	5024525	tb		f	342	25
320	388569	5035317	ms		f	278	41
321	388470	5035187	ms				
322	388284	5035006	ms				
323	387069	5037014	ms		p	170	67
324	386238	5037907	sf				
325	385500	5038531	sf				
326	385446	5038570	sf				
327	383739	5038389	ms				
328	377095	5025401	sf		f	56	48
329	376865	5025461	sf		f	62	25
330	377682	5024720	sf				
331	373920	5023924	sf		f	327	28
					f	286	25
332	373838	5024046	sf		p	282	44
333	373808	5024303	sf		f	282	48
334	373618	5024539	sf				
335	373432	5024758	sf		f	282	27
336	373289	5024879	sf				
337	373848	5018163	sf		f	198	42
338	373985	5018105	sf				
339	375874	5015060	sf		p	115	85
					p	61	50
340	375590	5014949	c		p	330	85
					l	52	58
341	383067	5012652	ob				
342	382845	5012609	ojg		p	278	82
343	382491	5012771	ojg		p	358	60
					p	8	58
					l	301	32
344	382415	5012845	carb				
345	382296	5012945	ojf		p	358	85
346	382078	5013307	ojf		p	8	80
347	382366	5013723	ojg				
348	382511	5013827	shm				
349	382385	5013925	shm		p	346	58
350	372090	5019353	sf		f	310	66
351	371796	5019761	sf				

Table B.1 continued

Location	Easting[a]	Northing[a]	Map unit[b]	Unit measured (if different)[b]	Data type[c]	Trend or Dip direction	Plunge or Dip
352	372948	5018801	sf				
353	373713	5018295	sf				
354	373993	5018239	sf		f	246	10
355	374275	5017760	sf				
356	374280	5017471	sf				
357	374751	5016963	sf		p	178	25
358	375148	5016389	sf		p	134	53
359	375618	5015778	sf				
360	375896	5015582	sf		f	146	71
361	375798	5015384	sf				
362	376093	5015273	sf		p	347	80
363	376468	5014987	obp				
364	376676	5014753	obt				
365	376745	5014602	obt				
366	377150	5013825	obt		x	132	70
367	377444	5013100	ojg				
368	371892	5020039	sf				
369	373135	5019837	sf		x	290	87
370	379948	5035593	sf		p	252	57
371	379970	5035633	amph				
372	380129	5035773	sf				
373	377357	5039340	Skinner				
374	383574	5038967	ms				
375	383258	5041050	ms				
376	374096	5018577	sf				
377	373978	5018807	sf		f	8	30
378	374101	5018983	sf		f	4	28
					x	144	80
379	379829	5026310	tb		f	328	16
					f	66	2
380	380094	5026436	tb				
381	380222	5026569	tb		f	167	20
382	380323	5026592	tb		f	282	15
					f	303	7
					l	314	6
383	380466	5026094	tb		f	7	10
384	382297	5033616					
385	371106	5015721	sf		f	140	28
					f	149	42
386	371118	5015911	sf				
387	371315	5016250	sf		f	122	22
388	371753	5016100	sf		f	159	57
389	370873	5015833	sf		p	106	35
390	370847	5015667	sf		p	167	71

Table B.1 continued

Location	Easting[a]	Northing[a]	Map unit[b]	Unit measured (if different)[b]	Data type[c]	Trend or Dip direction	Plunge or Dip
391	366399	5011439	obt				
392	366301	5011729	ob				
393	365963	5011780	obt		p	145	39
394	365782	5011522	ojf				
395	365573	5011537	ob				
396	365188	5011870	obt				
397	364871	5011815	ojf		b	170	64
					p	170	64
					b	152	69
					p	152	69
398	364809	5011867	obt				
399	364496	5011766	ojf		p	162	65
400	365433	5011354	ojf				
401	378410	5037445	sf		f	282	78
402	378162	5037460	ms				
403	377456	5037413	Skinner				
404	377635	5037676	sf		f	281	81
405	373097	5020059	sf				
406	373427	5013726	ob				
407	373607	5013583	obg				
408	382415	5043729	Skinner		p	292	82
409	382129	5044094	Skinner				
410	376563	5039824	Skinner				
411	361623	5010717	obs				
412	361723	5010567	obp				
413	365787	5013793	obp				
414	382094	5014852	t2				
415	384293	5018555	sf				
416	383427	5017654	sf				
417	366243	5015454	sf				
418	365970	5016751	sf		f	148	89
				dike	d	38	90
419	376270	5014990	obp				
420	376514	5039530	Skinner				
421	390799	5036076	Attean				

Table B.1 continued: notes

[a] Measurements refer to UTM grid 19T, NAD83 datum

[b] Codes to unit names

amph	Amphibolite lenses within the Chain lakes massif
Attean	Attean pluton
c	Chain Lakes massif-Boil Mountain Complex contact
d	Diabase dike
gabbro	Unassigned gabbro
ms	McKenney Stream facies of the Chain Lakes massif
ob	Boil Mountain Complex undivided
obg	Gabbro of the Boil Mountain Complex
obp	Ultramafic rocks of the Boil Mountain Complex
obs	Boil Mountain Complex serpentinite
obt	Tonalite of the Boil Mountain Complex
oj	Jim Pond Formation, undivided
ojf	Metasediments of the Jim Pond Formation
ojg	Greenstone member of the Jim Pond Formation
ojk	Felsic volcanic rocks of the Jim Pond Formation
sf	Sarampus Falls facies of the Chain Lakes massif
shm	Hardwood Mtn. Formation
Skinner	Skinner pluton
t2	Second tonalite body
tb	Twin Bridges facies of the Chain Lakes massif

[c] Code for data type

b	Bedding
c	Cleavage
d	Dike trend
f	Compositional banding
h	Hinge line
j	Joint
l	Lineation (stretching)
p	Penetrative foliation
x	Brittle fault
xl	Fault slickensides

Appendix C

ELECTRON PROBE CHEMICAL ANALYSES OF MUSCOVITE

Table C.1 Electron probe chemical analyses of muscovite in formula units

Sample	GCL382	GCL382	GCL382	GCL382	GCL382	GCL382	GCL382	GCL235	GCL235	GCL235	GCL235
Analysis	box2ms	box2ms	box4ms	box4ms	box1ms	box1ms	ms at bt1	box3ms	box3ms	box2ms	box2ms
Na_2O	0.14	0.14	0.14	0.14	0.15	0.15	0.14	0.11	0.11	0.09	0.11
MgO	0.09	0.08	0.08	0.08	0.08	0.08	0.09	0.08	0.11	0.15	0.11
Al_2O_3	5.46	5.54	5.52	5.64	5.54	5.59	5.59	5.48	5.29	5.23	5.34
SiO_2	6.14	6.15	6.10	6.14	6.12	6.10	6.17	6.13	6.16	6.21	6.13
K_2O	1.80	1.83	1.78	1.85	1.81	1.80	1.78	1.79	1.82	1.89	1.88
CaO	0.00	0.00	0.00	0.00	0.00	0.00	0.00	0.03	0.00	0.00	0.00
TiO_2	0.14	0.06	0.11	0.00	0.10	0.08	0.01	0.09	0.13	0.08	0.11
Cr_2O_3	0.00	0.00	0.00	0.00	0.00	0.00	0.00	0.00	0.00	0.00	0.00
MnO	0.00	0.00	0.02	0.00	0.00	0.00	0.00	0.00	0.00	0.00	0.01
FeO	0.20	0.20	0.23	0.19	0.19	0.19	0.21	0.29	0.41	0.44	0.40
wt% total	94.27	94.79	94.53	94.14	94.35	94.38	94.30	94.04	94.83	94.34	94.49
Fe/(Mg+Fe)	0.69	0.71	0.74	0.71	0.71	0.71	0.70	0.79	0.79	0.75	0.79
Na/(Na+K)	0.07	0.07	0.07	0.07	0.08	0.08	0.07	0.06	0.06	0.05	0.06
Al/(Si+Al)	0.47	0.47	0.47	0.48	0.48	0.48	0.48	0.47	0.46	0.46	0.47
Note	coarse	coarse	coarse	coarse	coarse	coarse	coarse	coarse	coarse	coarse	coarse

Table C.1 continued

Sample	GCL235	GCL235	GCL235	GCL235	GCL235	GCL235	GCL235	GCL193	GCL193	GCL193	GCL193
Analysis	box1ms	box1ms	box2fms	box2fms	box1fms	box3fms2	box3fms1	ms_m	ms_m	ms_m	ns_pseud
Na_2O	0.11	0.11	0.06	0.06	0.12	0.12	0.07	0.17	0.17	0.17	0.19
MgO	0.08	0.10	0.33	0.34	0.13	0.25	0.28	0.09	0.09	0.10	0.10
Al_2O_3	5.52	5.39	4.83	4.75	5.37	4.91	4.88	5.66	5.63	5.66	5.25
SiO_2	6.08	6.15	6.47	6.48	6.21	6.41	6.38	6.11	6.16	6.13	6.53
K_2O	1.81	1.82	1.90	1.89	1.88	1.87	1.86	1.78	1.78	1.78	1.62
CaO	0.02	0.00	0.00	0.08	0.00	0.01	0.00	0.00	0.00	0.00	0.00
TiO_2	0.12	0.09	-0.02	-0.01	0.00	0.04	0.02	0.02	0.01	0.01	0.00
Cr_2O_3	0.00	0.00	0.00	0.00	0.00	0.00	0.00	0.00	0.00	0.00	0.00
MnO	0.00	0.00	0.00	0.01	0.00	0.00	0.00	0.00	0.00	0.00	-0.03
FeO	0.26	0.37	0.54	0.54	0.40	0.49	0.63	0.18	0.14	0.15	0.09
wt% total	94.89	95.04	94.12	94.36	94.43	95.27	94.90	94.57	94.81	94.64	94.61
Fe/(Mg+Fe)	0.77	0.79	0.62	0.61	0.75	0.66	0.69	0.67	0.60	0.60	0.47
Na/(Na+K)	0.06	0.06	0.03	0.03	0.06	0.06	0.03	0.09	0.09	0.09	0.10
Al/(Si+Al)	0.48	0.47	0.43	0.42	0.46	0.43	0.43	0.48	0.48	0.48	0.45
Note	coarse	coarse	plag. alteration	plag. alteration	coarse	plag. alteration	plag. alteration	coarse	coarse	coarse	fine

Table C.1 continued

Sample	GCL193	GCL193	GCL193	GCL227-1	GCL227-1	GCL227-1	GCL227-1	GCL227-1	GCL227-1	GCL227-1
Analysis	mscg1-1	mscg1-2	mscg1-3	ms2sil-1	ms2sil-2	ms2sil-3	ms2sil-4	ms1cg-1	ms1cg-2	ms1cg-3
Na_2O	0.14	0.17	0.17	0.16	0.17	0.16	0.16	0.16	0.16	0.16
MgO	0.50	0.10	0.10	0.13	0.15	0.12	0.15	0.17	0.16	0.14
Al_2O_3	5.13	5.66	5.65	5.38	5.31	5.41	5.36	5.42	5.39	5.32
SiO_2	6.08	6.13	6.14	6.16	6.16	6.16	6.16	6.17	6.21	6.17
K_2O	1.78	1.74	1.81	1.78	1.77	1.77	1.78	1.74	1.80	1.76
CaO	0.00	0.00	0.00	0.00	0.00	0.00	0.00	0.00	0.00	0.00
TiO_2	0.00	0.01	0.01	0.06	0.08	0.07	0.07	0.00	0.00	0.08
Cr_2O_3	0.00	0.00	0.00	0.00	0.00	0.00	0.00	0.00	0.00	0.00
MnO	0.01	0.00	0.00	0.00	0.00	0.00	0.00	0.01	0.00	0.00
FeO	0.66	0.17	0.15	0.40	0.43	0.33	0.39	0.40	0.36	0.44
wt% total	94.73	95.58	94.93	93.79	93.77	94.22	94.23	93.47	93.93	93.62
Fe/(Mg+Fe)	0.57	0.62	0.61	0.75	0.73	0.73	0.73	0.70	0.69	0.75
Na/(Na+K)	0.07	0.09	0.08	0.08	0.09	0.08	0.08	0.08	0.08	0.08
Al/(Si+Al)	0.46	0.48	0.48	0.47	0.46	0.47	0.47	0.47	0.46	0.46
Note	coarse	coarse	coarse	coarse	coarse	coarse	coarse	coarse	coarse	coarse

Table C.1 continued

Sample	GCL227-1	GCL227-1	GCL227-1
Analysis	ms1ps-1	ms1ps-2	ms1ps-3
Na_2O	0.07	0.10	0.16
MgO	0.40	0.20	0.20
Al_2O_3	4.92	5.33	5.46
SiO_2	6.33	6.26	6.17
K_2O	1.82	1.82	1.79
CaO	0.01	0.00	0.00
TiO_2	0.02	0.00	0.00
Cr_2O_3	0.00	0.00	0.00
MnO	0.00	0.00	0.00
FeO	0.58	0.34	0.30
wt% total	93.73	94.40	94.46
Fe/(Mg+Fe)	0.59	0.63	0.60
Na/(Na+K)	0.03	0.05	0.08
Al/(Si+Al)	0.44	0.46	0.47
Note	fine	fine	fine

Appendix D

CHEMICAL MODELING PARAMETERS

Table D.1 Sample Table of Partition Coefficients

	CPX	OPX	Plagioclase	Olivine	Cr-Spinel
Cs	0.0014	0.555	0.0443	0.0049	0.0001
K	0.0029	0.0165	0.0798	0.0049	0.0001
Rb	0.0021	0.0165	0.0153	0.0049	0.0002
Ba	0.00067	0.0013	0.1805	0.0026	0.0005
Th	0.0062	0.0199	0.0074	0.0267	0.001
U	0.0046	0.0054	0.0181	0.0479	0.001
Nb	0.0044	0.0094	0.0102	0.004	0.01
Ta	0.0114	0.0216	0.0102	0.0714	0.01
La	0.0457	0.0034	0.114	0.00019	0.0006
Ce	0.0702	0.0057	0.1066	0.00041	0.0006
Pr	0.1017	0.0094	0.0956	0.00084	0.0006
Pb	0.0162	0.0318	0.4571	0.006	0.0006
Sr	0.0915	0.0318	1.5303	0.0078	0.0006
P	0.0421	0.0411	0.0579	0.0101	0.0006
Nd	0.1394	0.0151	0.0824	0.0017	0.0006
Sm	0.2135	0.0319	0.0576	0.0049	0.0006
Zr	0.0544	0.022	0.0017	0.0284	0.015
Hf	0.1525	0.0492	0.0017	0.0132	0.015
Ti	0.2871	0.0276	0.0328	0.029	0.125
Eu	0.1823	0.038	0.0481	0.0105	0.0006
Gd	0.2715	0.0567	0.0385	0.0112	0.0006
Tb	0.2931	0.0737	0.0305	0.0164	0.0011
Dy	0.3078	0.0941	0.0237	0.0232	0.0015
Y	0.3129	0.1085	0.0201	0.0285	0.002
Ho	0.3142	0.1162	0.0185	0.0314	0.0023
Er	0.314	0.1394	0.0145	0.0407	0.003
Tm	0.3087	0.1629	0.0115	0.0507	0.0038
Yb	0.3001	0.186	0.0092	0.0612	0.0045
Lu	0.2898	0.2079	0.0076	0.0716	0.0045
Ga	0.2686	0.2775	2	1.67	4
Cr	7.3	5.79	0.0326	1.225	
Co	0.7939	1.78	0.076	5.23	4
Ni	1.04	1.33	0.1201	23	10
Cu	0.263	0.0432	0.8	0.11	1
Zn	0.2398	1.78	0.0478	1.67	4
V	3.1	0.4706	0.03	0.15	10
Sc	7.32	1.07	0.0409	0.2795	0.1

This Table is appropriate to sample 112b and was calculated according to the methods of Bédard (in press, in review a, b), for an MgO (melt) content of 5.81, and a clinopyroxene Al^{iv} content of 0.075. Plagioclase D values are from an unpublished ms, and are appropriate for an An content of 83.99 (molar). The Cr-spinel data are from Bédard (1994, 2001). A different set of D values was calculated for every inversion calculation.

Table D.2 Results of Inversion Modeling, Preferred Solutions

	GCL 89	GCL 89	GCL 112b	GCL 131a	GCL 407	GCL 407	GCL 411	GCL 412	GCL 413	GCL 419
TMF	0.2	0.05	0.15	0.3	0.2	0.85	0.25	0.15	0.2	0.1
MgO melt wt%	4	4	6.04	6.1	4	8	7.33	4.23	5.57	4
Cs	0.09	0.155	nd	nd	nd	nd	nd	nd	nd	nd
K	813	2659	725	nd	997	289	nd	5866	nd	nd
Rb	2.44	8.81	1.368	nd	nd	nd	nd	nd	nd	nd
Ba	69.2	206.4	7.95	46.5	37.7	13.7	7.98	72.5	44.6	31.8
Nb	0.142	0.501	0.17	11.9	13.8	3.39	9.08	38.9	20.3	15.6
La	1.768	4.19	0.769	2.775	4.51	1.41	1.59	1.76	1.9	5.19
Ce	6.56	13.95	1.88	4.64	14.3	4.48	2.99	3.12	4.44	9.19
Pr	1.436	2.752	0.287	0.449	2.378	0.743	0.331	0.674	0.461	1.165
Pb	4.12	8.17	3.44	nd	nd	nd	nd	nd	nd	56.1
Sr	69	72.2	10.8	142	293	315	3.95	28.4	23.1	130
P	nd	nd	nd	135	891	254	nd	nd	nd	nd
Hf	0.551	0.933	0.23	0.884	3.62	0.985	1.058	4.99	1.99	1.031
Ti	4936	7090	2162	909	14000	4378	551	6553	682	4482
Eu	0.974	1.439	0.353	0.166	2.14	0.671	nd	0.914	nd	0.369
Gd	5.2	7.31	1.084	0.494	6.94	2.19	nd	3.6	0.592	2.23
Tb	0.844	1.138	0.176	nd	1.4	0.446	nd	0.777	nd	0.447
Dy	5.56	7.24	1.18	0.689	9.04	2.88	nd	4.64	0.575	2.74
Y	28.1	35.8	6.54	4.67	47.6	15.21	nd	24.3	3.91	12.1
Ho	1.055	1.32	0.218	nd	1.96	0.627	nd	0.966	nd	0.575
Er	2.85	3.48	0.602	0.524	6.398	2.053	nd	2.813	nd	1.786
Tm	0.383	0.463	0.0815	nd	1.008	0.324	nd	0.392	nd	0.264
Yb	2.38	2.85	0.513	0.6	6.19	2	nd	2.21	nd	1.62
Lu	0.35	0.415	0.0753	0.0925	1.01	0.326	nd	0.348	nd	0.247
Ga	nd	nd	nd	2.67	9.73	13.8	1.91	4.37	0.878	8.57
Cr	271	255	653	361	13.8	24.7	809	173	273	151
Co	42.9	43.8	28.8	39.3	12.9	22.1	46.2	27.1	35.8	41.7
Ni	60.8	60.9	37.6	85.9	4.76	16	162	10.5	32.5	70.4
Cu	266	334	45.2	39.5	49.6	32.8	298	447	265	811
Zn	87.1	91.8	48.7	36.7	97.1	79.7	58.6	71.8	43.3	74.5
V	112	113	102	65.4	547	403	16.1	280	107	118
Sc	15.2	14.8	13.9	14.3	36.4	61.1	14	43.4	26.7	15.9

Table D.2 continued

	83-5	83-27	83-30	83-32	83-70	83-83	83-85	83-106	83-133
TMF	0.1	0.3	0.1	0.2	0.1	0.2	0.1	0.2	0.2
MgO melt wt %	6.82	4.89	4	4.77	4.17	5.65	4	4	4
K	2101	80990	2830	1183	737	1614	5631	5786	nd
Rb	111	309	130	67.3	144	14.6	137	86.4	nd
Ba	nd	2104	nd	nd	350	nd	322	70.3	nd
La	nd	nd	nd	nd	nd	nd	nd	nd	5.92
Ce	nd	nd	nd	nd	nd	nd	nd	nd	13.7
Sr	53.5	66.7	57.2	52.6	68.2	nd	25.4	100	nd
P	301	119	287	179	322	616	298	184	nd
Hf	nd	nd	nd	nd	nd	nd	nd	nd	1.3
Ti	2673	1402	4481	2424	2437	537	4419	4692	nd
Eu	nd	nd	nd	nd	nd	nd	nd	nd	1.45
Tb	nd	nd	nd	nd	nd	nd	nd	nd	0.737
Y	15.1	nd	nd	21	15.1	17.3	24.5	14.1	nd
Yb	nd	nd	nd	nd	nd	nd	nd	nd	2.36
Lu	nd	nd	nd	nd	nd	nd	nd	nd	0.398
Cr	503	462	129	408	447	1500	282	35.2	nd
Ni	45.1	10.3	14.5	90.5	36.6	93.5	22.4	nd	nd
Sc	nd	nd	nd	nd	nd	nd	nd	nd	6.86

Appendix E

SKINNER PLUTON GEOCHEMISTRY

Table E.1 Geochemistry of the Skinner pluton

SAMPLE		GCL-421	GCL-410	GCL-373	GCL-373 Rep	GCL-409
SiO_2	%	77.17	65.09	70.99		69.85
Al_2O_3	%	12.77	14.13	14.41		13.79
Fe_2O_3	%	1.18	6.24	3.43		4.40
MnO	%	0.073	0.120	0.081		0.078
MgO	%	0.35	2.13	1.05		1.46
CaO	%	0.48	5.04	2.87		2.30
Na_2O	%	4.02	1.87	2.76		2.72
K_2O	%	3.22	1.69	2.72		2.36
TiO_2	%	0.079	0.414	0.345		0.544
P_2O_5	%	0.03	0.08	0.10		0.12
LOI	%	0.76	2.08	1.57		2.53
TOTAL	%	100.12	98.88	100.33		100.14
Ba		772	393	687		660
Sr		78	130	190		152
Y		36	12	20		29
Sc		12	25	14		17
Zr		63	106	153		263
Be		1	2	2		2
V		-5	141	54		61
V		5	128	49	50	56
Cr		-20	-20	-20	-20	22
Co		-1	13	6	6	8
Ni		-20	-20	29	-20	-20
Cu		-10	23	-10	-10	13
Zn		39	98	42	56	75
Ga		15	14	15	15	17
Ge		3	2	2	2	2
As		-5	-5	-5	-5	-5
Rb		93	54	79	81	88
Sr		74	130	182	191	150
Y		38	13	22	23	32
Zr		78	106	158	176	283
Nb		13	7	10	11	12
Mo		-2	-2	-2	-2	-2
Ag		-0.5	-0.5	-0.5	-0.5	-0.5
In		-0.2	-0.2	-0.2	-0.2	-0.2
Sn		2	1	2	2	2
Sb		-0.5	-0.5	1.0	0.5	-0.5
Cs		1.1	0.5	0.8	0.8	0.7
Ba		787	395	701	714	683
La		27.1	22.1	31.5	31.5	56.5
Ce		59.7	42.3	62.2	62.3	114
Pr		6.86	4.43	6.77	6.89	12.8
Nd		26.4	15.5	24.5	25.4	47.7
Sm		6.5	2.8	4.7	4.8	8.6
Eu		1.15	0.69	1.01	1.09	1.64
Gd		6.6	2.4	4.3	4.3	7.4

Table E.1 continued

SAMPLE	GCL-421	GCL-410	GCL-373	GCL-373 Rep	GCL-409
Tb	1.1	0.4	0.7	0.7	1.0
Dy	6.5	2.2	3.8	3.9	5.4
Ho	1.3	0.4	0.7	0.7	1.1
Er	4.3	1.5	2.5	2.6	3.3
Tm	0.70	0.23	0.38	0.41	0.48
Yb	4.2	1.5	2.4	2.6	2.9
Lu	0.66	0.24	0.40	0.42	0.44
Hf	3.2	3.0	4.5	5.4	7.2
Ta	0.8	0.5	0.8	0.8	0.6
W	-1	-1	-1	-1	-1
Tl	0.7	0.4	0.7	0.8	0.6
Pb	14	6	16	17	16
Bi	-0.4	-0.4	-0.4	-0.4	-0.4
Th	7.9	7.3	8.3	8.5	14.2
U	1.8	1.0	1.5	1.6	1.1

Notes:
Values in ppm unless otherwise noted
Analyses in italics by ICP-MS; others by ICP-AES
Negative value indicates concentration below detection limits
Analyses done by Activation Laboratories

BIOGRAPHY OF THE AUTHOR

Christopher Charles Gerbi was born on 12 December 1973 and raised in Concord, NH. A 1992 graduate of Concord High School, Chris entered Amherst College with plans to major in physics. After being exposed to geology, Chris quickly changed his plans. He undertook independent research in his senior year through the Keck Consortium, traveling to Cyprus to study the Troodos ophiolite, a fragment of oceanic crust thrust up on land. After graduating *summa cum laude* in May, 1996, Chris began graduate work at the University of California, Davis. His research there was based in Argentina, studying a terrane that had traveled from North America to South America over 450 million years ago. In July 1998, Chris married. Chris's third year in California he spent finishing his M.S. thesis, graduating in June 1999, and teaching mathematics at Lick-Wilmerding High School in San Francisco. Returning to New Hampshire in summer 1999, Chris and his wife took positions at Cardigan Mountain School, a junior boys boarding school. After this second year of teaching mathematics, Chris enrolled in the Ph.D. program at the University of Maine. Chris is a candidate for the Doctor of Philosophy degree in Earth Sciences from The University of Maine in May, 2005.